

ABSTRACT

BAHMANPOUR, HAMED. Synthesis and Deformation Behavior of Nanocrystalline Copper Alloys. (Under the supervision of Prof. Carl C. Koch and Prof. Ronald. O. Scattergood.)

It is well known that grain size has a significant effect on mechanical properties of metals and alloys. There has been a concern about the efficiency of the processing techniques for grain refinement and production of bulk artifact-free samples. Besides that, addition of solutes can dramatically change the stacking fault energy which in turn can have major effects on mechanical behavior. This research describes processing and deformation behavior of ultrafine grained and nanocrystalline copper base alloys.

Stacking fault energy was systematically changed in Cu-Zn and Cu-Zn-Al systems to study its effect on microstructure and deformation behavior. Considering the effect of deformation twins and stacking faults on deformation mechanisms and mechanical properties, different processing methods and conditions were shown to produce different results.

It was found that high energy ball milling at liquid nitrogen temperature can reduce the grain size of copper and copper base alloys down to 5nm. The grain size and hardness of the milling product saturates after 6-8h milling at liquid nitrogen temperature. A combination of cryomilling and room temperature milling resulted in production of sound artifact-free spheres with a homogeneous microstructure that were used for tensile tests. Furthermore, the product of the ball milling was used as a precursor for consolidation by HPT. It was found

that ultrahigh strain HPT deformation can successfully produce bulk nanocrystalline samples. Rolling and wire drawing at liquid nitrogen temperature were also utilized to obtain microstructures in ultrafine grain size regime to be compared with their coarse grained and nanocrystalline counterparts.

It was found that lowered stacking fault energy in Cu-Zn and Cu-Zn-Al systems facilitates twinning in favor of dislocation activity. When processing temperature is concerned, deformation at liquid nitrogen temperature increases the propensity of deformation via twinning in copper and copper alloys. Therefore, the utilized processing method, depending on the degree of deformation, could produce microstructures decorated with deformation twins and stacking faults.

In situ consolidated nanocrystalline Cu-12.1at.%Al-4.1at.%Zn with a low stacking fault energy of 7 mJ/m^2 was shown to have a high yield strength, 1067 MPa, compared with nanocrystalline copper with the same grain size, resulted from high density of deformation twins and stacking faults. The same composition, processed via rolling at liquid nitrogen, exhibited abundant deformation twins that did not significantly contribute to the mechanical response considering their size and distribution in the microstructure.

Nanocrystalline Cu-Zn alloys were processed with high energy ball milling followed by a consolidation step by high pressure torsion. As shown by tensile test results and electron microscopy studies the breakdown of Hall-Petch relation, for the first time, was found in Cu-30wt.%Zn. A high density of finely spaced deformation twins were observed in the microstructure that arise from high frequency multi directional forces during the ball milling

process. The softening behavior and breakdown of the Hall-Petch relation was attributed to detwinning.

Synthesis and Deformation Behavior of Nanocrystalline Copper Alloys

by
Hamed Bahmanpour

A dissertation submitted to the Graduate Faculty of
North Carolina State University
in partial fulfillment of the
requirements for the Degree of
Doctor of Philosophy

Materials Science and Engineering

Raleigh, North Carolina

2012

APPROVED BY:

Prof. Korukonda Murty

Prof. Yuntian T. Zhu

Prof. Carl C. Koch
Chair of Advisory Committee

Prof. Ronald. O. Scattergood
Co-Chair of Advisory Committee

DEDICATION

This work is dedicated to my loving family.

My forever love, Zahra, who means the world to me.

My parents, Ahmadreza and Ghodsieh, who have been always supporting to me.

My brother, Hanif, and my sisters, Zahra and Zeinab, whom I am proud of.

BIOGRAPHY

Hamed Bahmanpour was born in Najafabad, Iran on March 12, 1983 to Ahmadreza and Ghodsieh. After moving to Tehran at the age of 12 and finishing high school in Saheb Kowsar school, he got admission to Amirkabir University of Technology (Tehran Polytechnic) majoring in Metallurgical engineering. Hamed attended nationwide exam for graduate studies and got admitted to the School of Metallurgy and Materials Science and University of Tehran in 2004. Working in the field of synthesizing nanomaterials and microstructural studies of titanium alloys attracted his interest to research on the microstructure-properties relationship. Hamed came to US in 2008 and joined Profs. Koch and Scattergood group at North Carolina State University and took his PhD in Materials Science and Engineering in Jan 2012.

ACKNOWLEDGMENTS

I would like to sincerely thank all the members of my research group for their helpful discussions all over my PhD. Special appreciation is deserved for Dr. Koch and Dr. Scattergood for their great supervision, guidance, and support throughout this work. I would also like to thank Dr. Murty and Dr. Zhu for being members of my PhD committee and for thoughtful comments for editing this dissertation.

Many thanks to Dr. Eckert and Dr. Zehetbauer for their useful discussions, support for the experimental work, and inviting me for research stay at IFW, Dresden and University of Vienna. I would like to thank Dr. Youssef for helping me in experimental work at NCSU and sharing his experience in the field with me. I am grateful to all Materials World Network project members (Daria Setman, Jelena Horiky, Michael Kerber, Erhard Schafner, Mohsen Samadi Khoshkhou, Alexander Kauffmann, Miroslava Sakaliyska, Jens Freudenberger, and Sergio Scudino) for their help and contribution to this work.

I would also like to thank Edna Deas who gave me so much help on a daily basis since my admission to NCSU until my graduation.

Financial support from National Science Foundation under contract DMR-0806323 is gratefully acknowledged.

Finally, I would like to thank my wife, Zahra, for her great encouragement, patience, and understanding all along the way.

TABLE OF CONTENTS

LIST OF TABLES.....	xi
LIST OF FIGURES.....	xiii
1.0 CHAPTER ONE.....	1
1.0 INTRODUCTION.....	1
2.0 CHAPTER TWO.....	6
2.0 LITERATURE REVIEW.....	6
2.1 Introduction.....	6
2.2 Synthesis of ultrafine grain and nanostructure metals and alloys.....	7
2.2.1 Top-down synthesis methods.....	8
High pressure torsion.....	8
Equal channel angular pressing.....	13
High energy ball milling.....	15
Combined techniques.....	17
2.3 Mechanical properties of nanostructured metals and alloys.....	17
2.3.1 Hall-Petch relation.....	19
Hall-Petch theory.....	20
Cottrel's theory.....	21
Li's theory.....	22
Meyers-Ashworth theory.....	23
2.3.2 Breakdown of Hall-Petch relation in nanocrystalline regime.....	25
2.3.3 Stacking fault energy.....	27

2.3.4. Stacking fault energy effects on microstructure and mechanical properties.....	28
Twinning.....	30
Strength.....	32
Strain hardening and ductility.....	35
Strain rate sensitivity.....	38
2.4 References.....	41
3.0 CHAPTER THREE.....	47
3.0 EXPERIMENTAL PROCEDURE.....	47
3.1 Processing.....	47
3.1.1 Ball milling.....	47
3.1.2 High pressure torsion.....	49
3.1.3 Preparing master alloys for rolling experiments.....	50
3.1.4 Rolling.....	51
3.1.5 Wire drawing.....	52
3.2 Characterization.....	52
3.2.1 Microhardness.....	52
3.2.2 Tensile tests.....	53
3.2.3 X-ray line profile analysis.....	54
3.2.4 Scanning electron microscopy.....	55
3.2.5 Transmission electron microscopy and high resolution TEM.....	56
3.3 References.....	56
4.0 CHAPTER FOUR.....	57

4.0	MECHANICAL BEHAVIOR OF BULK NANOCRYSTALLINE COPPER ALLOYS PRODUCED BY HIGH ENERGY BALL MILLING.....	57
4.1	Abstract.....	57
4.2	Introduction.....	58
4.3	Experimental procedure.....	60
4.4	Results and discussion.....	60
4.5	Conclusion.....	75
4.6	References.....	76
5.0	CHAPTER FIVE.....	79
5.0	IN SITU CONSOLIDATION OF CU AND CU-ZN ALLOYS VIA ROOM TEMPERATURE BALL MILLING.....	79
5.1	Abstract.....	79
5.2	Introduction.....	80
5.3	Experimental procedure.....	83
5.4	Results and discussion.....	84
	Planetary ball mill.....	84
	Spex 8000 mill.....	88
5.5	Conclusion.....	96
5.6	References.....	96
6.0	CHAPTER SIX.....	99
6.0	MECHANICAL PROPERTIES OF LOW SFE CU-12.1AT.%AL-4.1AT.%ZN ALLOY PRODUCED VIA IN SITU CONSOLIDATION BALL MILLING.....	99
6.1	Abstract.....	99
6.2	Introduction.....	100

6.3	Experimental procedure.....	102
6.4	Results and discussion.....	103
6.5	Summary.....	116
6.6	References.....	117
7.0	CHAPTER SEVEN.....	121
7.0	BULK NANOSTRUCTURED COPPER PRODUCED VIA BALL MILLING FOLLOWED BY HIGH PRESSURE TORSION.....	121
7.1	Abstract.....	121
7.2	Introduction.....	121
7.3	Experimental procedure.....	123
7.4	Results and discussion.....	124
7.5	Summary.....	133
7.6	References.....	134
8.0	CHAPTER EIGHT.....	137
8.0	DEFORMATION TWINS AND RELATED SOFTENING BEHAVIOR IN NANOCRYSTALLINE CU-30%ZN.....	137
8.1	Abstract.....	137
8.2	Introduction.....	138
8.3	Experimental procedure.....	141
8.4	Results and discussion.....	143
8.5	Conclusion.....	157
8.6	References.....	158

9.0	CHAPTER NINE.....	164
9.0	EFFECT OF STACKING FAULT ENERGY ON DEFORMATION BEHAVIOR OF CRYO ROLLED COPPER AND COPPER ALLOYS.....	164
9.1	Abstract.....	164
9.2	Introduction.....	165
9.3	Experimental procedure.....	167
9.4	Results and discussion.....	169
9.5	Summary.....	184
9.6	References.....	185
10.0	CHAPTER TEN.....	189
10.0	SEVERE DEFORMATION TWINNING IN PURE COPPER BY CRYOGENIC WIRE DRAWING.....	189
10.1	Abstract.....	189
10.2	Introduction.....	190
10.3	Experimental procedure.....	193
10.4	Results and discussion.....	195
	10.4.1 Lubrication.....	195
	10.4.2 Stress state.....	198
	10.4.3 Texture evolution.....	201
	10.4.4 Microstructure.....	201
10.5	Conclusion.....	207
10.6	References.....	208

11.0	CHAPTER ELEVEN.....	211
11.0	CONCLUSIONS.....	211
12.0	CHAPTER TWELVE.....	215
12.0	SUGGESTIONS FOR FUTURE WORK.....	215
	APPENDIX.....	217
	APPENDIX A.....	218
	X-ray line profile analysis and Whole Powder Pattern Modeling (WPPM).....	218

LIST OF TABLES

CHAPTER THREE

Table 3.1- Oxygen and iron content of 8h cryomilled Cu, Cu-10wt.%Zn, and Cu-30wt.%Zn.....	49
---	----

CHAPTER SIX

Table 6.1- Tensile mechanical properties.....	109
---	-----

CHAPTER SEVEN

Table 7.1- Properties of as-cryomilled Cu and samples cut at $r=3.5\text{mm}$ from the HPT disks, comprising I_{200}/I_{111} , dislocation density, grain size, and microhardness.....	126
--	-----

CHAPTER EIGHT

Table 8.1- Grain size, dislocation density (ρ) and twin probability (β) of Cu-30%Zn samples.....	147
Table 8.2- Tensile properties of Cu-30%Zn and pure copper.....	150

CHAPTER NINE

Table 9.1- Stacking fault energy and tensile properties of pure copper and Cu-12.1%Al-4.1%Zn alloy rolled at 77K.....	170
Table 9.2- Microstructure and tensile properties of nanocrystalline and ultrafine grained pure copper samples processed with different routes.....	172
Table 9.3- Values of spacing between network dislocations and solute atoms, dislocation densities and predicted and measured yield strength.....	174
Table 9.4- Values of shear modulus and Burgers vector for pure copper and Cu-12.1%Al-4.1%Zn.	181

APPENDIX A

Table A.1- The most typical correlations between diffraction peak aberrations, i.e. broadening, shifts or asymmetries, and the different elements of microstructure [1].....	218
--	-----

LIST OF FIGURES

CHAPTER TWO

Figure 2.1- Schematic illustration of high pressure torsion.....	9
Figure 2.2- Vickers microhardness vs. shear strain for Al disks processed by HPT through different numbers of turns at (a) the upper and (b) the lower positions [14].....	10
Figure 2.3- Variation of microhardness in HPT-processed Cu samples [15].....	11
Figure 2.4- Schematic illustration of microstructural evolution with straining for grain refinement in pure Cu [15].....	12
Figure 2.5 – Schematic illustration of ECAP method [19].....	13
Figure 2.6- Schematic illustration of different ECAP routes [19].....	14
Figure 2.7- Microstructures in pure Cu after 10 pressings together with the corresponding SAED patterns [24].....	14
Figure 2.8- The five stages of powder evolution during ball milling.....	15
Figure 2.9- Minimum grain size versus the melting temperature of different elements [27].....	16
Figure 2.10- Deformation mechanism map for FCC metals [40].....	19
Figure 2.11- Frank–Read source operating in center of grain 1 and producing two pileups at grain boundaries; the Frank–Read source in grain 2 is activated by stress concentration [46].....	22
Figure 2.12 - Sequence of stages in (a) polycrystalline deformation, starting with (b) localized plastic flow in the grain-boundary regions (microyielding), forming (c) a work-hardened grain-boundary layer that effectively reinforces the microstructure [46].....	25
Figure 2.13- Yield stress versus inverse square root of grain size plot for a) Cu, b) Fe, c) Ni, and d) Ti. The plots show deviation from conventional H-P relation as the grain size falls below a critical size [49].....	26

Figure 2.14- Local change of stacking sequence from fcc to hcp by passage of a Shockly partial [51].....	27
Figure 2.15- Shows the dependence of SFE alloys on electron to atom ratio in a series of Cu-Zn and Cu-Al [53].....	29
Figure 2.16- Variation of the SFE with e/a in Cu base alloys [53].....	29
Figure 2.17- Fraction of grains showing deformation twins after quasi-static compressive deformation at different aluminum content in weight% [54].....	30
Figure 2.18- A map of deformation mode and strain-induced microstructures in the SFE–processing parameters (ln Z) space for the Cu-Al alloys, Ultrafine grain (UFG); nanoscale twin (NT); nanosized grain (NG) [55].....	32
Figure 2.19- Tensile engineering and true stress–strain curves of the HPT processed ultrafine grain Cu, Cu–10 wt.% Zn alloy, and Cu–30 wt.% Zn alloy [56].....	33
Figure 2.20- Variation in yield strength with SFE for Cu–Al alloys deformed by dynamic plastic deformation and quasi-static compression [55].....	34
Figure 2.21- Tensile elongation to failure versus grain size [61].....	36
Figure 2.22 – Tensile curves for Al-7.5%Mg alloy with bimodal microstructure [59].....	36
Figure 2.23 –Stress-strain curve for nanocrystalline Cu produced by in situ consolidation in ball milling [64].....	37
Figure 2.24- Strain rate sensitivity as a function of grain size for pure Cu [66, 67].....	39
Figure 2.25- Tensile strain to fracture vs. strain rate for coarse grained and nanocrystalline Cu [65]...40	
Figure 2.26- Comparison of experimental and computational results for tensile tests of nc and ufc Ni [68].....	41

CHAPTER THREE

Figure 3.1- Spex 8000 mill, a) room temperature mill, b) cryomill.....	48
Figure 3.2- Planetary ball mill.....	48
Figure 3.3- HPT machine.....	50
Figure 3.4- Rolling machine.....	51
Figure 3.5- Mini tensile test machine.....	53
Figure 3.6- Schematic representation of mini tensile test samples.....	54

CHAPTER FOUR

Figure 4.1- In situ consolidated samples of Cu-10wt.%Zn alloy. Left: different pieces of hollow and defect-free spheres. Right: A sound 6mm sphere.....	61
Figure 4.2- a) Bright field and b) dark field TEM image of in situ consolidated Cu-30wt.%Zn sample after 6h cryomilling and 2h milling at room temperature. Lower left inset in the bright field image shows the electron diffraction pattern.....	62
Figure 4.3 Microhardness vs. cryo-milling time for pure Cu, Cu-10wt.%Zn, Cu-20wt.%Zn, and Cu-30wt.%Zn alloys.....	63
Figure 4.4- Crystallite size vs. cryo-milling time for pure Cu, Cu-10wt.%Zn, Cu-20wt.%Zn, and Cu-30wt.%Zn alloys.....	65
Figure 4.5- Dislocation density vs. milling time for Cu-20wt.%Zn milled for 12h at 77K followed by 4h milling at room temperature.....	68
Figure 4.6- Microstructure of Cu-20wt.%Zn alloy milled for 3h at room temperature followed by 3h milling at 77K.....	69
Figure 4.7- Microhardness vs. milling time for Cu-10%Zn cryomilled for 4h at 77K followed by 6h room temperature milling.....	73
Figure 4.8- Crystallite size vs. milling time for the Cu-10wt.%Zn alloy processed 4h at 77K followed by 4h milling at room temperature.....	74
Figure 4.9- Tensile curve for Cu-30wt.%Zn sample milled for 6h at 77K and 2h at room temperature. Tensile curve for coarse grained brass is given for comparison.....	75

CHAPTER FIVE

Figure 5.1– a) In-situ consolidated nanostructured Cu. b) the nanostructured samples are in form of hollow spheres with wall size of about 1 mm.....	85
Figure 5.2– Maximum diameter of in situ consolidated Cu vs. milling time in a planetary ball mill.....	85
Figure 5.3- Microhardness maps of the in-situ consolidated nanostructured Cu produced by planetary ball mill.....	86
Figure 5.4- Vickers microhardness at the outer edge of the hollow spheres as a function of the milling time.....	87
Figure 5.5- A large piece of pure copper welded (~3 cm × 2 cm) around vial after few hours of room temperature milling using a Spex 8000 mill.....	88
Figure 5.6- Images taken from Cu-5%Zn after different milling times showing growing flakes and spheres.....	89

Figure 5.7- XRD profiles of Cu-30%Zn alloy milled with 0.125wt.%NaCl at different milling times.....	91
Figure 5.8- Crystallite size vs. milling time for different Cu-Zn alloys milled with 0.125wt.%NaCl..	91
Figure 5.9- SEM micrographs of Cu, Cu-10%Zn, and Cu-30%Zn alloys milled at room temperature. 0.25wt.% NaCl was added to Cu and 0.125wt.% NaCl was added to Cu-10%Zn and Cu-30%Zn alloys in order to control cold welding and consolidation behavior.....	93
Figure 5.10- TEM image of Cu-30%Zn alloy milled for 12h at room temperature with 0.125wt.%NaCl.....	94
Figure 5.11- Tensile stress-strain curves for in situ consolidated Cu-Zn alloys produced via surfactant assisted ball milling.....	95

CHAPTER SIX

Figure 6.1- Hardness variations as a function of cryo milling time, for nc Cu alloy.....	105
Figure 6.2- Williamson-Hall plot for nc Cu alloy (cryo milled for 10 h) and in-situ consolidated nc Cu alloy (cryo milled for 10 h and room temperature milled for 2h).....	106
Figure 6.3- TEM observations of the typical nanostructure in the in-situ consolidated nc Cu alloy. The bright-field TEM micrograph (a) and the SADP, the upper left inset in (a), show roughly equiaxed grains with random orientations. The statistical distribution of grain size (b) was obtained from multiple dark-field TEM images of the same sample.....	107
Figure 6.4- A typical tensile stress-strain curves for the bulk in-situ consolidated nc Cu and Cu alloy in comparison with that of cg Cu alloy sample (with an average grain size larger than 90 μm).....	109
Figure 6.5- (a) A HRTEM image of the nc Cu alloy showing stacking faults. (b) A HRTEM of the outlined area in (a) showing the presence of wide stacking faults and areas with severe lattice distortion and high density Shockley partials.....	111
Figure 6.6- (a) A HRTEM image of the nc Cu alloy showing twinning in the nano grains. (b) A HRTEM image of a nano twin in the nc Cu alloy revealing a twin boundary and the Burgers circuit around it that shows the presence of Shockley partials.....	112
Figure 6.7- Strain hardening coefficient, n , as a function of grain size of nc Cu and nc Cu alloy. For comparison, the n values for nc-Cu (\diamond [41], \blacklozenge [42], \blacktriangle [43]), ufg-Cu \blacktriangledown [43], cg-Cu \blacktriangleright [43] samples reported in the literature are included.....	114
Figure 6.8- The normalized strain hardening rate, Θ , as a function of the true plastic strain for nc Cu, nc Cu alloy, and cg-Cu.....	116

CHAPTER SEVEN

Figure 7.1- XRD profiles in as-cryomilled and cryomilled + HPT at $\gamma=2000, 2700, \text{ and } 4100$	126
--	-----

Figure 7.2– TEM micrograph of the a) as cryomilled, b) CM+HPT ($\gamma=2000$), c) CM+HPT ($\gamma=2700$), d) CM+HPT ($\gamma=4100$).....128

Figure 7.3 – Engineering stress-strain curves for samples produced with 8h cryomilling + HPT at 8GPa with $\gamma=2000$, 2700, and 4100.....132

Figure 7.4- Tensile properties of HPT samples as a function of applied shear strain.....133

CHAPTER EIGHT

Figure 8.1- TEM images of Cu-30%Zn samples processed by a) 8h cryomilling, b) 8h cryomilling + HPT, c) 2h cryomilling+4h RT milling. Lower left insets show electron diffraction patterns.....146

Figure 8.2- Grain size distribution obtained from bright field and dark field images for Cu-30%Zn alloy processed by a) 8h cryomilling, b) 8h cryomilling + HPT, and c) 2h cryomilling + 4h RT milling.....147

Figure 8.3- Engineering stress-strain curves for Cu-30%Zn alloy processed via cryomilling followed by consolidation by RT milling or HPT. Dashed line shows the yield strength of 8h cryomilled sample estimated from hardness measurement.....150

Figure 8.4- Hall-Petch plot for pure copper and Cu-30%Zn in a wide range of grain size. Solid and dashed lines represent the H-P relationship for pure copper and Cu-30%Zn from [43], respectively. It is seen that at small grain sizes, data points for Cu-30%Zn deviate from the classical H-P relationship. This deviation is shown by dotted lines. Pure copper and Cu-30%Zn data were extracted from [3, 51-58] and [3, 9, 13, 59-64], respectively.....153

Figure 8.5– a) High resolution TEM image of Cu-30%Zn sample processed by 8h cryomilling followed by HPT consolidation at room temperature. Finely spaced deformation nanotwins are marked. The dotted line represents the grain boundary. b) FFT processed image of the region marked with white box in (a). A twin boundary decorated with dislocations is shown.....155

CHAPTER NINE

Figure 9.1- Stress-strain curve for pure copper and Cu-12.1%Al-4.1%Zn alloy rolled at 77K.....170

Figure 9.2- Stress relaxation curves for pure copper and Cu-12.1%Al-4.1%Zn.....174

Figure 9.3- TEM micrograph of pure copper sample rolled at 77K. a) heavily deformed microstructure with few ultrafine grains, b) stack of deformation twins in an ultrafine grain.....177

Figure 9.4- TEM micrograph of Cu-12.1%Al-4.1%Zn sample rolled at 77K. a) heavily deformed microstructure containing twins, b) nano twins with thickness less than 10nm.....178

Figure 9.5- A periodic row of intersecting network dislocations produces resisting a force F_{jog} on a slip dislocation moving in the forward (upward) direction. One period length L is shown centered on a network dislocation. The forward force is τbL179

Figure 9.6- The work hardening rate, Θ , as a function of the true plastic strain for pure copper and Cu-12.1%Al-4.1%Zn.....182

CHAPTER TEN

Figure 10.1- Twinning in Cu single crystals under tensile load: (a) stress-strain response with respect to twinning at different temperatures in Cu crystals of an orientation suitable for twinning [6], (b) orientation dependence of twinning at cryogenic and room temperature [3, 6-10].....192

Figure 10.2- Scanning electron micrographs (secondary electron contrast) at different magnifications (overview on the left; in detail on the right) of the bonded coatings used in the present investigation: (a) graphite (dense coating top left and porous coating bottom left), (b) MoS₂ and (c) PTFE.....196

Figure 10.3- Drawing force as a function of time during wire drawing. Drawing takes place in a bath of liquid nitrogen: (a) comparison between non-lubrication and various bonded coatings and (b) drawing series of MoS₂ bonded coating. The drawing force of standard lubrication at room temperature is included in (a) for comparison. The wire surface at the final stage of the drawing process is shown in (c) as scanning electron micrographs (secondary electron contrast) at different magnifications after removal of the coating.....197

Figure 10.4- Scheme of wire drawing and stress state during wire drawing [15].....198

Figure 10.5- The $\{1\ 1\ 1\}$ pole figures on the wire cross-sections at different logarithmic degrees of deformation, g , within the wire drawing process at liquid nitrogen temperature.....201

Figure 10.6- Scanning electron micrograph (forward scattered electron contrast) of the severely twinned microstructure obtained by drawing at cryogenic temperature. The logarithmic degree of deformation is $\eta = 1.5$204

Figure 10.7- EBSD analysis of a cross-section of Cu drawn at room temperature ($\eta = 1.5$): (a) orientation map according to the inverse pole figure (grain boundaries in black, twin boundaries in green) and (b) the corresponding inverse pole figure (combined occupancy and contour diagram). The steps size was 1 μm . Warping of the image is due to off-line drift correction. Contours indicate multiples of the uniform distribution.....205

Figure 10.8- EBSD analysis of a severely twinned grain in the cross-section of a cryo-drawn wire ($\eta = 1.5$): (a) orientation map according to the inverse pole figure (grain boundaries in black, twin boundaries in green), (b) band contrast map (the contrast increases from black to white) and (c) corresponding inverse pole figure (combined occupancy and contour diagram). Contours indicate multiples of the uniform distribution. Warping of the images is due to off-line drift correction. (A) highlights prior annealing twins; (B1) and (B2) primary and secondary deformation twins; and (C) secondary deformations twins in the range of the step size of 100 nm.....206

CHAPTER ONE

1. INTRODUCTION

Materials with ultra fine and nano sized grains have been a focus of research in recent decades, since 1980s starting with pioneering work of Gleiter et al. [1], due to the exceptional properties of these materials compared with their coarse grained counterparts. Numerous research funds have been devoted to processing and characterization of these materials for understanding the microstructure-properties relationships. One of the major aspects in this field of research are the mechanical properties, i.e. strength and ductility.

Grain size dependence of mechanical properties has been studied in different metals and alloys via different experimental processing methods (e.g. [2-4]) and also simulation studies (e. g. [5, 6]). Although there is a remarkable progress towards understanding and controlling the properties of nanostructured materials for desired applications, several questions such as the deformation mechanisms in nanocrystalline materials have remained unanswered.

In this research, the role of stacking fault energy on deformation behavior of Cu base alloys is studied. Cu base alloys were chosen as a model since the stacking fault energy can be systematically controlled in a wide range of alloy content in single phase alloys. Since stacking fault energy controls the ease of cross-slip, various dislocation cell/array structures

can be produced in different alloys. Furthermore, twinning propensity is higher in low SFE alloys which can alter the microstructure and mechanical properties. Therefore, besides the grain size, other contributing factors in mechanical properties of Cu base alloys are studied in this work.

One of the major concerns in this research is production of bulk artifact-free samples. In situ consolidation technique via high energy ball milling (combination of cryomilling and room temperature milling) was used to synthesize nanostructured samples. Considering the capability of ball milling in grain refinement, this technique enabled us to produce bulk samples with small grain sizes, e.g. 23 and 22nm for Cu and Cu-12.1at.%Al-4.1at.%Zn, respectively. Therefore, we were able to separate the effect of grain size in the small grain size regime and compare samples in terms of other microstructural features such as stacking faults and twinning. In situ consolidation via surfactant assisted ball milling was also studied in this work. NaCl was used successfully for production of bulk in situ consolidated samples during high energy ball milling at room temperature.

Another approach in this work is to produce bulk nanostructured samples in two steps, i.e. synthesizing nanostructured material through high energy ball milling and then consolidation at room temperature via high pressure torsion. Our collaborative experiments with University of Vienna, showed that the two-step approach is capable of producing high strength nanostructured samples, e.g. yield strength of 930 MPa in Cu-30at.%Zn with 24nm grains.

Given the wide range of the grain sizes studied in this research via different techniques and compared to the data in literature, we, for the first time, found a breakdown in Hall-Petch relation in Cu-30%Zn. It was shown that despite the solid solution strengthening and high density of deformation twins and stacking faults, Cu-30at.%Zn shows strength that is comparable to that of pure copper in small grain sizes. HRTEM studies revealed that detwinning in this low SFE material is responsible for the decreased strength.

Rolling at liquid nitrogen temperature was also utilized as a severe plastic deformation route for microstructural refinement of cast Cu and Cu-12.1at.%Al-4.1at.%Zn alloy. It was found that although low temperature deformation retards dynamic recovery and facilitates twinning in processed samples, the strength of the samples is mainly originates from a high density of dislocations accumulated in the microstructure.

Wire drawing of Cu samples at 77K was also investigated in this work. Severe deformation twinning was observed in deformed samples and the extent of the twinning formation is discussed with respect to the state of stress and the texture evolution.

Chapter 2 is dedicated to the literature survey and background of the subject.

Chapter 3 summarizes the experimental procedure we used for this work.

Chapter 4 is based on a presentation at MS&T 2010, Houston and a published paper: H. Bahmanpour, K. Youssef, R. Scattergood, C. C. Koch, Journal of Materials Science (2011), pp. 1-7

Chapter 5 is based on presentations given at TMS 2011 annual meeting, San Diego (M. S. Khoshkhoo, H. Bahmanpour, S. Scudino, J. Freudenberger, M. J. Zehetbauer, C. C. Koch, J. Eckert) and MRS Fall 2011 meeting, Boston (H. Bahmanpour, K. M. Yousseff, M. Samadi Khoshkhoo, S. Scudino, J. Eckert, R. O. Scattergood, C. C. Koch)

Chapter 6 is based on a published paper: K. Youssef, M. Sakaliyska, H. Bahmanpour, R. Scattergood, C. C. Koch, *Acta Materialia* 59 (2011) pp. 5758-5764

Chapter 7 is based on a paper to be submitted to *Scripta Materialia*

Chapter 8 is based on a paper submitted to *Acta Materialia*

Chapter 9 is based on a published paper: H. Bahmanpour, A. Kauffmann, M. S. Khoshkhoo, K. M. Youssef, S. Mula, J. Freudenberger, J. Eckert, R. O. Scattergood, C. C. Koch, *Materials Science and Engineering A* 529 (2011) pp. 230-236

Chapter 10 is based on a published paper: A. Kauffmann, J. Freudenberger, D. Geissler, S. Yin, W. Schillinger, V. Subramanya Sarma, H. Bahmanpour, R. Scattergood, M.S. Khoshkhoo, H. Wendrock, C.C. Koch, J. Eckert, L. Schultz, *Acta Materialia* 59 (2011) pp. 7816-7823

Chapter 11 briefly summarizes the concluding remarks of this work.

Chapter 12 is dedicated to suggestions for future work.

References

- [1] H. Gleiter, *Prog. Mater. Sci.*, 33 (1989) 223-315.
- [2] S.R. Agnew, B.R. Elliott, C.J. Youngdahl, K.J. Hemker, J.R. Weertman, *Mater. Sci. Eng., A*, 285 (2000) 391-396.
- [3] H. Conrad, *Mater. Sci. Eng., A*, 341 (2003) 216-228.
- [4] T. Hanlon, Y.N. Kwon, S. Suresh, *Scripta Mater.*, 49 (2003) 675-680.
- [5] H. Mirkhani, S.P. Joshi, *Acta Mater.*, 59 (2011) 5603-5617.
- [6] J. Schiotz, K.W. Jacobsen, *Science*, 301 (2003) 1357-1359.

CHAPTER TWO

2.0. LITERATURE REVIEW

2.1. Introduction

Since early studies on metals and alloys, it has been well known that microstructure refinement brings about attractive mechanical properties such as increased strength and toughness [1]. Nanocrystalline materials that are known as the materials with grain size of less than 100 nm, typically have shown superior mechanical properties in terms of strength compared to their coarse grained counterparts. One of the major roadblocks for application of nanostructured materials is the low ductility that might be related to the intrinsic properties of these materials or the processing artifacts [2].

Literature survey shows that there are numerous reports on the role of microstructural features such as grain size and distribution [3], twin size and spacing [4], stacking faults [5, 6], dislocation density [7], and concentration of vacancies [8, 9] on mechanical response of nanostructured metals and alloys. From application perspective, it is important to understand the role of the abovementioned features on the deformation behavior and control them to obtain optimum properties.

Dislocation activity is the major deformation mechanism in coarse grained materials [10]. Considering the small size of grains and significant volume fraction of boundaries, e.g.

grain boundaries or twin boundaries, in a nanocrystalline material, the contribution of intragranular dislocation activity vanishes as the grain size decreases to nano regime. This incorporates other deformation mechanisms involving grain boundary shear [10].

2.2. Synthesis of ultrafine grain and nanostructure metals and alloys

Several methods have been developed to synthesize ultra fine grain and nanocrystalline materials. The typical methods are categorized in two major categories of “Top-down” and “Bottom-up” approaches. The bottom-up approach starts with atoms, ions, or molecules as “building blocks” and assembles nano scale clusters or bulk material from them. The top-down methods for processing of nanostructured materials involve starting with a bulk solid and obtaining a nanostructure by structural decomposition. Typical Top-down synthesis methods are high pressure torsion (HPT), equal channel angular pressing (ECAP), high energy ball milling (BM), dynamic plastic deformation (DPD), surface mechanical attrition treatment (SMAT) and accumulative roll bonding (ARB). On the other hand, typical “bottom-up” approaches are inert gas condensation (IGC), and electrodeposition (ED). Discussing all the abovementioned methods is beyond the scope of this research and therefore, some top-down synthesis methods, i.e. “high pressure torsion”, “equal channel angular pressing”, and “high energy ball milling”, are briefly introduced in this chapter.

2.2.1. Top-down synthesis methods

In a review by Xun and Mohamed [11] the microstructure refinement efficiency of ECAP, HPT, ARB, and ball milling processes are discussed. It is believed that the structure refining behavior can be related to the deformation details of each technique. In the following an introduction to each technique is given and their grain refining capability is addressed.

High pressure torsion

High Pressure Torsion (HPT), involves torsion at high hydrostatic compression stresses that basically enhances the strain to fracture to infinity [12]. In this process, a disk-shaped sample is deformed between two anvils that rotate with respect to each other, Figure 2.1. The equivalent shear strain can be calculated based on the following relation;

$$\gamma = \frac{2\pi nr}{t} \quad (2.1)$$

where r , n and t are the distance from the center of the axis of rotation, the number of revolutions and the thickness of the sample, respectively.

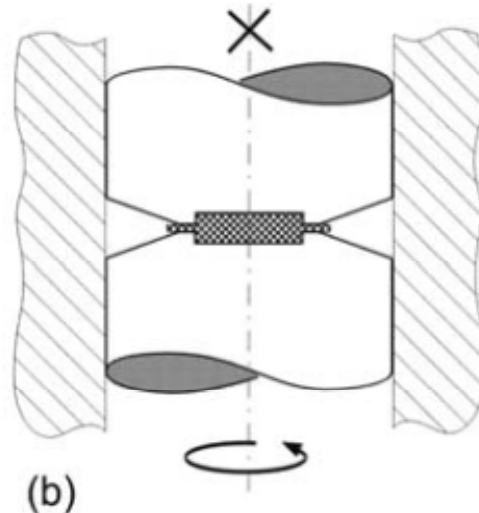


Figure 2.1- Schematic illustration of high pressure torsion.

HPT is capable of applying high shear strains on the sample and therefore, with controlling the number of revolutions, the applied shear strain can be controlled accordingly. Due to the radial dependence of the shear strain, a radial dependence of properties is expected in HPT samples. It should be mentioned that due to the nature of the HPT process, the central part of HPT disks remains undeformed even after large shear strains [13]. Regardless of the presence of an undeformed central region, literature survey shows that for different materials and various applied hydrostatic pressures, the saturation of properties occurs at different number of revolutions. For example, Kawasaki et al. [14], reported that in pure Al, 20 revolutions, $\gamma=10$, is necessary to achieve a homogeneous microhardness across the HPT disk, Figure 2.2.

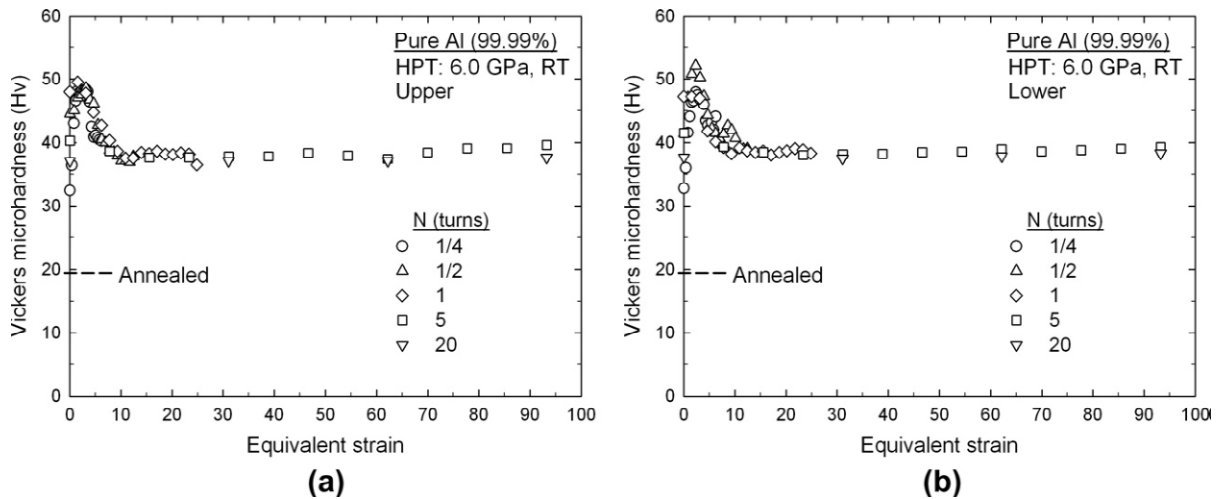


Figure 2.2- Vickers microhardness vs. shear strain for Al disks processed by HPT through different numbers of turns at (a) the upper and (b) the lower positions [14].

In the case of pure copper, a hydrostatic pressure of 2GPa and 4 revolutions were shown to produce a uniform distribution of the microhardness across the HPT sample, Figure 2.3 [15]. Different HPT conditions for obtaining homogeneous microstructure and properties is related to different rate of recovery of different metals [14]. Edalati et al. [15] discussed that the hardness variation may be divided into two regions, Figure 2.4. In the first region (I), dislocations accumulate to form subgrains with an increasing population within individual grains. With further straining, the subgrain size decreases, the subgrain boundary width becomes better defined and the misorientation angle increases. In this change in the microstructure, the hardness levels off and reaches saturation. No change in hardness occurs with further straining and a steady-state is entered because a balance now holds between the hardness increase due to accumulation of dislocations and the decrease due to recrystallization with few dislocations within individual grains.

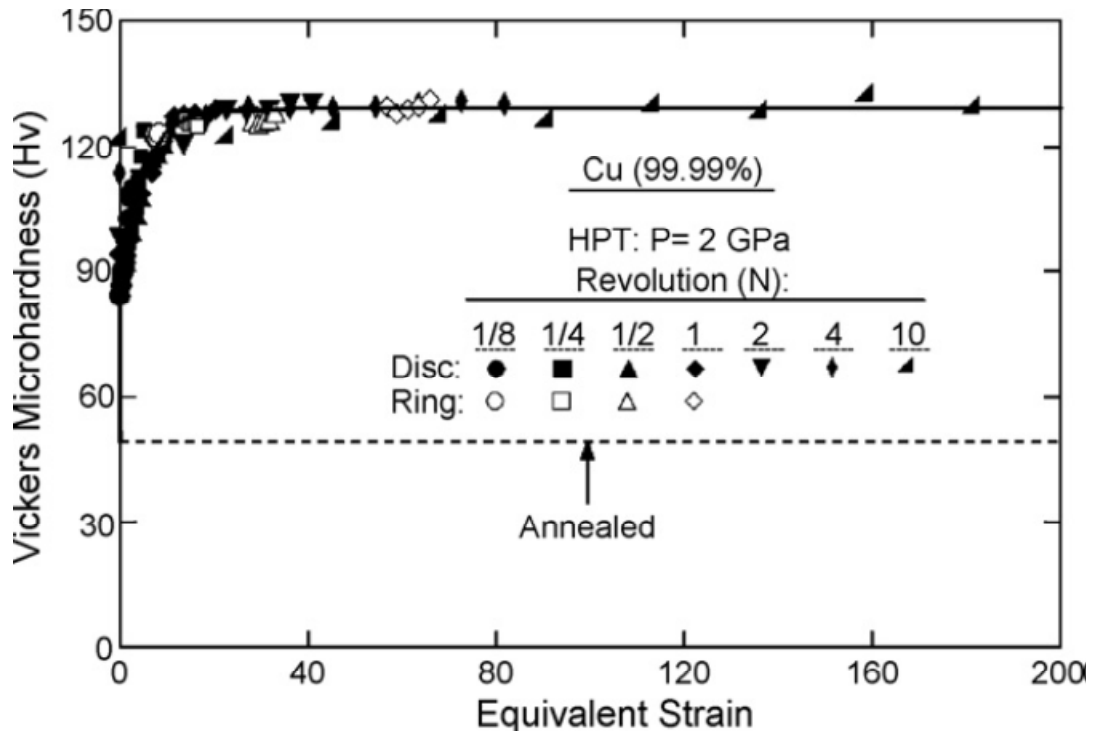


Figure 2.3- Variation of microhardness in HPT-processed Cu samples [15].

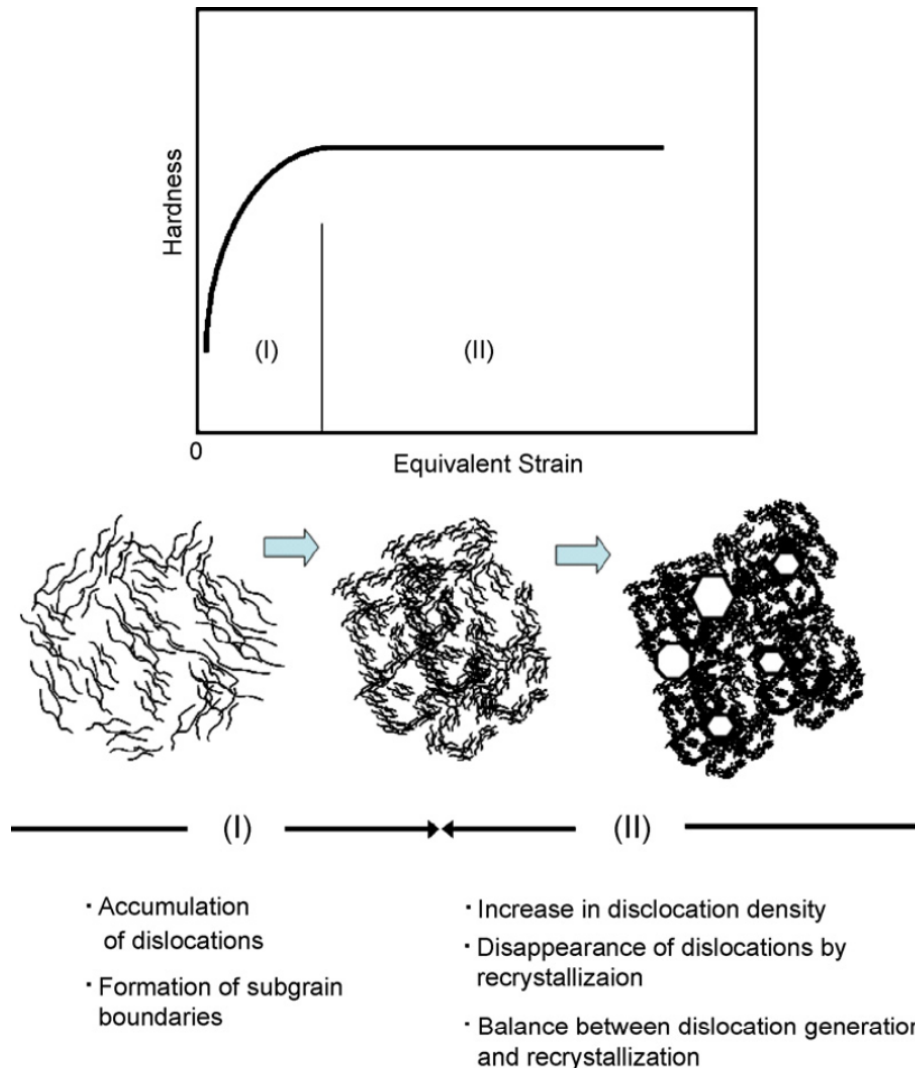


Figure 2.4- Schematic illustration of microstructural evolution with straining for grain refinement in pure Cu [15].

It is worthy to note that despite the effective contribution of high pressure torsion in grain refinement of metals and alloys to obtain nanocrystalline microstructures, there are reports on deformation induced grain growth in HPT-processed nanocrystalline Cu and Ni that inhibits further grain refinement. [16, 17].

Equal channel angular pressing

In Equal Channel Angular Pressing (ECAP) process the sample is pressed through a channel having an equal cross section but bending in a solid die, Figure 2.5. The bending in the channel imposes strain on the sample. The sample cross section remains unchanged during the process and hence, repetitive pressing is possible. The total equivalent strain ϵ_N is a function of number of passes, N , the channel bending angle (internal angle), ϕ , and the angle at the outer arc of curvature (outer angle) at the bending point, ψ [18].

$$\epsilon_N = \frac{N}{\sqrt{3}} \left[2 \cot \left(\frac{\phi}{2} + \frac{\psi}{2} \right) + \psi \operatorname{cosec} \left(\frac{\phi}{2} + \frac{\psi}{2} \right) \right] \quad (2.2)$$

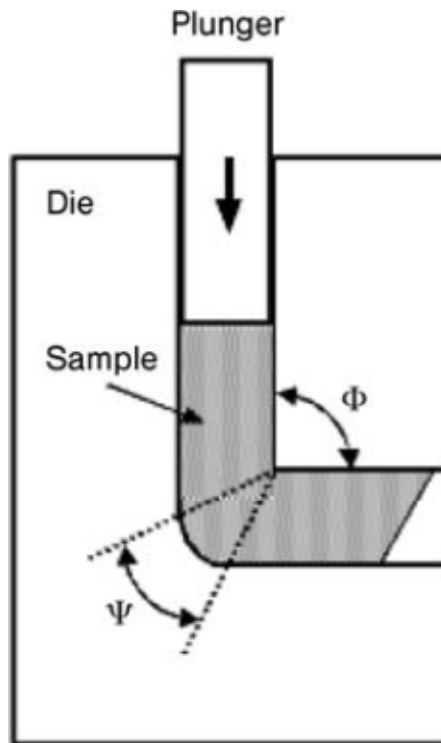


Figure 2.5 – Schematic illustration of ECAP method [19].

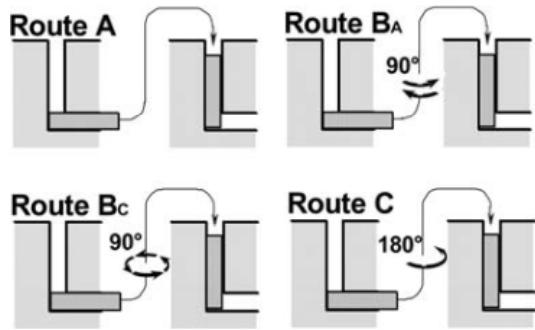


Figure 2.6- Schematic illustration of different ECAP routes [19].

Several different routes can be applied to the specimen to produce ultrafine or nanostructure as shown in Figure 2.6. It is found that the four passes of route B_C produce a fairly homogeneous microstructure in pure Al (with a grain size of ~1.2–1.3 μm) [20-22] and Ti [23]. On the other hand, ECAP processed pure Cu does not demonstrate a homogeneous microstructure even after 10 passes, due to the very slow rate of recovery in Cu, and the equilibrium grain size is ~0.27 μm [24], Figure 2.7.

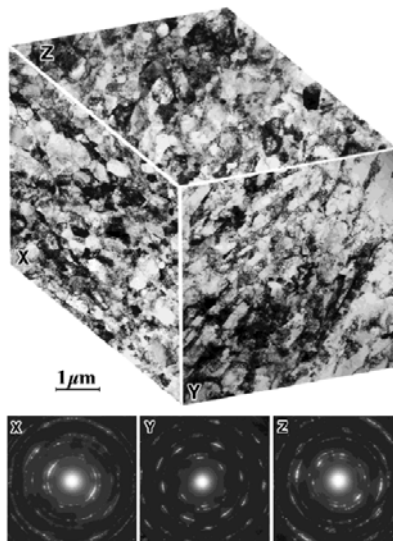


Figure 2.7- Microstructures in pure Cu after 10 pressings together with the corresponding SAED patterns [24].

High energy ball milling

During the high energy ball milling the metal powder particles are subjected to severe plastic deformation from collisions with the milling media. As a result, plastic deformation occurs at high strain rates ($\sim 10^3$ - 10^4 s⁻¹) and the grain size is decreased as the milling time increases [1]. Evolution of powder particles in the ball milling process involves five stages, i.e. particle flattening as a result of plastic deformation, welding-dominance stage, fracturing and equiaxed particle formation, random welding orientation of the powder particles and a steady state, during which microstructural refinement continues, as shown in Figure 2.8 [25].

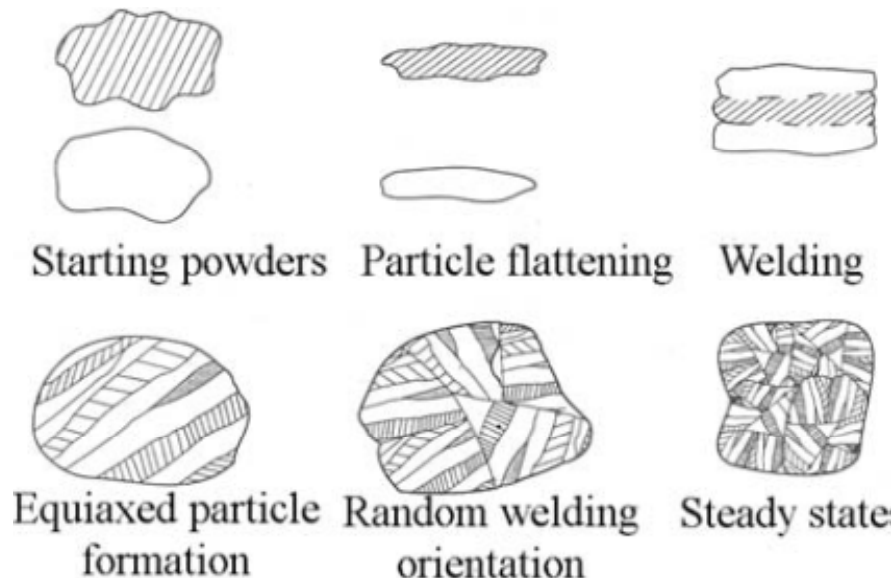


Figure 2.8- The five stages of powder evolution during ball milling.

The deformation mechanism at high strain rates is dominated by formation of ~ 0.5 μm wide shear bands with dense network of dislocations. The strain level in the early stages of ball milling increases due to the increased dislocation density. At a critical dislocation density the microstructure decomposes into dislocation cell/subgrain structure which are

initially separated by low angle grain boundaries. Further milling imposes deformation in shear bands located in unstrained parts of the material and the size of the subgrains in existing bands is further reduced to the final grain size. Once the minimum grain size is achieved throughout the microstructure, further refinement becomes impossible [26]. The competitive processes of grain refinement by the severe impact deformation of milling and the thermal recovery determine the minimum grain size obtainable by ball milling [27]. Furthermore, an inverse relation between the minimum grain size and melting temperature was found in lower melting fcc metals such as Al, Ag, Ni, and Cu [28]. Comparing to the higher melting point fcc metals and bcc and hcp metals it was found that $d_{\min}^{\text{fcc}} < d_{\min}^{\text{bcc}} < d_{\min}^{\text{hcp}}$, Figure 2.9 [28-33]. Also, the mill energy, milling temperature and alloying has been reported to affect the minimum grain size in ball milled samples [27].

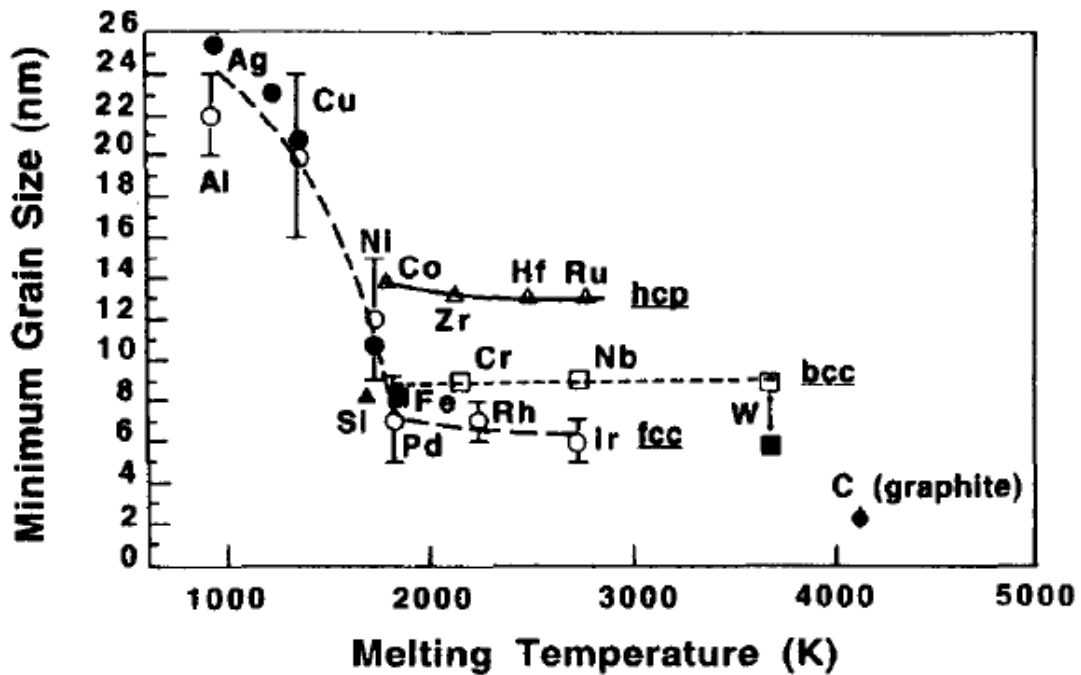


Figure 2.9- Minimum grain size versus the melting temperature of different elements [27].

Combined techniques

Recently, combinations of processing techniques have been used to synthesize nanostructured materials. Due to limitations imposed by each processing method, combined synthesis might be helpful for obtaining bulk samples with small grain sizes. This aspect is especially important when a consolidation of nanostructured powder is concerned. There are reports in the literature on production of nanostructured samples followed by a consolidation step with ECAP [34, 35] or HPT [36-39].

2.3. Mechanical properties of nanostructured metals and alloys

A major driver for production of nanostructured metals and alloys is the superior mechanical properties of these materials compared to their coarse grained counterparts. Therefore, it is important to understand the deformation mechanisms when the determining microstructural features are in the nano regime. For example, in a coarse grain metal such as Cu the deformation is mainly controlled by dislocation activity but when the grain size is reduced to 10 nm, due to the increased contribution of the boundaries and limited room for dislocation activity, the expected behavior of the material changes and grain boundary mediated mechanisms take over.

Figure 2.10 represents the different grain size regimes, proposed by Cheng et al. [40], in fcc metals considering the deformation mechanisms for each regime. At the smallest grain size regime, Nano-1, lattice dislocation activity has not been observed and molecular

dynamics simulation predicts grain boundary mediated deformation mechanisms such as grain boundary sliding. The boundary of Nano-1 and Nano-2 regimes is the grain size above which partial dislocations first become active in fcc metals. This critical grain size was found, by MD simulation, to be 8 nm and 12 nm for Cu and Ni, respectively [41]. Predicted by MD simulation, Shockley partials may shear grains and leave intrinsic stacking faults behind in Nano-2 regime. The lower boundary of next regime, Ultrafine, is the grain size above which unit dislocations can shear the grains in fcc metals. It is shown by MD simulation that this boundary is a function of stacking fault energy [42, 43]. In ultrafine regime, lattice dislocations nucleate in grain boundaries and shear the grains. At larger grain sizes, finally, intragranular dislocation sources compete with grain boundary dislocation sources to sustain plastic deformation.

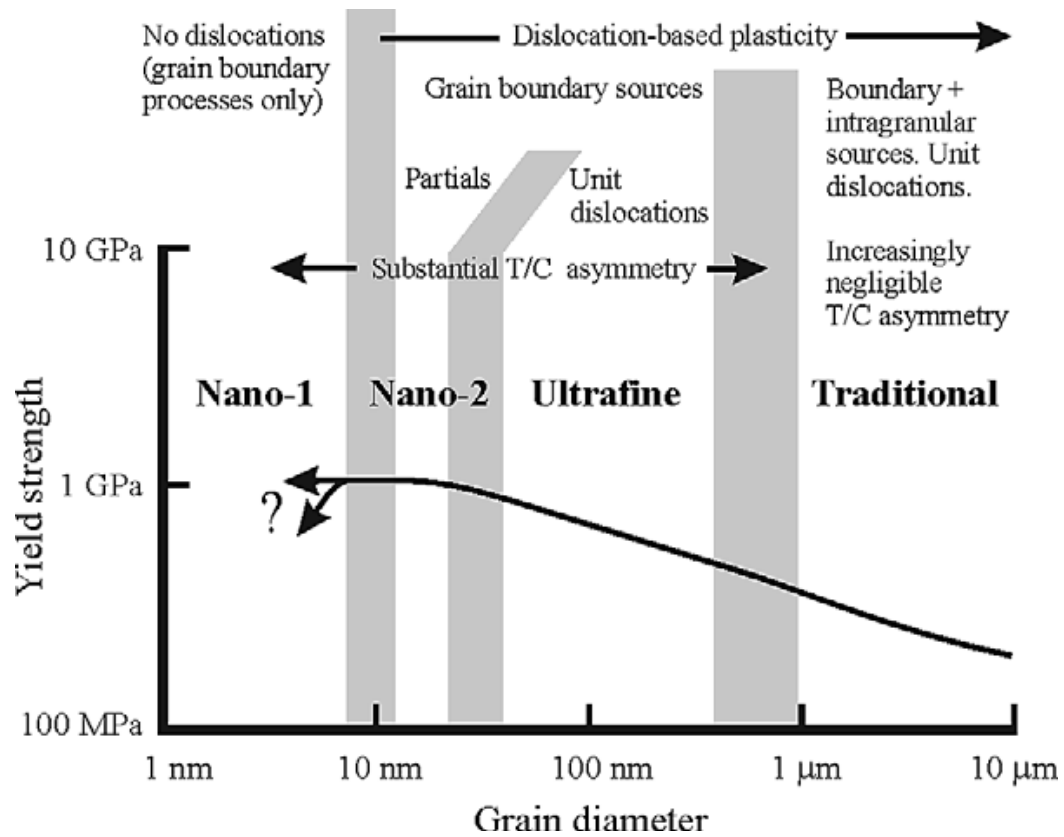


Figure 2.10- Deformation mechanism map for FCC metals [40].

2.3.1. Hall-Petch relation

Grain boundaries play an important role in mechanical behavior and strengthening of metals and alloys. Hall-Petch relation describes the role of grain boundaries in determining strength of different materials;

$$\sigma_y = \sigma_0 + kD^{-1/2} \quad (2.3)$$

where σ_y is the yield stress, σ_0 is the frictional stress required to move dislocations, k is the H-P slope, and D is the grain size. There are a large number of papers in the literature

reporting different aspects of the Hall-Petch relation and its applicability to different grain size regimes. We briefly address the different theories explaining the Hall-Petch relation considering the role of dislocations.

Hall-Petch theory

Based on this theory given separately by Hall [44] and Petch [45], the stress concentration at the head of a pile up dislocation, causes the pile up to burst through the grain boundary. If τ_a is the resolved shear stress applied on the slip plane, then the stress acting at the head of a pileup containing n dislocations is $n\tau_a$. The number of dislocations in a pileup depends on the length of the pileup, which, in turn, is proportional to the grain diameter D . The length of the pileup under an applied shear stress τ is given by;

$$L = \frac{\alpha n G b}{\pi \tau} \quad (2.4)$$

where, n is the number of dislocations in the pile up, G is the shear modulus, b is the burgers vector. α is the geometrical constant that is equal to unity for screw dislocations and equal to $1/(1-\nu)$ for edge dislocations.

If τ_c is the critical stress required to overcome the grain-boundary obstacles, then the dislocations of the pileup will be able to traverse the grain boundary if $n\tau_a \geq \tau_c$. This results in the $\tau_a \geq \tau_0 + kD^{-1/2}$ that is identical to Hall-Petch relation.

Cottrell's theory

Cottrell's theory assumes that the stress concentration produced by a pileup in one grain activated dislocation sources in the adjacent grain. Figure 2.11 shows how a Frank-Read source at a distance r from the boundary is activated by the pileup produced by a Frank-Read source in the adjacent grain. The slip band blocked in the boundary was treated by Cottrell as a shear crack. The maximum shear stress at a distance r ahead of a shear crack is given by;

$$\tau = (\tau_a - \tau_0) \left(\frac{D}{4r} \right)^{0.5} \quad (2.5)$$

where τ_0 is the frictional stress required to move dislocations and $r < D/2$. The stress required to activate the Frank-Read source in the neighboring grain is given by;

$$\tau_c = (\tau_a - \tau_0) \left(\frac{D}{4r} \right)^{0.5} \quad (2.6)$$

or

$$\tau_a = \tau_0 + 2\tau_c r^{1/2} D^{-1/2} \quad (2.7)$$

This equation is of a Hall-Petch form.

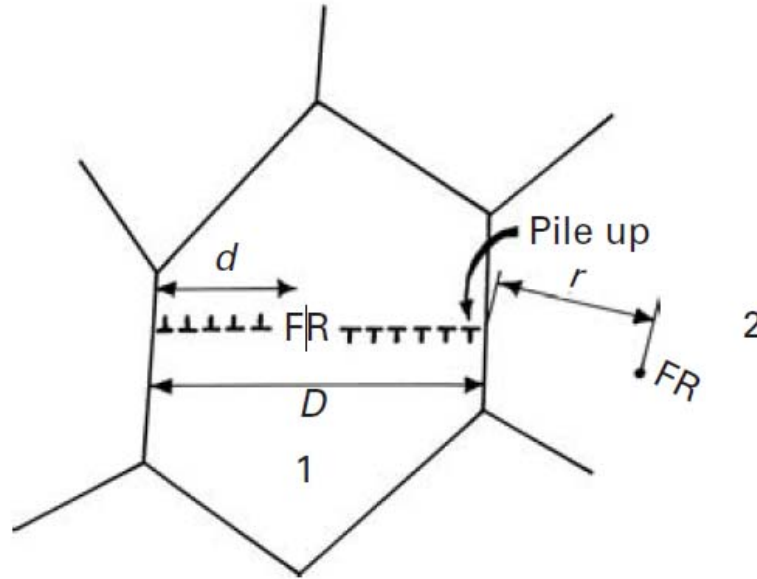


Figure 2.11- Frank–Read source operating in center of grain 1 and producing two pileups at grain boundaries; the Frank–Read source in grain 2 is activated by stress concentration [46].

Li's theory

Li considered the grain boundary to be a source of dislocations and suggested that the grain-boundary ledges generated dislocations, pumping them into the grain. Dislocation pile ups or emitted dislocations from boundary act as dislocation forests in regions close to the boundary. According to Li, the yield stress is the stress required to move dislocations through these forests. For many metals, the flow stress is related, under most conditions, to the dislocation density by the following relation;

$$\tau = \tau_0 + \alpha Gb\sqrt{\rho} \quad (2.8)$$

where τ_0 is the friction stress, α is a numerical constant, and ρ is the dislocation density. ρ was taken to be inversely proportional to the grain diameter, D , and therefore;

$$\tau = \tau_0 + GbD^{-1/2} \quad (2.9)$$

Again, this is a Hall--Petch equation.

Meyers-Ashworth theory

Meyers and Ashworth [46, 47] discussed that the compatibility requirement at the grain boundaries due to the differences in orientation applied to anisotropic crystals creates additional stresses, τ_I . The incompatibility stress was found to be 1.37 times the applied normal stress, σ_{AP} for Ni, $\tau_I=1.37\sigma_{AP}$ [47]. When comparing to the resolved shear stress, $\tau_H=\sigma_{AP}/2$, we find that the τ_I is almost three times higher than the resolved shear stress homogeneously applied on the grain. This comparison shows that the dislocation activity at the grain boundary starts before the dislocation activity at the center of the grains.

When the stress reaches the critical level required for emission, localized plastic deformation will start, Figure 2.12. These dislocations do not propagate throughout the grain because there is a stress gradient around grain boundary. Furthermore, the center of the grains is under homogeneous shear stress control, which is maximum at 45° to the tensile axis. On the other hand, the interfacial and homogeneous shear stresses have different orientations. The plastic flow of the grain-boundary region attenuates the stress concentration; geometrically necessary dislocations accommodate these stresses. This marks the onset of microyielding, Figure 2.12. The work hardened grain-boundary layer has a flow stress σ_{GB} , while the bulk has a flow stress σ_B ($\sigma_{GB}>\sigma_B$). The material behaves, at increasing

applied loads, as a composite made out of a continuous network of grain-boundary film with flow stress σ_{GB} and of discontinuous “islands” of bulk material with flow stress σ_B . The increasing applied stress σ_{AP} does not produce plastic flow in the bulk in spite of the fact that $\sigma_{AP} > \sigma_B$, because the continuous grain-boundary network provides rigidity to the structure. The total strain in the continuous grain-boundary network does not exceed 0.005, since it is elastic; hence, plastic deformation in the bulk is inhibited. This situation can be termed “plastic incompatibility”. When the applied load is such that the stress in the grain boundary region becomes equal to σ_{GB} , plastic deformation reestablishes itself in this region. The plastic deformation of the continuous matrix results in increases in stress in the bulk with plastic flow, Figure 2.12. This marks the onset of macroyielding. After a certain amount of plastic flow, dislocation densities in the bulk and grain-boundary regions become the same; then, since both regions have the same flow stress, plastic incompatibility disappears, and we have $\sigma_{AP} = \sigma_{GB} = \sigma_B$. The following relation describes the material behavior based on Meyers-Ashworth theory;

$$\sigma_y = \sigma_B + 8k(\sigma_{GB} - \sigma_B)D^{-1/2} - 16k^2(\sigma_{GB} - \sigma_B)D^{-1} \quad (2.10)$$

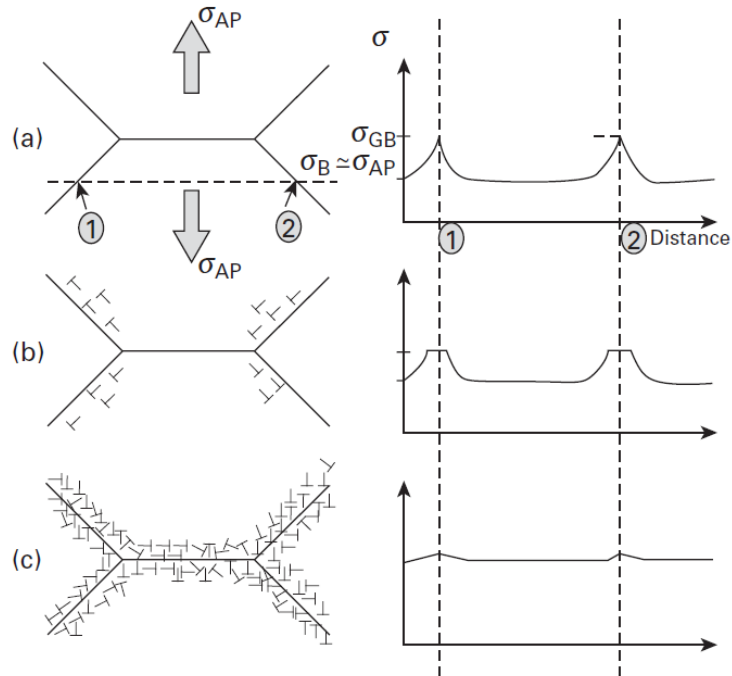


Figure 2.12 - Sequence of stages in (a) polycrystalline deformation, starting with (b) localized plastic flow in the grain-boundary regions (microyielding), forming (c) a work-hardened grain-boundary layer that effectively reinforces the microstructure [46].

2.3.2. Breakdown of Hall-Petch relation in nanocrystalline regime

Keeping in mind the Hall-Petch behavior and its mechanism at conventional grain sizes, it is observed that there is a deviation from the expected Hall-Petch behavior in small grain size regimes. The first report of an apparent inverse Hall-Petch effect was given by Chokshi et al. [48] on nc Cu and Pd prepared by the gas condensation method. The observed behavior in gas condensed samples might be related to processing artifacts that influence the hardness results remarkably. However, deviation from conventional H-P relation is reported for different metals at grain sizes in the nano regime, Figure 2.13 [49].

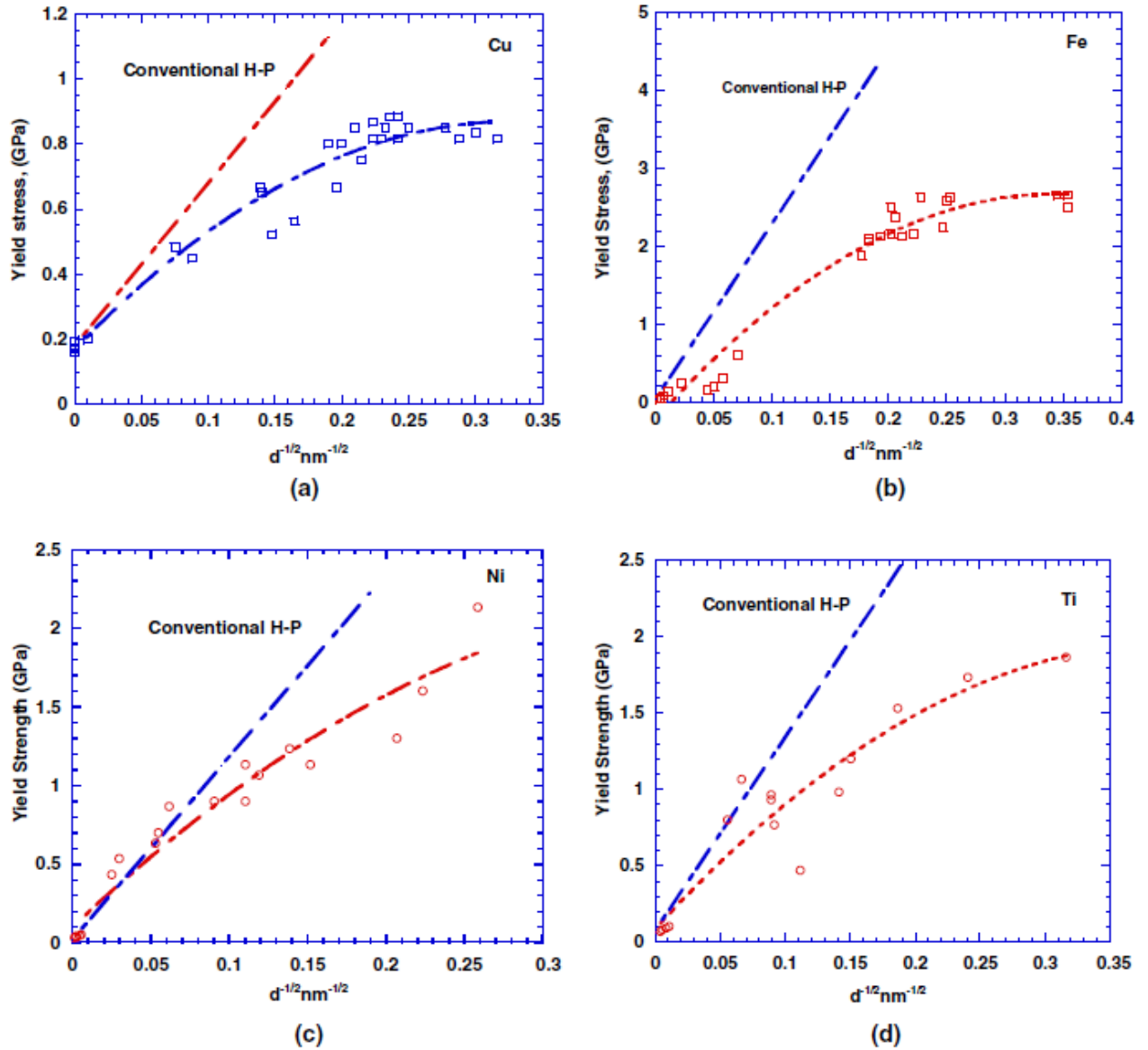


Figure 2.13- Yield stress versus inverse square root of grain size plot for a) Cu, b) Fe, c) Ni, and d) Ti. The plots show deviation from conventional H-P relation as the grain size falls below a critical size [49].

2.3.3. Stacking fault energy

Movement of partial dislocations produces a change in the stacking sequence from the fcc type -ABCABCABC- to include a local perturbation involving the formation of a layer of hcp material -ABCACABC, Figure 2.14. For an fcc crystal, the layer of hcp material that is introduced will elevate the total energy of the system. Therefore, the equilibrium distance of separation of two partials reflects a balance of the net repulsive force between the two partial dislocations containing Burgers vector components of the same sign and the energy of the associated stacking fault. This separation distance varies inversely with the stacking fault energy and may be given by;

$$d = \frac{Gb_1.b_2}{2\pi\gamma} \left[\cos \theta_1 \cos \theta_2 + \frac{\sin \theta_1 \sin \theta_2}{2-\nu} \right] \quad (2.11)$$

where, d is the partial dislocation separation, b1 and b2 are partial dislocation Burgers vectors, G is the shear modulus, γ is the stacking fault energy (SFE) (free energy of hcp minus free energy of fcc), and θ is the angle of the Burgers vector with the dislocation line. [50].

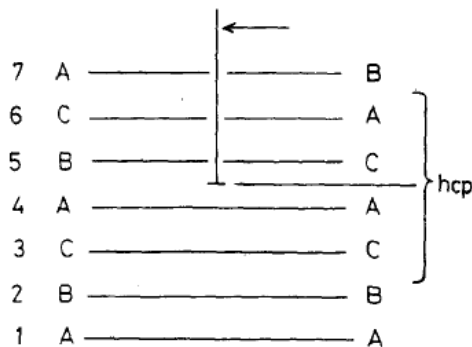


Figure 2.14- Local change of stacking sequence from fcc to hcp by passage of a Shockley partial [51].

2.3.4. Stacking fault energy effects on microstructure and mechanical properties

The movement of the two Shockley partial dislocations is restricted to the plane of the fault. Therefore, cross-slip of an extended screw dislocation is not permitted without thermally activated processes. Such is the case for a low SFE materials with widely separated partial dislocations. This type of dislocation movement is called planar glide. It is important to note that restricted cross-slip in low SFE metals and alloys results in higher propensity for twinning. On the other hand, when cross-slip is easy, i.e. high SFE, slip offset on a polished surface takes on a wavy pattern and this deformation is called wavy glide [50]. One major implication of the dependence of cross-slip on stacking fault energy is the dominant role the latter plays in determining the strain-hardening characteristics of a material. When the stacking fault energy is low, cross-slip is restricted so that barriers to dislocation movement remain effective to higher stress levels than in material of higher stacking fault energy. Therefore, the low SFE material strain hardens to a greater extent [50].

A solute concentration dependence for SFE has been reported in the literature [52, 53]. This solute content dependence can be normalized by considering electron/atom (e/a) ratio. Figure 2.15, shows the solute content dependence and e/a dependence of SFE in Cu-Zn and Cu-Al alloys. The variation of SFE at different e/a ratio is shown for a wide range of Cu base alloys in Figure 2.16.

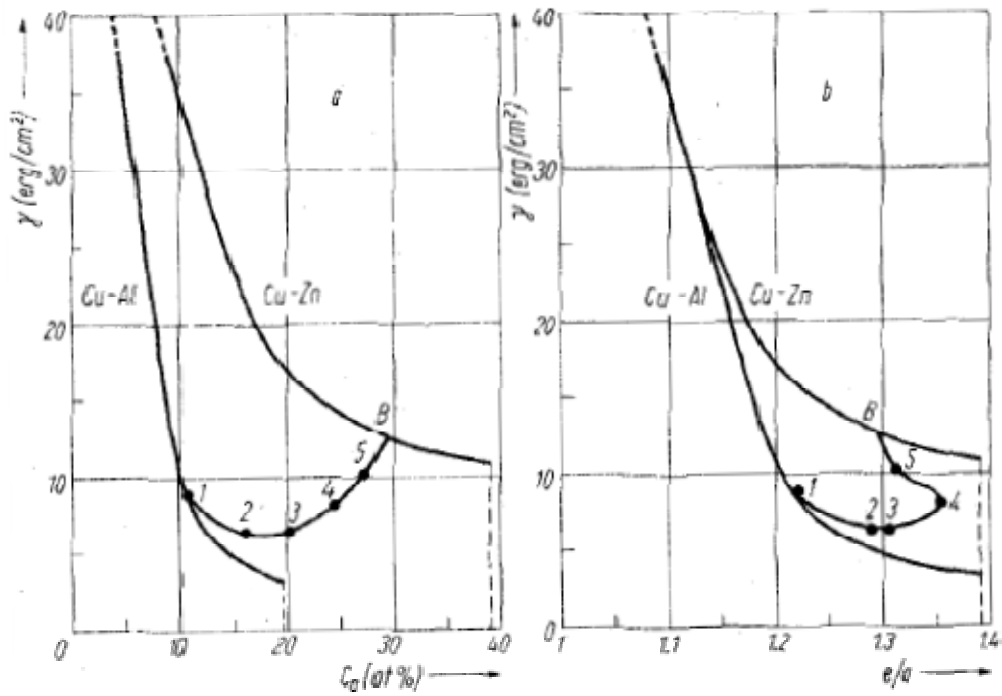


Figure 2.15- Shows the dependence of SFE alloys on electron to atom ratio in a series of Cu-Zn and Cu-Al [53].

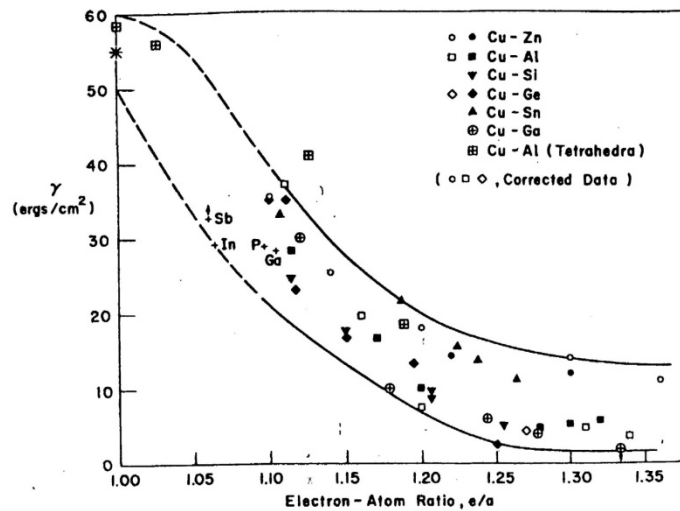


Figure 2.16- Variation of the SFE with e/a in Cu base alloys [53].

Twinning

Cu based alloys are good models for controlling SFE and studying its effect on microstructure and mechanical properties. As an example, a series of Cu-Al alloys deformed in compression, with grain sizes of 113-260 μm , showed higher twinning propensity at lower stacking fault energies, Figure 2.17 [54]. Considering the strengthening effect of twin boundaries and with some modifications to the Hall-Petch relation, using inter-twin spacing as the “effective” grain size, Rohatgi et al. [54] reported a good agreement between experimental flow stresses and calculated strength.

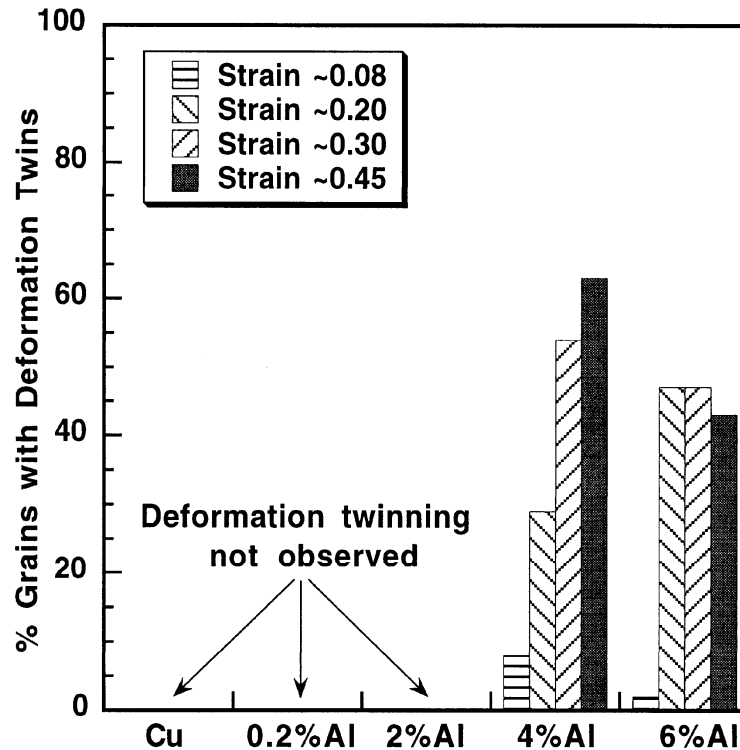


Figure 2.17- Fraction of grains showing deformation twins after quasi-static compressive deformation at different aluminum content in weight% [54].

Taking into account the temperature and strain rate by using Zener-Hollomann parameter;

$$\ln Z = \ln \dot{\epsilon} + Q/RT \quad (2.12)$$

where $\dot{\epsilon}$ is the strain rate, Q is the activation energy for diffusion, T is temperature and R is gas constant) Zhang et al. [55] constructed a deformation mechanism map for Cu base alloys in a wide range of stacking fault energy, Figure 2.18. In region I, deformation is dominated by dislocation slip and microstructures are characterized by ultrafine grains derived from dislocation cells with sizes of 100–300 nm. In region II, dislocation slip and deformation twinning compete with each other, forming a mixed microstructure of nanoscale twin/matrix lamellae, nanosized grains derived from twin/matrix lamellae and ultrafine grains from dislocation cells. The proportion of nanoscale twin/matrix lamellae and nanosized grains increases with decreasing SFE or increasing $\ln Z$. Furthermore, decreasing SFE and increasing $\ln Z$ leads to smaller twin spacing and grain size. In region III, deformation occurs mainly by deformation twinning. The microstructure is mainly composed of nanoscale twins and nanosized grains, and twin spacing and grain size decrease with decreasing SFE or increasing $\ln Z$. It is apparent from this map that decreasing SFE and increasing $\ln Z$ play a similar role in enhancing the tendency to deformation twinning and to achieve the mixed nanostructure of nanoscale twin/matrix lamellae and nanosized grains.

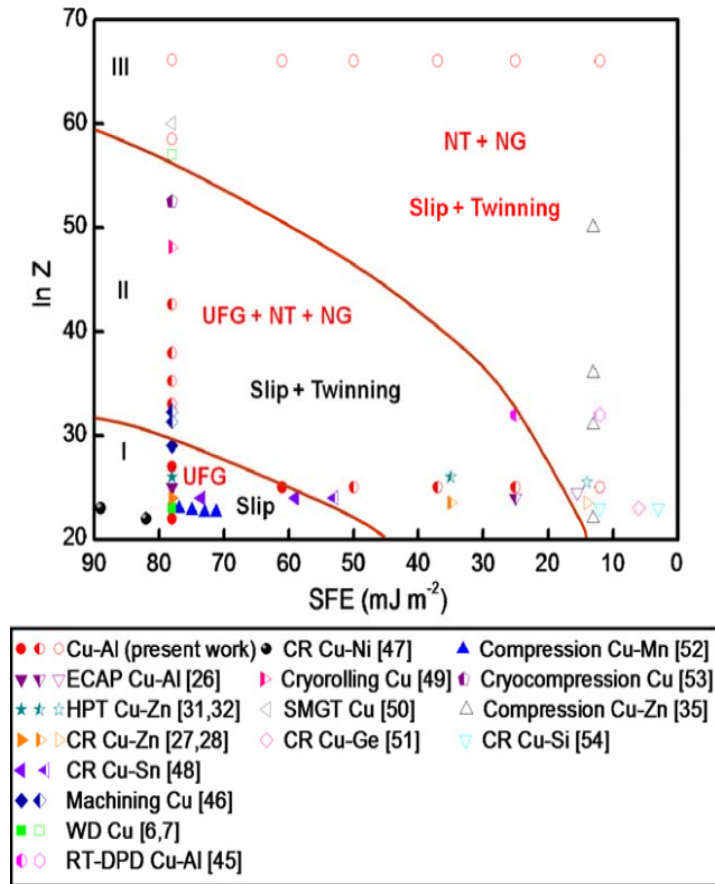


Figure 2.18- A map of deformation mode and strain-induced microstructures in the SFE–processing parameters ($\ln Z$) space for the Cu-Al alloys, Ultrafine grain (UFG); nanoscale twin (NT); nanosized grain (NG) [55].

Strength

There are a notable number of publications in the literature on the effect of SFE on mechanical properties of structural metals and alloys. For example, Cu-Zn alloys processed by HPT [56] and ball milling [57], Cu-Al alloys processed by dynamic plastic deformation [55], and Cu-Ge alloys processed by cold rolling [58] were systematically studied to investigate the effect of stacking fault energy on mechanical properties. As an example,

Figure 2.19 demonstrates the tensile stress-strain curves obtained from HPT-processed Cu-Zn alloys [56]. Zhao et al. [56] concluded that there is an optimum stacking fault energy in Cu-Zn alloys, Cu-10%Zn, at which the highest ductility with good yield strength can be obtained. Low stacking fault energy of Cu-30%Zn was found responsible for achieving a very small grain size of 15nm after HPT deformation. Low SFE also resulted in saturation of stacking faults and prohibited accumulation of dislocations and deformation twins during the tensile test [56].

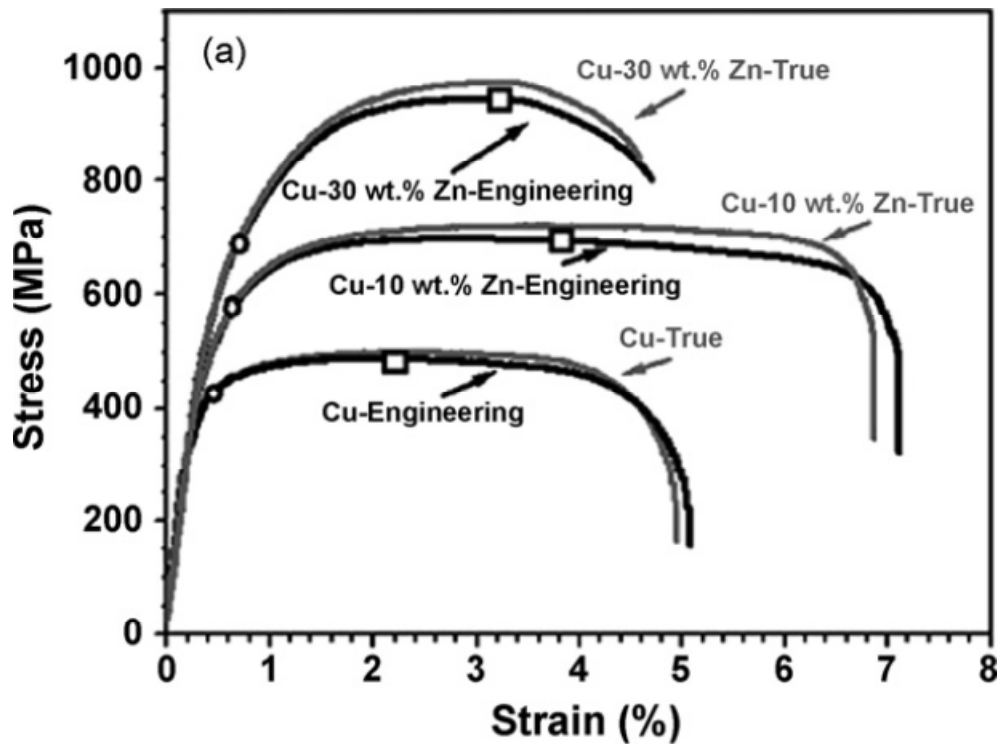


Figure 2.19- Tensile engineering and true stress-strain curves of the HPT processed ultrafine grain Cu, Cu-10 wt.% Zn alloy, and Cu-30 wt.% Zn alloy [56].

Cu-Al alloys processed with dynamic plastic deformation and quasi-static compression also showed a similar trend of monotonic increase in yield strength with reducing the SFE, Figure 2.20 [55]. Increased strength was attributed to the increased volume fraction of twinned regions in the microstructure at lower SFE alloys due to higher twinning tendency. Furthermore, smaller grain sizes and twin/matrix lamellae can be obtained at lower SFE alloys that bring about an elevation in strength.

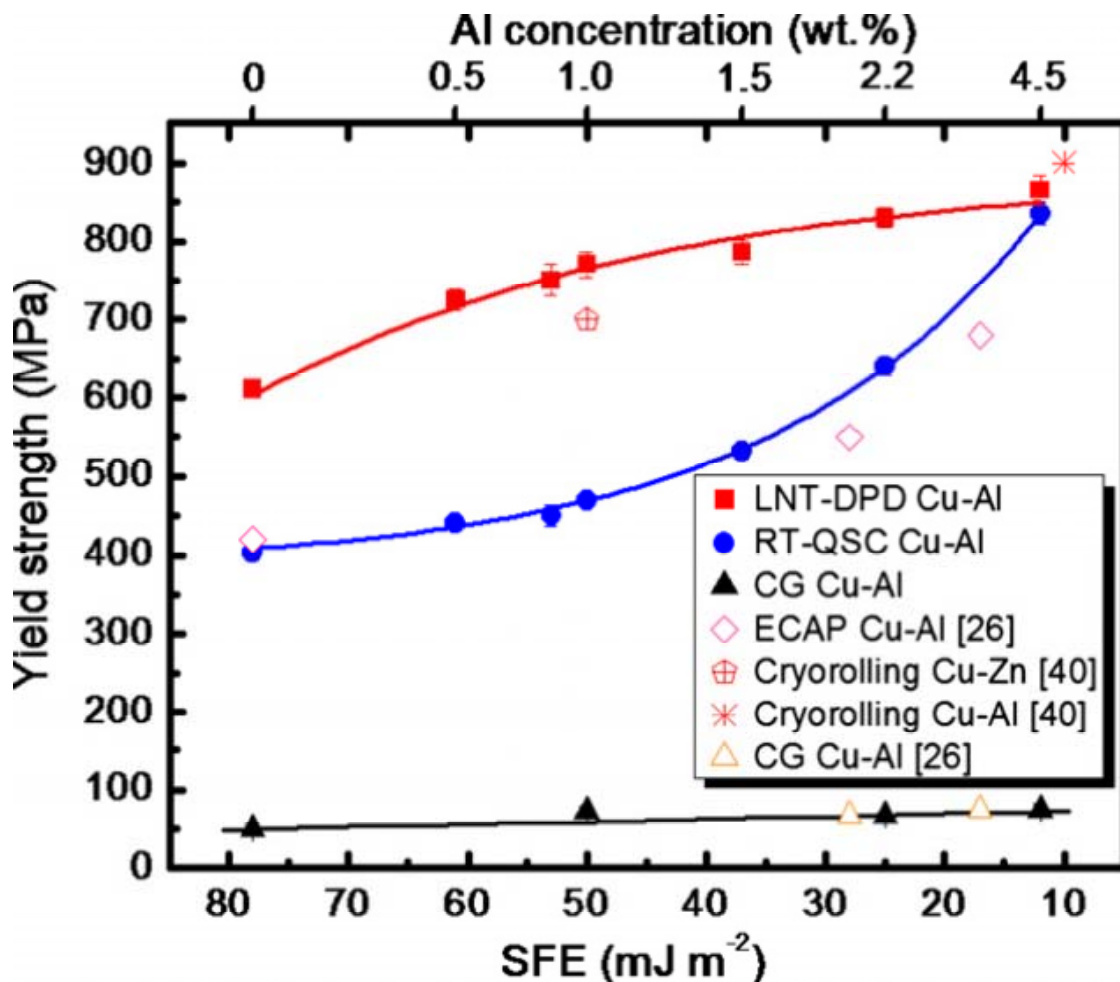


Figure 2.20- Variation in yield strength with SFE for Cu-Al alloys deformed by dynamic plastic deformation and quasi-static compression [55].

Strain hardening and ductility

Nanocrystalline materials usually demonstrate limited uniform elongation, Figure 2.21, after an initial stage of rapid strain hardening that is due to lack of strain hardening, i.e. limited dislocation activity. There are some concerns about the presence of artifacts in tensile samples used for determining mechanical properties [2]. These artifacts can cause premature failure of the sample. In order to obtain ductility, it is necessary to minimize mechanical instability that results in necking and failure of the material [2]. Using appropriate processing routes, a bimodal grain structure can be produced in which the larger sized grains sustain plastic deformation via dislocation activity and smaller sized grains provide high strength. An example is shown in Figure 2.22, where a bimodal microstructure could improve the tensile ductility in Al-7.5%Mg processed by cryomilling and subsequent consolidation by hot isostatic pressing and extrusion [59, 60].

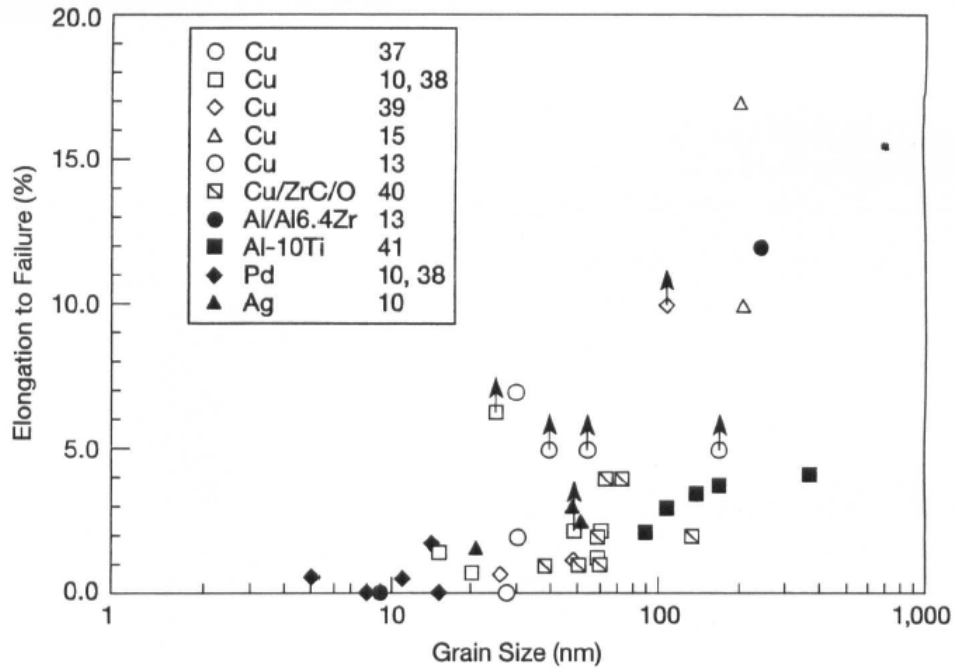


Figure 2.21- Tensile elongation to failure versus grain size [61].

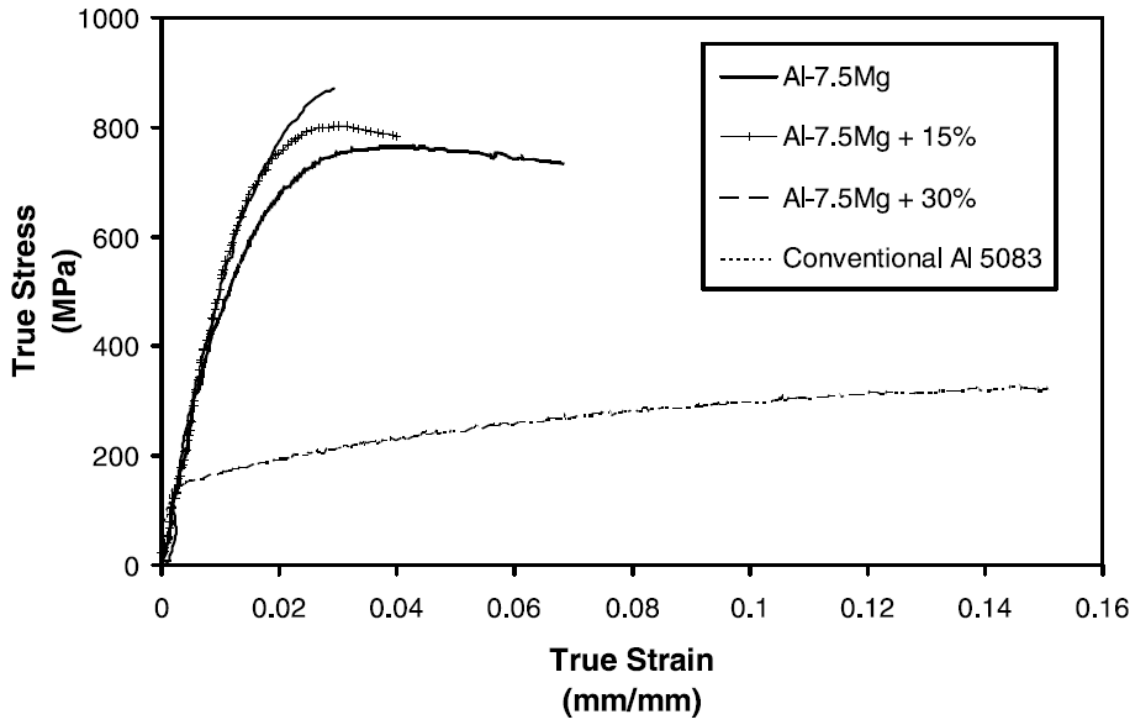


Figure 2.22 – Tensile curves for Al-7.5%Mg alloy with bimodal microstructure [59].

It is worthy to mention that there are reports in the literature on good ductility of nanostructured materials with narrow grain size distributions. Electrodeposited nanocrystalline Co with a grain size of 12 nm and elongation to failure of 6-9% [62], electrodeposited Ni with grain size of 44nm and elongation to failure of ~9% [63], and nanocrystalline Cu processed by in situ consolidation in ball milling with grain size of 23 nm and elongation to failure of 14%, Figure 2.23 [64], are among examples for good tensile ductility in a real nanostructured material.

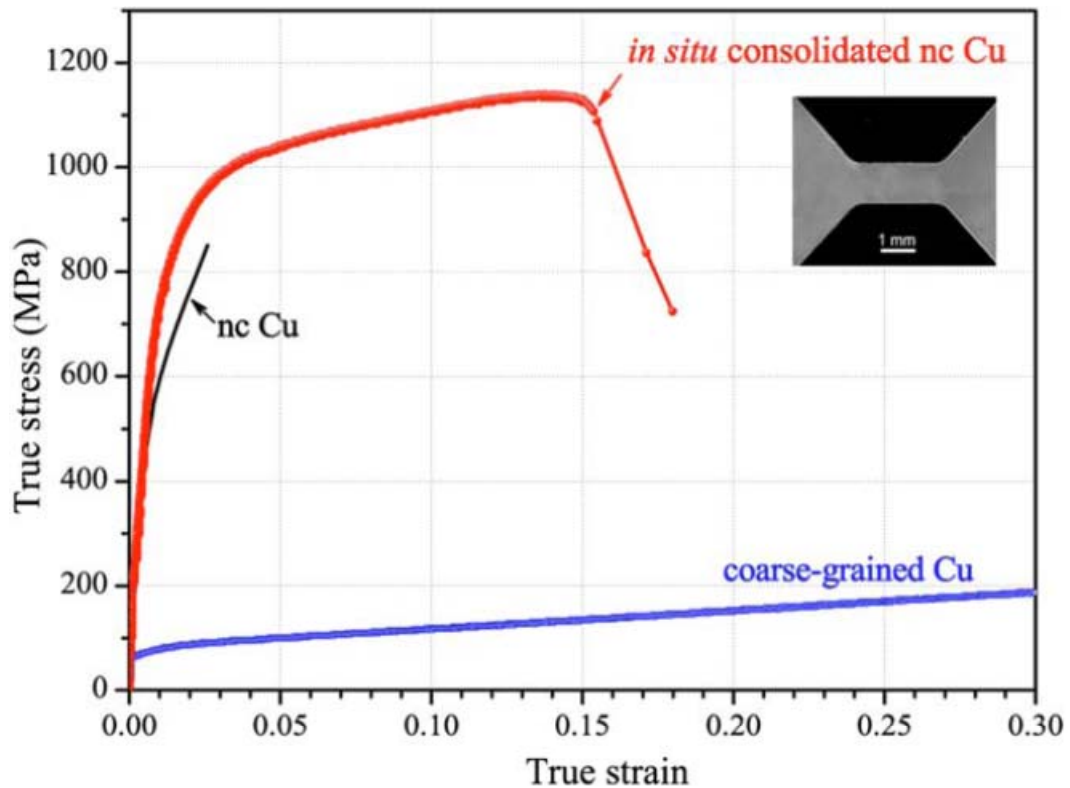


Figure 2.23 –Stress-strain curve for nanocrystalline Cu produced by in situ consolidation in ball milling [64].

Strain rate sensitivity

The yield stress and flow stresses at different values of strain increase with strain rate.

Strain rate sensitivity which is define as $m = \left. \frac{\partial \ln \sigma}{\partial \ln \dot{\epsilon}} \right|_{\epsilon, T}$, is an important mechanical property.

The strain rate sensitivity, m, can also be expressed as;

$$m = \frac{\sqrt{3}kT}{V\sigma_y} \quad (2.13)$$

where, V is the activation volume for plastic deformation, T is the temperature, and σ_y is the yield stress. Conventional FCC metals have a large activation volume, $V \sim 10^2-10^3 b^3$. This large activation volume is related to dislocations cutting through forest dislocations. On the other hand, the activation volume for grain-boundary mediated processes in nanocrystalline materials is on the order of the atomic volume, $V \sim (1-10) b^3$.

There are reports in the literature on higher strain rate sensitivity in nanocrystalline metals [65]. For example, Figure 2.24 shows the enhanced strain rate sensitivity as the grain size decreases in pure Cu [66, 67].

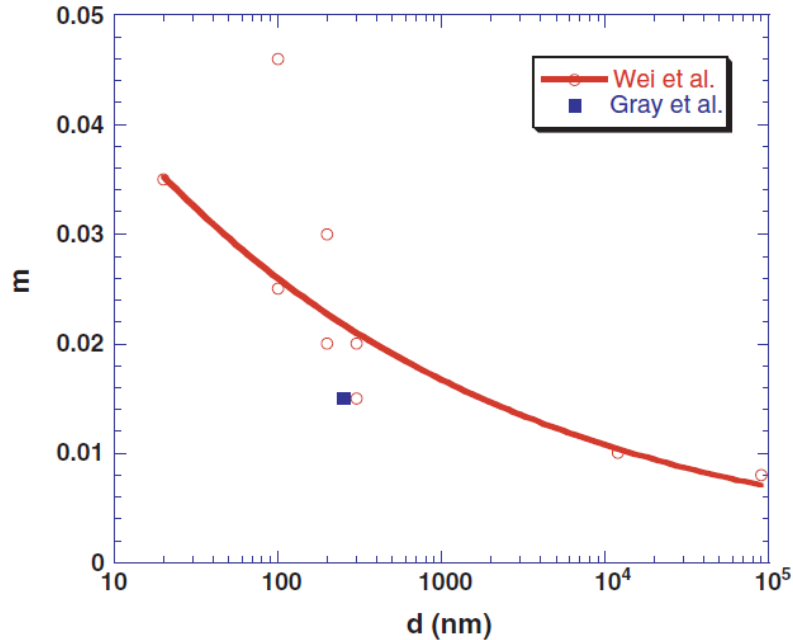


Figure 2.24- Strain rate sensitivity as a function of grain size for pure Cu [66, 67].

On the other hand, Lu et al. [65] reported an increased fracture strain at higher strain rates in electrodeposited nanocrystalline Cu, Figure 2.25. This abnormal behavior was correlated to different fracture behavior of nc Cu in which a much higher strain rate sensitivity was observed. In contrast to nc Cu, electrodeposited nanocrystalline Ni, despite some concerns about inhomogeneous microstructure and impurities, showed an increased strength and decreased ductility at higher strain rates, Figure 2.26 [68]. Considering the high volume of grain boundaries in nanocrystalline materials, Schwaiger et al. [68] proposed the concept of Grain Boundary Affected Zone (GBAZ) to model the strain rate behavior of nanocrystalline Ni. GBAZ refers to the area surrounding grain boundaries where the lattice is elastically strained and atoms within the GBAZ are involved in plastic deformation. Supported by experiments on nc Ni and a computational model, Schwaiger et al. [68]

discussed the conflicting trends in strain rate dependence of mechanical properties, Figure 2.26. Although they reported an increased uniform strain with increasing strain rate, they discussed that the failure strain is sensitive to the defects in the sample and therefore it is not sufficiently reliable to determine strain rate effects.

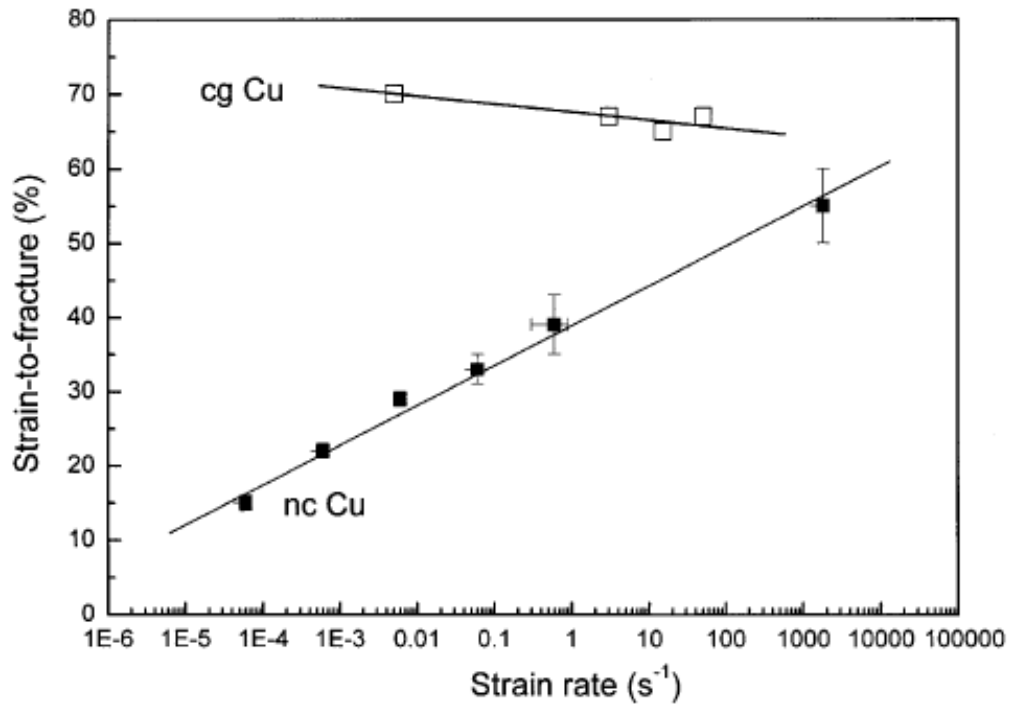


Figure 2.25- Tensile strain to fracture vs. strain rate for coarse grained and nanocrystalline Cu [65].

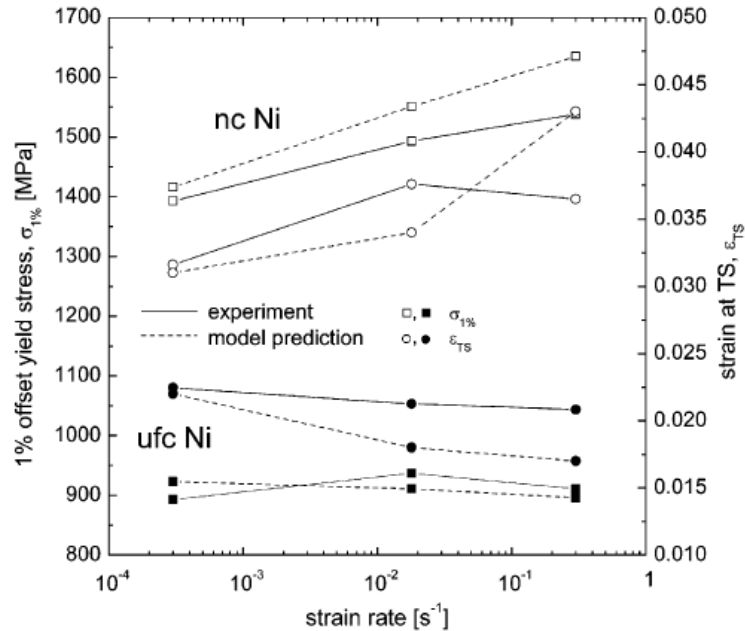


Figure 2.26- Comparison of experimental and computational results for tensile tests of nc and ufc Ni [68].

2.4. References

- [1] C.C. Koch, Nanostructured materials : processing, properties, and applications, 2nd ed., William Andrew Pub., Norwich, NY, 2007.
- [2] C.C. Koch, Adv. Eng. Mater., (2005) 787-794.
- [3] H. Conrad, J. Narayan, Scripta Mater., 42 (2000) 1025-1030.
- [4] M. Dao, L. Lu, Y.F. Shen, S. Suresh, Acta Mater., 54 (2006) 5421-5432.
- [5] K. Youssef, M. Sakaliyska, H. Bahmanpour, R. Scattergood, C. C. Koch, Acta Mater., 59 (2011) 5758-5764.
- [6] H. Bahmanpour, A. Kauffmann, M.S. Khoshkhoo, K.M. Youssef, S. Mula, J. Freudenberger, J. Eckert, R.O. Scattergood, C.C. Koch, Mater. Sci. Eng., A, 529 (2011) 230-236.

- [7] I. Dragomir-Cernatescu, M. Gheorghe, N. Thadhani, R.L. Snyder, *Powder Diffr.*, 20 (2005) 109-111.
- [8] M. Zehetbauer, Effects of nonequilibrium vacancies on strengthening, in: P. Lukac (Ed.) *Plasticity of Metals and Alloys - Ispma 6*, Trans Tech Publications, Clausthal Zellerfe, 1994, pp. 287-306.
- [9] J. Cizek, M. Janecek, O. Srba, R. Kuzel, Z. Barnovska, I. Prochazka, S. Dobatkin, *Acta Mater.*, 59 (2011) 2322-2329.
- [10] H. Conrad, *Metall. Mater. Trans. A*, 35A (2004) 2681-2695.
- [11] Y. Xun, F.A. Mohamed, *Mater. Sci. Eng., A*, 528 (2011) 5446-5452.
- [12] R. Pippan, High-Pressure Torsion – Features and Applications, in: *Bulk Nanostructured Materials*, Wiley-VCH Verlag GmbH & Co. KGaA, 2009, pp. 217-233.
- [13] A. Vorhauer, R. Pippan, *Scripta Mater.*, 51 (2004) 921-925.
- [14] M. Kawasaki, R.B. Figueiredo, T.G. Langdon, *Acta Mater.*, 59 (2011) 308-316.
- [15] K. Edalati, T. Fujioka, Z. Horita, *Mater. Sci. Eng., A*, 497 (2008) 168-173.
- [16] E.J. Lavernia, H.M. Wen, Y.H. Zhao, Y. Li, O. Ertorer, K.M. Nesterov, R.K. Islamgaliev, R.Z. Valiev, *Philos. Mag.*, 90 (2010) 4541-4550.
- [17] X.Z. Liao, A.R. Kilmametov, R.Z. Valiev, H.S. Gao, X.D. Li, A.K. Mukherjee, J.F. Bingert, Y.T. Zhu, *Appl. Phys. Lett.*, 88 (2006) 021909.
- [18] Y. Iwahashi, J.T. Wang, Z. Horita, M. Nemoto, T.G. Langdon, *Scripta Mater.*, 35 (1996) 143-146.
- [19] Z. Horita, ECAP: Processing Fundamentals and Recent Progresses, in: *Bulk Nanostructured Materials*, Wiley-VCH Verlag GmbH & Co. KGaA, 2009, pp. 201-215.

- [20] C. Xu, M. Furukawa, Z. Horita, T.G. Langdon, *Mater. Sci. Eng., A*, 398 (2005) 66-76.
- [21] S.D. Terhune, D.L. Swisher, K. Oh-Ishi, Z. Horita, T.G. Langdon, T.R. McNelley, *Metall. Mater. Trans. A*, 33 (2002) 2173-2184.
- [22] P.L. Sun, P.W. Kao, C.P. Chang, *Metall. Mater. Trans. A*, 35A (2004) 1359-1368.
- [23] V.V. Stolyarov, Y.T. Zhu, I.V. Alexandrov, T.C. Lowe, R.Z. Valiev, *Mater. Sci. Eng., A*, 299 (2001) 59-67.
- [24] S. Komura, Z. Horita, M. Nemoto, T.G. Langdon, *J. Mater. Res.*, 14 (1999) 4044-4050.
- [25] B.Q. Han, J. Ye, A.P. Newbery, Y.T. Zhu, J.M. Schoenung, E.J. Lavernia, *Bulk Nanostructured Metals from Ball Milling and Consolidation*, in: *Bulk Nanostructured Materials*, Wiley-VCH Verlag GmbH & Co. KGaA, 2009, pp. 273-291.
- [26] H.J. Fecht, E. Hellstern, Z. Fu, W.L. Johnson, *Metallurgical Transactions a-Physical Metallurgy and Materials Science*, 21 (1990) 2333-2337.
- [27] C.C. Koch, *Nanostructured Materials*, 9 (1997) 13-22.
- [28] J. Eckert, J.C. Holzer, C.E. Krill, W.L. Johnson, *J. Mater. Res.*, 7 (1992) 1751-1761.
- [29] E. Hellstern, H.J. Fecht, Z. Fu, W.L. Johnson, *J. Appl. Phys.*, 65 (1989) 305-310.
- [30] D. Oleszak, P.H. Shingu, *J. Appl. Phys.*, 79 (1996) 2975-2980.
- [31] E. Gaffet, M. Harmelin, *Journal of the Less-Common Metals*, 157 (1990) 201-222.
- [32] T.D. Shen, C.C. Koch, T.L. McCormick, R.J. Nemanich, J.Y. Huang, J.G. Huang, *J. Mater. Res.*, 10 (1995) 139-148.
- [33] T.D. Shen, W.Q. Ge, K.Y. Wang, M.X. Quan, J.T. Wang, W.D. Wei, C.C. Koch, *Nanostructured Materials*, 7 (1996) 393-399.

- [34] M. Haouaoui, I. Karaman, H.J. Maier, K.T. Hartwig, *Metall. Mater. Trans. A*, 35A (2004) 2935-2949.
- [35] M. Moss, R. Lapovok, C.J. Bettles, *Jom-U.S.*, 59 (2007) 54-57.
- [36] K. Edalati, Z. Horita, *Scripta Mater.*, 63 (2010) 174-177.
- [37] K. Edalati, Z. Horita, H. Fujiwara, K. Ameyama, *Metall. Mater. Trans. A*, 41A (2010) 3308-3317.
- [38] Z. Lee, F. Zhou, R.Z. Valiev, E.J. Lavernia, S.R. Nutt, *Scripta Mater.*, 51 (2004) 209-214.
- [39] J. Sort, D.C. Ile, A.P. Zhilyaev, A. Concustell, T. Czeppe, M. Stoica, S. Surinach, J. Eckert, M.D. Baro, *Scripta Mater.*, 50 (2004) 1221-1225.
- [40] S. Cheng, J.A. Spencer, W.W. Milligan, *Acta Mater.*, 51 (2003) 4505-4518.
- [41] H. Van Swygenhoven, M. Spaczer, A. Caro, *Acta Mater.*, 47 (1999) 3117-3126.
- [42] V. Yamakov, D. Wolf, S.R. Phillpot, A.K. Mukherjee, H. Gleiter, *Nature Materials*, 3 (2004) 43-47.
- [43] V. Yamakov, D. Wolf, M. Salazar, S.R. Phillpot, H. Gleiter, *Acta Mater.*, 49 (2001) 2713-2722.
- [44] E.O. Hall, *P Phys Soc Lond B*, 64 (1951) 747-753.
- [45] N.J. Petch, *J Iron Steel I*, 174 (1953) 25-28.
- [46] M.A. Meyers, K.K. Chawla, *Mechanical behavior of materials*, 2nd ed., Cambridge University Press, Cambridge ; New York, 2009.
- [47] M.A. Meyers, E. Ashworth, *Philosophical Magazine a-Physics of Condensed Matter Structure Defects and Mechanical Properties*, 46 (1982) 737-759.

- [48] A.H. Chokshi, A. Rosen, J. Karch, H. Gleiter, *Scripta Metallurgica*, 23 (1989) 1679-1683.
- [49] M.A. Meyers, A. Mishra, D.J. Benson, *Prog. Mater. Sci.*, 51 (2006) 427-556.
- [50] R.W. Hertzberg, *Deformation and fracture mechanics of engineering materials*, 4th ed., J. Wiley & Sons, New York, 1996.
- [51] D.A. Porter, K.E. Easterling, *Phase transformations in metals and alloys*, Van Nostrand Reinhold, New York, 1981.
- [52] M.F. Denicot, J.P. Villain, *Phys. Status Solidi A*, 8 (1971) 125-127.
- [53] P.C.J. Gallagher, *Metall. Trans.*, 1 (1970) 2429-2461.
- [54] A. Rohatgi, K.S. Vecchio, G.T. Gray, *Metall. Mater. Trans. A*, 32 (2001) 135-145.
- [55] Y. Zhang, N.R. Tao, K. Lu, *Acta Mater.*, 59 (2011) 6048-6058.
- [56] Y.H. Zhao, X.Z. Liao, Z. Horita, T.G. Langdon, Y.T. Zhu, *Mater. Sci. Eng., A*, 493 (2008) 123-129.
- [57] H. Bahmanpour, K. Youssef, R. Scattergood, C. Koch, *J. Mater. Sci.*, (2011) 1-7.
- [58] X.Y. San, X.G. Liang, L.P. Chen, Z.L. Xia, X.K. Zhu, *Mater. Sci. Eng., A*, 528 (2011) 7867-7870.
- [59] D. Witkin, Z. Lee, R. Rodriguez, S. Nutt, E. Lavernia, *Scripta Mater.*, 49 (2003) 297-302.
- [60] Z. Lee, D.B. Witkin, E.J. Lavernia, S.R. Nutt, *Nanomaterials for Structural Applications*, 740 (2003) 21-26.
- [61] C.C. Koch, D.G. Morris, K. Lu, A. Inoue, *Mrs Bulletin*, 24 (1999) 54-58.
- [62] A.A. Karimpoor, U. Erb, K.T. Aust, G. Palumbo, *Scripta Mater.*, 49 (2003) 651-656.

- [63] H.Q. Li, F. Ebrahimi, *Appl. Phys. Lett.*, 84 (2004) 4307-4309.
- [64] K.M. Youssef, R. O. Scattergood, K. L. Murty, J. A. Horton, C. C. Koch, *Appl. Phys. Lett.*, 87 (2005) 0919041.
- [65] L. Lu, S.X. Li, K. Lu, *Scripta Mater.*, 45 (2001) 1163-1169.
- [66] G.T. Gray, T.C. Lowe, C.M. Cady, R.Z. Valiev, I.V. Aleksandrov, *Nanostructured Materials*, 9 (1997) 477-480.
- [67] Q. Wei, S. Cheng, K.T. Ramesh, E. Ma, *Mater. Sci. Eng., A*, 381 (2004) 71-79.
- [68] B.M. Schwaiger, M. Dao, N. Chollacoop, S. Suresh, 51 (2003).

CHAPTER THREE

3.0. EXPERIMENTAL PROCEDURE

3.1. Processing

3.1.1. Ball milling

Elemental powders of copper, zinc, and aluminum (Alfa AesarTM) were used for ball milling experiments. The powder mixture and 440C martensitic stainless steel balls were loaded in stainless steel vials in a glove box under argon atmosphere with oxygen content of less than 1ppm. For some room temperature experiments NaCl was added to control the cold welding and fracture processes and also to inhibit sticking of the powder to the milling media. All ball milling experiments were done at a ball to powder ratio of 10:1 with 5.1g of powder. It is worth to mention that the material of the vial affects sticking of the powder to the milling media. Therefore, for all experiments stainless steel vials were used instead of hardened steel ones. In order to avoid argon entrapment in the structure of samples, the vial was left under vacuum for at least 10min (to minimize the presence of argon gas in the vial) and then sealed. Experiments were done at different milling times and temperatures using Spex 8000 mill. For cryomilling experiments, a specially designed nylon container and modified Spex 8000 mill were utilized, Figure 3.1. The nylon container maintains the flow of liquid nitrogen during the milling process, and keeps the vial temperature close to 77K. Some

ball milling experiments were also done at IFW, Dresden on in situ consolidation of pure copper at room temperature using a planetary ball mill, Figure 3.2.

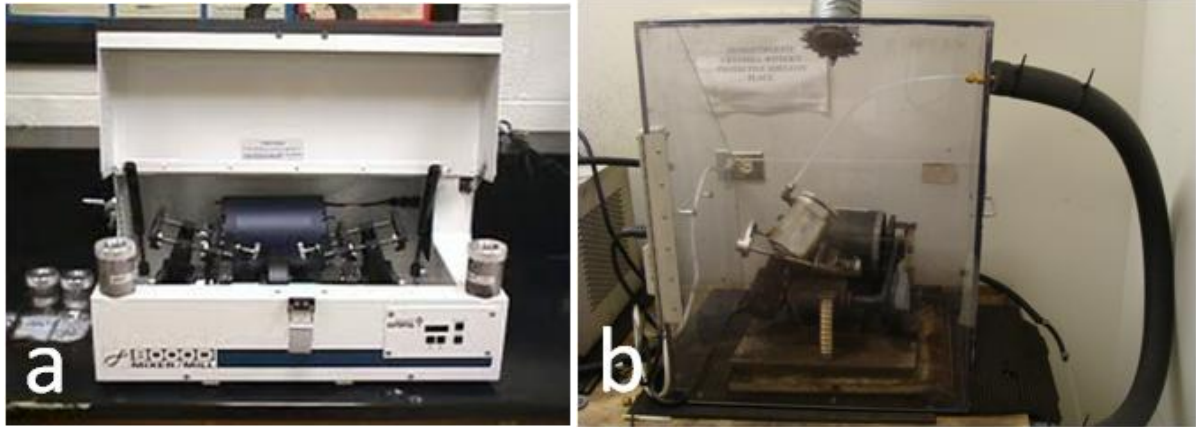


Figure 3.1- Spex 8000 mill, a) room temperature mill, b) cryomill.



Figure 3.2- Planetary ball mill.

Possible contamination of ball milled product was checked by inert gas fusion (ASTM E 1019-08) for oxygen and direct current plasma emission spectroscopy (ASTM E

1097-07) for iron. Table 3.1 shows the results for Cu, Cu-10wt.%Zn, and Cu-30wt.%Zn cryomilled for 8h.

Table 3.1- Oxygen and iron content of 8h cryomilled Cu, Cu-10wt.%Zn, and Cu-30wt.%Zn.

	Oxygen (wt.%)	Iron (wt.%)
Cu	0.356	0.54
Cu-10wt.%Zn	0.486	0.17
Cu-30wt.%Zn	0.343	0.33

3.1.2. High pressure torsion

A HPT press type WAK-01 Mark 1 (located at University of Vienna), Figure 3.3, was utilized to consolidate Cu and Cu-Zn ball milled flakes. Constrained dies were used to make HPT disks. In order to provide enough friction between the die and sample and minimize the slippage, surface of the dies were sand blasted before each HPT experiment. A computerized system attached to the HPT machine was used to control the speed and number of rotations and also record the torque by means of a torque cell.

8h cryomilled samples were used as precursors for HPT-consolidation. Our experience showed that consolidation of powder material with HPT techniques requires application of a high pressure of 8 GPa and ultra high strain of minimum $\gamma=2000$, that is equal to 75 revolutions. All HPT tests were performed at 0.3 rpm.



Figure 3.3- HPT machine.

3.1.3. Preparing master alloys for rolling experiments

Low stacking fault energy Cu-12.1at.%Al-4.1at.%Zn alloy was prepared by casting in an induction furnace at IFW, Dresden. In order to homogenize the composition, samples were kept at 800 °C for 14 h under argon. Hot rolling was done by preheating to 600 °C and rolling from 25 mm to 20.5 mm to remove the cast microstructure. Another homogenization step was done at 800 °C for 14 h under argon atmosphere and subsequent water quenching to avoid short range ordering. The samples exhibit grain sizes of several hundred micrometers, and approximately random distribution of grain orientations.

3.1.4. Rolling

Rolling experiments were performed at liquid nitrogen temperature using a motorized lab scale rolling machine, Figure 3.4. In order to minimize possible temperature increase of the samples and dynamic recovery, working zone of rollers were kept in liquid nitrogen with a specially designed plastic container. Samples were soaked in liquid nitrogen before deformation to cool down to 77K. Continuous feed of liquid nitrogen was kept around the rollers to maintain a stable temperature profile before, during and after deformation. Successive passes of rolling deformation were applied on the sample to attain the desired degree of deformation.



Figure 3.4- Rolling machine.

3.1.5. Wire drawing

Wire drawing at liquid nitrogen temperature was performed at IFW, Dresden. Drawing dies with a cone angle of $2\alpha = 12^\circ$ were used to deform copper samples. Prior to each drawing step of about 0.2 logarithmic deformation strain, η , the wire and the dies were immersed in liquid nitrogen. The drawing process was carried at a speed of 0.5 m/min using molybdenum disulphide, MoS_2 , as lubricant.

3.2. Characterization

3.2.1. Microhardness

The local mechanical properties of the samples were assessed using Vickers hardness tests with a Buehler Micromet II. A mirror polished surface prepared by mechanical grinding and polishing was used for all samples to get accurate hardness data. In the case of powder samples, hardness tests were performed on cold compacted disks. The dwell time of 15 seconds for each indent was concurrent with ASTM standards (ASTM Standard Test Method for Vickers Hardness of Metallic Materials). Eight indentations were used for each data point in this work to obtain reasonably accurate data and standard deviation.

3.2.2. Tensile tests

Tensile tests were performed on small sized samples using a miniaturized tensile test machine, Figure 3.5. Strain measurements were done using a LVDT. Unfortunately there is no standard test procedure and dimension for assessment of the tensile behavior of nanocrystalline material. To assure the accuracy of the tensile properties reported in this work, the load cell were formerly calibrated using dead weights and the miniaturized tensile tests were found to be in good agreement with standard sized samples tested with commercial tensile test frames.

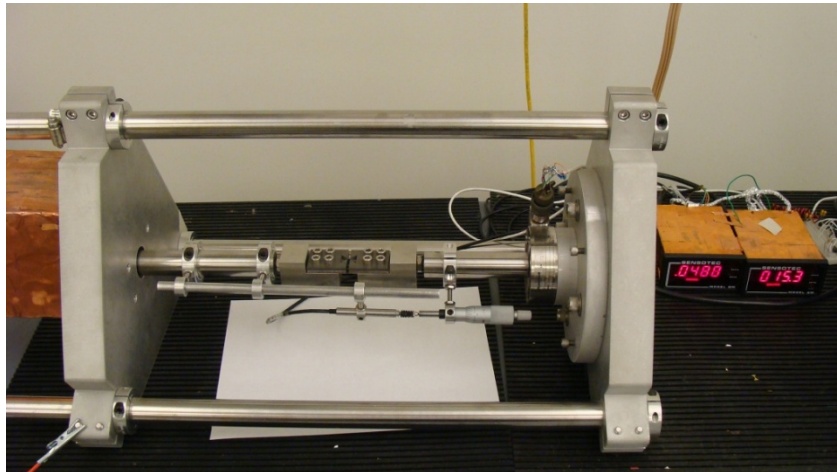


Figure 3.5- Mini tensile test machine.

Figure 3.6 demonstrates the dimensions of the samples used in this research. In the case of ball milled experiments, the in situ consolidated samples are usually in the shape of round spheres that can be sliced and pressed into 6-7mm disks. These disks can then be cut with a computer controlled milling machine with precise dimensions. The gauge of the

samples is extended to the shoulders with a 0.5mm curvature to avoid stress concentration on the corners and limit the deformation to the gauge length.

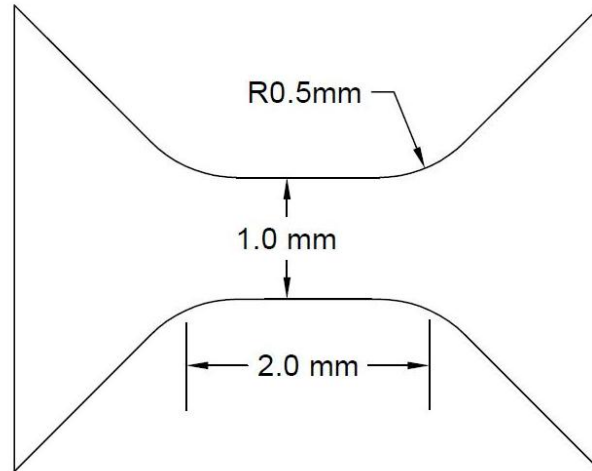


Figure 3.6- Schematic representation of mini tensile test samples.

3.2.3. X-ray line profile analysis

XRD technique was used to acquire data on crystallite size and dislocation density of processed samples. For the work in this research, x-ray diffraction analysis was performed with a Rigaku x-ray diffractometer using CuK_α ($\lambda = 0.1542 \text{ nm}$) radiation, with a diffracted beam graphite monochromator having instrumental broadening $\approx 0.1^\circ$ at an angle of 69.13° . Instrumental broadening of the x-ray machine was calculated using a standard alumina sample. Powder samples were pressed into 6-mm dies and mounted onto sample holder for XRD measurements. Bulk samples (such as rolled or HPT deformed samples) were ground to obtain a mirror polished surface for XRD measurements.

Acquired XRD profiles were analyzed with PM2K software based on Whole Powder Pattern Modeling approach (WPPM) [1]. A brief description of the WPPM approach is given in Appendix A. Built-in Caglioti formula parameterizes the instrumental profile component;

$$\text{FWHM}^2 = W + V \tan(\theta) + U \tan^2(\theta) \quad (3.1)$$

$$\eta = a + b \theta_{\text{deg}} + c (\theta_{\text{deg}})^2 \quad (3.2)$$

where, W, V, U, a, b, and c are parameters for instrumental broadening of the x-ray diffractometer used.

Size broadening was modeled assuming “sphere” domain shape. Built-in functions were used to calculate analytical Fourier coefficients corresponding to a distribution of domains of a given shape. Estimation of dislocation density was performed based on Wilkens theory [2].

3.2.4. Scanning electron microscopy

A Tabletop SEM - (Hitachi TM3000) was used to acquire images from surface of some ball milled products.

3.2.5. Transmission electron microscopy and high resolution TEM

3-mm electron transparent samples were prepared by mechanical polishing down to the thickness of 100 μm and then perforated using a Fischione twin-jet polish with a solution of Methanol-20 (vol.%) Nitric acid at a DC voltage of about 60. The electropolishing temperature was kept around -20°C using dry ice. It is worthy to mention that cryomilled samples, that are in the shape of micron sized flakes, were pressed into gallium lumps to prepare TEM disks. Gallium, which is a low melting temperature metal, flows easily and binds ball milled particles together. 3-mm disks can be then punched from the gallium-flake composite and electropolished.

TEM studies were done using a JEOL 2000 TEM at an accelerating voltage of 200kV. Bright field and dark field images were used to determine grain size distribution of the samples. HRTEM studies were performed with a JEOL 2010 TEM to acquire high resolution images from stacking faults and deformation twins.

3.3. References

- [1] P. Scardi, M. Leoni, Acta Crystallographica Section A, 58 (2002) 190-200.
- [2] M. Wilkens, physica status solidi (a), 104 (1987) K1-K6.

CHAPTER FOUR

4.0. MECHANICAL BEHAVIOR OF BULK NANOCRYSTALLINE COPPER ALLOYS PRODUCED BY HIGH ENERGY BALL MILLING

H. Bahmanpour, K. M. Youssef, R. O. Scattergood, C. C. Koch

Journal of Materials Science, 2011, Vol. 46, No. 19, pp. 6316-6322.

MS&T conference, 2012, Houston, Texas

4.1. Abstract

Copper alloys with different amounts of zinc were synthesized via high energy ball milling at liquid nitrogen and room temperature. Bulk samples were produced in situ by controlling the milling temperature. It is shown that temperature plays an important role in formation of artifact-free consolidated samples via its effect on defect formation and annihilation during the milling process. The mechanical behavior of Cu-Zn nanocrystalline alloys was examined using Vickers microhardness and tensile tests. The nanostructure of the alloys was investigated by X-ray diffraction (XRD) and transmission electron microscopy (TEM). The hardness results of processed alloys vary as a function of the alloying elements. Considering typical low ductility of nanocrystalline materials, the improved ductility with the

high strength observed in these alloys suggests that they are artifact-free and may have several deformation mechanisms, which may include dislocation activity and nano-twinning.

4.2. Introduction

Production of bulk nanostructured materials has been a challenging issue since introduction of superior properties of these materials such as ultra high strength and good ductility compared to microcrystalline materials. Several processing methods such as equal channel angular pressing (ECAE), high pressure torsion (HPT), and ball milling were examined and proposed to break down the grain size of samples to nano scale. Nanostructured materials produced by ball milling have the advantage of smaller crystallite sizes and also more homogeneous microstructure compared to other techniques. Ball milling has been of great interest due to its ability to produce a homogeneous mixture of powders with unique microstructural and mechanical properties. Its limitation has been consolidation of powders to produce bulk samples for testing.

Combination of milling at liquid nitrogen temperature and room temperature milling resulted in formation of sound and defect-free bulk samples that can compete very well with their counterparts produced by other methods such as ECAE or HPT. Youssef et al. reported successful production of bulk nanocrystalline copper samples with a narrow grain size distribution and average grain size of ~23 nm using high energy ball milling at liquid nitrogen and room temperature. Ultra high strength of 791 MPa and uniform elongation of 14% were obtained by in situ consolidation of ball milled samples [1, 2]. The in situ consolidation of powder samples during the ball milling process has been reported in the

literature [3-5] but there is no systematic research on this process to find the optimum milling conditions to produce artifact-free samples.

Milling of ductile metals or alloys at room temperature in a dry and inert atmosphere causes welding to predominate and sample size will steadily increase with milling time. Milling at room temperature can result in formation of hollow spheres with inhomogeneous microstructure that contain cracks and pores. It is of great interest to understand and control the milling conditions and produce defect-free samples with superior mechanical and microstructural properties [6]. It has been shown that the temperature of the milling process plays an important role on the quality of the in situ consolidated samples [3, 7]. Although the mechanism of growth of small spheres is not very clear, it is believed that material transfer from one sphere to another via the milling produces coalescence of particles [3].

In this paper the in-situ consolidation behavior of Cu-Zn alloys is investigated. Successful experiments of in situ consolidation on pure copper are extended to copper alloys. As expected, alloying changes the microstructural and mechanical behavior of samples and therefore the in situ consolidation behavior also changes. Materials produced in this research are examined in order to study governing parameters for in situ consolidation of Cu alloys. Furthermore, mechanical properties of the bulk nanostructured copper alloys are investigated by microhardness and tensile tests. Considering the low stacking fault energy of the alloys studied, possible deformation mechanisms determining the high strength and good ductility are discussed.

4.3. Experimental procedure

Nanostructured Cu and Cu-Zn alloys were synthesized via mechanical alloying of elemental powders using a Spex 8000 mixer/mill. Hardened steel vials were loaded under argon atmosphere with oxygen content of less than 1ppm. Different milling regimes were studied to assess the effect of temperature on the properties of the ball milled samples. Powders were first milled at liquid nitrogen temperature and subsequent processing was followed by milling at room temperature to get sound and defect-free spheres.

X-ray diffraction was used to estimate the crystallite size, dislocation density, and dislocation character of samples. PM2K [8] software was utilized to fit the x-ray profiles, model the experimental pattern, and to extract microstructural data. Hardness of the milled samples was measured using Vickers microhardness at 50g load. Tensile tests were performed on the artifact-free bulk nc samples using a miniaturized tensile test machine. TEM samples were prepared by electro polishing and the microstructure of the produced samples was studied using a JEOL transmission electron microscope at 200 kV.

4.4. Results and discussion

Figure 4.1 shows different pieces of in situ consolidated samples of a Cu-10wt.%Zn alloy. Various products are seen after mechanical milling of ductile metals. As shown in Figure 4.1, spheres as large as ~6mm in diameter can be formed after ball milling process. These samples can be pressed and sliced to make tensile test specimens. It is believed that

formation of sound and defect-free samples is very sensitive to milling temperature such that a range of hollow spheres with different size and sound samples can be produced.

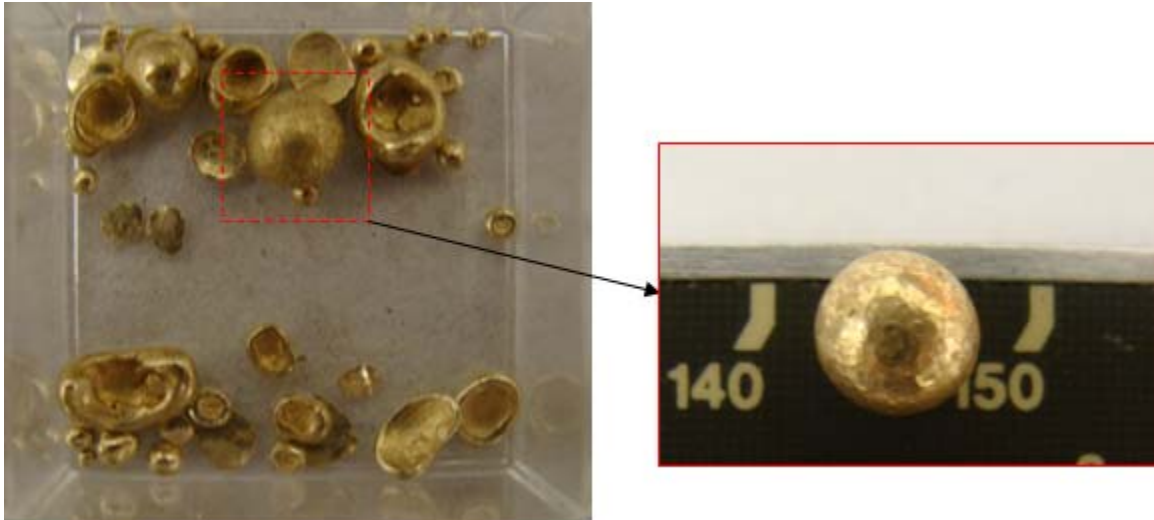


Figure 4.1- In situ consolidated samples of Cu-10wt.%Zn alloy. Left: different pieces of hollow and defect-free spheres. Right: A sound 6mm sphere.

Figure 4.2 demonstrates the microstructure of a Cu-30wt.%Zn sample milled for 6h at 77K followed by 2h of room temperature milling. Bright field and dark field images show that nanostructure produced by this processing route is fairly homogeneous and consists of twinned grains, typical microstructure for Cu-Zn samples prepared in this research. Corresponding selected area diffraction pattern (SADP), lower left inset in Figure 4.2-a, represents a microstructure with randomly oriented grains. Image analysis showed that the average crystallite size for this sample is 21 nanometers.

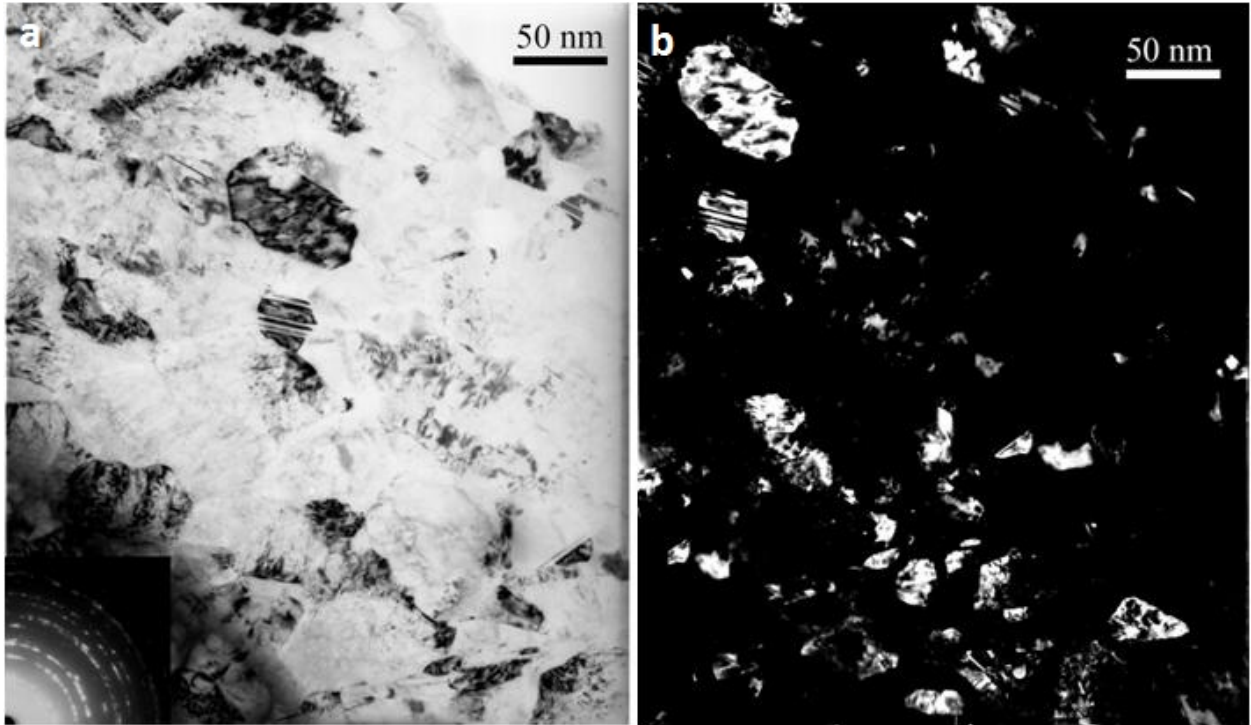


Figure 4.2- a) Bright field and b) dark field TEM image of in situ consolidated Cu-30wt.%Zn sample after 6h cryomilling and 2h milling at room temperature. Lower left inset in the bright field image shows the electron diffraction pattern.

Figure 4.3 shows hardness results as a function of milling time for pure Cu, Cu-10wt.%Zn, Cu-20wt.%Zn, and Cu-30wt.%Zn alloys processed at liquid nitrogen temperature. For each sample almost constant hardness is obtained after a few hours of the milling process. Powder evolution during the milling process involves five stages including particle flattening due to plastic deformation, particle welding, equiaxed particle formation, random welding of powder particles and steady-state deformation, during which a balance between fracture and cold welding is established as microstructural refinement progresses [9]. From Figure 4.3 it is seen that compared to copper alloys, longer time is needed for pure copper to achieve steady-state deformation due to a higher rate of dynamic recovery in pure copper. This is reflected as a gradual increase of hardness in pure copper.

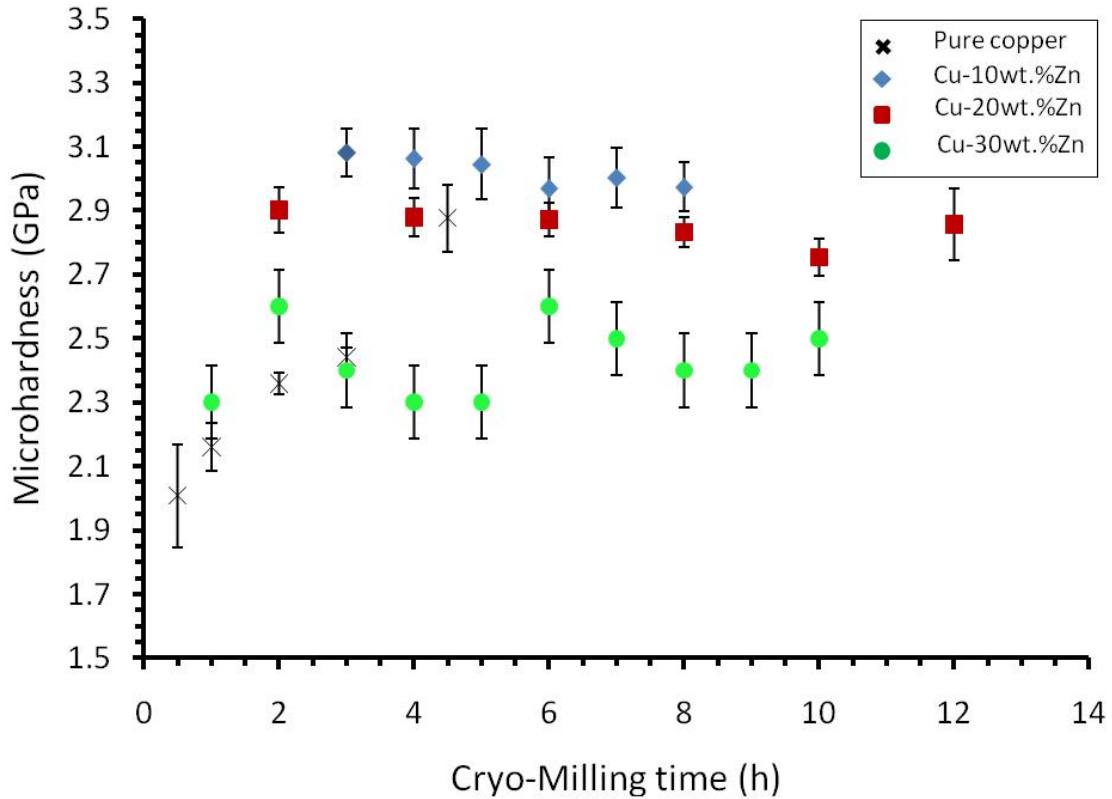


Figure 4.3 Microhardness vs. cryo-milling time for pure Cu, Cu-10wt.%Zn, Cu-20wt.%Zn, and Cu-30wt.%Zn alloys.

Assuming that the hardness and yield strength correlate with Tabor relation, $H_v \approx 3\sigma_y$, the strength obtained in these Cu-Zn alloys are higher than the results published in the literature on the same alloys with different processing such as high pressure torsion. For example Zhao et al. [10] reported 1.7 and 2.1 GPa for Cu-10wt.%Zn and Cu-30wt. %Zn, respectively. Mean grain size obtained by HPT in [10] was 110 and 10 nm for Cu-10w.%Zn and Cu-30wt.%Zn, respectively. High frequency multi axial loads could result in smaller crystallite size, higher density of lattice defects, and hence higher strength for samples produced by high energy ball milling compared to plastic deformation induced by high

pressure torsion, a typical severe plastic deformation process to make bulk ultrafine materials.

Small crystallite size obtained by ball milling at 77K is demonstrated in Figure 4.4 that shows the change in crystallite size, calculated from x-ray profile, as milling time increases. It can be seen that the crystallite size also stays almost constant over the milling period. Electrical resistivity measurements showed saturation of lattice defects after a certain time period in low temperature fatigue tests of copper crystals [11]. It could be also true for ball milled materials when saturation of hardness and crystallite size is observed after 4-6 hours of cryo-milling for Cu-Zn alloys. Possible dynamic recovery of defects generated due to severe plastic deformation results in a stable microstructure after a certain milling time. At very low processing temperature of these alloys, i.e. 77K, the rate of recovery should be less than the rate of defect formation for the first few hours of the process and hence a microstructure with lower crystallite size and higher defect density is expected to be generated during the cryo-milling process.

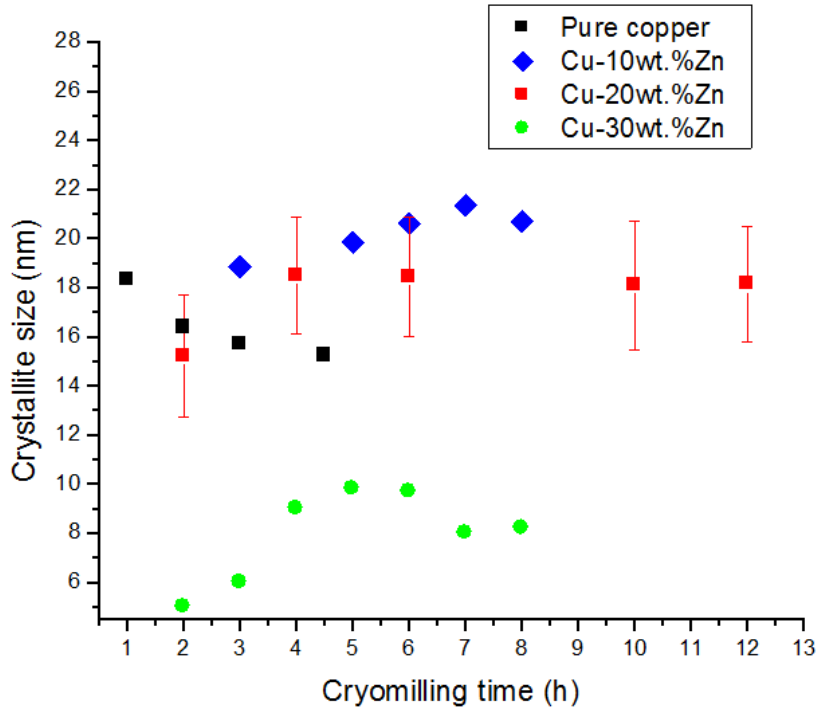


Figure 4.4- Crystallite size vs. cryo-milling time for pure Cu, Cu-10wt.%Zn, Cu-20wt.%Zn, and Cu-30wt.%Zn alloys.

It is noteworthy to address the distinct grain refinement behavior of Cu-30wt.%Zn alloy observed in this research, Figure 4.4. Smaller crystallite size obtained in this composition is also observed by Zhao et al. [10] for HPT processed samples. As mentioned earlier, severe plastic deformation by HPT results in a crystallite size of 110nm and 10nm for Cu-10wt.%Zn and Cu-30wt.%Zn alloys, respectively [10]. Wang et al. [12] suggested that the grain size of ~10nm in HPT-processed Cu-30wt.%Zn is related to the very low stacking fault energy of the alloy, 7 mJ/m², making the sample capable of producing a high density of stacking faults and deformation twins. It was found that incoherent high angle grain boundaries can be formed by the accumulation of a high density of dislocations at stacking faults and twin boundaries. These boundaries emit secondary stacking faults and twins that give rise to further refinement of the grains [12]. The differences in crystallite size of copper

and copper alloys processed by ball milling could also be related to the stacking fault energy and capability of different alloys to break down the initial microstructure to nano sized grains.

Although the crystallite size of samples with higher zinc content is equal or smaller than alloys with lower concentration of zinc, Figure 4.4, there is a decreasing trend of hardness as zinc content increases to more than 10 weight percent, Figure 4.3. It is also worthy to note that the hardness of pure copper sample after 4.5h cryomilling is less than the hardness of Cu-10wt.%Zn and almost equal to the hardness of Cu-20wt.%Zn. This is rather an unusual trend seen in these alloys. Samples with the same compositions but processed with other severe plastic deformation techniques, e.g. high pressure torsion, show the expected results of hardening by increasing solute content of the material [10]. Shen and Koch [13] reported apparent solid solution softening observed in Ni-Cu, Fe-Cu and Cr-Cu systems prepared by mechanical attrition is due to increase of crystallite size. Governing strengthening mechanisms in nanostructured materials such as solid solution and grain boundary hardening should be considered. For Ni in [13], it is believed that decreased grain boundary hardening is the reason for total reduction of hardness. The small contribution of grain boundary hardening to total strength of the material due to grain size increase results in the observed decrease of hardness [13]. But this is not the case for copper and copper-zinc system in this research and further studies are needed to investigate the hardening up to 10wt.% zinc and then softening behavior of Cu-Zn alloys at nanoscale grain sizes.

To have a deeper understanding of microstructure and mechanical properties, we need to consider dislocation density and arrangement in the microstructure. Arrangement of dislocations in these samples and effect of temperature on their activity are studied by Whole Powder Pattern Modeling approach. WPPM, has been applied to different metallic systems such as nanocrystalline FeMo [14] and Cu [15] to derive information about line defects. In this research, the Wilkens approach [16] was used by PM2K software [8] to calculate dislocation density and model the contribution of edge and screw dislocations to the x-ray profile of the processed alloys. Figure 4.5 demonstrates the effect of milling time on dislocation density and character for Cu-20wt.%Zn sample. Dislocation density decreases at the beginning of cryomilling and then stays almost constant. First two hours of cryomilling results in high dislocation density and further milling at 77K up to 6h brings about formation of dislocation cell structure. Figure 4.6 shows the TEM bright field image of the Cu-20wt.%Zn alloy milled for 3h at room temperature followed by 3h cryomilling. The heavily deformed microstructure shown in Figure 4.6 demonstrates dislocation cell-wall structures formed during the ball milling process. Movement of dislocations is constrained to local regions during low temperature processing of these low stacking fault energy alloys. With restricted cross-slip, continued deformation leads to reorganization of dislocations into cell-wall configurations to reduce the strain energy. Subsequent stabilization of the microstructure takes place by formation of sub-grains. This eventually leads to formation of new crystallite boundaries and, consequently a reduction of the X-ray coherent domain. This is consistent with the fact that the average dislocation density, obtained from X-ray diffraction, decreases as the milling time increases, i.e. the initial dislocation density of $0.55 \times 10^{18} \text{ m}^{-2}$ at 2h is

decreased to $0.39 \times 10^{18} \text{ m}^{-2}$ at 6h cryomilling. The slight increase in dislocation density with increase in deformation from 6h to 10h can be explained by the nucleation of a new generation of dislocations as the dislocation cell-wall configuration saturates. Further milling at room temperature leads to decrease of dislocation density that could be an evidence for annihilation of edge dislocations at primary grain boundaries or dislocation walls formed during cryomilling period by providing enough thermal energy to the system.

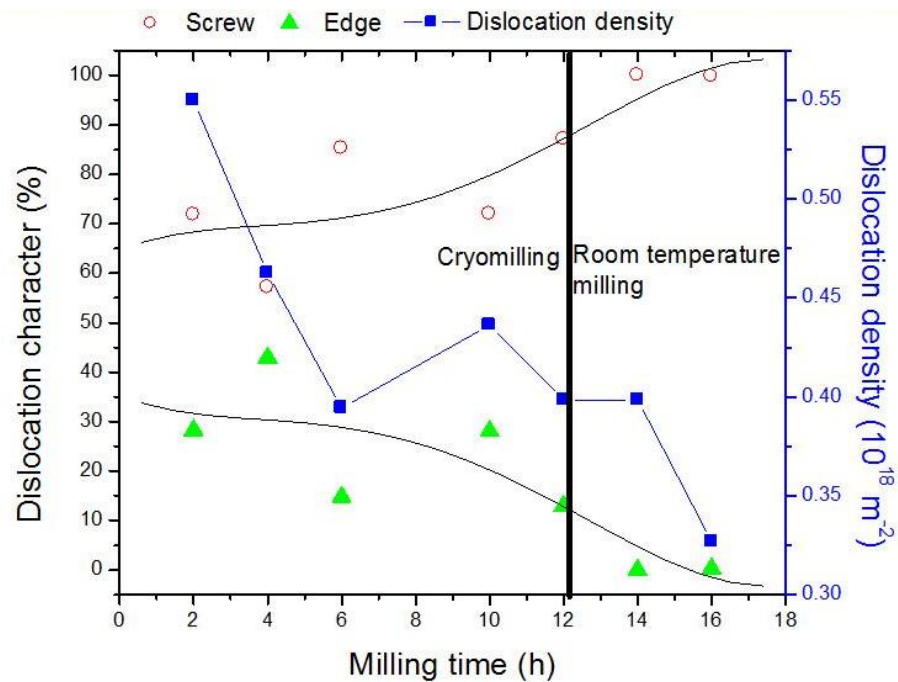


Figure 4.5- Dislocation density vs. milling time for Cu-20wt.%Zn milled for 12h at 77K followed by 4h milling at room temperature.

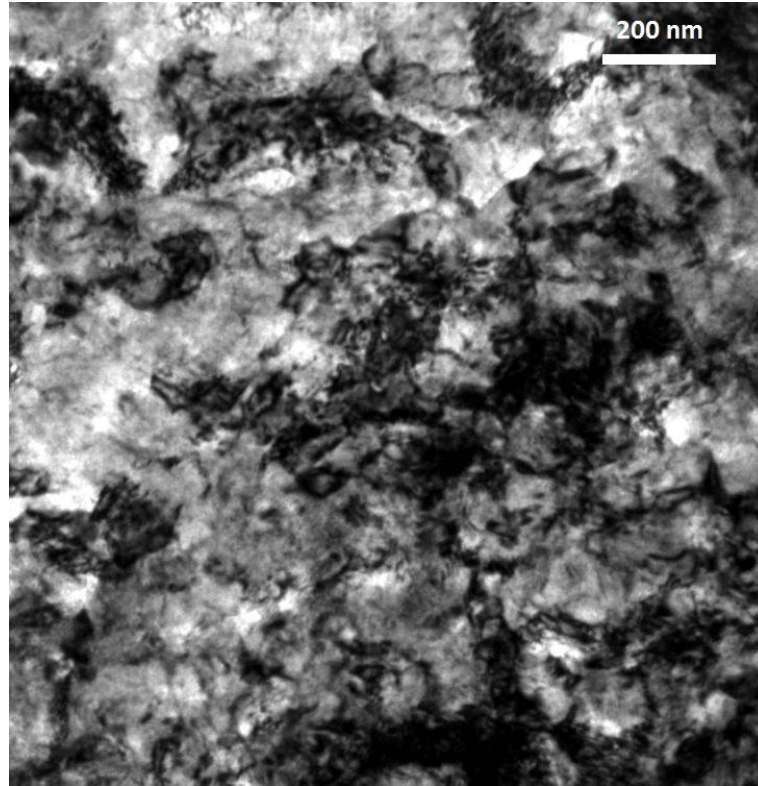


Figure 4.6- Microstructure of Cu-20wt.%Zn alloy milled for 3h at room temperature followed by 3h milling at 77K.

As shown in Figure 4.5 the dislocation character of the cryo-milled sample is a mixture of edge and screw dislocations but when the processing temperature is increased by milling at room temperature, the share of screw dislocations is increased. In light of temperature increase during room temperature milling, the decrease of dislocation density, and change of dislocation character can be understood. Several researchers reported different values for temperature rise during mechanical milling. Using a computer model, Davis et al. reported that the temperature increase in a Spex mixer/miller is less than 350K [17]. Xi et al. concluded that under the maximum milling intensity the temperature rise is not more than 125K [18]. Joardar et al. reported a maximum of $\sim 473\text{K}$ temperature increase for

$\text{Al}_{35}\text{Ni}_{35}\text{Fe}_{30}$ system in a planetary ball mill [19]. Although there are some discrepancies between results obtained by different researchers, the temperature rise during room temperature ball milling seems to be enough to trigger thermally activated processes such as diffusion of vacancies and annihilation of dislocations.

It is well known that plastic deformation generates lattice defects such as dislocations and vacancies. Vacancy concentration in the order of 10^{-4} are found in pure copper processed by HPT and ECAP [20-23] that is considerably higher than the $\sim 3 \times 10^{-20}$ calculated for the thermal equilibrium vacancy concentration at room temperature, but close to the $\sim 1.5 \times 10^{-4}$ calculated at the melting temperature [24]. Ungar showed that for ECAP processed material, deformation induced vacancy concentrations in the grain boundaries of compressed copper polycrystals are close to the equilibrium values at the melting temperature [25]. This result is interpreted by assuming that the vacancy accumulation in the grain boundary region is larger than in the grain interior or matrix regions. This would indicate that the state of the grain boundary region in strongly deformed metals is somewhat similar to the state at or close to the melting temperature [25]. Such high concentration of point defects should be considered as they can alter mechanical properties and work hardening behavior of the material in two ways [23]:

(1) An indirect one allowing edge dislocations to annihilate via climb, e.g. in recovery or recrystallization, (2) A direct one which gets apparent when the vacancies collect to clusters and/or agglomerates markedly impeding the dislocation motion.

Considering the above explanation about the role of vacancies in mechanical properties and microstructure of these alloys, one can assume that vacancies annihilate at edge dislocations upon temperature rise during room temperature milling and cause the dislocation density and share of edge dislocations to decrease, Figure 4.5. Studies on the kinetics of recovery of the complex dislocation structures have shown that recovery is controlled by dislocation climb and/or thermally activated glide of dislocations [26]. As far as low stacking fault energy materials are concerned, glide of dislocations is less important as the dislocation motion through glide is limited in low SFE samples. Hence, dislocation climb is the controlling mechanism for the recovery process. Dislocation climb is controlled by formation and movement of vacancies in the microstructure. It is well known that severe plastic deformation causes a high concentration of vacancies in the sample [27]. Therefore, it is also expected that a high concentration of vacancies is generated in cryomilled samples processed at 77K. Higher thermal energy provided at room temperature milling results in higher mobility for the deformation induced vacancies that are already formed at 77K. These vacancies can be absorbed to the dislocation cores helping the climb process and recovery to occur. This significantly helps the annihilation process and the recovery and hence contributes to the reduction in dislocation density and lower microhardness values. It should be considered that cross-slip is the key process for annihilation of screw dislocations. Therefore, in copper alloys with low stacking fault energy and limited cross-slip, thermal activation leads to annihilation of edge dislocations and leaves screw dislocations in the microstructure. On the other hand, as the milling process proceeds new generation of dislocations, screw or edge, are being formed. Competitive processes of annihilation of edge

dislocations at room temperature and formation of new generation of edge and screw dislocations lead to the observed behavior of the dislocation character and density at room temperature, Figure 4.5.

Figure 4.7 demonstrates the effect of processing temperature on microhardness of the Cu-10wt.%Zn alloy. Change of milling temperature after 4h of cryomilling results in about 200MPa decrease in microhardness of the sample. The softening and decrease of strength after milling at room temperature could be due to partial annihilation of dislocations and increase in grain size as shown in Figure 4.7 and 4.8. Figure 4.8 demonstrates the change of crystallite size upon temperature increase by switching from cryomilling to room temperature milling. It is obvious that temperature rise is sufficient to decrease dislocation density, increase grain size and alter mechanical properties of the highly deformed samples milled at 77K.

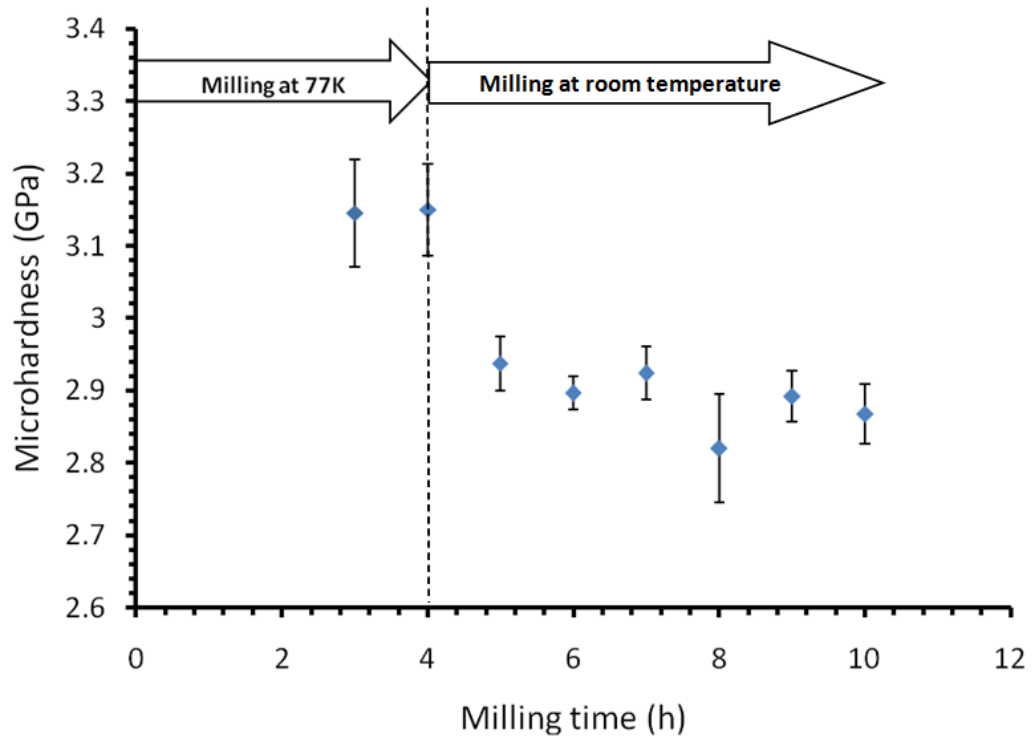


Figure 4.7- Microhardness vs. milling time for Cu-10%Zn cryomilled for 4h at 77K followed by 6h room temperature milling.

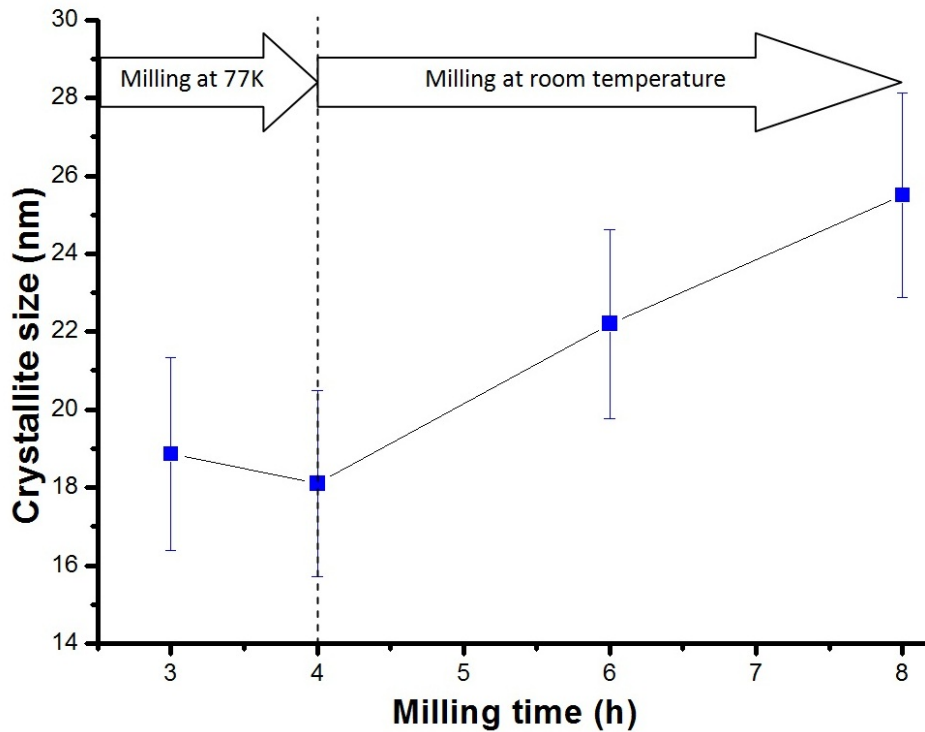


Figure 4.8- Crystallite size vs. milling time for the Cu-10wt.%Zn alloy processed 4h at 77K followed by 4h milling at room temperature.

Considering the changes in properties upon switching to room temperature processing, the cryomilled powder is then a good precursor for successful in situ consolidation via room temperature milling. Easier plastic flow of the particles prepared at 77K leads to coalescence and welding of small particles and formation of defect-free samples with superior mechanical properties.

As an example, Figure 4.9 shows the tensile behavior of Cu-30wt.%Zn sample produced by cryomilling for 6h and subsequently milled for 2h to consolidate the particles at room temperature. Yield strength of 877 MPa for the in situ consolidated sample is well above the 690 MPa for the sample processed by HPT. 9.7% elongation to failure is almost twice of the 4.7% for the counterpart of this sample processed by HPT [10].

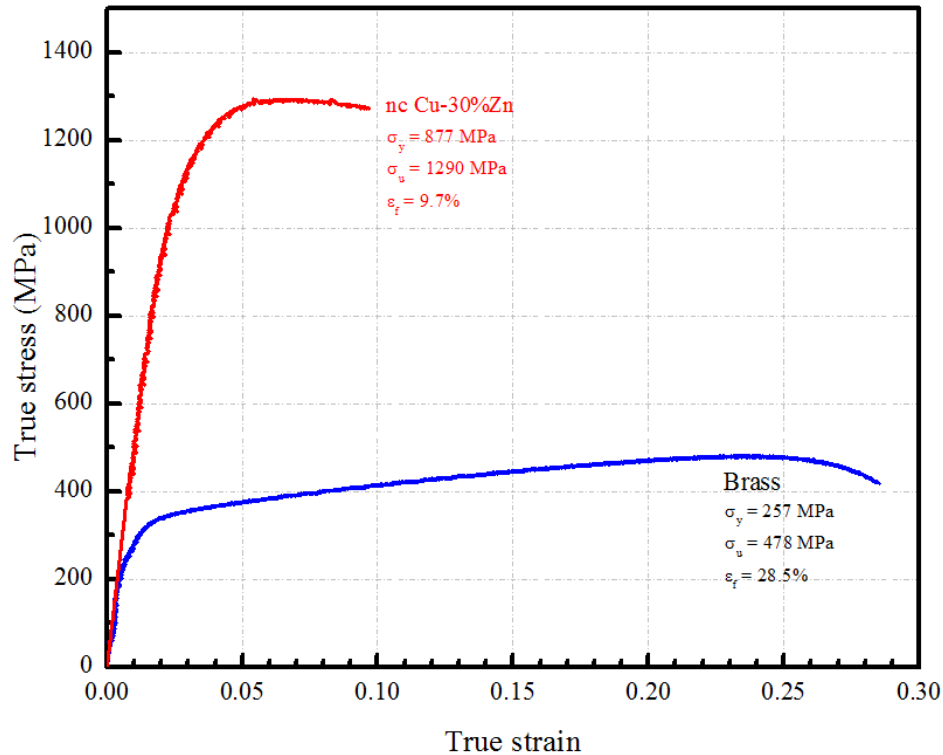


Figure 4.9- Tensile curve for Cu-30wt.%Zn sample milled for 6h at 77K and 2h at room temperature. Tensile curve for coarse grained brass is given for comparison.

4.5. Conclusion

Nanocrystalline Cu-Zn alloys were synthesized using high energy ball milling at liquid nitrogen and room temperature. Combination of cryogenic and room temperature milling results in production of bulk nanostructured spheres with superior mechanical properties. The highly defected and fine nanostructured sample prepared at 77K is a very good precursor for in situ consolidation when it is followed by a few hours of room temperature milling. When the milling temperature is increased, thermal energy necessary for diffusion assisted processes is provided. Therefore, the cryo-milled powder is consolidated to get defect-free spheres with a homogeneous microstructure. Higher strength, better ductility and finer

crystallite size are obtainable via controlled milling of Cu-Zn alloys compared to processing with HPT.

Softening was observed in ball milled samples upon increase of zinc content. Decreased hardness of these alloys at nano scale crystallite size has not been reported in the literature and further investigation is needed to understand the softening behaviour of nanostructured Cu-Zn alloys.

4.6. References

- [1] K.M. Youssef, R. O. Scattergood, K. L. Murty, J. A. Horton, C. C. Koch, *Appl. Phys. Lett.*, 87 (2005) 0919041.
- [2] K.M. Youssef, Scattergood RO, Murty KL, Koch CC, *Appl. Phys. Lett.*, 85 (2004) 929-931.
- [3] A.M. Harris, Schaffer GB, Page NW, *J. Mater. Sci. Lett.*, 12 (1993) 1103-1104.
- [4] X.K. Zhu, X. Zhang, H. Wang, A.V. Sergueeva, A.K. Mukherjee, R.O. Scattergood, J. Narayan, C.C. Koch, *Scripta Mater.*, 49 (2003) 429-433.
- [5] X. Zhang, H. Wang, M. Kassem, J. Narayan, C.C. Koch, *Scripta Mater.*, 46 (2002) 661-665.
- [6] A.M. Harris, Schaffer GB, Page NW *Scripta Mater.*, 34 (1996) 67-73.
- [7] A. Calka, Wexler D, A study of the evolution of particle size and geometry during ball milling, in: P. Schumacher, Warren P, Cantor B (Ed.) *Metastable, Mechanically Alloyed and*

Nanocrystalline Materials, ISMANAM-2000, Trans Tech Publications Ltd, Zurich-Uetikon, 2001, pp. 301-310.

[8] M. Leoni, T. Confente, P. Scardi, *Z. Kristallogr.*, 23 (2006) 249-254.

[9] E.J. Lavernia, B.Q. Han, J.M. Schoenung, *Mater. Sci. Eng., A*, 493 (2008) 207-214.

[10] Y.H. Zhao, X.Z. Liao, Z. Horita, T.G. Langdon, Y.T. Zhu, *Mater. Sci. Eng., A*, 493 (2008) 123-129.

[11] Z.S. Basinski, S.J. Basinski, *Acta Metall.*, 37 (1989) 3275-3281.

[12] Y.B. Wang, X.Z. Liao, Y.H. Zhao, E.J. Lavernia, S.P. Ringer, Z. Horita, T.G. Langdon, Y.T. Zhu, *Mater. Sci. Eng., A*, 527 (2010) 4959-4966.

[13] T.D. Shen, C.C. Koch, *Acta Mater.*, 44 (1996) 753-761.

[14] P. Scardi, M. D'Incau, M. Leoni, A. Fais, *Metall. Mater. Trans. A*, 41 (2010) 1196-1201.

[15] A. Fais, P. Scardi, *Z. Kristallogr.*, 27 (2008) 37-44.

[16] M. Wilkens, *J. Res. Nat. Bur. Stand.*, A 73 (1969) 552-560.

[17] R.M. Davis, McDermott B, Koch CC, *Metall. Mater. Trans. A*, 19 (1988) 2867-2874.

[18] S.Q. Xi, J.G. Zhou, X.T. Wang, *Powder Metall.*, 50 (2007) 367-373.

[19] J. Joardar, S.K. Pabi, B.S. Murty, *Scripta Mater.*, 50 (2004) 1199-1202.

[20] E. Schafner, Steiner G, Korznikova E, Kerber M, Zehetbauer MJ, *Mater. Sci. Eng., A*, 410-411 (2005) 169-173.

[21] T. Ungar, Schafner E, Hanak P, Bernstorff S, Zehetbauer M, *Mater. Sci. Eng., A*, 462 (2007) 398-401.

[22] M.J. Zehetbauer, Kohout J, Schafner E, Sachslehner F, Dubravina A, *J. Alloys Compd.*, 378 (2004) 329-334.

- [23] M.J. Zehetbauer, Steiner G, Schafner E, Korznikov A, Korznikova E, Deformation induced vacancies with severe plastic deformation: Measurements and modelling, in: Z. Horita (Ed.) Nanomaterials by Severe Plastic Deformation, Trans Tech Publications Ltd, Zurich-Uetikon, 2006, pp. 57-64.
- [24] W.Q. Cao, Gu CF, Pereloma EV, Davies CHJ, Mater. Sci. Eng., A, 492 (2008) 74-99.
- [25] T. Ungar, Subgrain size-distributions, dislocation structures, stacking- and twin faults and vacancy concentrations in SPD materials determined by X-ray line profile analysis, in: Z. Horita (Ed.) Nanomaterials by Severe Plastic Deformation, Trans Tech Publications Ltd, Zurich-Uetikon, 2006, pp. 133-140.
- [26] F.J. Humphreys, M. Hatherly, Recrystallization and related annealing phenomena, 2nd ed., Elsevier, Amsterdam ; Boston, 2004.
- [27] M. Zehetbauer, E. Schafner, T. Ungar, Zeitschrift Fur Metallkunde, 96 (2005) 1044-1048.

CHAPTER FIVE

5.0. IN SITU CONSOLIDATION OF CU AND CU-ZN ALLOYS VIA ROOM TEMPERATURE BALL MILLING

H. Bahmanpour, K. M. Yousseff, M. Samadi Khoshkhoo, S. Scudino, J. Eckert, R. O. Scattergood, C. C. Koch

MRS Fall 2011 meeting, Boston

M. S. Khoshkhoo, H. Bahmanpour, S. Scudino, J. Freudenberger, M. J. Zehetbauer, C. C. Koch, J. Eckert

TMS 2011 annual meeting, San Diego

5.1. Abstract

Cu and single phase Cu-Zn alloys were processed by high energy ball milling (using planetary ball mill and Spex 8000 mill) of elemental powder at room temperature. It was found that planetary ball mill produces hollow spheres which grow upon extended milling times. In situ consolidated hollow spheres, produced by planetary ball mill, have a uniform microhardness at the beginning of the milling process. Non-uniform microhardness was observed at the intermediate milling times (34 h) and finally the uniformity is retained at long milling times (70 h).

The cold welding behavior was found to be different in experiments with Spex 8000 mill. Severe cold welding and sticking of the powder to the milling media happens in the first few hours. Sodium chloride was used to control the deformation process and prevent cold welding of the powder to the milling media. It was found that 0.125wt.% NaCl can effectively control the consolidation behavior of the powder and produce in situ consolidated samples. Vickers microhardness and tensile tests were utilized to investigate the mechanical properties. It is shown that room temperature ball milling of Cu and Cu-Zn alloys can be controlled to produce in situ consolidated nanostructured samples with good mechanical properties, e. g. yield strength of 741 MPa and elongation to failure of 10% for Cu-5wt.%Zn. X-ray line profile analysis and electron microscopy were used to characterize the microstructure of the ball milled samples and microstructure-properties relationships were discussed accordingly.

5.2. Introduction

Nanostructured materials with superior properties such as ultra high strength and good ductility have been subject of research for the recent decades. One of the major drawbacks for industrial application of these materials is the difficulty for production of bulk samples. Typical “top-down” processing methods that are mostly used for production of larger sized samples are equal channel angular pressing (ECAE), high pressure torsion (HPT), accumulative roll bonding (ARB), and ball milling (BM). These methods involve structural decomposition of the starting material to achieve nanoscale microstructural features in a bulk sample. Ball milling process that involves severe plastic deformation via

multi directional collisions between powder material and milling media, has the advantage of smaller grain sizes and also more homogeneous microstructures in the final product compared to other severe plastic deformation techniques. On the other hand, another post-deformation process is usually necessary for consolidation of ball milled powders to produce bulk samples.

Formation of bulk hollow spheres containing smaller spheres, Russian dolls, was introduced by Harris et al. [1] using high energy ball milling of Cu at room temperature up to 222h. Further studies have shown successful in situ consolidation results by utilizing ball milling for different ductile metals and alloys such as Cu [2, 3], Al [4], Zn [5, 6], Cu-Zn [7], Cu-Al-Zn [8], Cu-2.5%Al₂O₃ [9], and Al-Mg [10]. Although successful in situ consolidation of Al is reported by just prolonged low energy room temperature milling [4], most of the literature data on in situ consolidation by ball milling involve combination of cryomilling and room temperature milling to achieve full density and to produce large sized samples. Therefore, it appears that temperature plays the major role for a successful in situ consolidation experiment. In other words, controlling the cold welding and fracture behavior of the powder by temperature control has been found to be the key factor for in situ consolidation. Homogeneous microstructures with good mechanical properties were reported for these bulk artifact free samples. For example, Youssef et al. reported a narrow grain size distribution with an average of ~23 nm for in situ consolidated Cu that shows an ultra high strength of 791 MPa and uniform elongation of 14% [2, 3].

Process control agent (PCA) or surfactants are usually added to control cold welding and fracture of powder particles during milling and increasing the yield of the product [11]. Several PCAs such as NaCl and stearic acid were reported in the literature for prevention of severe cold welding of ductile materials. The surfactant adsorbs on particle surfaces and interferes with cold welding and hence, results in a lower surface tension of the powder [11]. Since the energy required for the physical process of size reduction, E is given by

$$E = \gamma \cdot \Delta S$$

where γ is the specific surface energy and ΔS is the increase of surface area, a reduction in surface energy results in the use of shorter milling times and/or generation of finer powders [11].

Milling of ductile metals or alloys at room temperature in a dry and inert atmosphere causes welding to predominate and sample size will steadily increase with milling time. Milling at room temperature can result in formation of hollow spheres with an inhomogeneous microstructure that contains cracks and pores. It is of great interest to understand and control the milling conditions and produce defect-free samples with superior mechanical and microstructural properties [12]. It has been shown that the temperature of the milling process plays an important role on the quality of the in situ consolidated samples [1, 13]. Although the mechanism of growth of small spheres is not very clear, it is believed that material transfer from one sphere to another via the milling produces coalescence of particles [1].

In this paper the in-situ consolidated Cu-Zn alloys were processed and investigated. Sodium chloride was used as a surfactant to prevent cold welding and control the milling behavior. It was found that depending on the alloy composition, a small amount of NaCl, as low as 0.125wt.%, can successfully inhibit cold welding of the powder to the milling media. Although NaCl, prevents sticking of the powder to the milling media, it was found that artifact-free in situ consolidated samples can be produced at room temperature milling of Cu and Cu-Zn alloys. XRD was utilized to investigate the crystallite size and morphology and microstructure of processed samples were examined by SEM and TEM, respectively. Vickers microhardness and tensile tests were performed on processed samples and mechanical properties of these samples are discussed.

5.3. Experimental procedure

Nanostructured Cu, Cu-10%Zn, and Cu-30%Zn alloys were synthesized via mechanical alloying of elemental powders using a Spex 8000 mixer/mill with ball to powder mass ratio of 10:1. Hardened steel vials were loaded under an argon atmosphere with oxygen content of less than 1ppm. To avoid argon trapping in the structure of the alloy, the vial was sealed under vacuum. High energy ball milling was conducted at room temperature to obtain bulk nanostructured samples. Due to high ductility of these alloys and hence severe cold welding of the sample to the milling media, NaCl was added as a surfactant to the powder to control the milling procedure and prevent sticking of the powder material. Room temperature milling of Cu with a planetary ball mill was also investigated in this part of the work to study the mechanical properties of in situ consolidated samples.

X-ray diffraction was utilized to estimate the crystallite size of ball milled samples using CuK_α radiation. Hardness of the milled samples was measured using Vickers microhardness at 50g load. Tensile tests were performed on the artifact-free bulk nc samples using a miniaturized tensile test machine. TEM samples were prepared by electro polishing and the microstructure of the produced samples was studied using a JEOL transmission electron microscope at 200 kV.

5.4. Results and discussion

Planetary ball mill

Figure 5.1 shows the in situ consolidated pure copper produced by planetary ball milling process. All the product is in the form of hollow spheres which form due to cold welding of micron sized particles in the first few hours of the milling process. A detailed study of the microstructure and mechanical properties of these samples was performed at IFW, Dresden. Figure 5.1-b represents a typical hollow sphere with a wall size of about 1mm. Material transfer between in situ consolidated spheres during the ball milling process leads to an increase in the diameter of the spheres, as shown in Figure 5.2.

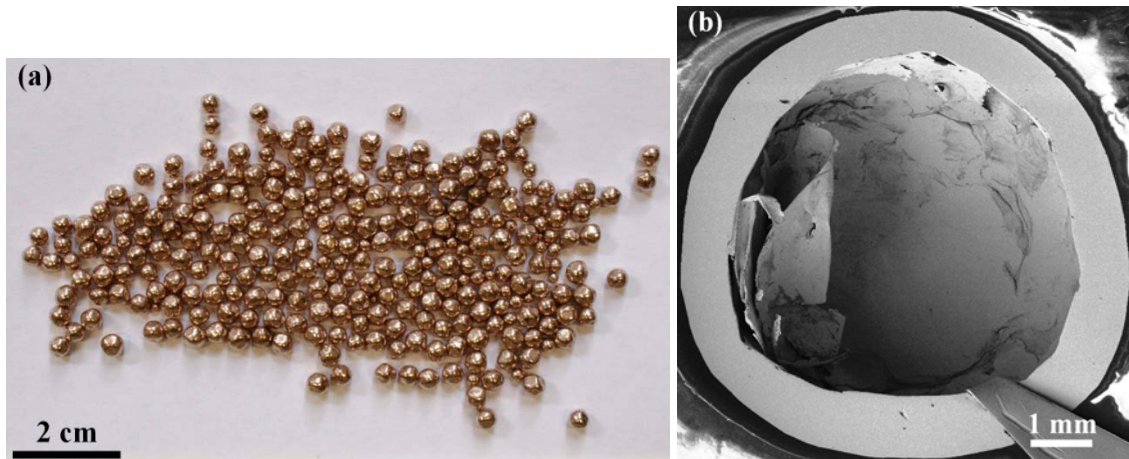


Figure 5.1– a) In-situ consolidated nanostructured Cu. b) the nanostructured samples are in form of hollow spheres with wall size of about 1 mm.

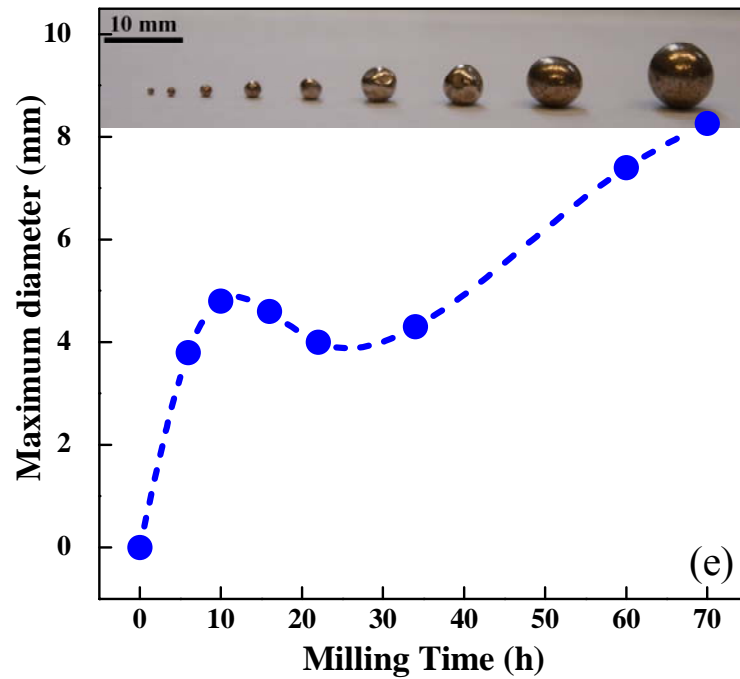


Figure 5.2– Maximum diameter of in situ consolidated Cu vs. milling time in a planetary ball mill.

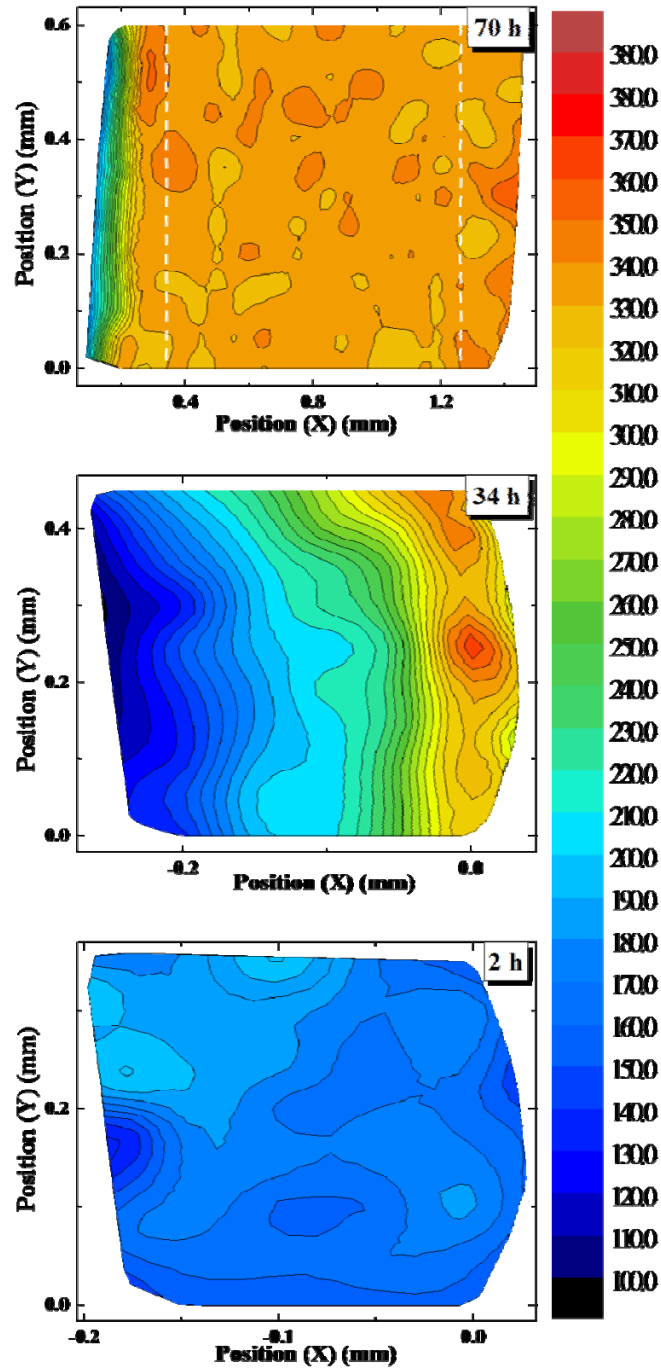


Figure 5.3- Microhardness maps of the in-situ consolidated nanostructured Cu produced by planetary ball mill.

Microhardness mapping revealed that at the initial few hours of the milling process, a uniform hardness is maintained for a hollow sphere that range between 130 and 190 HV (1.3 and 1.8 GPa), Figure 5.3. Extension of the milling process to about 34 h, Figure 5.3, produces a non-uniform hardness distribution throughout the sample, changing from > 300 HV (2.9 GPa) at the outer edge to < 200 HV (1.9 GPa) on the inner edge. The uniformity is again maintained after 70 h of milling to the average of 330 HV (3.2 GPa) all over the sample. The hardness value on the outer edge has an increase with the milling time as shown in Figure 5.4.

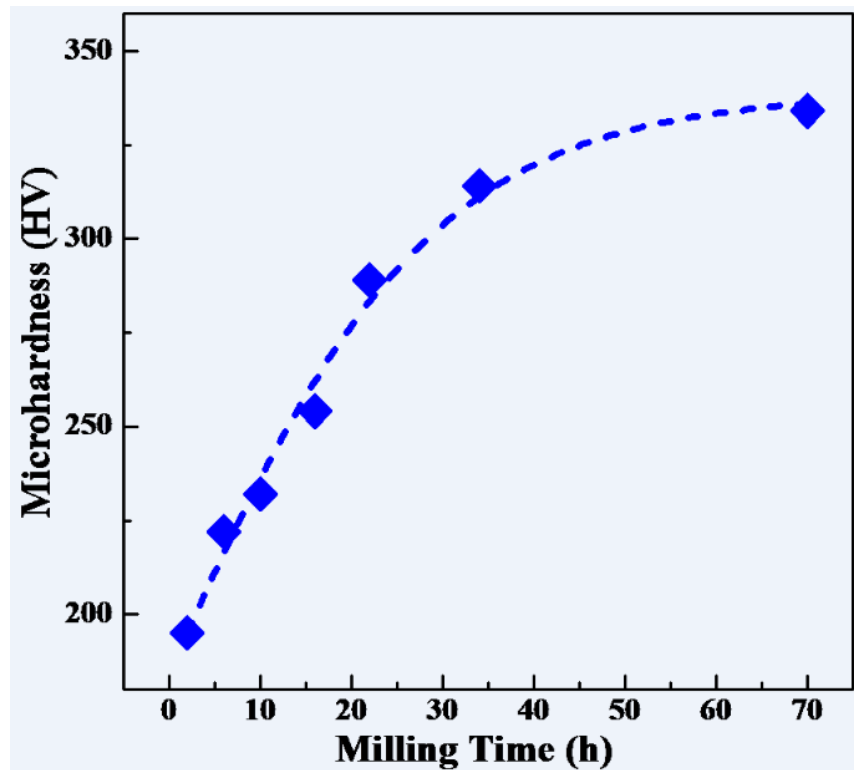


Figure 5.4- Vickers microhardness at the outer edge of the hollow spheres as a function of the milling time.

Spex 8000 mill

During room temperature milling of ductile metals and alloys the powder cold welds to the vial and balls. The cold welding is not desirable since it decreases the yield of the process and the resulting material is also not quite useful for microstructure studies and mechanical tests. As an example, Figure 5.5 shows how pure copper is cold welded to the milling vial after a few hours of room temperature milling in a Spex 8000 mill.



Figure 5.5- A large piece of pure copper welded ($\sim 3 \text{ cm} \times 2 \text{ cm}$) around vial after few hours of room temperature milling using a Spex 8000 mill.

It was found that small amount of NaCl can significantly change the cold welding behavior of Cu and Cu-Zn alloys. Since the surfactant contaminates the powder, we added

different amount of NaCl to the powder to find the optimum amount that inhibits sticking with minimum contamination. For pure copper, 0.25wt.% NaCl is enough to prevent cold welding but in Cu-10%Zn and Cu-30%Zn which are less ductile, 0.125wt.% NaCl is an appropriate amount for controlling the cold welding. For instance, Figure 5.6 shows Cu-5%Zn milled with 0.125wt.%NaCl at different milling times. The product of the surfactant assisted milling is in the form of small sized flakes and spheres in the first few hours of milling. Cohesion of small particles due to plastic deformation between colliding balls and the vial causes formation of larger sized flakes and spheres. These small flakes and spheres grow upon further milling, Figure 5.6.

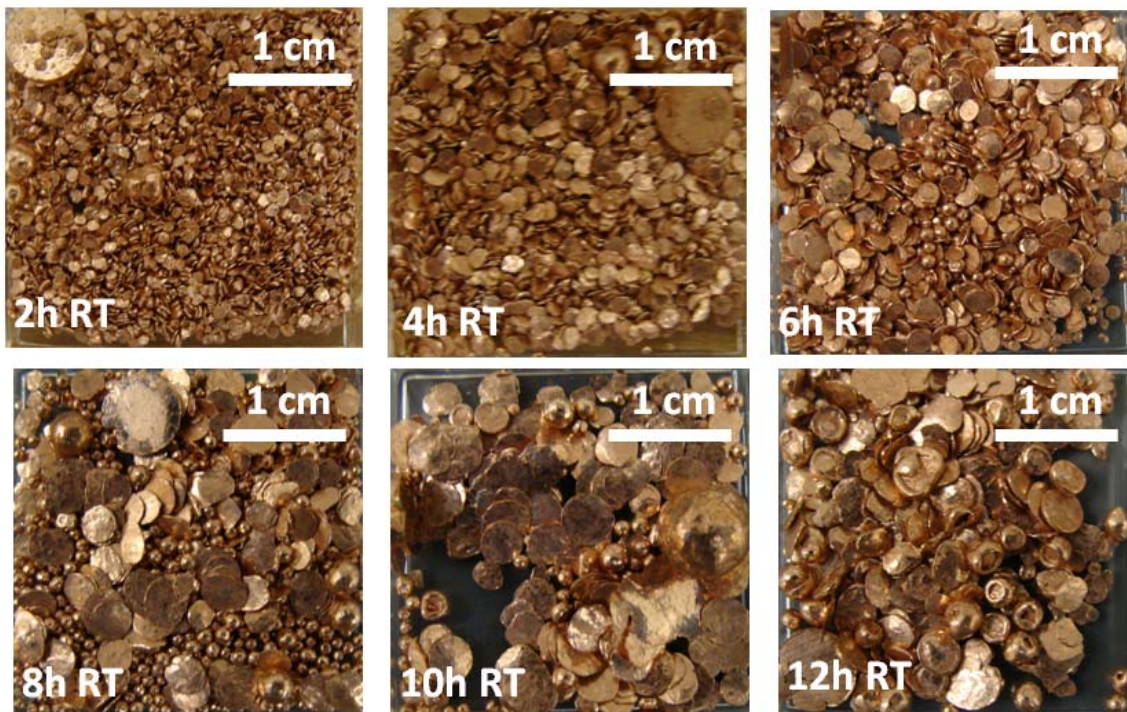


Figure 5.6-Images taken from Cu-5%Zn after different milling times showing growing flakes and spheres.

Crystallite size of the ball milled samples was investigated by the XRD technique. Figure 5.7 demonstrates the XRD profiles of Cu-30%Zn alloy at different milling times. Detailed analysis of the XRD profiles, given in Figure 5.8, shows a slight increase in the crystallite size, within a ~5nm range, and then a plateau for all compositions. It should be mentioned that the smaller crystallite size at higher zinc content was also observed in cryomilling of the Cu-Zn alloys without addition of surfactant, see Chapter Four, that might be related to the effect of stacking fault energy on the deformation behavior and capability of the alloy for microstructure decomposition.

Microstructure refinement in the ball milling process is controlled by severe impact deformation of milling and the thermal recovery [14]. From Figure 5.8 it appears that, for all compositions, the minimum grain size is obtained in first few hours of milling and the thermal recovery and possibly grain growth takes over the defect formation and controls the microstructure evolution at longer milling times. This behavior is related to the temperature rise during the room temperature milling. A wide range of temperature increase in ball milling is reported by different researchers. Davis et al. [15] reported that the temperature increase in a Spex mixer/miller is less than 350 K. On the other hand, Xi et al. [16] reported that under the maximum milling intensity the temperature rise is not more than 125 K. Despite the fact that the reported temperature rise is wide, probably due to different milling conditions, it is obvious that the increased temperature is enough to trigger dynamic recovery and grain growth.

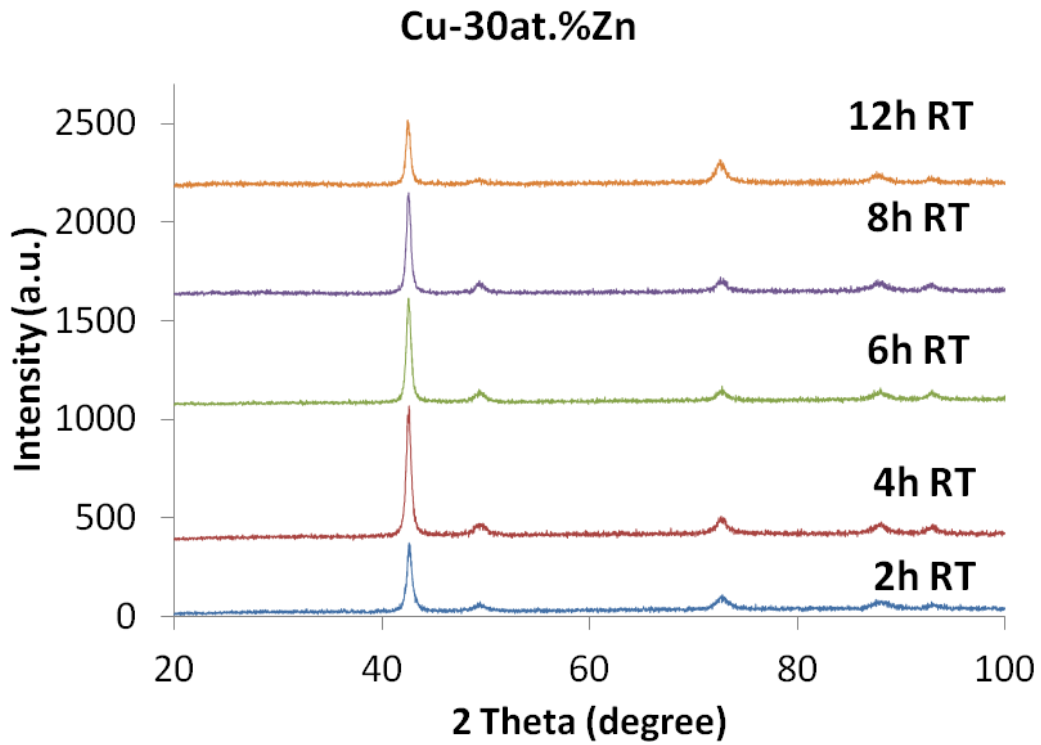


Figure 5.7- XRD profiles of Cu-30%Zn alloy milled with 0.125wt.%NaCl at different milling times.

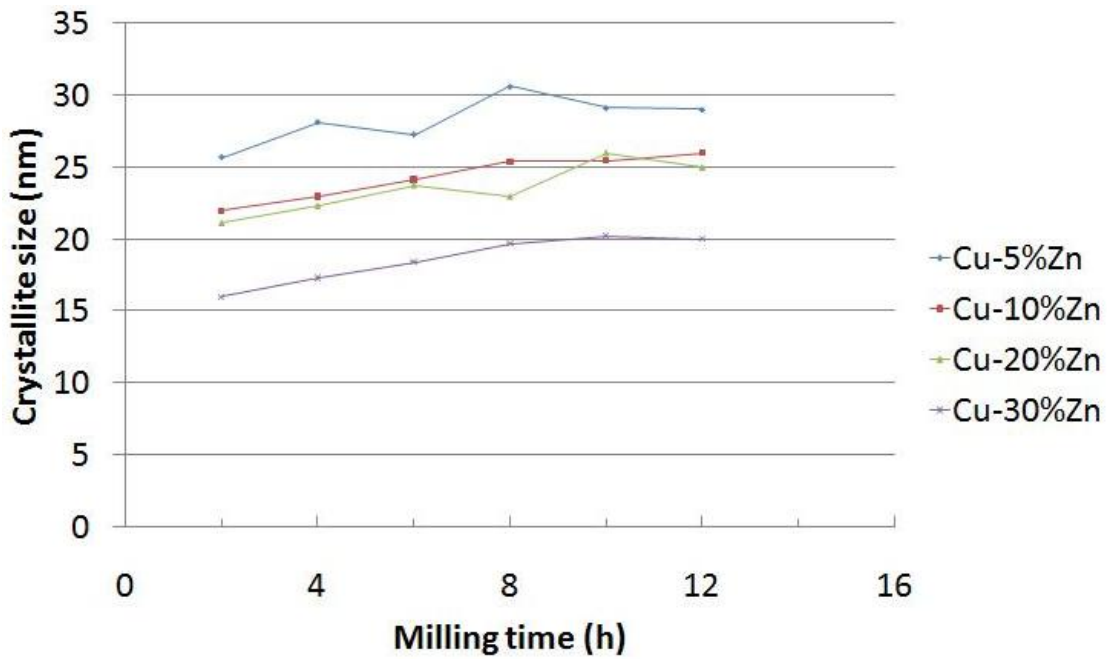


Figure 5.8- Crystallite size vs. milling time for different Cu-Zn alloys milled with 0.125wt.%NaCl.

SEM studies of selected samples after 2 and 6h milling, Figure 5.9, shows the typical size and surface condition of the flakes. 2h room temperature milling produces small sized flakes. It is seen that the zinc content also affects the flake size, i.e. Cu-30%Zn flakes are smaller than Cu and Cu-10%Zn ones. At longer milling times, the smaller flakes trap between colliding balls and stick together to form larger sized disks as it is seen in the 6h milled samples, Figure 5.9. In the meantime, some rounded spheres are also formed, shown in Figure 5.6, presumably due to multi directional deformation from different sides in the milling process, which packs smaller flakes together to form round spheres.

TEM observations prove that the product of the surfactant assisted milling has a homogeneous nanostructure within a narrow distribution, Figure 5.10. Bright field and dark field images showed that the average grain size for Cu-30%Zn sample milled for 12 h is 34 nm. Selected area diffraction pattern also confirms the very small grain size of this sample.

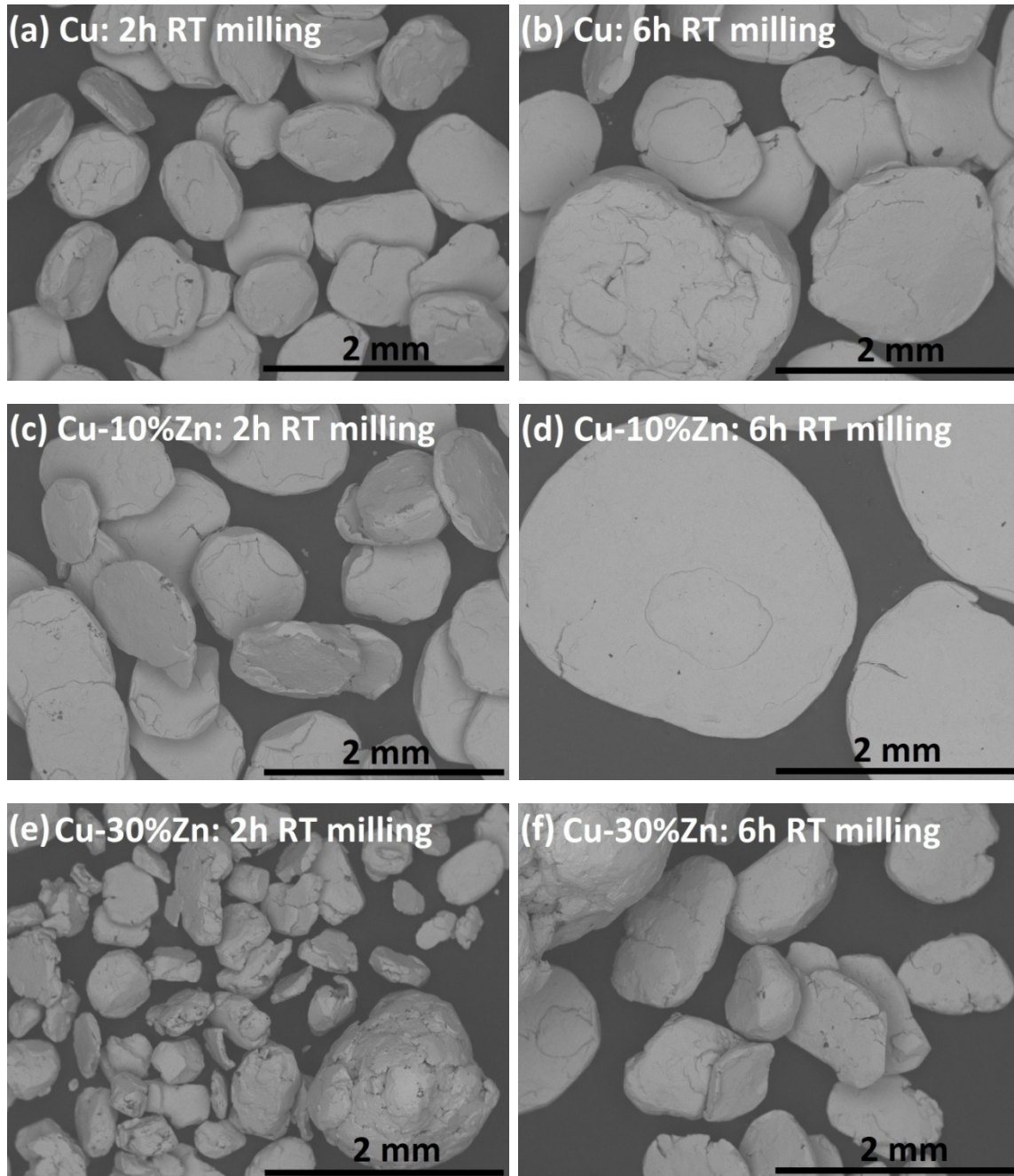


Figure 5.9- SEM micrographs of Cu, Cu-10%Zn, and Cu-30%Zn alloys milled at room temperature. 0.25wt.% NaCl was added to Cu and 0.125wt.% NaCl was added to Cu-10%Zn and Cu-30%Zn alloys in order to control cold welding and consolidation behavior.

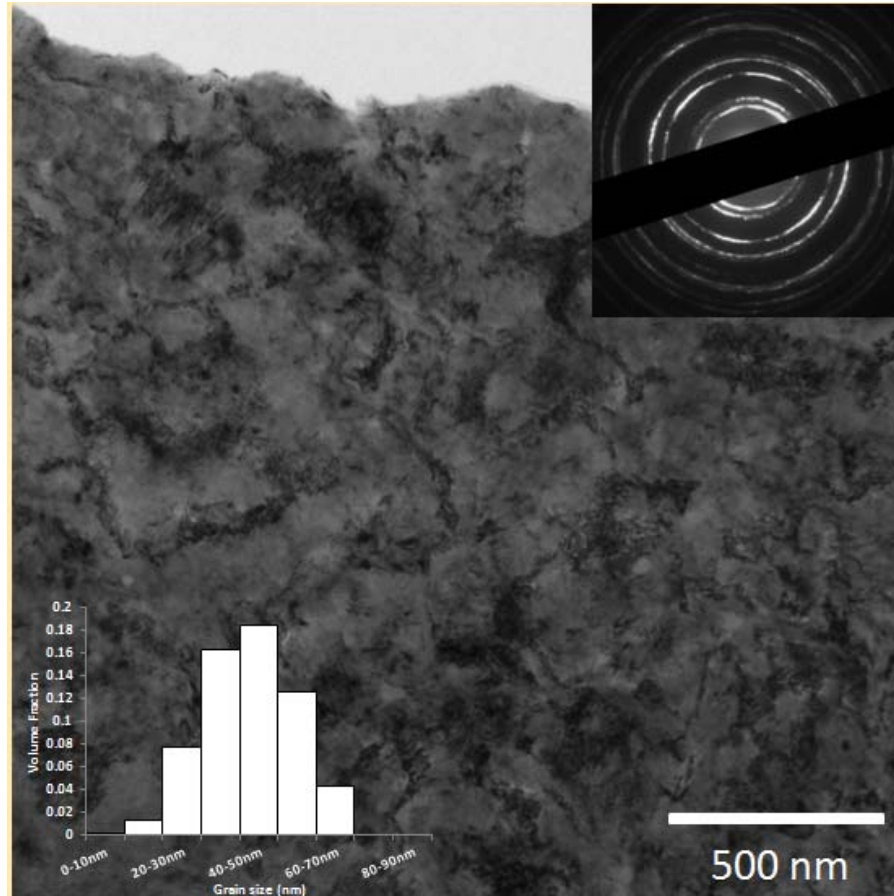


Figure 5.10- TEM image of Cu-30%Zn alloy milled for 12h at room temperature with 0.125wt.%NaCl.

Production of bulk artifact-free samples via in situ consolidation during ball milling was a major driver for this part of this work. It is interesting that the disk shaped flakes and sound spheres produced by surfactant assisted ball milling are artifact-free. These samples can be used for making tensile test samples for further investigation on mechanical properties. As an example, Figure 5.11 shows tensile curves of Cu-5%Zn, Cu-10%Zn, and Cu-20%Zn alloys milled with 0.125wt.% NaCl. Tensile curves show a plastic region followed by necking and post-necking stages without premature failure due to particle debonding. This is a good indication of achieving full density in these samples. Regarding the

mechanical properties, high strength and fairly good ductility was observed, Figure 5.11. Cu-5%Zn, Cu-10%Zn, and Cu-30%Zn showed yield strength of 740, 640, 760 MPa and elongation to failure of 10%, 4.7%, and 7.3%, respectively. The observed mechanical properties can be related to the microstructural features considering the different milling times for each alloy. A detailed analysis of the microstructure-mechanical properties relationship with focus on Hall-Petch relation of Cu and Cu-30%Zn is given in Chapter Eight.

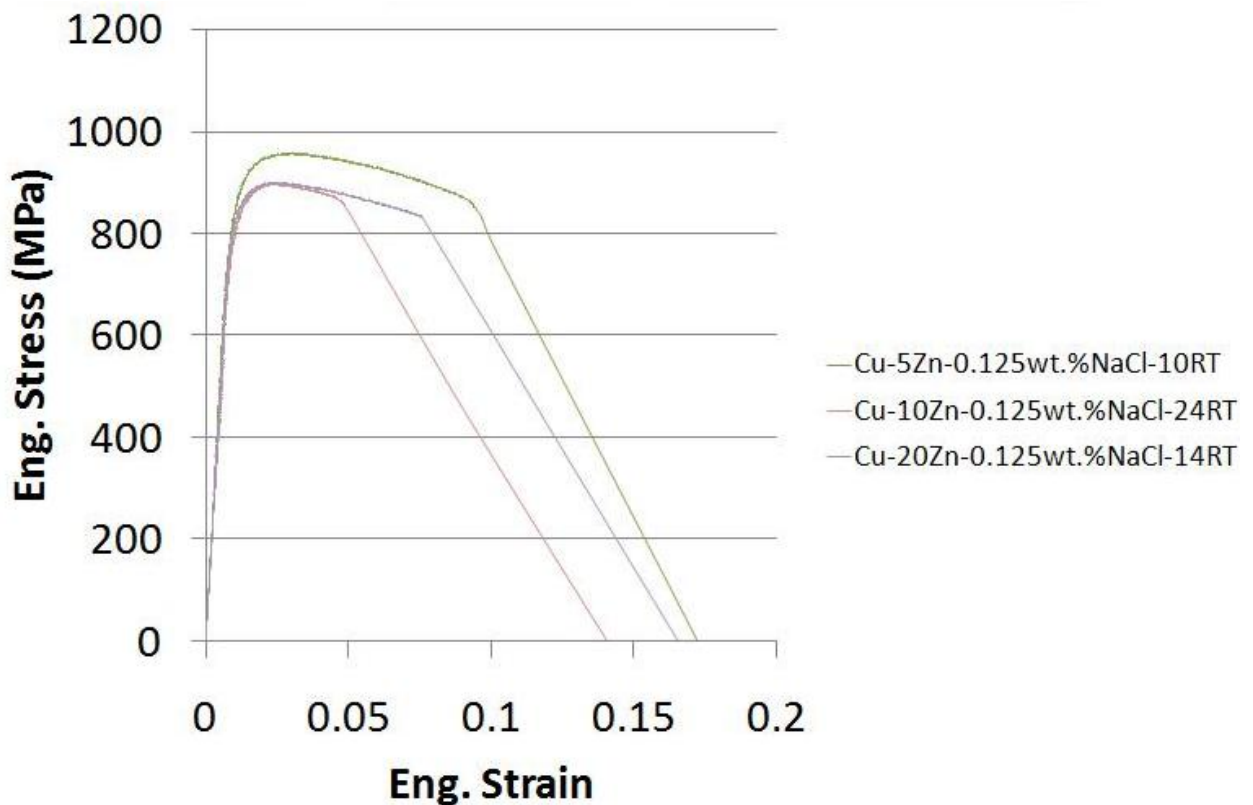


Figure 5.11- Tensile stress-strain curves for in situ consolidated Cu-Zn alloys produced via surfactant assisted ball milling.

5.5. Conclusion

It is shown that room temperature ball milling of Cu using planetary mill and Spex 8000 mill produce different samples. In the case of planetary ball mill, hollow spheres are formed from the first few hours of the milling. These spheres have a non-uniform hardness distribution in the intermediate milling times. With increasing the milling time to 72 h, hardness reaches a constant value all over the sample. On the other hand, milling of Cu with Spex 8000 results in severe cold welding and sticking of the material to the milling media.

NaCl was successfully used as a surfactant to control cold welding behavior of Cu and Cu-Zn alloys in experiments with the Spex 8000 mill. It was found that the crystallite size of the milled product increases slightly at longer milling times and it was related to temperature rise during ball milling. In situ consolidated disks and spheres, formed during the ball milling process, are large enough for making tensile test samples. Tensile properties were found to be a function of the milling time. Given the homogeneous microstructure of the in situ consolidated samples and the successful tensile tests, with no premature failure of the samples, the microstructure properties relationship and deformation behavior of Cu-Zn alloys at small grain sizes can be studied according to this method.

5.6. References

- [1] A.M. Harris, Schaffer GB, Page NW, J. Mater. Sci. Lett., 12 (1993) 1103-1104.
- [2] K.M. Youssef, Scattergood RO, Murty KL, Koch CC, Appl. Phys. Lett., 85 (2004) 929-931.

- [3] K.M. Youssef, R. O. Scattergood, K. L. Murty, J. A. Horton, C. C. Koch, *Appl. Phys. Lett.*, 87 (2005) 0919041.
- [4] K.Y. Zhao, C.J. Li, J.M. Tao, D.H.L. Ng, X.K. Zhu, *J. Alloys Compd.*, 504, Supplement 1 (2010) S306-S310.
- [5] X.K. Zhu, X. Zhang, H. Wang, A.V. Sergueeva, A.K. Mukherjee, R.O. Scattergood, J. Narayan, C.C. Koch, *Scripta Mater.*, 49 (2003) 429-433.
- [6] X.K. Zhu, K.Y. Zhao, C.J. Li, X. Zhang, C.C. Koch, A. Sergueeva, A. Mukherjee, The ultra fine grained (UFG) Zn produced by ball milling, in: J.H. Sung, C.G. Lee, Y.Z. You, Y.K. Lee, J.Y. Kim (Eds.) *Heat Treatment of Materials*, Trans Tech Publications Ltd, Stafa-Zurich, 2006, pp. 609-613.
- [7] H. Bahmanpour, K. Youssef, R. Scattergood, C. Koch, *J. Mater. Sci.*, (2011) 1-7.
- [8] K. Youssef, M. Sakaliyska, H. Bahmanpour, R. Scattergood, C. C. Koch, *Acta Mater.*, 59 (2011) 5758-5764.
- [9] D.L. Zhang, S. Raynova, C.C. Koch, R.O. Scattergood, K.M. Youssef, *Mater. Sci. Eng., A*, 410 (2005) 375-380.
- [10] K.M. Youssef, R.O. Scattergood, K.L. Murty, C.C. Koch, *Scripta Mater.*, 54 (2006) 251-256.
- [11] C. Suryanarayana, *Prog. Mater. Sci.*, 46 (2001) 1-184.
- [12] A.M. Harris, Schaffer GB, Page NW *Scripta Mater.*, 34 (1996) 67-73.
- [13] A. Calka, Wexler D, A study of the evolution of particle size and geometry during ball milling, in: P. Schumacher, Warren P, Cantor B (Ed.) *Metastable, Mechanically Alloyed and*

Nanocrystalline Materials, ISMANAM-2000, Trans Tech Publications Ltd, Zurich-Uetikon, 2001, pp. 301-310.

[14] B.Q. Han, J. Ye, A.P. Newbery, Y.T. Zhu, J.M. Schoenung, E.J. Lavernia, Bulk Nanostructured Metals from Ball Milling and Consolidation, in: Bulk Nanostructured Materials, Wiley-VCH Verlag GmbH & Co. KGaA, 2009, pp. 273-291.

[15] R.M. Davis, McDermott B, Koch CC, Metall. Mater. Trans. A, 19 (1988) 2867-2874.

[16] S.Q. Xi, J.G. Zhou, X.T. Wang, Powder Metall., 50 (2007) 367-373.

CHAPTER SIX

6.0. EFFECT OF STACKING FAULT ENERGY ON MECHANICAL BEHAVIOR OF BULK NANOCRYSTALLINE CU AND CU ALLOYS

K. Youssef, M. Sakaliyska, H. Bahmanpour, R. Scattergood, C. C. Koch

Acta Materialia, 2011, Vol. 59, pp. 5758-5764

6.1. Abstract

Twinning and dislocation slip are two major and competing modes of plastic deformation in metals and alloys. In addition to controlling the dislocation substructure in coarse grained materials, stacking fault energy (SFE) also affects the propensity to form deformation twins. However, the influence of SFE has not been fully explored in nanocrystalline materials. Here the role of SFE in deformation twinning and work hardening was systematically studied in bulk artifact-free, nanocrystalline (nc) Cu (SFE 55 mJ m^{-2}), and a nc Cu-12.1at.%Al-4.1at.%Zn alloy (SFE 7 mJ m^{-2}). The nc Cu (23 nm) and nc Cu alloy (22 nm) were synthesized using in situ consolidation during cryo and room temperature milling. Both materials showed ultra-high tensile strength, significant strain hardening, and good ductility. The nc Cu alloy exhibits a higher yield strength and lower uniform elongation ($1067 \pm 20 \text{ MPa}$, 6.5%) than that of nc Cu ($790 \pm 12 \text{ MPa}$, 14%). The SFE variation played a

significant role in strengthening the nc Cu alloy. High resolution transmission electron microscopy analyses revealed that the low SFE of the nc Cu alloy alters the deformation mechanism from a dislocation-controlled deformation, which allows for the higher strain hardening observed in the nc Cu, to a twin-controlled deformation.

6.2. Introduction

Nanocrystalline (grain size <100 nm) materials have been the subject of widespread research over the past couple of decades. One of the main motivations for this overwhelming research stems from the expectation of unprecedented mechanical strength, as predicted by the well-known Hall–Petch relationship, which posits a continuous rise in strength with decreasing grain size [1]. In spite of the ultra-high strength at room temperature of these materials, early experimental results showed that they suffer from poor ductility (elongation to failure <2% [2]). The low ductility of nanocrystalline materials has been attributed to processing artifacts (e.g. porosity) and mechanical instability due to a lack of strain hardening [3, 4]. However, in the last few years significant advances were achieved in improving their ductility without losing the high strength [5-12]. For example, Karimpoor et al. [6] used pulse electrodeposition to synthesize a 200 μm thick nanocrystalline (12 nm) Co deposit. This nanocrystalline (nc) Co showed a strength about four times its coarse grained counterpart and elongation to fracture values of up to 9%. The deposit exhibited an unusual faulted structure indicative of a high concentration of stacking faults/microtwins, which is consistent with the low stacking fault energy of Co. We were able to produce bulk artifact-free nc Cu spheres using an in situ consolidation technique during ball milling [7, 12]. The

nanostructure of this Cu is mainly nano-grains (average 23 nm) surrounded by high angle grain boundaries (HAGB), and it exhibits a yield strength of 791MPa with a uniform tensile elongation value of 14%. In situ transmission electron microscopy (TEM) tensile straining revealed the existence of dislocation pile-ups and glide activity in the nano-grains, which would contribute to the significant strain hardening observed and the resulting superior mechanical properties. Lu et al. [8] were able to replace the general HAGB with coherent twin boundaries and obtain high strength with good ductility in Cu using pulse electrodeposition. Although the final microstructure in this case consists of high densities of growth nanotwins (twin lamella spacing ~15 nm) imbedded in micron to submicron grains, its yield strength reached 900MPa with a total tensile elongation of 13.5%.

This series of breakthroughs in improving the strength and ductility of nanocrystalline materials requires researchers to fully understand the dependence of deformation mechanisms on the nanostructure of these materials. Of particular interest, the poor ductility of most nanocrystalline materials has been associated with a lack of strain hardening (normal dislocation activity) [3, 4, 13]. Notably, most of the promising examples of good ductility showed significant strain hardening, indicative of dislocation-mediated deformation that allows the material to stabilize uniform tensile deformation. However, supportive experimental evidence of this concept has not been reported up to now. In addition, twinning- and dislocation mediated deformation are two major and competing modes of plastic deformation in these materials [14-16]. During plastic deformation the operative mode is determined by the conditions of deformation and the intrinsic properties of the deformed nanomaterial; of which stacking fault energy (SFE) is one of the most important parameters

[17-26]. For instance, conventional grain size face-centered cubic (fcc) materials with low SFE, such as brass, have a higher twinning tendency than fcc materials with high SFE, such as aluminum [14]. The nature of twinning in nanocrystalline materials can be very different, e.g. twinning has been observed in nc Al [26, 27]. However, the influence of SFE on the mechanical properties and deformation mechanism in true nanocrystalline materials (grain size <100 nm and HAGB) has not been explored.

Therefore, it is the purpose of this investigation to study the influence of SFE on deformation behavior utilizing an artifact-free in situ consolidation technique involving milling at room and liquid nitrogen temperature. Eliminating processing artifacts is necessary to understand the influence of SFE on the mechanical behavior of bulk artifact-free nc Cu and a Cu alloy, and also to reveal the possibility of storing dislocations and/or deformation twins in a single phase material. In this paper we present the mechanical properties and deformation mechanism of an artifact-free bulk nc Cu-12.1at.%Al-4.1at.%Zn alloy and compare it with previous work on nc Cu [7]. This alloy composition has been chosen as a model because it is a complete solid solution and it has the lowest reported stacking fault energy ($\gamma \approx 7 \text{ mJ m}^{-2}$) among the Cu–Al and Cu–Zn alloys [28, 29].

6.3. Experimental procedure

A nanocrystalline bulk composition of Cu-12.1at.%Al-4.1at.%Zn (hereafter designated the nc Cu alloy) was prepared in a SPEX 8000 shaker mill (Spex Certiprep, Metuchen, NJ) in a tool steel vial with martensitic stainless steel (440) balls. The starting materials were elemental powders of Cu (99.9%), Al (99.8%), and Zn (99.9%). The ball to

powder mass ratio was 10:1. The ball milling was carried out at both liquid nitrogen temperature and room temperature under a purified argon atmosphere (<1 p.p.m. oxygen). During cryo milling a specially designed nylon vial holder was used with liquid nitrogen flowing around the vial to maintain its temperature at about 77 K. Nanocrystalline Cu spheres produced by mechanical milling were compressed into disks for characterization. Uniaxial tensile tests were performed on a miniaturized tensile testing machine at a constant strain rate of $9.4 \times 10^{-4} \text{ s}^{-1}$ at ambient temperature. Dog-bone shaped tensile specimens with a gage length of 2 mm, a width of 1 mm, and a thickness of $400 \pm 50 \text{ }\mu\text{m}$ were cut from the prepared samples using a Micro Mill 2000HD/LE (Micro Proto Systems Inc.). This mechanical behavior is compared with that of a coarse grained (cg), solution treated Cu master alloy having the same composition of Al and Zn. The tensile tests were carried out three times for each sample. Microhardness was measured during milling using a Buehler Micromet microhardness tester with a Vickers indenter at 10 and 25 g loads and a loading time of 15 s. TEM samples were prepared with a Fischione twin jet electropolisher. A JEOL-2000 TEM and a JEOL 2010 TEM at an accelerating voltage of 200 keV were used to determine the grain size distribution and to obtain high resolution TEM images of the nc Cu alloy, respectively.

6.4. Results and discussion

Figure 6.1 shows the hardness variation as a function of cryomilling (CM) time. The X-ray diffraction patterns (not shown) revealed complete disappearance of the Al and Zn peaks after 1h CM. This indicates an early alloying stage of Al and Zn into the Cu crystal

structure to form a solid solution. Therefore, the gradual increase in hardness with milling time is believed to be due to grain refinement and the introduction of various crystal defects during milling. As can be seen from Figure 6.1, the maximum hardness (3.6 ± 0.08 GPa) was achieved after 10 h of cryo milling. Any further milling had little effect on the hardness. It is worth mentioning that the morphology of the milled alloy at all stages of cryo milling consists of small rounded flakes about 1–2 μm in diameter. In order to produce the bulk in situ consolidated alloy room temperature milling (RTM) was performed for 2h after 10h cryo milling. The final product was fully dense, spherical shaped balls with sizes of up to 6 mm diameter. Density measurements and cross-section optical microscopy observations showed that our novel nc Cu alloy spheres exhibit full density with no pores. The hardness of the in situ consolidated alloy (CM 10 h, RTM 2 h) dropped to 3.2 ± 0.05 GPa. Williamson and Hall analysis [30] was used to calculate the grain size (d) and lattice microstrain (ϵ) from the X-ray diffraction (XRD) line broadening of the cryo milled (10 h) sample and the in situ consolidated sample. This analysis presumes that the grain size broadening and strain broadening profiles can be approximated by the equation:

$$\beta \cos \theta = (k\lambda/d) + \epsilon \sin \theta \quad (6.1)$$

where β is the measured integral breadth, θ is the peak maximum position, k is a constant, and λ is the wavelength. Figure 6.2 shows a linear fit of $\beta \cos \theta/\lambda$ against $\sin \theta/\lambda$ for all measured peaks of the two samples. As can be seen from this figure, a good fit is obtained for the cryo milled and in situ consolidated samples with average crystallite sizes of 22 and 28 nm and lattice strain values of 0.74% and 0.43%, respectively. The relatively high temperature during room temperature milling is believed to be responsible for the slight

increase in grain size and decrease in lattice strain due to dislocation annihilation processes.

This could explain the decrease in hardness from 3.6 to 3.2 GPa after 2 h RTM.

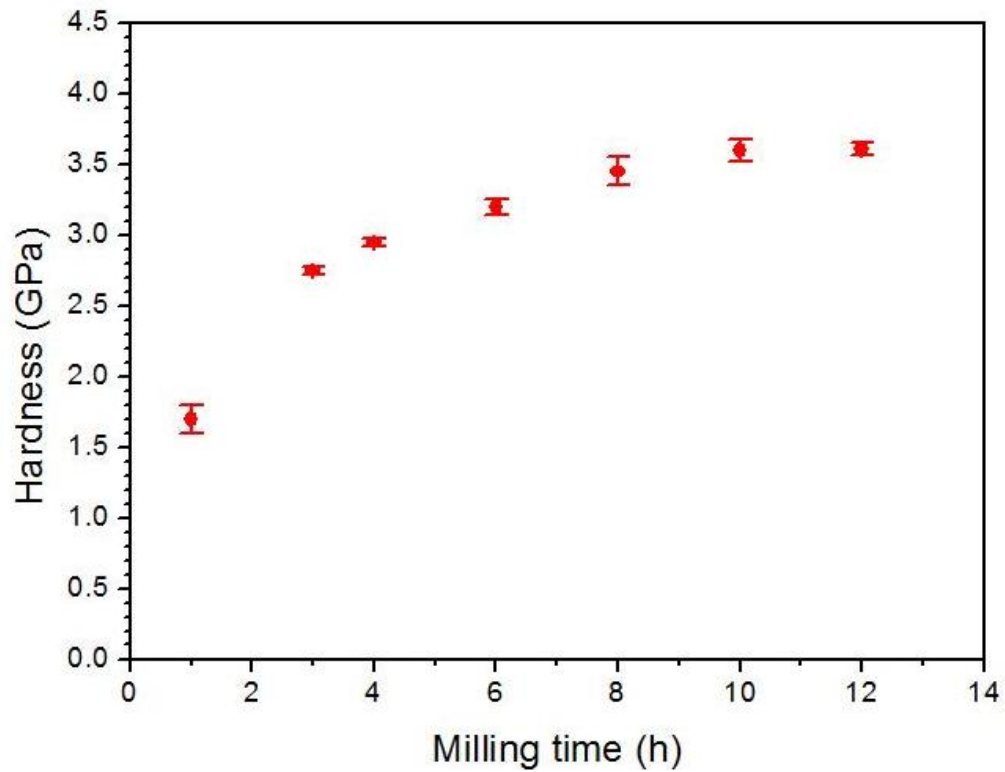


Figure 6.1- Hardness variations as a function of cryo milling time, for nc Cu alloy.

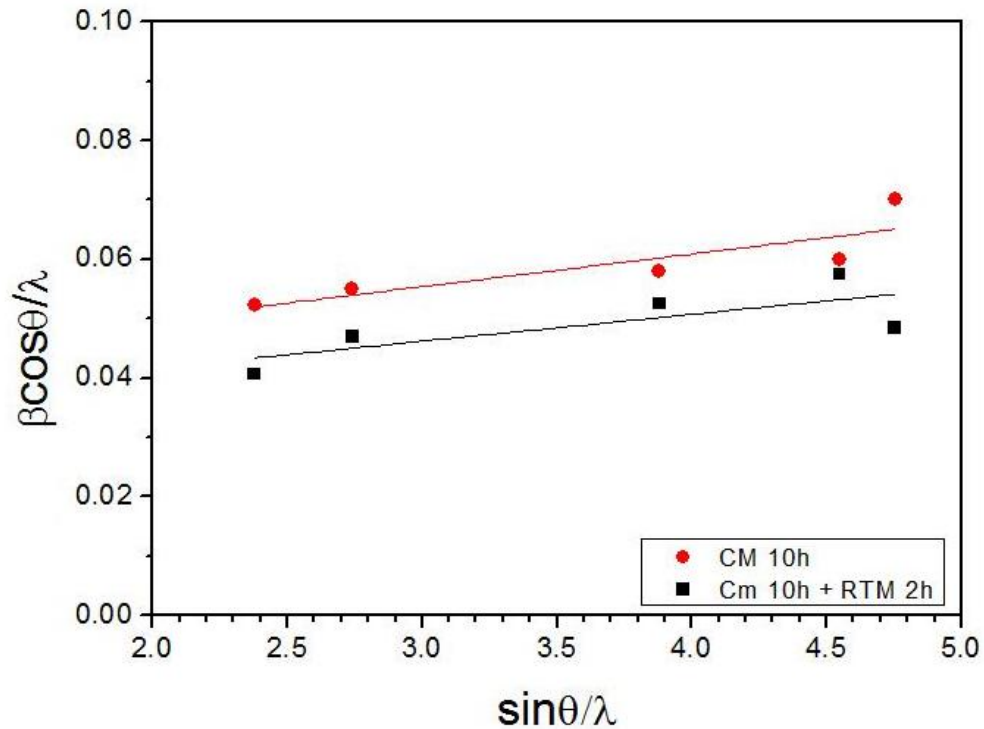


Figure 6.2- Williamson-Hall plot for nc Cu alloy (cryo milled for 10 h) and in-situ consolidated nc Cu alloy (cryo milled for 10 h and room temperature milled for 2h).

Figure 6.3-a shows a TEM bright field micrograph and electron diffraction pattern (inset in Figure 6.3-a) for the in situ consolidated nc Cu alloy. The grains appear to be equiaxed and randomly distributed within the structure. Statistical measurements of the grain size distribution (Figure 6.3-b) for this nc Cu alloy based on a total grain count of 320 shows an average grain size of 22 nm. This grain size value is consistent with that determined from the XRD calculations (28 nm). Another important feature of the Cu alloy nanostructure is that the grain size distribution is monotonic and lies within a narrow range (Figure 6.3-b). Tilting numerous grains around certain zone axes in the TEM revealed no dislocations in the grains and only twins in many nanograins, as indicated by the arrows in Figure 6.3-a. This does not exclude the presence of dislocations in the nanostructure. The strong difference in

the contrast among the dark grains (close to the zone axis) and their neighboring light grains indicates that the grain boundaries (GB) are mainly of high angle type. The HAGB are mainly formed during the cryo milling process, while a significant reduction in dislocation density occurs during room temperature milling. The combination of dislocation free grains and HAGB makes this nanostructure very unique and different from the nanostructures produced by high pressure torsion (high dislocation density within and around the grains) [31, 32] and pulse electrodeposition (nano-twins embedded in large grains) [8] techniques.

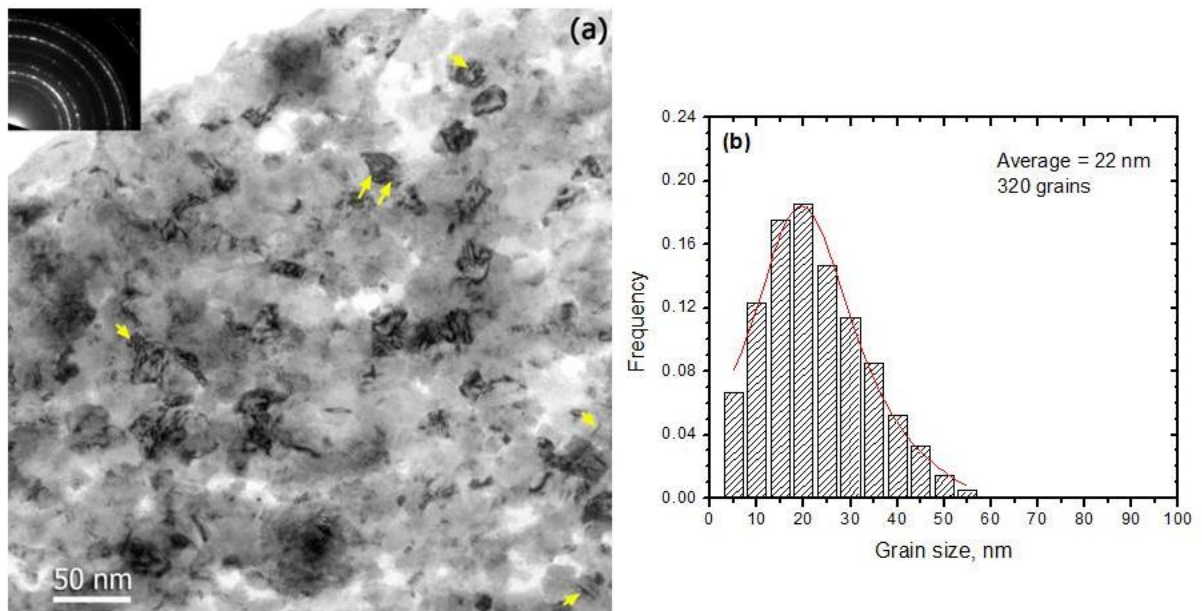


Figure 6.3- TEM observations of the typical nanostructure in the in-situ consolidated nc Cu alloy. The bright-field TEM micrograph (a) and the SADP, the upper left inset in (a), show roughly equiaxed grains with random orientations. The statistical distribution of grain size (b) was obtained from multiple dark-field TEM images of the same sample.

Figure 6.4 represents the uniaxial tensile true stress–strain curve for the in situ consolidated nc Cu alloy. Also included are two stress–strain curves obtained for a cast cg Cu alloy of the same composition and nc Cu (23 nm) that was in situ consolidated by the same

technique of cryo and room temperature milling [7]. A comparison of the tensile mechanical properties is shown in Table 6.1. These curves were included in Figure 6.4 in order to investigate: (1) the dependence of the mechanical behavior on grain size by comparing the mechanical properties of the nc Cu and cg Cu alloys (same SFE); (2) the effect of SFE on the mechanical properties of nc materials, bearing in mind that the nc Cu alloy has a SFE of 7 mJ m^{-2} [28, 29], which is much lower than that of Cu (55 mJ m^{-2} [28]), while both materials have the same grain size. It can be seen from Figure 6.4 and Table 6.1 that both nc Cu and the nc Cu alloy exhibit extremely high yield and ultimate tensile strengths. The 0.2% offset yield strength (σ_y) for the nc Cu and nc Cu alloy were 790 ± 12 and 1067 ± 20 MPa, respectively, while their ultimate tensile strengths (σ_u) were 1120 ± 29 and 1200 ± 35 MPa, respectively. The σ_y value of the nc Cu alloy is at least one order of magnitude higher than that of the cg Cu counterpart and the σ_u value is about four times higher (see Figure 6.4 and Table 6.1). In addition, significant high tensile ductility and strain hardening were observed in nc Cu and the nc Cu alloy, which is rarely observed in other nanostructured materials. As seen in Figure 6.4, the nc Cu alloy showed 6.5% uniform tensile elongation and 11% elongation to failure, while the nc Cu sample also showed significant tensile ductility, with 14% uniform elongation and 15.5% elongation to failure.

Table 6.1- Tensile mechanical properties.

	Yield strength, σ_y (MPa)	Tensile strength, σ_u (MPa)	Uniform elongation (%)	Total elongation (%)
nc Cu	790 ± 12	1120 ± 29	14 ± 0.3	15 ± 1
nc Cu alloy	1067 ± 20	1200 ± 35	6.5 ± 0.4	11 ± 0.6
cg-Cu alloy	133	300	57	63

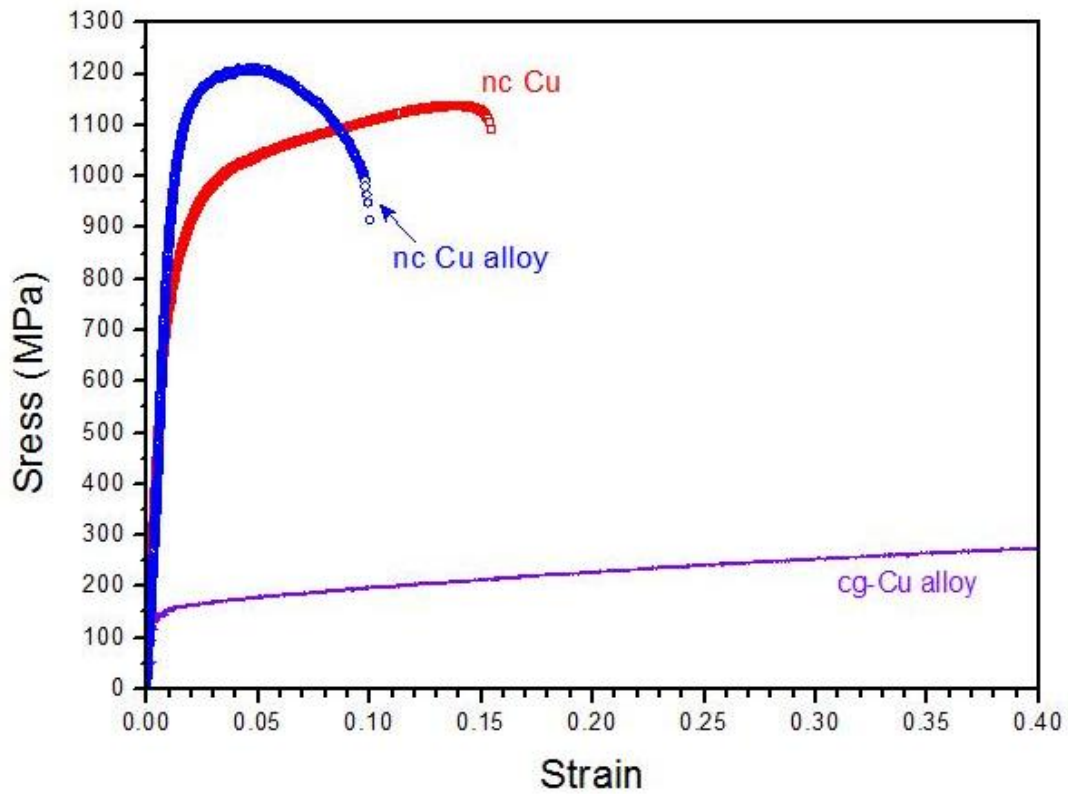


Figure 6.4- A typical tensile stress-strain curves for the bulk in-situ consolidated nc Cu and Cu alloy in comparison with that of cg Cu alloy sample (with an average grain size larger than 90 μm).

Grain size refinement made the main contribution to the strengthening of both nc Cu and the nc Cu alloy. However, the nc Cu alloy exhibits a higher yield strength (1067 ± 20 MPa) than that of nc Cu (790 ± 12 MPa). The lower SFE of the nc Cu alloy is expected to make a significant contribution to its higher strength than nc Cu of the same grain size. To explore the origin of the stacking faults that give rise to the higher strength we carried out detailed structural characterization of the nc Cu alloy sample.

Figure 6.5-a shows a HRTEM image of the nc Cu alloy. As can be seen in Figure 6.5-a, several stacking faults were observed in the Cu alloy nano-grains (see colored arrows). Figure 6.5-b is an enlarged image of the area inside the square frame shown in Figure 6.5-a, showing a high density of dislocations with dissociated partials forming wide stacking faults. The relative boundaries of two such wide stacking faults are marked with pairs of yellow lines. We measured the width of eight stacking faults from different HRTEM images and found that the width range varied from 2.1 to 8.4 nm, with an average of 4.3 nm. It is also worth mentioning that no stacking faults were observed in the nc Cu sample. Therefore, we believe that the low SFE of the nc Cu alloy makes it easier for a full dislocation to split into partials with a wide stacking fault ribbon and create the observed high density of stacking faults. These stacking faults act as a barrier for the full dislocation to cross slip or climb and accordingly improve the strength of the nc Cu alloy over that of nc Cu. Zhao et al. [33] studied the effect of stacking faults on the strength of ultra-fine grained (ufg) Cu and a Cu–10% Zn alloy. The authors attributed the higher strength of the ufg Cu–10% Zn alloy (580 MPa) than that of the ufg Cu (420 MPa) to the lower SFE of the alloy, which is consistent with our results.

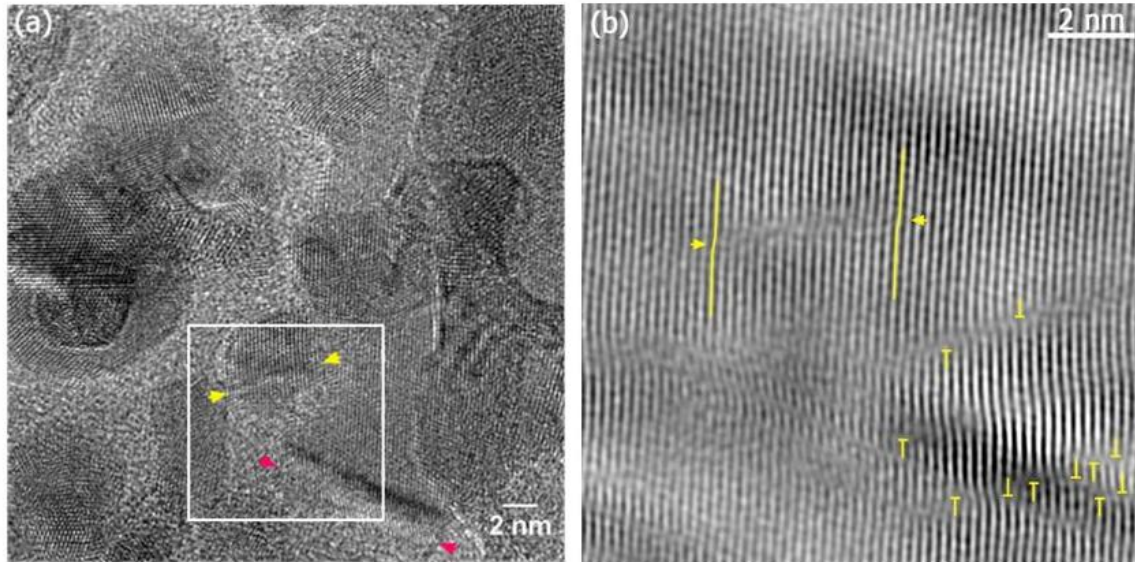


Figure 6.5- (a) A HRTEM image of the nc Cu alloy showing stacking faults. (b) A HRTEM of the outlined area in (a) showing the presence of wide stacking faults and areas with severe lattice distortion and high density Shockley partials.

It is well known that alloying Cu with Zn and Al reduces the SFE and changes the energy path for twinning, i.e. the general planar fault energy (GPFE) curves, and hence facilitates twinning [28, 34, 35]. A severe lattice distortion is clearly visible in Figure 6.5-a and b. Such lattice distortion attests to high residual stresses that could also help overcome the energy barrier for nucleation of extended partials and twins. Figure 6.6-a shows a HRTEM image of several nanograins in the Cu alloy. Interestingly, twins are observed in almost every nano-grain. This result is consistent with the discussion above and other reports that once a stacking fault is formed it is relatively easy to nucleate the twin [17, 28, 36, 37]. Molecular dynamic (MD) simulations also showed that after a stacking fault is formed a twin partial with the same Burgers vector as the initial leading partial could be emitted on an adjacent plane to nucleate a twin [16, 38]. The observation of large quantities of deformation twins (see Figure 6.6-a) indicates that twins can be easily formed and control the deformation

mechanism of the nc Cu alloy. These deformation twins may contribute to strengthening of the nc Cu alloy by acting as a GB and blocking the lattice dislocation motion. The high strength obtained in nano-twinned Cu synthesized by pulse electrodeposition was attributed to the high density of nano-twins in the submicron grains, which impede the movement of dislocations [39]. In addition to the strengthening by stacking faults and twins, the Al and Zn alloying elements used to lower the SFE also cause solid solution hardening, which increases the strength of the nc Cu alloy.

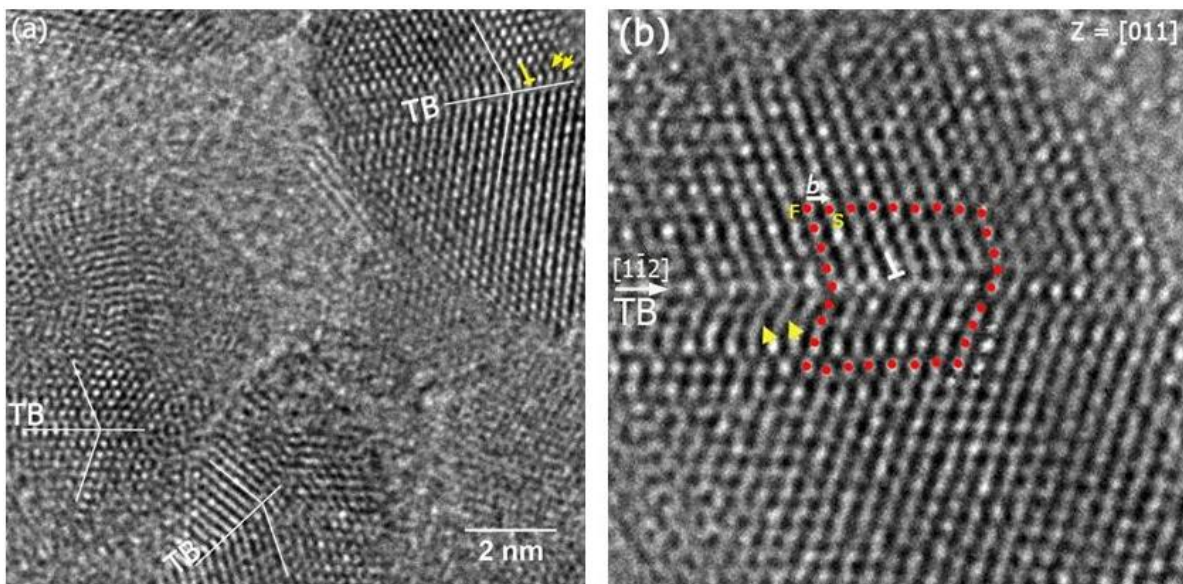


Figure 6.6- (a) A HRTEM image of the nc Cu alloy showing twinning in the nano grains. (b) A HRTEM image of a nano twin in the nc Cu alloy revealing a twin boundary and the Burgers circuit around it that shows the presence of Shockley partials.

To understand the significant strain hardening observed in both nc Cu and the nc Cu alloy (see Figure 6.4) we further analyzed the nanostructure of the nc Cu and nc Cu alloy. TEM observations reveal that the deformation mechanism in nc Cu is mainly controlled through dislocation activity (dislocation glide and pile-up at GB) within grains of 8–25 nm

[7]. The absence of other deformation mechanisms in nc Cu, such as deformation by twinning, could be attributed to the relatively high SFE of Cu. Thus we believe that dislocation plasticity in nc Cu might be responsible for producing the strain hardening effect observed in Figure 6.4. In contrast, a high density of stacking faults and Shockley partials associated with the twin boundaries were found to characterize the nanostructure of the nc Cu alloy (see Figures 6.5 and 6.6). Recent MD simulations [38, 40] showed that when two Shockley partials connected by a stacking fault ribbon (extended dislocation) is forced by an external stress into a twin boundary it recombines or constricts into a perfect dislocation configuration at the twin boundary and then slips through the boundary by splitting into three Shockley partials. Two of them glide in the slip plane of the adjacent twin boundary, constituting a new extended dislocation, whereas the third, a twinning partial, glides along the twin boundary and forms a step. It is expected that with increasing strain during milling such an interaction will generate a high density of partial dislocations along twin boundaries and stacking faults that align with the slip planes in the twin boundary. Figure 6.6-b shows such a configuration of dislocations along the twin boundary. For clarification, a Burgers circuit was drawn around that partial, which has its Burgers vector parallel to the twin plane. Such a finding suggests that stacking faults and twinning make a major contribution to the deformation mechanism of the nc Cu alloy. This mechanism facilitates the interaction of partial dislocations with twin boundaries and, therefore, affords a location for storage of dislocations, which sustain a significant strain hardening in the nc Cu alloy, as shown in Figure 6.4.

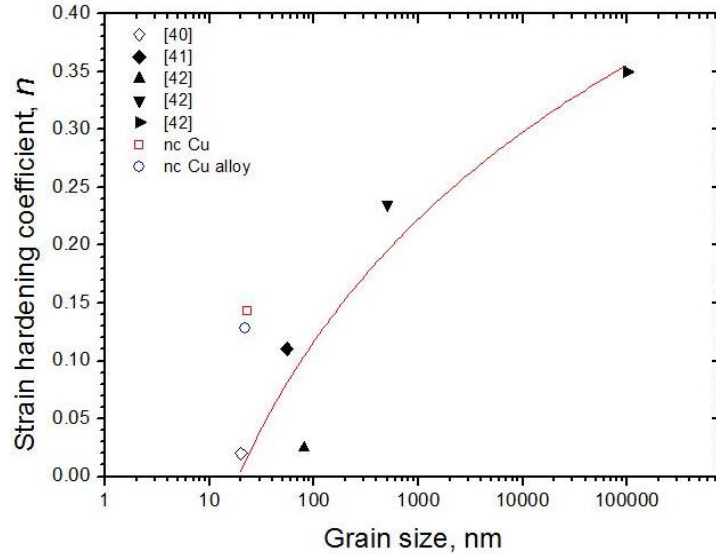


Figure 6.7- Strain hardening coefficient, n , as a function of grain size of nc Cu and nc Cu alloy. For comparison, the n values for nc-Cu (\diamond [41], \blacklozenge [42], \blacktriangle [43]), ufg-Cu \blacktriangledown [43], cg-Cu \blacktriangleright [43] samples reported in the literature are included.

To elaborate more on how the two different deformation mechanisms in the nc Cu and nc Cu alloy yield varying ductility (uniform elongation) and strain hardenings, their strain hardening coefficients (n) as a function of grain size were calculated and compared with other nanostructured Cu processed using different techniques (see Figure 6.7). The n values of nc Cu and the nc Cu alloy were determined by fitting the uniform plastic deformation region (see Figure 6.4) to the equation [44]:

$$\sigma = \sigma_0 + K\varepsilon^n \quad (6.2)$$

where σ_0 represents the yield strength and K is the strength increment due to strain hardening at strain $\varepsilon=1$ [44, 45]. It is shown in Figure 6.7 that n continuously decreases with decreasing the grain size. However, the higher n values of our nc Cu and nc Cu alloy (~6-8 times) than that of nc Cu (~20 nm) prepared by a surface mechanical attrition treatment (SMAT) technique [41] is an indication of the high ability of these nanostructures to sustain strain

hardening and significant ductility. The n value of nc Cu is slightly higher than that of the nc Cu alloy. Furthermore, the difference in deformation mechanism is also evident if the work hardening rate Θ is plotted as a function of the true plastic strain for the materials studied. Figure 6.8 shows that variation of the normalized work hardening rate Θ , which is defined as $\Theta = 1/\sigma (\partial\sigma/\partial\varepsilon)$, where σ is the true stress and ε is the true strain. The nc Cu has a higher normalized work hardening rate than that of the nc Cu alloy (see Figure 6.8). These observations suggest that the dislocation glide and pile-up deformation mechanism in the relatively high SFE nc Cu produces high strain hardening that prevents plastic instability during tension and yields a high uniform tensile elongation of 14% (see Figure 6.4). However, due to the low SFE of the nc Cu alloy the deformation mode is dominated by twinning (see Figures 6.5 and 6.6). Lu et al. [43] reported improved strain hardening and tensile ductility in nano-twinned Cu deposits. They suggested that decreasing the twin thickness, i.e. increasing the twin density, facilitates the dislocation–twin boundary interaction and affords more room for dislocations that sustain pronounced strain hardening and ductility. The storage capacity for dislocations in these nano-twinned deposits is provided by the high density and length of the nanotwins (mainly nano-twins in micron size grains). This mechanism is consistent with the observed strain hardening in the nc Cu alloy, however, the uniform ductility is much lower (6.5%) in our case due to the limited length of the twins in the nano-grains (5–50 nm). In addition, the dislocation-twin boundary interactions in the nc Cu alloy are less effective, as revealed from the n and Θ values, than the dislocation pile-ups at the HAGB of the nc Cu sample in sustaining a high level of

stabilized uniform elongation. This explains the lower uniform elongation obtained in the case of the nc Cu alloy (6.5%) than nc Cu (14%).

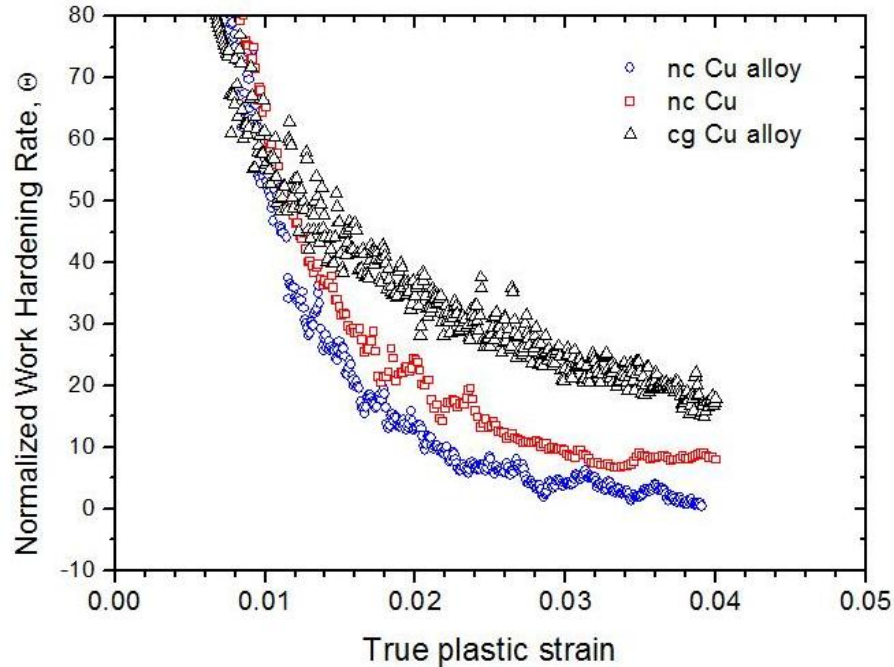


Figure 6.8- The normalized strain hardening rate, Θ , as a function of the true plastic strain for nc Cu, nc Cu alloy, and cg-Cu.

6.5. Summary

An artifact-free bulk nc Cu alloy can be synthesized by an in situ cryo and room temperature milling technique, which allows the intrinsic deformation to be determined without failures induced by processing defects. Very high yield and ultimate tensile strengths can be achieved combined with good ductility. The low SFE of the Cu alloy greatly affects its mechanical properties and deformation mechanism. The higher σ_y value of the nc Cu alloy (1067±20 MPa for a 22 nm grain size) than of the nc Cu (790±12 MPa for a 23 nm grain size) is attributed mainly to the lower SFE, which facilitates full dislocations to split into

partials with a wide stacking fault ribbon and to create a high density of stacking faults. These stacking faults act as a barrier for the full dislocation to cross slip or climb and accordingly improve the strength of the nc Cu alloy over that of nc Cu. The low SFE of the nc Cu alloy also induces the formation of a high density of deformation twins in the nanograins that contributes to the high strength and controls its deformation mechanism. Significant strain hardening and ductility were also observed in both nc Cu and the nc Cu alloy. The relatively lower strain hardening and uniform elongation (6.5%) of the nc Cu alloy than those of nc Cu (14%) derive from its lower n and θ values, which is caused by dislocation–twin boundary interactions. This mode of deformation is found to be less effective than dislocation pile-ups at the HAGB of nc Cu in sustaining a high value of stabilized uniform elongation.

6.6. References

- [1] S. Cheng, J.A. Spencer, W.W. Milligan, *Acta Mater.*, 51 (2003) 4505-4518.
- [2] C.C. Koch, D.G. Morris, K. Lu, A. Inoue, *Mrs Bulletin*, 24 (1999) 54-58.
- [3] J.R. Weertman, D. Farkas, K. Hemker, H. Kung, M. Mayo, R. Mitra, H. Van Swygenhoven, *Mrs Bulletin*, 24 (1999) 44-50.
- [4] C.C. Koch, *Journal of Metastable and Nanocrystalline Materials*, 18 (2003) 9-20.
- [5] Y.M. Wang, M.W. Chen, F.H. Zhou, E. Ma, *Nature*, 419 (2002) 912-915.
- [6] A.A. Karimpoor, U. Erb, K.T. Aust, G. Palumbo, *Scripta Mater.*, 49 (2003) 651-656.
- [7] K.M. Youssef, R. O. Scattergood, K. L. Murty, J. A. Horton, C. C. Koch, *Appl. Phys. Lett.*, 87 (2005) 0919041.

- [8] L. Lu, Y.F. Shen, X.H. Chen, L.H. Qian, K. Lu, *Science*, 304 (2004) 422-426.
- [9] R.Z. Valiev, I.V. Alexandrov, Y.T. Zhu, T.C. Lowe, *J. Mater. Res.*, 17 (2002) 5-8.
- [10] K.M. Youssef, R.O. Scattergood, K.L. Murty, C.C. Koch, *Scripta Mater.*, 54 (2006) 251-256.
- [11] C.C. Koch, R.O. Scattergood, K.M. Youssef, E.H. Chan, Y.T.T. Zhu, *J. Mater. Sci.*, 45 (2010) 4725-4732.
- [12] K.M. Youssef, Scattergood RO, Murty KL, Koch CC, *Appl. Phys. Lett.*, 85 (2004) 929-931.
- [13] E. Ma, *JOM Journal of the Minerals, Metals and Materials Society*, 58 (2006) 49-53.
- [14] Y.T. Zhu, B.Q. Han, E.J. Lavernia, *Deformation Mechanisms of Nanostructured Materials*, in: *Bulk Nanostructured Materials*, Wiley-VCH Verlag GmbH & Co. KGaA, 2009, pp. 87-108.
- [15] J. He, K. Chung, E. Lavernia, X. Liao, Y. Zhu, *Metall. Mater. Trans. A*, 34 (2003) 707-712.
- [16] H. Van Swygenhoven, P.M. Derlet, A.G. Froseth, *Nature Materials*, 3 (2004) 399-403.
- [17] A. Rohatgi, K.S. Vecchio, G.T. Gray, *Metall. Mater. Trans. A*, 32 (2001) 135-145.
- [18] X.L. Wu, Y.T. Zhu, *Appl. Phys. Lett.*, 89 (2006).
- [19] K.J. Hemker, *Science*, 304 (2004) 221-+.
- [20] C.N.J. Wagner, *Acta Metall.*, 5 (1957) 427-434.
- [21] X.L. Wu, Y.T. Zhu, E. Ma, *Appl. Phys. Lett.*, 88 (2006).
- [22] M. Niewczas, G. Saada, *Philosophical Magazine a-Physics of Condensed Matter Structure Defects and Mechanical Properties*, 82 (2002) 167-191.

- [23] Y.H. Zhao, X.Z. Liao, Z. Horita, T.G. Langdon, Y.T. Zhu, *Mater. Sci. Eng., A*, 493 (2008) 123-129.
- [24] Z.W. Wang, Y.B. Wang, X.Z. Liao, Y.H. Zhao, E.J. Lavernia, Y.T. Zhu, Z. Horita, T.G. Langdon, *Scripta Mater.*, 60 (2009) 52-55.
- [25] Y.H. Zhao, J.F. Bingert, Y.T. Zhu, X.Z. Liao, R.Z. Valiev, Z. Horita, T.G. Langdon, Y.Z. Zhou, E.J. Lavernia, *Appl. Phys. Lett.*, 92 (2008) -.
- [26] X.Z. Liao, S.G. Srinivasan, Y.H. Zhao, M.I. Baskes, Y.T. Zhu, F. Zhou, E.J. Lavernia, H.F. Xu, *Appl. Phys. Lett.*, 84 (2004) 3564-3566.
- [27] M.W. Chen, E. Ma, K.J. Hemker, H.W. Sheng, Y.M. Wang, X.M. Cheng, *Science*, 300 (2003) 1275-1277.
- [28] P.C.J. Gallagher, *Metall. Trans.*, 1 (1970) 2429-2461.
- [29] M.F. Denicot, J.P. Villain, *Phys. Status Solidi A*, 8 (1971) 125-127.
- [30] G.K. Williamson, W.H. Hall, *Acta Metall.*, 1 (1953) 22-31.
- [31] R. Valiev, *Nature Materials*, 3 (2004) 511-516.
- [32] M.A. Meyers, A. Mishra, D.J. Benson, *Prog. Mater. Sci.*, 51 (2006) 427-556.
- [33] Y.H. Zhao, Y.T. Zhu, X.Z. Liao, Z. Horita, T.G. Langdon, *Appl. Phys. Lett.*, 89 (2006) 121906.
- [34] S.A. Kibey, L.L. Wang, J.B. Liu, H.T. Johnson, H. Sehitoglu, D.D. Johnson, *Physical Review B*, 79 (2009) -.
- [35] S. Kibey, J.B. Liu, D.D. Johnson, H. Sehitoglu, *Appl. Phys. Lett.*, 89 (2006) -.
- [36] J.W. Christian, S. Mahajan, *Prog. Mater. Sci.*, 39 (1995) 1-157.
- [37] J.B. Bilde-Sorensen, J. Schiotz, *Science*, 300 (2003) 1244-1245.

- [38] S.I. Rao, P.M. Hazzeldine, *Phil. Mag.*, A80 (2000) 2011.
- [39] X.H. Chen, L. Lu, K. Lu, *Scripta Mater.*, 64 (2011) 311-314.
- [40] Z.H. Jin, P. Gumbsch, K. Albe, E. Ma, K. Lu, H. Gleiter, H. Hahn, *Acta Mater.*, 56 (2008) 1126-1135.
- [41] J. Chen, L. Lu, K. Lu, *Scripta Mater.*, 54 (2006) 1913-1918.
- [42] S. Cheng, E. Ma, Y.M. Wang, L.J. Kecskes, K.M. Youssef, C.C. Koch, U.P. Trociewitz, K. Han, *Acta Mater.*, 53 (2005) 1521-1533.
- [43] L. Lu, X. Chen, X. Huang, K. Lu, *Science*, 323 (2009) 607-610.
- [44] M.A. Meyers, K.K. Chawla, *Mechanical behavior of materials*, 2nd ed., Cambridge University Press, Cambridge ; New York, 2009.
- [45] A. Misra, X. Zhang, D. Hammon, R.G. Hoagland, *Acta Mater.*, 53 (2005) 221-226.

CHAPTER SEVEN

7.0. BULK NANOSTRUCTURED COPPER PRODUCED VIA BALL MILLING FOLLOWED BY HIGH PRESSURE TORSION

H. Bahmanpour, D. Setman, J. Horky, M. Kerber, K. Youssef, M. Zehetbauer, R. O. Scattergood, C. C. Koch

To be submitted to: Scripta Materialia

7.1. Abstract

8h cryomilled Cu with a fine grain size of 28nm were used as a precursor for consolidation by high pressure torsion. It was found that intense HPT conditions, hydrostatic pressure of 8GPa and shear strains of more than 2000, produces fully dense samples. TEM investigations showed a grain growth during HPT deformation producing a bimodal microstructure. Tensile tests revealed that combined ball milling and HPT produces samples with high strength and good ductility.

7.2. Introduction

Combination of severe plastic deformation techniques have been used to produce bulk ultrafine and nanocrystalline samples [1-5]. Consolidation of powder samples via HPT

and ECAP techniques involves plastic deformation on individual particles resulting in fracture of the brittle oxide layer. This mechanism is different from the thermally assisted sintering in which the mass transport through diffusion of atoms helps densification of the sample [2]. Xia [2] discussed that since diffusion is not required in SPD consolidation to bond particles, the process can be done at lower temperatures compared to sintering, and consolidation is obtained instantaneously as the particles are deformed. For full consolidation, i.e. good bonding between particles with no porosity, it is critical that the particles be shear deformed, rather than slide over each other. The particle characteristics and processing conditions that promote particle deformation and thus full consolidation include larger particle sizes, irregular particle shapes, softer particles, high friction between particles, higher temperatures and higher pressures [2].

High pressure torsion (HPT) has been used by several researchers as a tool for consolidation of powder samples. Different systems such as Co [1], Ni [6], Ti [3], Cu [7], Al-5%CNT [8], Al-7.5%Mg [9], Cu-Ag [10], Fe-based amorphous alloys [11], and Al-Fe-Nd [12] were subjected to HPT pressures and strains sufficiently high to achieve fully dense samples with highly refined microstructure and enhanced mechanical properties. In contrast to typical HPT experiments with about 6GPa pressure and 10 revolutions on bulk samples, the applied pressure and strain on the powder samples should be much higher in order to disrupt the oxide layer and achieve full bonding between particles. Using HPT as a consolidation method and application of ultra high pressure with intense strain opens room for producing bulk nanostructured materials with high strength and good ductility.

In this paper, microstructure and mechanical properties of pure copper subjected to ball milling at 77K followed by HPT are reported. Based on earlier ball milling studies by the authors [13], high energy ball milling can produce a very fine microstructure after 6-8h at 77K. Cryogenic deformation provides effective microstructure refinement and suppresses dynamic recovery [14]. Ball milled powder with a grain size of 28 nm was used as a precursor for HPT deformation. Application of intense HPT deformation conditions, 8GPa and up to 150 revolutions (shear strain of 4100) resulted in successful production of bulk samples with a mean grain size of <60 nm and a density higher than 99% which distinguishes this work. Microstructure of the ball milled and HPT consolidated samples was studied by TEM and their mechanical properties were investigated by tensile tests.

7.3. Experimental procedure

Micron sized pure copper powder, 99.9wt.% purity, was processed by high energy ball milling at 77K using a Spex 8000 mixer/mill. Hardened steel vials were loaded under argon atmosphere with an oxygen content of less than 1 ppm. Continuous cryomilling was performed up to 8h to achieve saturation in grain size and microhardness [13]. Oxygen content of the cryomilled samples was analyzed using inert gas fusion. It was found that the as-milled sample contains 0.36wt.% oxygen. The product of the cryomilling is micron sized flakes that were used as the precursor for consolidation by HPT. Earlier experiments on coarse grained pure copper powder showed that a high pressure of 8GPa and an extended number of revolutions are necessary to produce fully dense HPT disks. In this regard, 10mm

disks of green compacted cryomilled samples were subjected to HPT with a hydrostatic pressure of 8GPa and 75, 100, and 150 revolutions to obtain defect-free and flawless samples. The applied shear strain on the HPT disk varies with the number of revolutions, n , and the distance from disc center, r , and can be calculated by the following relation [15];

$$\gamma = \frac{2\pi.n.r}{h} \quad (7.1)$$

where, h is the sample thickness after deformation. Samples for tensile tests and TEM were prepared from an area with $r=3.5\text{mm}$ from center of the disk, and having strain values, γ , being listed in Table 7.1. TEM samples with diameter of 3mm were prepared using 90% phosphoric acid solution in a Fischione twin-jet system. For the case of cryomilled samples, the small copper flakes were pressed into pieces of gallium to bond the particles together and 3-mm disks were punched from the gallium-copper composite. XRD was used to study texture evolution and PM2K software [16] was utilized to analyze XRD profiles to determine the dislocation density of the processed samples. Mechanical properties were investigated by tensile tests and standard Vickers microhardness test. Miniaturized tensile test samples measuring 2mm in gauge length and 1mm in width were cut from HPT disks, and were investigated by a microtensile test setup. At least two samples were tested for each tensile test. Details on the tensile test setup can be found elsewhere [17].

7.3. Results and discussion

Figure 7.1 shows the XRD profiles of the as-cryomilled and deformed samples at different HPT conditions. It is seen that applied HPT deformation brings about a texture in

the samples as the number of revolutions increases. The ratio of the intensities of (200) and (111) peaks, (I_{200}/I_{111}), for the as-cryomilled sample is 0.28, Table 7.1, in contrast to the ratio for a randomly oriented material being 0.42. This indicates that the orientation distribution of the as-cryomilled sample is obviously not random. Processing with HPT up to $\gamma=2700$ decreases the I_{200}/I_{111} to about 0.08. Further deformation till $\gamma=4000$ decreases I_{200}/I_{111} to 0.06, that indicates a further increase of the texture. The effect of HPT deformation on evolution of texture in Cu single and poly- crystals was studied by Bonarski et al. [18]. It is reported that the rearrangement of dislocation structure by dynamic and static recovery is responsible for observed texture in the copper samples. Investigation on HPT deformation of coarse grained copper also revealed that higher applied pressure and strains result in a gradual increase in dislocation density [19]. Therefore, recrystallization has been excluded from the possible mechanism of microstructure evolution in Cu subjected to HPT [19]. Our results indicate that the initial microstructure of the sample has a significant impact on the final grain size and defect structure of the HPT-deformed sample. In agreement with another study on ball milling of Cu and Cu alloys [13], X-ray line profile analysis, Table 7.1, shows that 8h cryomilling produces a dislocation density as high as $2.4 \times 10^{17} \text{ m}^{-2}$ due to suppressed dynamic recovery at low temperature deformation. This high density of defects in combination with a quite small grain size results in a microhardness of 2.9 GPa in the as-cryomilled sample, Table 7.1. Room temperature deformation by HPT produces a decrease in dislocation density and an increase in grain size, and hence results in lower hardness, Table 7.1. It appears that microstructure evolution of the cryomilled sample during room temperature HPT processing involves dislocation annihilation and rearrangement of the

dislocation structure into stable configurations resulting in larger grains, lower dislocation density, and hence lower microhardness.

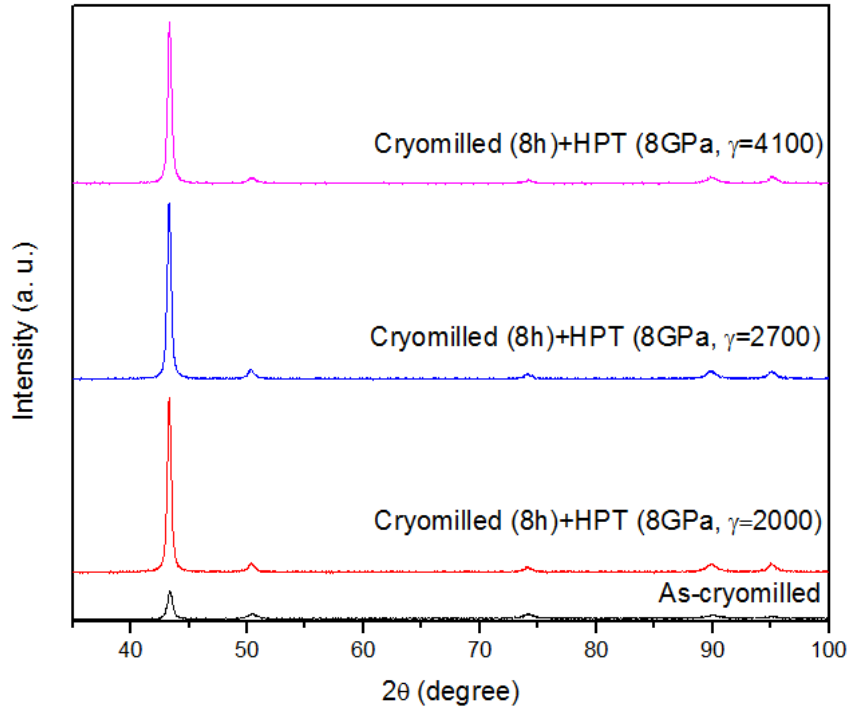


Figure 7.1– XRD profiles in as-cryomilled and cryomilled + HPT at $\gamma=2000$, 2700, and 4100.

Table 7.1- Properties of as-cryomilled Cu and samples cut at $r=3.5$ mm from the HPT disks, comprising I_{200}/I_{111} , dislocation density, grain size, and microhardness.

	Shear strain, γ , at $r=3.5$ mm	I_{200}/I_{111}	Dislocation density ($\times 10^{17} \text{ m}^{-2}$)	Grain size by TEM (nm)	Microhardness (GPa)
As cryomilled	-	0.28	2.4	28	2.90 ± 0.01
Cryomilled+HPT (75 revs.)	2000	0.08	0.9	39	2.75 ± 0.02
Cryomilled+HPT (100 revs.)	2700	0.08	0.9	37	2.73 ± 0.08
Cryomilled+HPT (150 revs.)	4100	0.06	1.0	54	2.78 ± 0.06

TEM observations show a microstructure consisting of dislocation cell/wall structures for the as-cryomilled sample, Figure 7.2a, with some well defined grains with an average grain size of 28 nm. This is in agreement with our observation on ball milling of Cu-Zn alloys [13] and cryorolling of Cu and Cu-Al-Zn alloy [14] where deformation at 77K produced microstructures with a high dislocation density due to suppressed dynamic recovery. The development of ultrafine grained microstructure in pure copper subjected to multidirectional forging at 195K was studied by Kobayashi et al. [20]. They concluded that strain-induced reactions are involved in formation of ultrafine grains and continuous dynamic recrystallization assisted by dynamic recovery is responsible for grain refinement. Formation of nanosized grains in as-cryomilled copper could also be related to strain-induced formation of dislocation sub-boundaries followed by gradual increase of sub-boundary misorientation up to typical values of high angle grain boundaries.

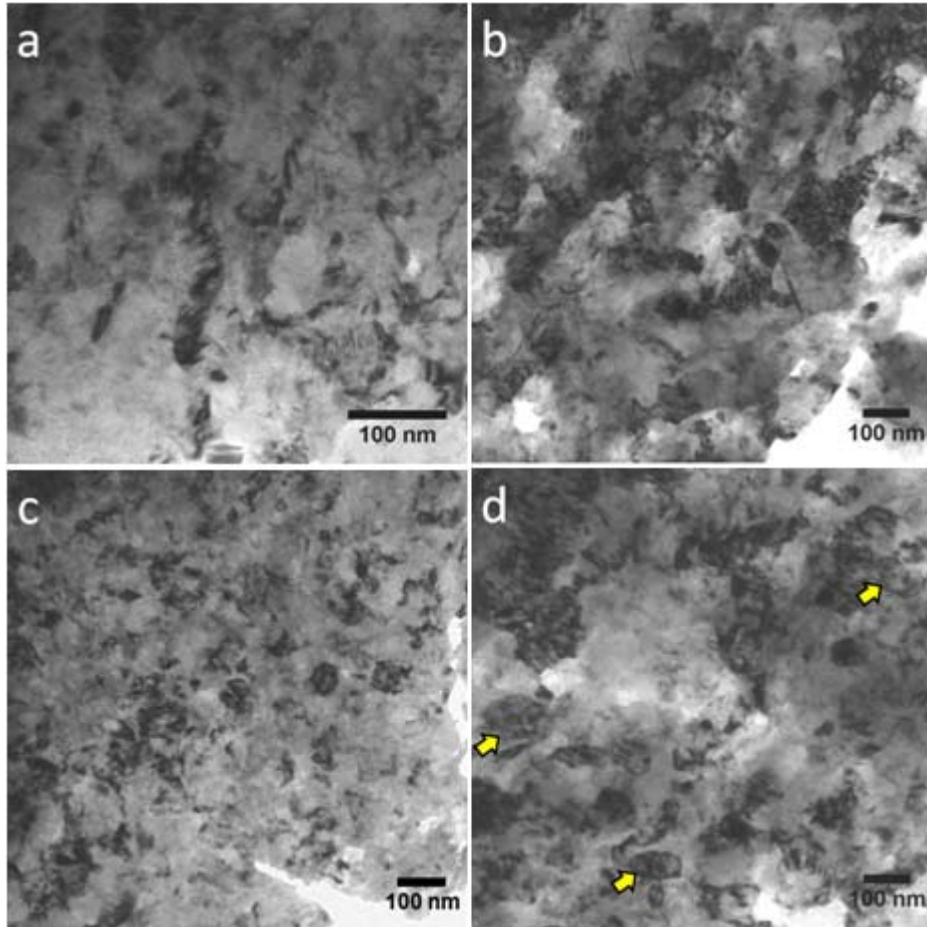


Figure 7.2– TEM micrograph of the a) as cryomilled, b) CM+HPT ($\gamma=2000$), c) CM+HPT ($\gamma=2700$), d) CM+HPT ($\gamma=4100$).

Grain size measurements on HPT deformed samples revealed that shear strain of 2000 and 2700 revolutions result in some grain growth to about the same grain size in both samples, 39 and 37 nm, respectively (Table 1 and Fig. 2b and c). Increased number of revolutions to 150, $\gamma=4100$, brings about further grain growth to 54 nm, Table 7.1 and Figure 7.2d. This is remarkable that even after intense deformation by HPT, at an ultra high strain of more than 4000, the mean grain size is still less than 60 nm. This can be compared to the minimum grain size obtainable by HPT deformation at room temperature on coarse grained pure Cu that is reported to be about 180nm [21]. The observed increase in grain size can be

related to strain-induced grain growth, especially if the applied strain arises from a different deformation path, i.e. HPT following ball milling. Strain-driven grain coarsening was previously reported on electrodeposited nanocrystalline Ni [22], ultrafine grained Al [23], and nanocrystalline and ultrafine grained Cu [24, 25]. Atomic simulation also proved the occurrence of strain-induced grain growth in nanocrystalline Cu [26]. As an example, 5 revolutions of HPT, $\gamma=350$, at 7GPa can increase the grain size of the electrodeposited Ni from 30nm to 129nm [22]. This is a significant change in the microstructure compared to the negligible increase of the grain size from 28 nm to 39 nm in our case. The mechanism of HPT-induced grain growth has been studied by Lavernia et al. [27]. HRTEM investigations on Cu samples processed by HPT revealed that at grain sizes less than 100nm grain growth is controlled by grain rotation-induced grain coalescence while at grain sizes larger than 100nm the grain growth is primarily attributed to stress-coupled grain boundary migration [27]. In an attempt to control the final grain size of the HPT processed Ni, Bachmier et al. [28] applied HPT deformation with 6GPa on pre-oxidized nickel powder. They reported that the minimum grain size can be as small as 29nm in pre-oxidized + HPT deformed Ni sample. It was concluded that oxide particles pin grain boundaries and prevent grain growth during HPT deformation. This issue is also addressed by Edalati et al. [3] on Ti who applied HPT (6GPa and $\gamma=1600$) to ball milled Ti powder with initial oxygen content of 0.35%. The final grain size was 150nm and pinning effect of oxide particles were considered responsible for the small grain size obtained after HPT [3]. Besides the role of the highly dislocated microstructure of the as-milled sample addressed above, we can also conclude that final grain size in HPT deformed Cu is affected by presence of oxide particles according to chemical

analysis of as-cryomilled product showing 0.36% oxygen in Cu flakes. The oxide particles can pin grain boundaries to some extent resulting in small grain size after HPT deformation. It should be pointed out, however, that at very high strains the strain-driven grain growth can overcome the pinning effect and cause grain growth as revealed by careful examination of the TEM images, Figure 7.2d. It is seen that large grains of the order of 100nm, marked with arrows, did evolve in the sample deformed up to $\gamma=4100$. The decrease of the I_{200}/I_{111} ratio in the sample with $\gamma=4100$ can also be reconciled with the formation of these large grains, resulting in a stronger texture.

Mechanical properties in terms of tensile strength and ductility of bulk nanocrystalline materials are of great interest. Although hardness results are typically reported as a measure of the local mechanical properties, there are very few publications [3, 8] on the tensile behavior of the HPT consolidated samples. The homogeneity of microstructure and properties of HPT disks has been investigated on Cu [29, 30], Al [31], and austenitic steel [32]. Vorhauer et al. [32] discussed the homogeneity of austenitic steel HPT disks after 16 revolutions, $\gamma=420$, at 5.3 GPa. They showed that the microhardness of the deformed samples reaches a plateau after shear strains above 20. On the other hand, it was shown that pure Al reaches a homogenized microstructure and microhardness after an equivalent HPT strain of 10 [31]. In addition to the hardness measurements that show homogeneity across the diameter of the HPT disks, not shown here, we performed tensile tests on the Cu samples subjected to ultra high strain and found that the combined SPD techniques, cryomilling and HPT, can produce high strength Cu with good ductility. It is seen in Figure 7.3 that tensile curves show an initial plastic deformation region followed by

necking and a post-necking deformation without early failure of the sample due to debonding of the particles. It was observed recently by Tian et al. [33] that HPT on Cu-Ag at 6GPa with shear strain as high as 400 cannot produce samples without premature failure during tensile tests. It is demonstrated in Figure 7.3 and 7.4, that samples produced by $\gamma=2000$ and 2700 show almost the same tensile properties in terms of strength and elongation to failure, yield strength of 730MPa and elongation to failure of 6%. In an attempt to consolidate Cu powder size using ECAP method, Haouaoui et al. [5] obtained samples with fracture tensile stress of 730MPa but negligible ductility, i.e. less than 1%. This indicates that combination of cryogenic ball milling and intense HPT as the consolidation step can produce markedly better mechanical properties. This can be explained by the fact that HPT processing provides much higher hydrostatic pressures -here 8GPa- instead of only about 1GPa with ECAP processing. Our results can also be compared with HPT on bulk Cu samples. Application of 6GPa and five revolutions ($\gamma=120$) of HPT at room temperature is reported to produce a mean grain size of 180nm with yield strength of 420MPa and an elongation to failure of 5.1% [34]. It becomes evident that high strength obtained in our samples is related to high defect density and small grain size, as it is true for the high yield strength of 791MPa obtained in *in situ* consolidated Cu by high energy ball milling [35]. On the other hand, the lower ductility of 5.6% of our samples and 5.1% in HPT processed bulk Cu ones [34] compared to 15.5% of *in situ* consolidated Cu made by ball milling [35], is probably due to the stronger texture of the HPT samples. As shown in Figure 7.4, further deformation up to $\gamma=4100$ decreases the yield strength to 687MPa and increases the elongation to failure to 8.4%. Considering the microstructure observations it can be concluded that it is the formation

of larger grains during HPT up to $\gamma=4100$ (see arrows in Figure 7.2d) which allows for increased dislocation activity and plasticity compared to samples made by shear strains up to 2000 and 2700.

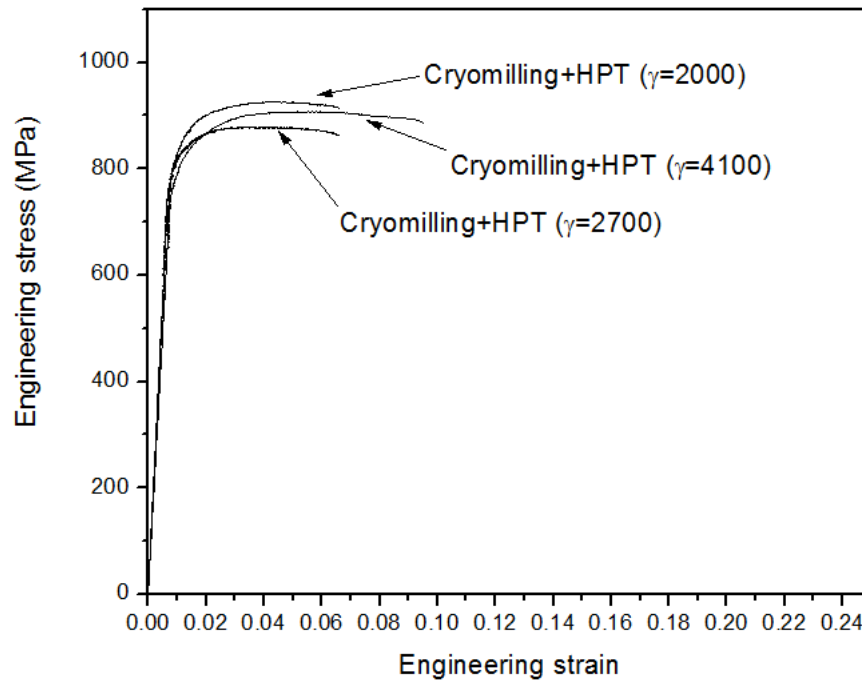


Figure 7.3 – Engineering stress-strain curves for samples produced with 8h cryomilling + HPT at 8GPa with $\gamma=2000$, 2700, and 4100.

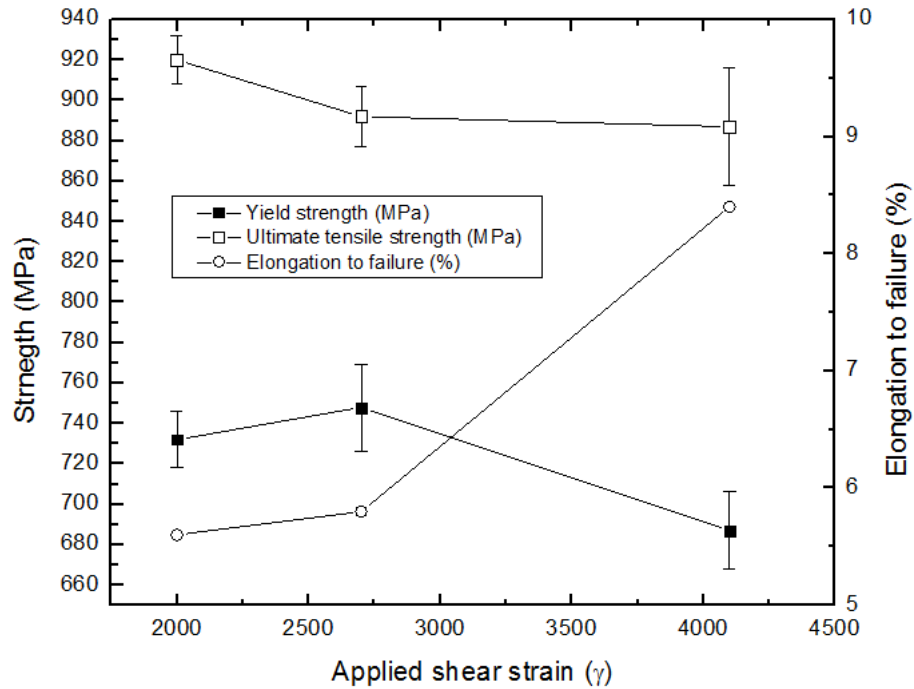


Figure 7.4- Tensile properties of HPT samples as a function of applied shear strain.

7.4. Summary

In summary, a combination of high energy ball milling and HPT was utilized to produce bulk nanocrystalline copper samples. High pressure and ultra high strain applied on ball milled copper samples helped to disrupt the surface oxide layer and thus to fully consolidate the micron sized flakes. It is shown that the high dislocation density and fine microstructure obtained by ball milling at 77K can be inherited to HPT deformed samples showing high strength and good ductility. It is observed that the mean grain size obtained even after ultra high strain of 4100 is still below 60 nm although some larger grains evolved due to strain-

induced grain growth. Higher ductility observed at higher HPT strains appears to be related to accommodation of plastic strain by these large grains.

7.5. References

- [1] J. Sort, A. Zhilyaev, M. Zielinska, J. Nogués, S. Surinach, J. Thibault, M.D. Baro, *Acta Mater.*, 51 (2003) 6385-6393.
- [2] K.N. Xia, *Adv. Eng. Mater.*, 12 (2010) 724-729.
- [3] K. Edalati, Z. Horita, H. Fujiwara, K. Ameyama, *Metall. Mater. Trans. A*, 41A (2010) 3308-3317.
- [4] M. Moss, R. Lapovok, C.J. Bettles, *Jom-U.S.*, 59 (2007) 54-57.
- [5] M. Haouaoui, I. Karaman, H.J. Maier, K.T. Hartwig, *Metall. Mater. Trans. A*, 35A (2004) 2935-2949.
- [6] R.Z. Valiev, R.S. Mishral, J. Grozal, A.K. Mukherjee, *Scripta Mater.*, 34 (1996) 1443-1448.
- [7] A.P. Zhilyaev, A.A. Gimazov, G.I. Raab, T.G. Langdon, *Mater. Sci. Eng., A*, 486 (2008) 123-126.
- [8] T. Tokunaga, K. Kaneko, Z. Horita, *Mater. Sci. Eng., A*, 490 (2008) 300-304.
- [9] Z. Lee, F. Zhou, R.Z. Valiev, E.J. Lavernia, S.R. Nutt, *Scripta Mater.*, 51 (2004) 209-214.
- [10] H. Shen, Z. Li, B. Gunther, A.V. Korznikov, R.Z. Valiev, *Nanostructured Materials*, 6 (1995) 385-388.
- [11] J. Sort, D.C. Ile, A.P. Zhilyaev, A. Concustell, T. Czeppe, M. Stoica, S. Surinach, J. Eckert, M.D. Baro, *Scripta Mater.*, 50 (2004) 1221-1225.

- [12] A.R. Yavari, W.J. Botta, C.A.D. Rodrigues, C. Cardoso, R.Z. Valiev, *Scripta Mater.*, 46 (2002) 711-716.
- [13] H. Bahmanpour, K. Youssef, R. Scattergood, C. Koch, *J. Mater. Sci.*, (2011) 1-7.
- [14] H. Bahmanpour, A. Kauffmann, M.S. Khoshkhoo, K.M. Youssef, S. Mula, J. Freudenberger, J. Eckert, R.O. Scattergood, C.C. Koch, *Mater. Sci. Eng., A*, 529 (2011) 230-236.
- [15] R.Z. Valiev, Y.V. Ivanisenko, E.F. Rauch, B. Baudelet, *Acta Mater.*, 44 (1996) 4705-4712.
- [16] M. Leoni, T. Confente, P. Scardi, *Z. Kristallogr.*, 23 (2006) 249-254.
- [17] R.K. Guduru, K.A. Darling, R.O. Scattergood, C.C. Koch, K.L. Murty, *J. Mater. Sci.*, 42 (2007) 5581-5588.
- [18] B.J. Bonarski, B. Mikulowski, E. Schafler, C. Holzleithner, M.J. Zehetbauer, *Archives of Metallurgy and Materials*, 53 (2008) 117-123.
- [19] E. Schafler, A. Dubravina, B. Mingler, H.P. Karnthaler, M. Zehetbauer, *Mater. Sci. Forum*, 503-504 (2006) 51-56.
- [20] C. Kobayashi, T. Sakai, A. Belyakov, H. Miura, *Phil. Mag. Lett.*, 87 (2007) 751-766.
- [21] A.V. Korznikov, A.N. Tyumentsev, I.A. Ditenberg, *Phys. Metals Metallogr.*, 106 (2008) 418-423.
- [22] X.Z. Liao, A.R. Kilmametov, R.Z. Valiev, H.S. Gao, X.D. Li, A.K. Mukherjee, J.F. Bingert, Y.T. Zhu, *Appl. Phys. Lett.*, 88 (2006) 021909.
- [23] M. Jin, A.M. Minor, E.A. Stach, J.W. Morris, *Acta Mater.*, 52 (2004) 5381-5387.
- [24] K. Zhang, J.R. Weertman, J.A. Eastman, *Appl. Phys. Lett.*, 85 (2004) 5197-5199.

- [25] K. Zhang, J.R. Weertman, J.A. Eastman, *Appl. Phys. Lett.*, 87 (2005) 061921.
- [26] J. Schiotz, *Mater. Sci. Eng., A*, 375-77 (2004) 975-979.
- [27] E.J. Lavernia, H.M. Wen, Y.H. Zhao, Y. Li, O. Ertorer, K.M. Nesterov, R.K. Islamgaliev, R.Z. Valiev, *Philos. Mag.*, 90 (2010) 4541-4550.
- [28] A. Bachmaier, A. Hohenwarter, R. Pippan, *Scripta Mater.*, 61 (2009) 1016-1019.
- [29] X.H. An, S.D. Wu, Z.F. Zhang, R.B. Figueiredo, N. Gao, T.G. Langdon, *Scripta Mater.*, 63 (2010) 560-563.
- [30] J. Cizek, O. Melikhova, M. Janecek, O. Srba, Z. Barnovska, I. Prochazka, S. Dobatkin, *Scripta Mater.*, 65 (2011) 171-174.
- [31] M. Kawasaki, R.B. Figueiredo, T.G. Langdon, *Acta Mater.*, 59 (2011) 308-316.
- [32] A. Vorhauer, R. Pippan, *Scripta Mater.*, 51 (2004) 921-925.
- [33] Y.Z. Tian, S.D. Wu, Z.F. Zhang, R.B. Figueiredo, N. Gao, T.G. Langdon, *Acta Mater.*, 59 (2011) 2783-2796.
- [34] Y.H. Zhao, X.Z. Liao, Z. Horita, T.G. Langdon, Y.T. Zhu, *Mater. Sci. Eng., A*, 493 (2008) 123-129.
- [35] K.M. Youssef, R. O. Scattergood, K. L. Murty, J. A. Horton, C. C. Koch, *Appl. Phys. Lett.*, 87 (2005) 0919041.

CHAPTER EIGHT

8.0. DEFORMATION TWINS AND RELATED SOFTENING BEHAVIOR IN NANOCRYSTALLINE CU-30%ZN ALLOY

H. Bahmanpour, K. Youssef, J. Horkey, D. Setman, M. Atwater, M. Zehetbauer, R. O. Scattergood, C. C. Koch

Manuscript submitted to: Acta Materialia

8.1. Abstract

Nanocrystalline Cu-30%Zn samples were produced by high energy ball milling at 77K and room temperature. Cryomilled flakes were processed further by ultrahigh strain high pressure torsion or room temperature milling to produce bulk artifact-free samples. Deformation induced grain growth and reduction of twin probability were observed in HPT consolidated sample. Investigations on mechanical properties by hardness measurements and tensile tests revealed that at small grain sizes of less than $\sim 35\text{nm}$, Cu-30%Zn deviates from the classical Hall-Petch relation and the strength of nanocrystalline Cu-30%Zn is comparable to that of the nanocrystalline pure copper. HRTEM studies show a high density of finely spaced deformation nanotwins that were formed due to the low stacking fault energy of 14 mJ/m^2 and low temperature severe plastic deformation. Possible softening mechanisms proposed in the literature for nanotwin copper are addressed and the twin related softening

behavior in nanotwinned Cu is extended to the Cu-30%Zn alloy based on detwinning mechanisms.

8.2. Introduction

Stacking fault energy (SFE), that is the energy associated with change of lattice structure due to dissociation of partial dislocations, is a determining factor in deformation behavior of metals and alloys. Many publications have been devoted to investigations on the effect of SFE on microstructure and mechanical properties [1-9]. Besides pure fcc metals such as Ni, Al and Cu with different stacking fault energies, single phase solid solution Cu-based alloys have been of great interest to understand microstructure-properties relationships and effect of alloying content and hence SFE on the observed mechanical response. In this regard, Cu-Zn [3, 4, 6, 9-15], Cu-Al [8, 16], Cu-Al-Zn [7, 17], and Cu-Si [18] systems were used as models to study the role of stacking fault energy on the deformation behavior in various solid solutions. These solid solution systems were subjected to different severe plastic deformation methods such as high pressure torsion [9-11], equal channel angular pressing [14, 19], high energy ball milling [2, 7], and rolling [20] to produce a wide range of grain size and different microstructures in terms of dislocation and twin structures. Restricted cross-slip and higher twinning tendency of low SFE alloys produces nanostructures with high dislocation and twin density [2, 15] upon severe plastic deformation.

Grain size strengthening, described by the Hall-Petch relation, is a well-known mechanism for controlling mechanical properties of metals and alloys. Despite some controversy on the quality of the nanocrystalline samples with grain size $< \sim 10\text{nm}$, the

breakdown of the Hall-Petch relation at small grain size regime seems to be valid [21]. The softening behavior, inverse Hall-Petch effect, is attributed to grain boundary mediated mechanisms such as grain boundary diffusion [22] and grain boundary shear [23]. Twin boundaries can also serve as effective dislocation barriers and strengthen the material. Taking twin boundaries into account, it is reported that the Hall-Petch slope for twinning is typically higher than that of slip in coarse grained materials, e.g. for Cu-10%Zn $K_{slip}=8.4$ MPa.mm^{0.5} and $K_{twin}=16.7$ MPa.mm^{0.5} [24]. Therefore, it is expected that a twinned microstructure shows higher strength compared to an untwined microstructure or one with lower frequency of twins. Interestingly, it was observed experimentally on the coarse grained nanotwin copper with grain size of 400-600nm that twin boundary strengthening breaks down at a critical twin thickness, 15 nm [25]. In an experimental work by Konopka et al. [26] the observed softening behavior in pure copper is attributed to the capability of twin boundaries for generating dislocations. Molecular dynamics simulations [27] and computational models [28] also provided insight into the governing deformation mechanisms in nanotwinned copper. MD simulations show that dislocation nucleation controlled mechanisms are responsible for strength-softening in nanotwined metals. Li et al. [29] concluded that when the twin spacing is less than a critical value, that depends on the grain size, nucleation and motion of partial dislocations parallel to twin boundaries take place resulting in strength-softening. It is also shown by simulation that the strength-softening is caused by dislocation nucleation at twin boundary-grain boundary intersection [29]. Partial dislocations nucleate at grain boundaries and glide along the twin planes. Furthermore, the critical twin-boundary spacing for the occurrence of softening and activation of dislocation-

nucleation-controlled mechanisms depend on grain size; i.e. the smaller the grain size the smaller the critical twin boundary spacing, and the higher the maximum strength of the material [29]. It is worth to note that crystal models by Dao et al. [30] considered a twin boundary affected zone near twin boundaries and Mirkhani et al. [28] incorporated this idea to capture the effect of twin thickness on the strengthening and softening of nanotwin copper. These models assume that the dominant plastic deformation in the vicinity of a twin boundary is controlled by dislocation activity.

In this paper, we report our observation on the softening behavior of nanocrystalline Cu-30%Zn alloy. Considering the competitive nature of grain boundaries and twin boundaries on strengthening and softening at different grain size regimes, it is important to compare mechanical properties of the nanocrystalline copper and copper alloys at the same grain size regime. Due to limitation imposed by the processing methods in grain refinement of the metallic samples, most of the reported data in the literature compare microstructure and mechanical properties of Cu and Cu-Zn alloys with different grain size regimes. In a recent paper, Youssef et al. [7] investigated the microstructure and mechanical properties of pure copper and a low stacking fault energy alloy, Cu-12.1%Al-4.1%Zn, at the same grain size. In the present work, softening behavior of nanocrystalline Cu-30%Zn is addressed. Nanocrystalline Cu-30%Zn samples were produced via high energy ball milling at 77K and room temperature. NaCl and stearic acid were used for room temperature milling to avoid sticking and the cryomilled flakes were used as the precursor for a consolidation step via room temperature milling or HPT. The mechanical properties of bulk samples were studied by tensile tests and the microstructure-mechanical behavior relationship is compared with

pure copper in light of the Hall-Petch relation. It is found that at the same grain size in the small grain size regime, Cu-30%Zn shows a comparable strength to that of the nanocrystalline copper, resulting in the breakdown of H-P relation. The idea of strength softening at very small twin spacing in nanotwin copper is extended to nanocrystalline Cu-30%Zn alloys in which a low stacking fault energy and low processing temperature produced abundant deformation twins. The role of a high density of deformation nanotwins on deformation behavior is discussed and possible mechanisms are addressed accordingly.

8.3. Experimental procedure

Nanocrystalline Cu-30%Zn alloy was synthesized using a SPEX 8000 shaker mill with stainless steel vial and martensitic stainless steel (440) balls. Elemental powders of Cu (99.9%) and Zn (99.9%) with the ball to powder mass ratio of 10:1 were loaded in the vial under purified argon with <1 ppm oxygen. To avoid argon trapping in the structure of the alloy, the vial was sealed under vacuum. In order to obtain small grain sizes, the ball milling step was carried out at liquid nitrogen temperature using a specially designed nylon vial holder that carries liquid nitrogen flow around the vial. Temperature measurements showed that the external temperature of the vial is about 77 K. The product of the cryomilling step is micron sized flakes that can be used as the precursor for the consolidation step. In this regard, the cryomilled product was further processed via room temperature ball milling or ultrahigh strain high pressure torsion at 8GPa with 100 rotations to produce bulk artifact-free samples. These consolidation steps guarantee production of sound samples appropriate for tensile

tests. Another series of samples were also produced via surfactant assisted room temperature ball milling. 0.125wt.% NaCl or stearic acid were added to the powder in order to control the cold welding of the powder to the milling media. The surfactants enabled us performing longer milling times which results in microstructures with small grain sizes.

Mechanical properties of the processed samples were investigated by microhardness measurements and tensile tests. Microhardness was measured using a Buehler Micromet microhardness tester with a Vickers indenter at 50 g load and a loading time of 15 s. Tensile test samples with gauge dimension of 2×1 mm were cut from in situ consolidated spheres and HPT disks and were tested with a miniaturized tensile testing machine at strain rate of $9.4 \times 10^{-4} \text{ s}^{-1}$.

X-ray diffraction technique was utilized to estimate crystallite size of samples ball milled with NaCl and stearic acid. Furthermore, dislocation density and twin probability of the cryomilled and consolidated samples were estimated by XRD technique. TEM samples were prepared from cryomilled and consolidated samples with a Fischione twin jet electropolisher. A JEOL-2000 TEM and a JEOL 2010 TEM at an accelerating voltage of 200 keV were used to determine the grain size distribution and to obtain high resolution TEM images of the samples, respectively.

8.4. Results and discussion

Microstructure of cryomilled and consolidated Cu-30%Zn

8h cryomilled samples, and samples consolidated via room temperature ball milling and HPT were selected for microstructural studies. Figure 8.1-a presents a TEM image of the Cu-30%Zn sample produced by 8h high energy ball milling at 77K. Grain size measurement using bright field and dark field imaging techniques and diffraction patterns, lower left inset in Figure 8.1-a, revealed that the microstructure of this sample consists of fine equiaxed grains with a narrow size distribution, Figure 8.2-a, and a mean grain size of 28nm, Table 8.1. Due to the effect of grain size and the possible contribution of bimodal structures on deformation behavior, it is important to compare mechanical properties of processed samples considering the grain size distribution. Figure 8.1-b and 8.1-c show TEM images of 8h cryomilled samples consolidated by HPT deformation or room temperature ball milling. Grain size measurements on the consolidated samples proved that the average grain size of the 2h CM+4 h RT sample, 26 nm, is very close to that of the 8h cryomilled sample, 28 nm, Table 8.1. The grain size distribution of these two samples, Figure 8.2-a and 8.2-c, are also almost identical. On the other hand, the sample consolidated by HPT shows a bimodal microstructure, Figure 8.2-b, with an average grain size of 28 nm, Table 8.1. It appears that the ultrahigh strain HPT causes the nanograins, inherited from 8h cryomiling, to grow. This is similar to the reported deformation induced grain growth during HPT processing of cryomilled Cu [31], electrodeposited Ni [32] and Ni-20wt.%Fe alloy [33]. Grain rotation-induced grain coalescence is proposed to be responsible for the deformation induced grain growth at grain sizes smaller than 100 nm [31, 34] which is also the case in this report.

Wang et al. [34] discussed that the grain rotation leads to grain coalescence via decrease of the grain boundary angle or elimination of the grain boundaries. This process is initiated by gliding of grain boundary dislocations along their boundaries upon plastic deformation. Subsequent splitting of gliding grain boundary dislocations at triple junctions into two climbing grain boundary dislocations results in rotational deformation and hence this continuous process leads to coalescence of small grains into a larger grain [34].

Estimated dislocation density, ρ , and twin probability, β , by means of XRD technique are listed in Table 8.1. The 8 h cryomilled sample shows a high dislocation density of $\rho=4 \times 10^{16} \text{ m}^{-2}$ which is reduced to $\rho=0.27 \times 10^{16} \text{ m}^{-2}$ after subsequent consolidation step by HPT. This is in agreement with the observed grain growth during HPT-deformation of the cryomilled flakes, Figure 8.2-b. It seems that the coalescence of nanograins of the cryomilled sample into larger grains during HPT deformation causes the dislocation density to decrease. Rearrangement of dislocation cell/wall structure to form high angle grain boundaries could also be responsible for a drop in dislocation density. The dislocation density of the 2 h CM+4 h RT milled sample is of the same order as that of the HPT-consolidated sample. Shorter cryomilling time and temperature rise during the subsequent room temperature milling resulted in a dislocation density of $\rho=0.25 \times 10^{16} \text{ m}^{-2}$, Table 8.1. Table 8.1 shows that prolonged cryogenic severe plastic deformation of the low SFE Cu-30%Zn, 8 h cryomilled sample, provides twin probability of $\beta=3.5\%$. Low temperature processing and high frequency multidirectional impacts during the ball milling deformation together with the low SFE, 14 mJ/m² facilitate formation of the deformation twins. Subsequent ultra high strain HPT deformation resulted in a lower twin probability of $\beta=1.2\%$, Table 8.1. The 2 h CM+4 h

RT sample also shows a lower twin probability of $\beta=0.1\%$. The decreased twin probability is possibly due to the detwinning process which has been observed experimentally and reported in several papers [31, 35-40]. Further discussion on detwinning of Cu-30%Zn is given in the following sections of this paper.

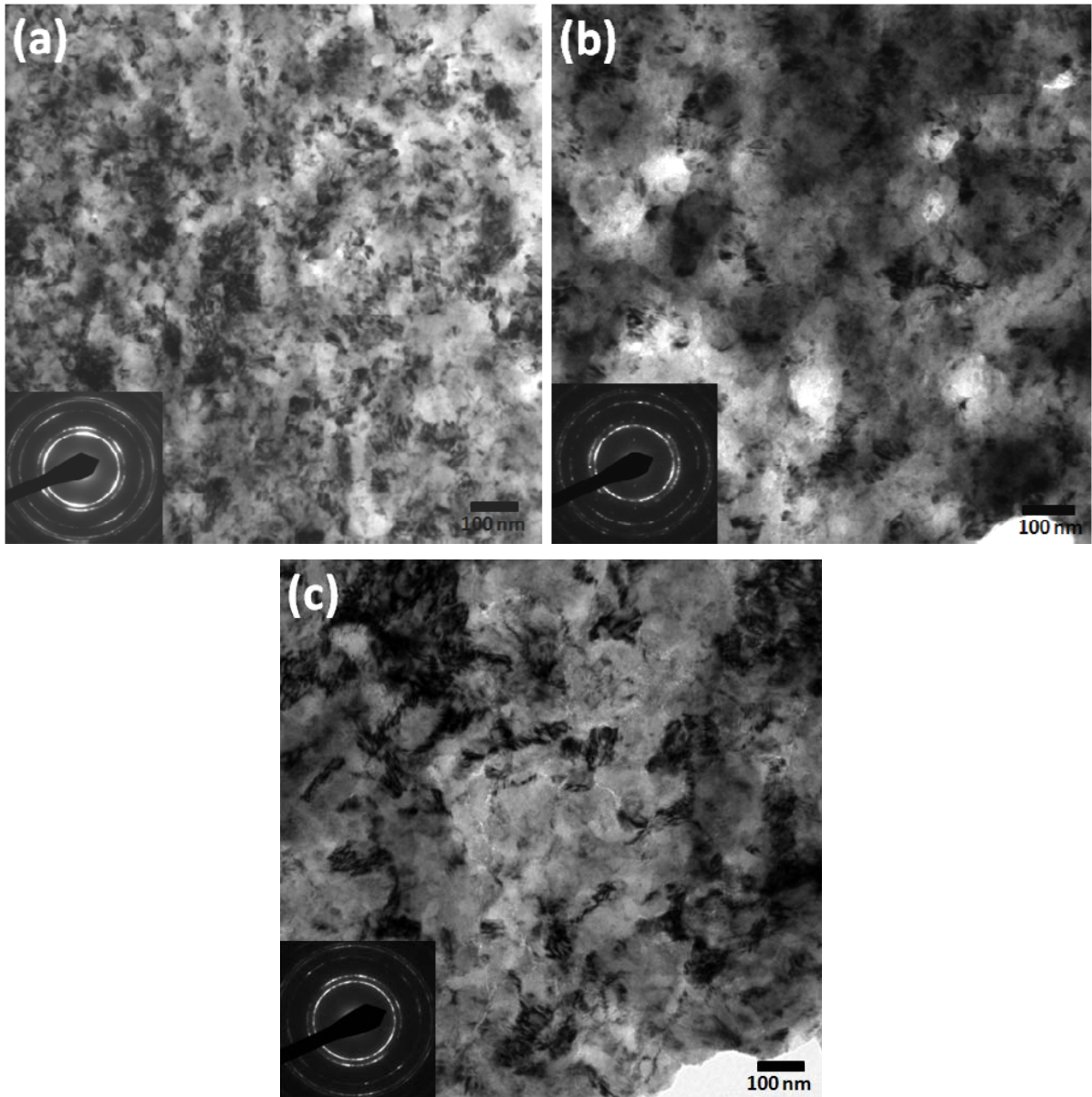


Figure 8.1- TEM images of Cu-30%Zn samples processed by a) 8h cryomilling, b) 8h cryomilling + HPT, c) 2h cryomiling+4h RT milling. Lower left insets show electron diffraction patterns.

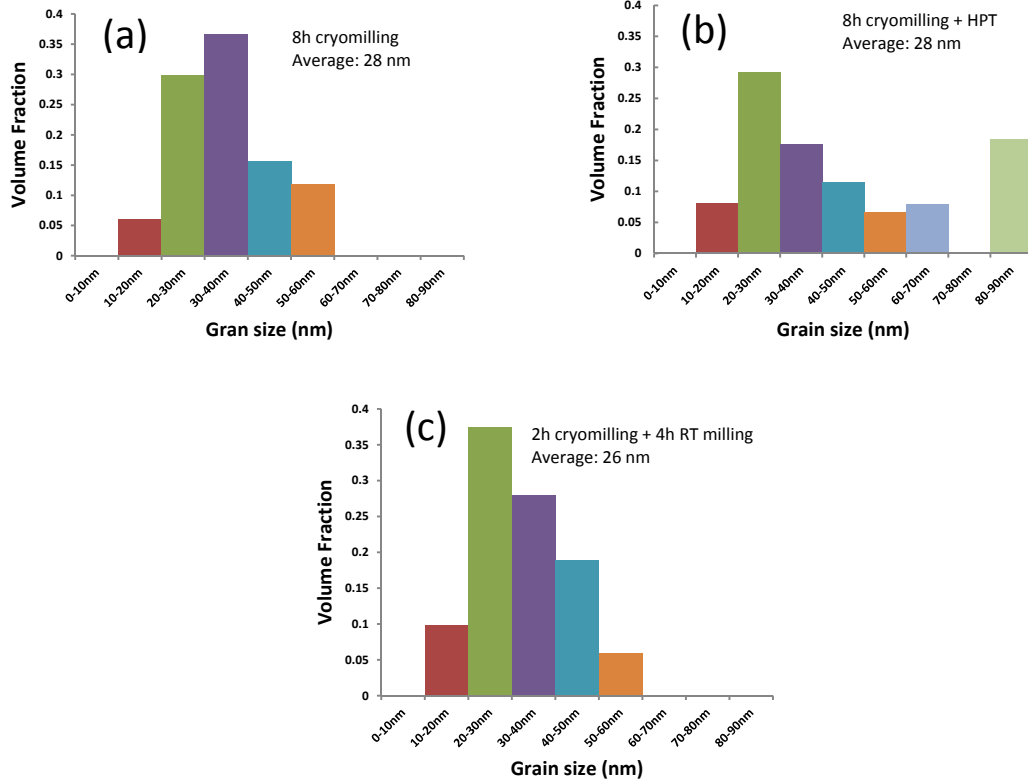


Figure 8.2- Grain size distribution obtained from bright field and dark field images for Cu-30%Zn alloy processed by a) 8h cryomilling, b) 8h cryomilling + HPT, and c) 2h cryomilling + 4h RT milling.

Table 8.1- Grain size, dislocation density (ρ) and twin probability (β) of Cu-30%Zn samples.

	Grain size (nm)	Dislocation density ($\times 10^{16} \text{ m}^{-2}$)	Twin probability (%)
8h cryomilling	28	4.0	3.5
8h cryomilling+HPT	28	0.27	1.2
2h cryomilling+4h RT milling	26	0.25	0.1

Mechanical properties of cryomilled and consolidated Cu-30%Zn

Selected samples were prepared for mechanical tests using microhardness and tensile tests. Figure 8.3 shows engineering stress-strain curves for bulk samples produced via cryomilling followed by a consolidation step using room temperature milling or ultrahigh strain HPT. The dotted line represents the estimated yield strength, σ_y , from Vickers microhardness, H_v , following the Tabor equation $\sigma_y = H_v/3$ [41], for the 8h cryomilled sample. Mechanical properties of these samples are listed in Table 8.2. As discussed earlier, TEM investigations showed a nanostructure with narrow grain size distribution in 8 h CM and 2 h CM+4 h RT samples and a bimodal distribution in 8 h CM+HPT sample, Figure 8.2. It should be noted that a high density of deformation nanotwins were observed in all TEM images, which will be addressed further in this paper. Due to limitations in grain size refinement capability, imposed mainly by severe plastic deformation techniques such as HPT or cold rolling, different grain sizes are reported in the literature at different stacking fault energies [5, 10]. For example, HPT deformation (6GPa and 5 rotations) produces grain sizes of 75nm, 50nm, and 10nm in Cu, Cu-10%Zn, and Cu-30%Zn, respectively [10]. In contrast, we successfully produced samples with the same grain size regimes to compare with the mechanical properties data available in the literature on pure copper. In this regard, the effect of a grain size mediated mechanism on mechanical properties can be clearly separated and other possible mechanisms can be studied accordingly. As an example, grain size and mechanical properties of nanocrystalline copper produced by in situ consolidation in ball milling [7] are included in Table 8.2. It is seen that depending on the processing route, different mechanical properties were obtained at the same grain size. Generally, from the low

stacking fault energy of Cu-30%Zn alloy, 14 mJ/m^2 [42], it is expected that dislocation activity via cross-slip is limited due to the wide separation between partial dislocations. Furthermore, low temperature severe plastic deformation suppresses dynamic recovery and promotes plastic deformation via twinning activity. In a study on cryomilling of Cu and Cu-Zn alloys, it was shown that a 6-8h milling at 77K results in the highest hardness and smallest grain size achievable via high energy ball milling [2]. The higher strength of ~ 970 MPa obtained in the 8h cryomilled sample is mainly attributed to the higher dislocation and twin density, Table 8.1, after prolonged processing at liquid nitrogen temperature. In the case of the sample processed by 2h CM+4h RT milling, it appears that shorter milling time at 77K followed by a consolidation step at room temperature gives rise to a lower dislocation density and twin probability, Table 8.1, which might be responsible for lower yield strength, i. e. 730 MPa, and a higher elongation to failure of 10%. This is in agreement with the Ref. [2] that a temperature increase in RT ball milling causes the dislocation density to decrease via annihilation of dislocations on grain boundaries. The 8h cryomilled sample consolidated via HPT at room temperature shows a yield strength of 930 MPa and elongation to failure of 5%. It was shown that ultra high strain applied to the cryomilled powder during HPT brings about a bimodal microstructure which in turn shows a higher uniform elongation compared to that the 2h CM+4 h RT sample.

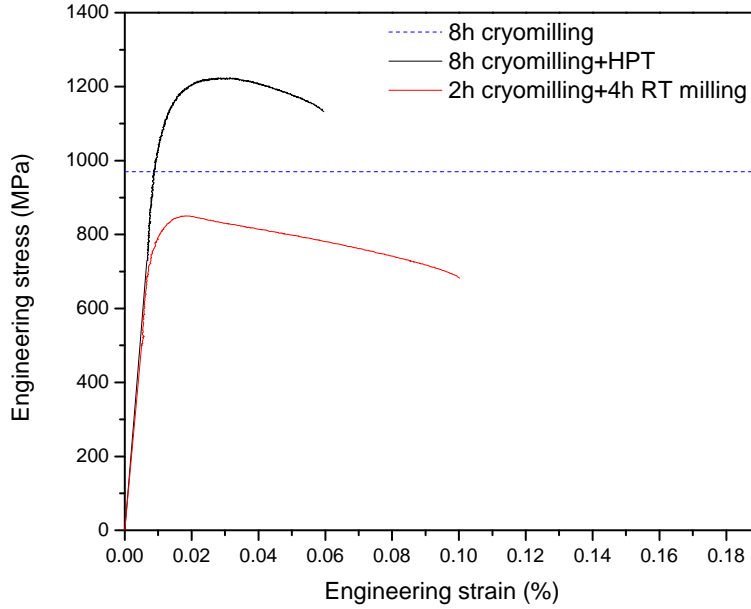


Figure 8.3- Engineering stress-strain curves for Cu-30%Zn alloy processed via cryomilling followed by consolidation by RT milling or HPT. Dashed line shows the yield strength of 8h cryomilled sample estimated from hardness measurement.

Table 8.2- Tensile properties of Cu-30%Zn and pure copper.

	Microhardness (GPa)	Yield strength (MPa)	Ultimate tensile strength (MPa)	Uniform elongation (%)	Elongation to failure (%)
Cu-30%Zn					
8h cryomilling	2.91±0.12	970*	-	-	-
8h cryomilling+HPT	3.20±0.50	930	1220	2.8	5
2h cryomilling+4h RT milling	2.50±0.14	730	850	1.8	10
Pure copper**		790	1120	14	15

* Hardness value was used to estimate yield strength, i. e. $\sigma_y = H_v/3$.

** 23 nm grains in in situ consolidated sample via high energy ball milling [7].

Breakdown of the Hall-Petch relation

In order to have a better comparison between the mechanical behavior of copper and the Cu-30%Zn alloy, a Hall-Petch plot is constructed including data from the literature on Cu and Cu-30%Zn for a wide range of grain size, Figure 8.4. Cryomilled and surfactant assisted ball milled Cu-30%Zn samples were used to collect hardness data and crystallite size and construct the Hall-Petch plot. Solid and dashed lines represent Hall-Petch lines from the literature for Cu and Cu-30%Zn, respectively ($k_{\text{Cu}}=0.11 \text{ MN/m}^{3/2}$ and $k_{\text{Cu-30\%Zn}}=0.31 \text{ MN/m}^{3/2}$) [43]. There are several reports on the breakdown of the Hall-Petch relationship at small grain sizes in Cu, Fe, Ni, and Ti [44]. Similarly, Cu-30%Zn shows a deviation from the classical Hall-Petch relation, Figure 8.4. It is seen in Figure 8.4 that at grain sizes larger than about 35nm, Cu-30%Zn shows higher hardness than copper. However, there is a significant deviation from the classic Hall-Petch relation, dashed line, when the grain size falls below ~35nm. It should be noted that this small grain size regime is attributed to samples processed by HPT [3] and ball milling, i.e. severe plastic deformation methods incorporating high strain. Data points at the small grain size regime diverge from the expected trend, dashed line, and even cut off the Hall-Petch curve of the pure copper. This deviation follows the dotted line in Figure 8.4 and as seen, the strength of the Cu-30%Zn is comparable to its Cu counterpart at the very small end of the grain size regime.

One may consider different strengthening and softening mechanisms in order to explain the reason for this unusual solid solution softening behavior. It is discussed by Shen and Koch [45] that the hardness increase due to solid solution hardening in nanocrystalline alloys is of the same magnitude as that in conventional polycrystalline alloys. Therefore,

with the same grain size (Table 8.1), the Cu-30%Zn alloy should be always at least ~80 MPa stronger than its pure copper counterpart, due to solid solution hardening [46], unless an interfering mechanism causes softening.

There are several strengthening mechanisms that determine the strength of the Cu-30%Zn alloy. Determining factors are the strengthening effect of grain boundaries, twin boundaries and stacking faults, which are expected to be abundant in Cu-30%Zn, with low SFE, 14 mJ/m², compared to pure copper with a higher SFE of 55 mJ/m² [42]. It is well known that alloying Cu with Zn facilitates twinning [47, 48]. Kibey et. al. [49, 50] have shown that twinning propensity in Cu-Al alloys is attributed not only to the intrinsic SFE but also on the dependency of the generalized planar fault energy (GPFE) to the composition. They concluded that at higher alloying content, the bonding-charge redistribution changes resulting in lower fault energy. Increased bonding charge at higher solute content correlates with decrease in fault energies and twinning stress.

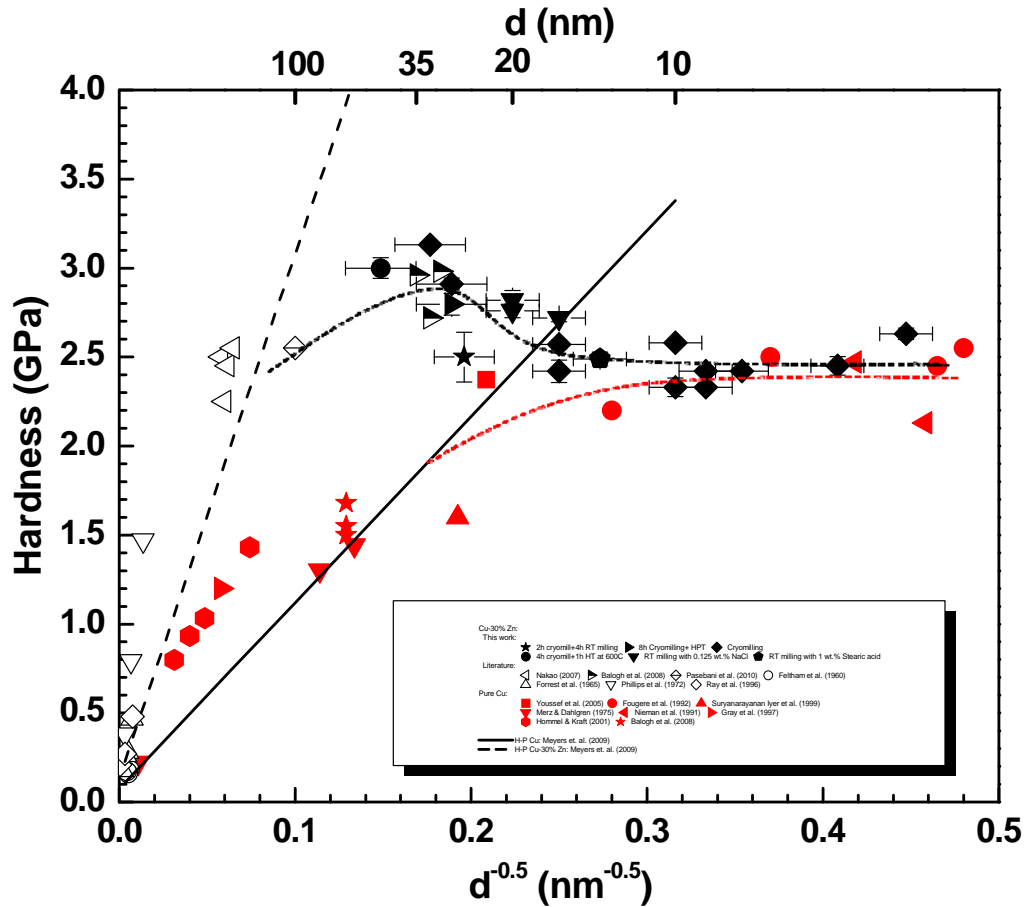


Figure 8.4- Hall-Petch plot for pure copper and Cu-30%Zn in a wide range of grain size. Solid and dashed lines represent the H-P relationship for pure copper and Cu-30%Zn from [43], respectively. It is seen that at small grain sizes, data points for Cu-30%Zn deviate from the classical H-P relationship. This deviation is shown by dotted lines. Pure copper and Cu-30%Zn data were extracted from [3, 51-58] and [3, 9, 13, 59-64], respectively.

Detwinning in Cu-30%Zn

HRTEM studies were performed on the 8h cryomilled sample consolidated by HPT to elucidate the decreased twin probability, Table 8.1, and the breakdown of the Hall-Petch relation, Figure 8.4. Figure 8.5-a shows a grain boundary with several deformation twins originating at one side from the grain boundary, marked with dotted line, and running into

the grain interior on the other side. Figure 8.5-b is a Fast Fourier Transform (FFT) processed magnified image of the region delineated by a white box in Figure 8.5-a showing several intersecting deformation nanotwins. These deformation nanotwins are finely spaced and also have a thickness of less than ~ 5 nm. Dotted lines represent twin boundaries in Figure 8.5-b. It is seen that the twin boundary **MNO** is deviated and pushed towards twin boundary **ABC** and finally eliminated at point **O** beyond which the twin planes of **ABC** twin are extended all over the microstructure. Furthermore, twin planes of the **ABC** twin (**AA'**, **BO**, etc.) are successively shrinking towards the **C** end of this twin. The partial dislocation activity, marked with “T” signs in Figure 8.5-b, is seen which is apparently responsible for elimination of the twin **ABC**. Similar distortion and elimination of twin boundaries were reported for deformation twins in HPT-deformed Cu [31], and growth twins in sputtered Cu [37]. Wang et al. [37] discussed the detwinning mechanism and concluded that the collective glide of twinning dislocations, that form incoherent twin boundaries, is responsible for detwinning. The observed detwinning in the HPT deformed sample could also contribute to the low twin probability in the 2 h CM+4 h RT milled sample, Table 8.1, which showed a lower hardness and yield strength in comparison to that of the HPT consolidated sample, Table 8.2.

Several microstructural studies have been devoted to nanotwins in copper and copper based alloys [7, 19, 25]. Dynamic plastic deformation (DPD) of Cu-32%Zn at 77K revealed that twin thickness and twin boundary spacing decrease with applied strain [6, 13]. It was also found that a twin thickness of ~ 10 nm can be obtained in the Cu-Al system by DPD as the stacking fault energy decreases to 12 mJ/m^2 [8]. Furthermore, according to Li et al. [19],

twin width decreases with decreasing grain size and, as an example, severe plastic deformation routes such as ECAP+95% rolling and conventional HPT deformation (6GPa and 5 revolutions) produce an average twin width of 12nm (Grain size=110nm) and 11nm (Grain size=70nm) in the Cu-30%Zn alloy, respectively. XRD measurements on HPT processed Cu and Cu-Zn alloys were also revealed that twinning density increases with decreased crystallite size and stacking fault energy [3]. These results are in good agreement with our observations on the higher strained Cu-30%Zn alloy processed with high energy ball milling followed by ultrahigh strain HPT that show twin widths of roughly less than 5nm in samples with much smaller grain sizes, i.e. ~28nm (Table 8.1).

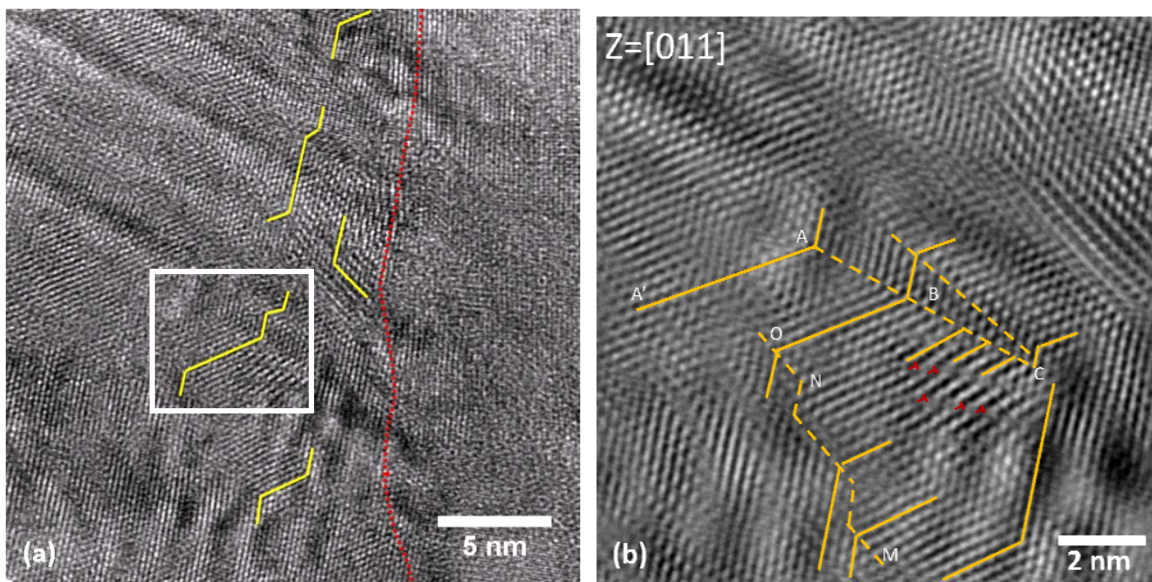
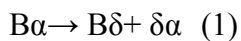


Figure 8.5– a) High resolution TEM image of Cu-30%Zn sample processed by 8h cryomilling followed by HPT consolidation at room temperature. Finely spaced deformation nanotwins are marked. The dotted line represents the grain boundary. b) FFT processed image of the region marked with white box in (a). A twin boundary decorated with dislocations is shown.

It is well known that twin boundaries can act as barriers to dislocation motion and contribute to strengthening of the material [65]. On the other hand, there are reports on the

ability of twin boundaries to generate dislocations [66]. In this regard, a higher frequency of twin boundaries in copper and austenitic stainless steel was found to decrease the yield stress [26]. The strengthening effect of twin boundaries was found to be effective down to 15nm twin thicknesses in nanotwinned copper [25]. Twin boundary mediated strengthening fades at ~15nm and nanotwin copper softens with an enhanced strain hardening and improved ductility at smaller twin thicknesses [67]. In a report on rolling of nanotwinned copper, You et al. [68] concluded that twin partial dislocation activities can result in softening of the material. MD simulations also show that twin-twin interactions can lead to loss of strength below a critical twin thickness [69]. The mechanism involved in the softening phenomenon is described as a partial dislocation emission mechanism from grain boundaries or dislocation-twin boundary reactions [40]. A detailed study on the possible reactions between twin boundaries and dislocations in fcc crystals is published by Zhu et al [70]. Among possible dislocation-twin boundary reactions in fcc crystals, cross-slip of 30° Shockly partials, $B\alpha$, into a twin boundary results in growth of twins or de-twinning, eq. (1).



This reaction, eq. (1), produces stepped twin boundaries such as those shown in Figure 8.5-b. Based on energy calculations and under the appropriate stress conditions, the stair-rod dislocation, $\delta\alpha$, resulting from the partial dislocation-twin boundary reaction, can further dissociate into two partial dislocations, eq. (2).



In this case, the de-twinning process continues until complete removal of the twin has occurred. High local stress is required to start nucleation of twinning partial dislocations. According to [40], a high density of initial dislocations and high energy grain boundaries in electrodeposited nanotwinned Cu facilitates motion and/or nucleation of twinning partial dislocations. Given the decreased twin probability in 8h cryomilled sample consolidated by HPT and the observed detwinning in HRTEM images, Figure 8.5, this might be an explanation for decreased strength in nanocrystalline Cu-30%Zn alloy in this research. It seems that highly deformed Cu-30%Zn alloy at 77K under severe multidirectional forces in ball milling enhanced formation of dense deformation twins. Also, the low SFE of 14 mJ/m² and restricted cross-slip facilitates twinning instead of dislocation activity. Considering the possible contributions from nanotwins to the strength softening, the decreased strength and breakdown of the Hall-Petch relationship can be rationalized. However, a detailed microstructure study on nanostructured Cu-30%Zn is still needed to prove the contribution of the detwinning to the deformation mechanisms and breakdown of the Hall-Petch relation at grain sizes <10nm at which grain boundary mediated deformation mechanisms may interfere with detwinning mechanisms.

8.5. Conclusion

Nanocrystalline Cu-30%Zn alloy was synthesized via high energy ball milling at 77K and room temperature. NaCl and stearic acid were used for room temperature milling to produce a range of grain sizes. Bulk artifact-free specimens with average nanograin sizes of

~26-28nm were produced through two different consolidation steps; i. e. room temperature ball milling and ultrahigh strain HPT.

It was found that HPT deformation could result in grain growth and decrease the twin probability. HRTEM investigations revealed that the detwinning process contributes to the decreased twin probability.

Microstructure-mechanical properties relationship was discussed based on the Hall-Petch relationship. Similar to the breakdown of the Hall-Petch relation in pure copper at small grain sizes, a deviation from the classical Hall-Petch relation was found in Cu-30%Zn. Considering the low SFE of this composition, 14 mJ/m^2 , and also the HRTEM studies that show a high density of finely spaced deformation nanotwins, we attributed the observed softening behavior and breakdown of the Hall-Petch relation to a detwinning process. Further microstructural studies are suggested to investigate this phenomenon at grain sizes $<10\text{nm}$.

8.6. References

- [1] S. Asgari, E. ElDanaf, S.R. Kalidindi, R.D. Doherty, Metall. Mater. Trans. A, 28 (1997) 1781-1795.
- [2] H. Bahmanpour, K. Youssef, R. Scattergood, C. Koch, J. Mater. Sci., (2011) 1-7.
- [3] U.T. Balogh L, Zhao Y, Zhu YT, Horita Z, Xu C, Langdon TG Acta Mater., 56 (2008) 809-820.
- [4] F.I. Grace, M.C. Inman, Metallography, 3 (1970) 89-98.

- [5] X.Y. San, X.G. Liang, L.P. Chen, Z.L. Xia, X.K. Zhu, *Mater. Sci. Eng., A*, 528 (2011) 7867-7870.
- [6] G.H. Xiao, N.R. Tao, K. Lu, *Scripta Mater.*, 59 (2008) 975-978.
- [7] K. Youssef, M. Sakaliyska, H. Bahmanpour, R. Scattergood, C. C. Koch, *Acta Mater.*, 59 (2011) 5758-5764.
- [8] Y. Zhang, N.R. Tao, K. Lu, *Scripta Mater.*, 60 (2009) 211-213.
- [9] Y.H. Zhao, X.Z. Liao, Z. Horita, T.G. Langdon, Y.T. Zhu, *Mater. Sci. Eng., A*, 493 (2008) 123-129.
- [10] Y.H. Zhao, X.Z. Liao, Y.T. Zhu, Z. Horita, T.G. Langdon, *Mater. Sci. Eng., A*, 410 (2005) 188-193.
- [11] Y.H. Zhao, Y.T. Zhu, X.Z. Liao, Z. Horita, T.G. Langdon, *Appl. Phys. Lett.*, 89 (2006) 121906.
- [12] Y.H. Zhao, Y.T. Zhu, X.Z. Liao, Z.J. Horita, T.G. Langdon, *Mater. Sci. Eng., A*, 463 (2007) 22-26.
- [13] G.H. Xiao, N.R. Tao, K. Lu, *Mater. Sci. Eng., A*, 513-14 (2009) 13-21.
- [14] Z.J. Zhang, Q.Q. Duan, X.H. An, S.D. Wu, G. Yang, Z.F. Zhang, *Mater. Sci. Eng., A*, 528 (2011) 4259-4267.
- [15] Y.H. Zhao, Z. Horita, T.G. Langdon, Y.T. Zhu, *Mater. Sci. Eng., A*, 474 (2008) 342-347.
- [16] X.H. An, Q.Y. Lin, S.D. Wu, Z.F. Zhang, R.B. Figueiredo, N. Gao, T.G. Langdon, *Scripta Mater.*, 64 (2011) 249-252.

- [17] H. Bahmanpour, A. Kauffmann, M.S. Khoshkhoo, K.M. Youssef, S. Mula, J. Freudenberger, J. Eckert, R.O. Scattergood, C.C. Koch, Mater. Sci. Eng., A, *In Press* (2011).
- [18] W.Z. Han, Z.F. Zhang, S.D. Wu, S.X. Li, Philos. Mag., 88 (2008) 3011-3029.
- [19] Y. Li, Y.H. Zhao, W. Liu, C. Xu, Z. Horita, X.Z. Liao, Y.T. Zhu, T.G. Langdon, E.J. Lavernia, Mater. Sci. Eng., A, 527 (2010) 3942-3948.
- [20] H. Bahmanpour, A. Kauffmann, M.S. Khoshkhoo, K.M. Youssef, S. Mula, J. Freudenberger, J. Eckert, R.O. Scattergood, C.C. Koch, Mater. Sci. Eng., A.
- [21] C.C. Koch, J. Narayan, Mat. Res. Soc. Symp., 634 (2001).
- [22] B. Cai, Q.P. Kong, L. Lu, K. Lu, Scripta Mater., 41 (1999) 755-759.
- [23] H. Conrad, J. Narayan, Scripta Mater., 42 (2000) 1025-1030.
- [24] O. Vohringer, Zeitschrift Fur Metallkunde, 67 (1976) 518-524.
- [25] L. Lu, X. Chen, X. Huang, K. Lu, Science, 323 (2009) 607-610.
- [26] K. Konopka, J. Mizera, J.W. Wyrzykowski, Journal of Materials Processing Technology, 99 (2000) 255-259.
- [27] I. Shabib, R.E. Miller, Acta Mater., 57 (2009) 4364-4373.
- [28] H. Mirkhani, S.P. Joshi, Acta Mater., 59 (2011) 5603-5617.
- [29] X.Y. Li, Y.J. Wei, L. Lu, K. Lu, H.J. Gao, Nature, 464 (2010) 877-880.
- [30] L.L. Dao, Y.F. Shen, S. Suresh, Acta Mater., 54 (2006).
- [31] E.J. Lavernia, H.M. Wen, Y.H. Zhao, Y. Li, O. Ertorer, K.M. Nesterov, R.K. Islamgaliev, R.Z. Valiev, Philos. Mag., 90 (2010) 4541-4550.
- [32] X.Z. Liao, A.R. Kilmametov, R.Z. Valiev, H.S. Gao, X.D. Li, A.K. Mukherjee, J.F. Bingert, Y.T. Zhu, Appl. Phys. Lett., 88 (2006) 021909.

- [33] Y.B. Wang, J.C. Ho, X.Z. Liao, H.Q. Li, S.P. Ringer, Y.T. Zhu, *Appl. Phys. Lett.*, 94 (2009).
- [34] Y.B. Wang, B.Q. Li, M.L. Sui, S.X. Mao, *Appl. Phys. Lett.*, 92 (2008).
- [35] Y.B. Wang, M.L. Sui, E. Ma, *Phil. Mag. Lett.*, 87 (2007) 935-942.
- [36] L. Li, T. Ungar, Y.D. Wang, J.R. Morris, G. Tichy, J. Lendvai, Y.L. Yang, Y. Ren, H. Choo, P.K. Liaw, *Acta Mater.*, 57 (2009) 4988-5000.
- [37] J. Wang, N. Li, O. Anderoglu, X. Zhang, A. Misra, J.Y. Huang, J.P. Hirth, *Acta Mater.*, 58 (2010) 2262-2270.
- [38] S.Y. Hu, C.H. Henager, L.Q. Chen, *Acta Mater.*, 58 (2010) 6554-6564.
- [39] N. Li, J. Wang, J.Y. Huang, A. Misra, X. Zhang, *Scripta Mater.*, 64 (2011) 149-152.
- [40] Y. Wei, *Mater. Sci. Eng., A*, 528 (2011) 1558-1566.
- [41] D. Tabor, *The hardness of metals*, Clarendon Press, Oxford, 1951.
- [42] P.C.J. Gallagher, *Metall. Trans.*, 1 (1970) 2429-2461.
- [43] M.A. Meyers, K.K. Chawla, *Mechanical behavior of materials*, 2nd ed., Cambridge University Press, Cambridge ; New York, 2009.
- [44] M.A. Meyers, A. Mishra, D.J. Benson, *Prog. Mater. Sci.*, 51 (2006) 427-556.
- [45] T.D. Shen, C.C. Koch, *Acta Mater.*, 44 (1996) 753-761.
- [46] D.R. Askeland, *The Science and engineering of materials : sixth edition*, International Ed. ed., Cengage Learning, Mason, OH, 2010.
- [47] M.A. Meyers, O. Vohringer, V.A. Lubarda, *Acta Mater.*, 49 (2001) 4025-4039.
- [48] J.W. Christian, S. Mahajan, *Prog. Mater. Sci.*, 39 (1995) 1-157.
- [49] S. Kibey, J.B. Liu, D.D. Johnson, H. Sehitoglu, *Appl. Phys. Lett.*, 89 (2006) 191911.

- [50] S.A. Kibey, L.L. Wang, J.B. Liu, H.T. Johnson, H. Sehitoglu, D.D. Johnson, *Physical Review B*, 79 (2009) 214202.
- [51] K.M. Youssef, R. O. Scattergood, K. L. Murty, J. A. Horton, C. C. Koch, *Appl. Phys. Lett.*, 87 (2005) 0919041.
- [52] J. Chen, L. Lu, K. Lu, *Scripta Mater.*, 54 (2006) 1913-1918.
- [53] R. Suryanarayanan Iyer, C.A. Frey, S.M.L. Sastry, B.E. Waller, W.E. Buhro, *Materials Science and Engineering A*, 264 (1999) 210-214.
- [54] P.G. Sanders, J.A. Eastman, J.R. Weertman, *Acta Mater.*, 45 (1997) 4019-4025.
- [55] Y.T. Zhu, H.G. Jiang, D.P. Butt, I.V. Alexandrov, T.C. Lowe, *Mater. Sci. Eng., A*, 290 (2000) 128-138.
- [56] S.R. Agnew, B.R. Elliott, C.J. Youngdahl, K.J. Hemker, J.R. Weertman, *Mater. Sci. Eng., A*, 285 (2000) 391-396.
- [57] G.T. Gray, T.C. Lowe, C.M. Cady, R.Z. Valiev, I.V. Aleksandrov, *Nanostructured Materials*, 9 (1997) 477-480.
- [58] M. Haouaoui, I. Karaman, H.J. Maier, K.T. Hartwig, *Metall. Mater. Trans. A*, 35A (2004) 2935-2949.
- [59] Nakao, *Mater. Sci. Forum*, 558-559 (2007).
- [60] S. Pasebani, M.R. Toroghinejad, *Mater. Sci. Eng., A*, 527 (2010) 491-497.
- [61] P. Feltham, G.J. Copley, *Acta Metall.*, 8 (1960) 542-550.
- [62] P.G. Forrest, A.E.L. Tate, *Journal of the Institute of Metals*, 93 (1965) 438-444.
- [63] W.L. Phillips, *Armstrong*, *Metall. Trans.*, 3 (1972) 2571-2577.
- [64] K.K. Ray, K. Chakraborty, *J. Mater. Sci. Lett.*, 15 (1996) 727-730.

- [65] Y.B. Wang, B. Wu, M.L. Sui, *Appl. Phys. Lett.*, 93 (2008).
- [66] T. Malis, K. Tangri, D.J. Lloyd, *Philos. Mag.*, 26 (1972) 1081-&.
- [67] L. Lu, K. Lu, STRENGTHENING MECHANISM OF NANO-SCALE TWINS, in: J.C. Grivel, N. Hansen, X. Huang, D.J. Jensen, O.V. Mishin, S.F. Nielsen, W. Pantleon, H. Toftegaard, G. Winther, T. Yu (Eds.) *Nanostructured Metals: Fundamentals to Applications*, Riso Natl Laboratory, Roskilde, 2009, pp. 101-116.
- [68] Z.S. You, L. Lu, K. Lu, *Scripta Mater.*, 62 (2010) 415-418.
- [69] Y. Kulkarni, R.J. Asaro, *Acta Mater.*, 57 (2009) 4835-4844.
- [70] Y.T. Zhu, X.L. Wu, X.Z. Liao, J. Narayan, L.J. Kecskes, S.N. Mathaudhu, *Acta Mater.*, 59 (2011) 812-821.

CHAPTER NINE

9.0. EFFECT OF STACKING FAULT ENERGY ON DEFORMATION BEHAVIOR OF CRYO ROLLED COPPER AND COPPER ALLOYS

H. Bahmanpour, A. Kauffmann, M. S. Khoshkhoo, K. M. Youssef, S. Mula, J. Freudenberger, J. Eckert, R. O. Scattergood, C. C. Koch

Materials Science and Engineering: A, 2011. Vol. 529, pp. 230-236.

9.1. Abstract

Pure copper and Cu-12.1at.%Al-4.1at.%Zn alloy were subjected to rolling in liquid nitrogen. TEM studies showed that dynamic recovery during the deformation process was effectively suppressed and hence microstructures with dislocation substructure and deformation twins were formed. Mechanical properties were assessed via microtensile testing that shows improved yield strength, 520 ± 20 MPa, and ductility, 22%, in the case of pure copper. Alloying with Al and Zn results in reduction in stacking fault energy (SFE) which can contribute to enhanced strength and good ductility. Physical activation volume obtained via stress relaxation tests is $26b^3$, and $8b^3$ for pure copper, and Cu-12.1at.%Al-4.1at.%Zn, respectively. The effect of SFE on work hardening rate of samples is discussed. Although twinning is observed in the alloy, it is concluded that network dislocation strengthening plays the major role in determining the mechanical properties.

9.2. Introduction

Deformation mechanisms of ultrafine and nanocrystalline metals and alloys have been studied extensively to understand the superior mechanical properties of these materials compared to their microcrystalline counterparts. These studies have shown that grain boundaries can act as barriers to dislocation motion and bring about substantial increase in strength [1, 2]. Likewise, twin boundaries of deformation and growth twins can also obstruct dislocation motion and enhance mechanical properties [3]. Samples tailored with annealing or deformation twins have been reported to show higher strength compared to twin-free or microstructures with a low density of twins, e. g. 900MPa for yield strength in electrodeposited nano-twinned copper films with grain size of 400-600 nm and twin thickness of 15nm [4, 5]. Since typically a decrease in grain size and increase in strength is accompanied by loss of ductility, several researchers attempted to promote twin activity in nanostructures to obtain a material with both high strength and ductility, simultaneously [4, 6].

Ultrafine and nanocrystalline copper and copper alloys with twinned grains are produced by different approaches; 1) formation of growth twins through methods such as electrodeposition [4] or inert gas condensation [7], and 2) promoting deformation twins by either low temperature processing [8-10] or decreased stacking fault energy (SFE) via alloying combined with cold work [6, 11]. In coarse grained copper the Hall-Petch slope for twinning is larger than for slip, $k_{\text{twin}}=21.6 \text{ MPa}\cdot\text{mm}^{1/2}$ and $k_{\text{slip}}=5.4 \text{ MPa}\cdot\text{mm}^{1/2}$, respectively, and hence dislocation slip is the preferred deformation mode when grains are small [12]. In nano regime deformation twinning has been predicted by molecular dynamics in

nanocrystalline Al [13], Ni [14], and Cu [15]. Experimental observations by microscopy also showed deformation twinning in pure copper samples processed by HPT [16] and copper single crystal processed by ECAP [17]. Unfortunately, due to lack of data on mechanical properties of ultrafine/nanocrystalline Cu and Cu alloys containing deformation twins processed by severe plastic deformation methods, a conclusive assessment on the role of deformation twins in mechanical behavior of Cu and Cu alloys is not available.

Several processing parameters can be identified for improved mechanical properties. Typical manufacturing routes that can scale-up for industrial purposes such as rolling were reported to produce pure copper samples with yield strength of less than 450 MPa and 18% elongation to failure, e.g. cold rolling at room temperature with samples cooled down in liquid nitrogen between passes [9]. Short time post-processing annealing to enhance ductility results in loss of strength in pure copper, e. g. yield strength of 420MPa and elongation to failure of 26% for 93% cold work followed by annealing at 180°C for 3min [9]. On the other hand, processes such as inert gas condensation or electrodeposition can be used to produce samples with controlled microstructure tailored with twins [4, 7, 18]. Although these processes can produce samples with high yield strength of 900 MPa with ductility of 7.5%, the produced samples have micron range thicknesses [4]. The highest achieved yield strength reported on bulk nanostructured copper is 790 MPa obtained by means of in situ consolidation in ball milling that shows 14% elongation to failure [19]. Processing temperature plays an important role in evolution of microstructure and it has been shown that twinning activity is sensitive to processing temperature and deformation twinning is more pronounced when the temperature is less than 100K [12, 20]. The twinning start temperature

is also reported to decrease as the grain size decreases [12]. Dynamic plastic deformation at low temperature was shown to produce pure copper samples with a yield strength of 600 MPa and 11% elongation to failure [10]. Decreased deformation temperature results in suppression of dynamic recovery, higher dislocation density, promotion of twin activity, and hence higher strength accompanied by good ductility.

Reduced stacking fault energy also hinders dislocation slip in favor of twinning and is reported to improve work hardening rates and cause simultaneous increase in strength and ductility [21]. Since the obtainable minimum grain size is proportional to stacking fault energy, low stacking fault energy provides better grain refinement and enhanced mechanical properties compared to high SFE alloys [22, 23].

The motivation of this research is to control composition and processing parameters to improve microstructure and mechanical properties of copper and copper alloys. Pure copper and Cu-12.1at.%Al-4.1at.%Zn with low stacking fault energy were subjected to rolling in liquid nitrogen. Improved yield strength accompanied by significant ductility was obtained in as-deformed samples. Stress relaxation testing was performed on as-rolled samples and possible deformation mechanisms were discussed accordingly.

9.3. Experimental procedure

Pure copper and Cu-12.1%Al-4.1%Zn samples (all compositions are in atomic percent) with stacking fault energy of 55 [24], and 7 mJ/m², respectively, were prepared by casting in an induction furnace. The ternary alloy is especially designed to achieve minimum

stacking fault energy in copper rich alloys. Stacking fault energy of the ternary alloy was calculated using the following relation and available data on the stacking fault energy of binary alloys [25].

$$\frac{\gamma - \gamma_{Cu-Al}}{\gamma_{Cu-Zn} - \gamma_{Cu-Al}} = \frac{C_a - (Al)_E}{(Zn)_E - (Al)_E}$$

where, γ_{Cu-Al} and γ_{Cu-Zn} are stacking fault energies for binary alloys with the same electron/atom ratio as the ternary solid solution and with the respective atomic fraction contents $(Al)_E$ and $(Zn)_E$. C_a is the total atomic fraction of solute content.

In order to homogenize the composition, samples were kept at 800°C for 14h under argon. Hot rolling was done by pre-heating to 600°C and rolling from 25mm to 20.5mm to remove the cast microstructure. Another homogenization step was done at 800°C for 14h under argon atmosphere and subsequent water quenching to avoid short range ordering. The samples exhibit grain sizes of several hundred micrometers, and approximately random distribution of grain orientations. Samples measuring 10mmx10mmx10mm were cut from hot-rolled ingots and soaked in liquid nitrogen to reach the 77K. In order to effectively suppress dynamic recovery and recrystallization during the deformation process, the rolling setup was modified to keep the working zone of the rollers in the liquid nitrogen; hence samples were in liquid nitrogen before, during, and after rolling. This minimizes possible pre-deformation temperature increase that may cause dynamic recovery of defects and possible formation of recrystallized grains. Samples were subjected to consecutive rolling

passes until they reach their limit of deformation. All compositions were rolled to about 90% reduction in area, i. e. final thickness of ≈ 0.6 mm.

A microtensile test machine was used for tensile tests on miniaturized samples at a constant strain rate of $9.4 \times 10^{-4} \text{ s}^{-1}$ at ambient temperature. Stress relaxation testing was also done using this tensile test setup. PM2K software [26] was used to analyze XRD profiles and estimate the dislocation density of the deformed samples. Thin samples were prepared using a Fischione twin-jet electropolisher at low temperature (-30°C) with methanol+30% HNO_3 and a JEOL 2000 transmission electron microscope was used to analyze the microstructure of the rolled materials.

9.4. Results and discussion

Figure 9.1 shows the engineering stress-strain curve for as-rolled copper and copper alloy. Stacking fault energies of samples and tensile properties are listed in Table 9.1. Tensile curves show limited uniform elongation, Table 9.1, and peak immediately after yielding. This suggests that cross-slip or climb of dislocations responsible for dynamic recovery is suppressed effectively during the deformation process. Work hardening that is controlled by dislocation activity is limited due to high dislocation density in these samples caused by severe plastic deformation at 77K. As the samples were kept in the liquid nitrogen during the rolling process, the chance of dynamic recovery is minimized and fewer grains capable of handling plastic deformation via dislocation activity are available which results in low

uniform elongation and early plastic instability, as also observed in other researches on ultrafine and nanocrystalline copper [9, 27].

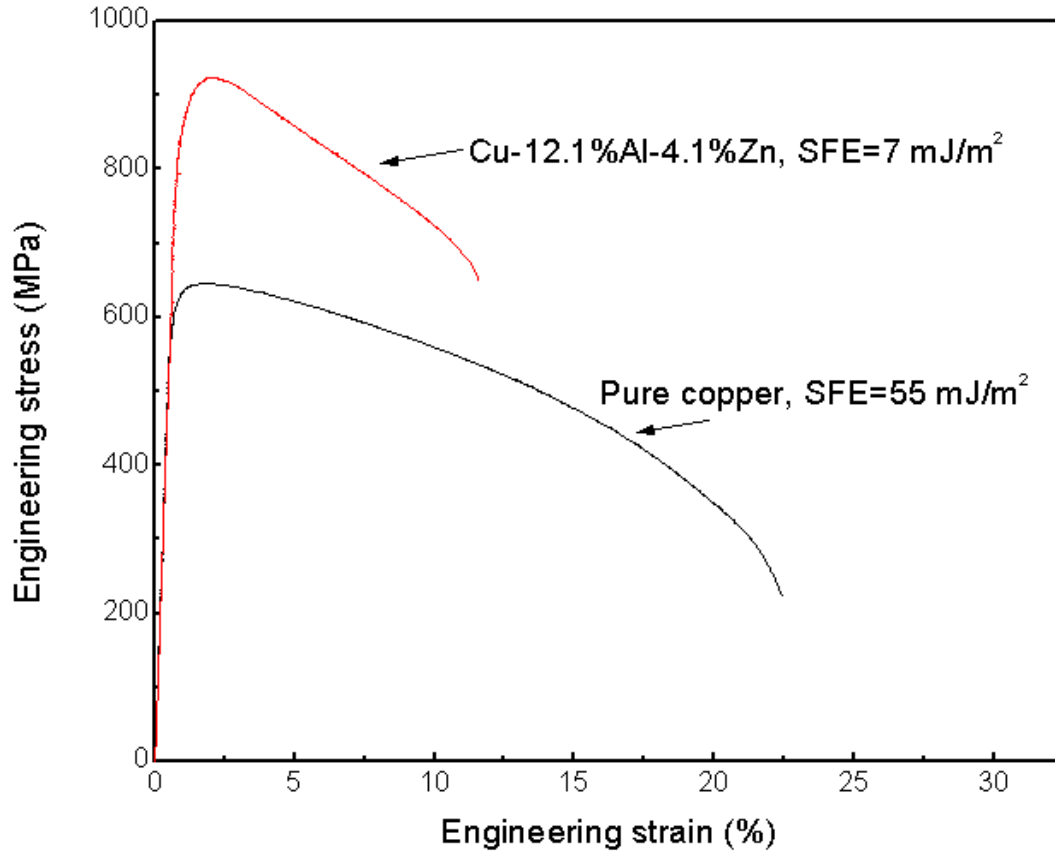


Figure 9.1- Stress-strain curve for pure copper and Cu-12.1%Al-4.1%Zn alloy rolled at 77K.

Table 9.1- Stacking fault energy and tensile properties of pure copper and Cu-12.1%Al-4.1%Zn alloy rolled at 77K.

	SFE (mJ/m ²)	Yield strength (MPa)	Ultimate tensile strength (MPa)	Elongation to failure (%)	Uniform elongation (%)
Pure copper	55	520±20	650±17	22	1.3
Cu-12.1%Al-4.1%Zn	7.0	790±21	970±19	11	1.1

A wide range of ductility and strength can be produced using different processing routes and post-processing treatments on pure copper. It is well known that while the grain size is reduced, strength increases at the expense of ductility. High strength and good ductility for pure copper have been reported by several researchers [4, 7, 9-11, 19, 28] utilizing different top-down and bottom-up approaches for synthesizing ultrafine and nanocrystalline materials [29]. The important role of processing temperature on the mechanical properties of pure copper in our research is reflected as high value for yield strength, 520 ± 20 MPa, together with ductility to failure of 22%. Table 9.2 summarizes the work that has been done on pure copper to enhance mechanical properties via different methods; - severe plastic deformation routes to induce high strains and decrease grain size and – processes such as inert gas condensation and electrodeposition to control twin thickness and density. Considering the industrial scaling up capability and improvement gained in strength and ductility, it can be seen that rolling in liquid nitrogen is a promising method to produce materials with improved properties.

Table 9.2- Microstructure and tensile properties of nanocrystalline and ultrafine grained pure copper samples processed with different routes.

Processing	Microstructure	Yield strength (MPa)	Elongation to failure (%)	Reference
<i>Rolling in liquid nitrogen</i>				
90% cold work	Heavily deformed microstructure with some nanocrystalline and ultrafine grains	520±20	22	This work
<i>Room temperature rolling, sample soaked in liquid nitrogen between rolling passes</i>				
93% cold work	Heavily deformed microstructure and 200nm grains	~450	~18	[9]
93% cold work+180°C for 3 min	Micron sized grains with a matrix of nano and ultrafine grains (<300 nm)	~420	~26	[9]
<i>Equal channel angular press</i>				
16 passes of ECAP	Ultrafine-grained structure having a mean grain size of about 100 nm	~380	~50	[27]
<i>Inert gas condensation</i>				
	20-30 nm grains	450-600	2-3	[7]
<i>Pulsed electrodeposition</i>				
	400-600 nm grains and twin thickness of 15 nm	~900	~7.5	[4]
<i>In situ consolidation via ball milling</i>				
	23 nm grains	~790	~14	[19]
<i>High pressure torsion (HPT)+ cold rolling</i>				
	180 nm grains	~420	~5.1	[11]
<i>Dynamic plastic deformation</i>				
	Heavily deformed microstructure	~600	~11	[10]

Tensile test curve for Cu-12.1%Al-4.1%Zn alloy, in Figure 9.1, demonstrates the important role of stacking fault energy and solid solution hardening on the mechanical

properties. Compared to pure copper, when SFE is reduced to 7 mJ/m^2 yield strength is increased by $\sim 270 \text{ MPa}$ which is related to the combined effect of solid solution hardening and reduction in SFE. As SFE is lowered, dislocation activity via cross-slip becomes more restricted and twinning activity is promoted. Alloying with Al and Zn involves loss of ductility from 22% in pure copper to 11% in Cu-12.1%Al-4.1%Zn. It appears that hardening and loss of ductility in Cu-12.1%Al-4.1%Zn is related to different deformation mechanisms that can control the mechanical behavior of the alloy compared to pure copper.

To further investigate the deformation mechanisms in cryo-rolled samples, the physical activation volume was determined using stress relaxation tests. Details on the stress relaxation test and its related calculations can be found in [30, 31]. Figure 9.2 shows stress relaxation curves obtained during the tensile tests. Slowing down of the relaxation along each series is due to the decrease in mobile dislocation density. Physical activation volumes of $26b^3$ and $8b^3$, Table 9.3, were calculated for pure copper and Cu-12.1%Al-4.1%Zn, respectively. Nanocrystalline fcc materials have small activation volumes due to the high percentage of grain boundaries and more interaction between dislocations. Using nanoindentation tests, Lu et al. [5] obtained $12b^3$ and $22b^3$ for nanotwinned copper with high and low twin density, respectively. Wei et al. [32] obtained $48b^3$ for the cold-deformed copper and $41b^3$ for the ECAPed and cold rolled copper, respectively. Guduru et al. reported activation volume of $20b^3$ for electrodeposited nanocrystalline Cu with average grain size of 74 nm [33]. They concluded that this activation volume reflects dislocation-based plasticity in nanocrystalline copper. It is important to note that although reported values from literature on V^* can be compared to discuss the deformation mechanisms and capacity of different

samples for dislocation activity, the microstructure of the samples produced via different processing routes have intrinsic differences.

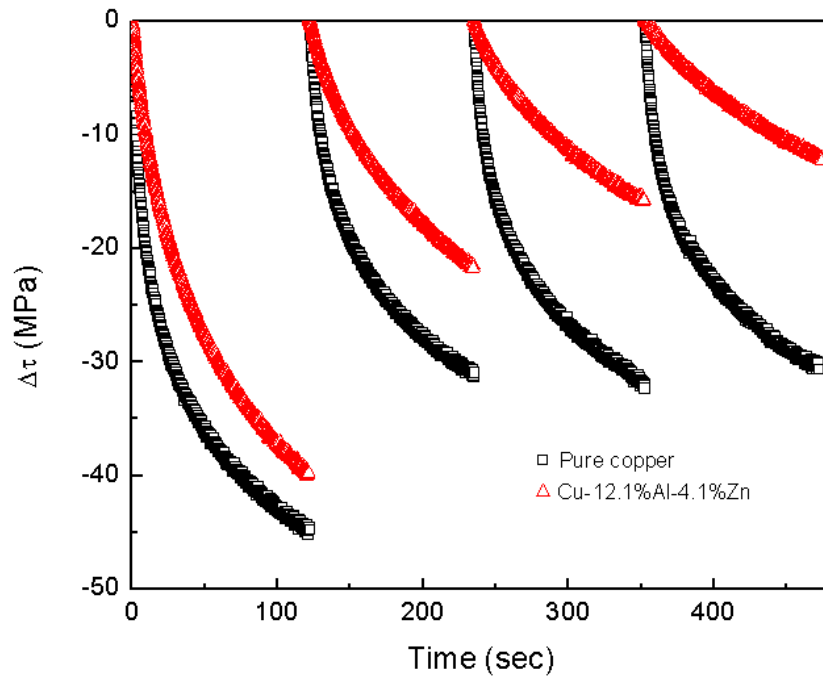


Figure 9.2- Stress relaxation curves for pure copper and Cu-12.1%Al-4.1%Zn.

Table 9.3- Values of spacing between network dislocations and solute atoms, dislocation densities and predicted and measured yield strength.

	V^* Physical activation volume (b^3)	L spacing between network dislocations (nm)	L spacing between solute atoms (nm)	ρ dislocation density by XRD (m^{-2})	$\sigma_{dislocation}$, dislocation network strength (MPa)	$\sigma_{exp.}$ measured yield strength (MPa)
Pure copper	26	6.8	-	1.9×10^{16}	540	520±20
Cu-12.1%Al- 4.1%Zn	8.0	4.8	0.45	4.3×10^{16}	720	790±21

In the case of Cu-12.1%Al-4.1%Zn, the physical activation volume of $8b^3$ shows the considerable effect of chemical composition and hence reduced stacking fault energy on activation volume. Small values of activation volume are typically considered as a sign of different deformation mechanism. Dislocation mediated deformation processes in coarse-grained metals have activation volumes on the order of $800-1000b^3$ [34]. Chen [35] suggested that for nc Cu with grain size of 10nm the activation volume of $8b^3$ shows an enhanced contribution of grain boundary diffusion related activities, but they are not the dominating mechanisms for plastic flow even at such small grain sizes. The mechanistic model based on emission of dislocations at a stress concentration at grain boundaries by Asaro and Suresh [34] suggests reduction of V^* with grain size down to $3-10b^3$. Travel distance and dislocation length are very small in nanograins and can result in small values for V^* . Asaro et al. [36] explored the contribution of nanotwins to the high strength and good ductility of nanotwinned copper via a model analysis of dislocation interaction with twin boundaries. They reported that cross-slip that leads to the absorption and transmission of slip through twin boundaries causes high strength and rate sensitivity. The contribution of nanotwins in ultrafine grains is also known to decrease the activation volume as compared to the values observed in microcrystalline metals [5].

In order to interpret tensile properties and activation volume of deformed samples, one should consider the configuration of defects and grain boundaries in processed samples. As can be seen in Figure 9.3-a, as-rolled copper has a severely deformed microstructure with highly dislocated areas in dark contrast. Except for a few grains, the rest of microstructure doesn't have well-defined grain boundaries. Deformation twins can be seen in some ultrafine

grains, which show that decreased processing temperature resulted in twinning activity. As an example, Figure 9.3-b shows an ultrafine grain containing a stack of deformation twins, marked with arrows. Evolution of ultrafine grains and twin activity are significant features of the pure copper sample. Strain-induced ultrafine grain evolution was observed in pure copper samples processed by multidirectional forging at 195K [37]. As our samples were also deformed in liquid nitrogen, it can be concluded that ultrafine grain formation is not related to thermally-activated dynamic recrystallization, and is caused by stress-induced evolution of grains. Although deformation twins can be formed via the pole mechanism due to low temperature processing [3], the grains present also provide preferred nucleation sites for deformation twins via emission of partial dislocations as suggested by Liao et al. [16]. Considering the role of different barriers to dislocation motion, i. e. grain boundaries and twin boundaries, a small value of activation volume for pure copper can be rationalized. As also reported by Zhao et al. [10] on pure copper samples processed at low temperature using dynamic plastic deformation, the contribution of grain boundary strengthening appears to be negligible despite the fact that some ultrafine grains present may be due to stress-induced recrystallization. Since grain boundaries are not well developed in the as-rolled condition, they cannot impede dislocation motion effectively. On the other hand, both TEM images, Figure 9.3, and XRD results, Table 9.3, show a high density of dislocations in the microstructure that can contribute to the small activation volume and the obtained yield strength of pure copper. Although deformation twins were observed in the microstructure of the pure copper sample, their presence is not significant and shouldn't have a major contribution to the strengthening and deformation mechanism of the as-rolled copper.

Therefore, it is assumed that high dislocation density can result in activation volume of $26b^3$ observed. This interpretation is further justified in next section using the network dislocation strengthening model.

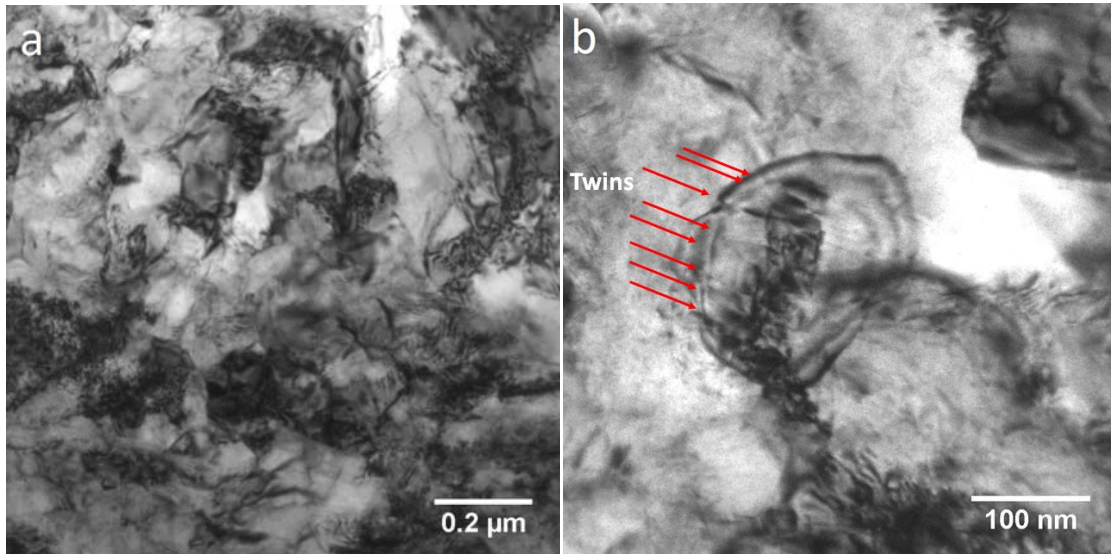


Figure 9.3- TEM micrograph of pure copper sample rolled at 77K. a) heavily deformed microstructure with few ultrafine grains, b) stack of deformation twins in an ultrafine grain.

In contrast to the microstructure of pure copper, dislocation walls formed via planar slip due to restricted cross slip in Cu-12.1%Al-4.1%Zn as a result of low SFE, 7 mJ/m^2 , and significant twinning activity is also observed, Figure 9.4. Decreased SFE promotes twinning and twin boundaries can potentially act as barriers to dislocation motion. Therefore, it is anticipated that reduction in SFE brings about more deformation twinning activity in the microstructure and more restricted dislocation activity. It should be pointed out that deformation twins are not homogeneously distributed all over the microstructure and the average twin spacing is $\approx 13 \text{ nm}$ for Cu-12.1%Al-4.1%Zn.

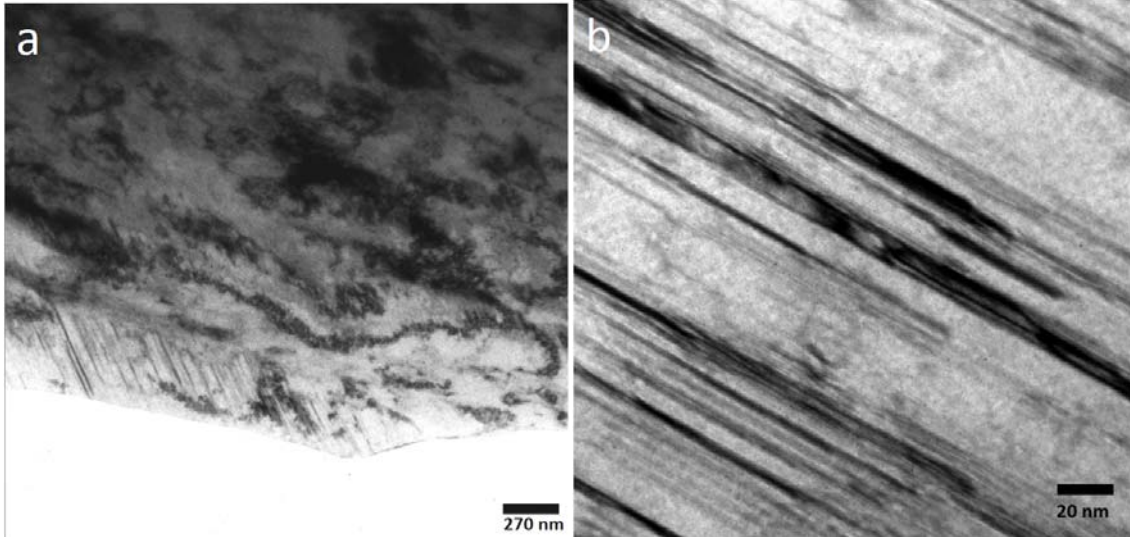


Figure 9.4- TEM micrograph of Cu-12.1%Al-4.1%Zn sample rolled at 77K. a) heavily deformed microstructure containing twins, b) nano twins with thickness less than 10nm.

From the microstructural point of view, two major considerations are the effect of SFE on restriction of dislocation activity and also its effect on promoting the twinning activity. As discussed above, the microstructure of the cryo-rolled samples consists of heavily deformed grains with some defined grain boundaries. It also appears that a higher dislocation density is maintained in Cu-12.1%Al-4.1%Zn due to the low SFE, Table 9.3. Furthermore, Figure 9.4-b confirms that at low SFE, deformation twins are more readily formed. The question is how reduced SFE and obtained mechanical properties can be linked to the observed microstructures with high dislocation density and significant twinning activity?

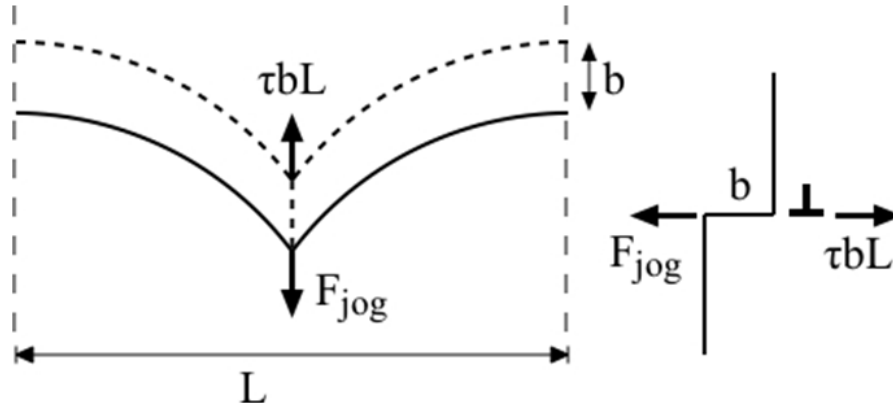


Figure 9.5- A periodic row of intersecting network dislocations produces resisting a force F_{jog} on a slip dislocation moving in the forward (upward) direction. One period length L is shown centered on a network dislocation. The forward force is τbL .

In light of the heavily deformed microstructures containing dislocation substructure and lack of grain boundaries observed by TEM micrographs in the cryo-rolled pure copper and Cu-12.1%Al-4.1%Zn, we can rationalize the strengthening behavior by considering the dislocation-network strengthening model shown in Figure 9.5. The network dislocation intersections in Figure 9.5 are assumed to form periodic rows of spacing L in the slip plane. A slip dislocation forms a jog of length b (Burgers vector) in the network dislocation and this gives rise to a resistance force F_{jog} . The net force in the forward direction due to the applied stress τ is τbL (line tension force makes no contribution over one period [38]). The work done by the applied stress for the jog length b is τb^2L , and this must equal the energy $U_{\text{jog}}b$ needed to form a jog with energy per unit length U_{jog} . Calculating U_{jog} is difficult because the jog stress field is heavily screened to the extent that core energy can dominate. Following [39], we take U_{jog} to be αGb^2 where G is the shear modulus and the value of α is estimated to

range between about 0.2 and 0.3. An energy balance $\tau b^2 L = \alpha G b^3$ gives the Von Mises tensile yield stress σ_0 ;

$$\sigma_0 = \sqrt{3}\tau = \sqrt{3}\alpha \frac{Gb}{L} \quad (9.1)$$

The spacing L is related to the network dislocation density ρ by $\rho = 1/L^2$. TEM micrographs indicate a large dislocation density after cryo-rolling, but it was not measured directly using TEM. The dislocation density can be estimated indirectly using the x-ray diffraction data, and the values obtained are given in Table 9.3. In the case of pure Cu, the physical activation volume V^* can also be used to estimate the dislocation density. The activation area in Figure 9.5 is $A^* = Lb$ and the measured activation volume $V^* = A^*b/b^3 = L/b = 26$ for Cu. This gives $\rho = 2.1 \times 10^{16} \text{ m}^{-2}$, which is in good agreement with the x-ray value $1.9 \times 10^{16} \text{ m}^{-2}$. The physical activation volume cannot be used to determine the network dislocation density for the alloys because additional interactions between slip dislocations and closely spaced solute atoms can reduce V^* values determined by stress relaxation [38]. The average spacing between solute atoms immediately above/below a slip plane is shown in Table 9.3.

The value of α can be obtained from the measured value of yield stress σ_0 for pure Cu in Table 9.1. Eq. (9.1) gives $\alpha = 0.21$ and 0.19 for the dislocation density determined by x-ray diffraction and V^* , respectively. The average $\alpha = 0.2$ is within the expected range. For consistency, we used the x-ray value $\alpha = 0.21$ to predict the σ_0 values given in Table 9.1 for dislocation network strengthening in the Cu-12.1%Al-4.1%Zn. Values of shear modulus and Burgers vector used in this model for both samples are listed in Table 9.4.

Table 9.4- Values of shear modulus and Burgers vector for pure copper and Cu-12.1%Al-4.1%Zn.

	G shear modulus (GPa)*	b Burgers vector (nm)**
Pure copper	43.0	0.256
Cu-12.1%Al-4.1%Zn	40.9	0.258

* Shear modulus for alloys was estimated by rule of mixture, $G_{Cu}=43.0$ GPa, $G_{Al}=26.0$ GPa, $G_{Zn}=42.0$ GPa.

** Burgers vector for alloys was calculated based on the X-ray data using, $\mathbf{b} = \frac{\sqrt{2}}{2} a_0$, where a_0 is lattice constant.

Given that the network dislocation model predicts the yield strength of the pure copper, there is a difference between the calculated and measured yield strengths in the Cu-12.1%Al-4.1%Zn. This is due to the solution hardening [40] and perhaps a minor effect of the deformation twins on the strengthening. As mentioned earlier the average twin spacing in Cu-12.1%Al-4.1%Zn is ≈ 13 nm. This value is much higher than what is calculated for the spacing between network dislocations, Table 9.3, and shows the negligible effect of twins in strengthening of both alloys. This observation justifies the role of high dislocation density in strengthening of the cryo-rolled samples with a wide range of SFE. It is worth to note that the good ductility, 11%, observed in Cu-12.1%Al-4.1%Zn can be related to the high twinning tendency in this sample. Deformation twins perhaps accommodate some portion of deformation in Cu-12.1%Al-4.1%Zn and compensate the hardening due to high solute content.

Possible deformation mechanisms in Cu-12.1%Al-4.1%Zn sample in situ consolidated via ball milling were discussed in [41]. This can be compared to the results in this paper to understand different deformation mechanisms involved in mechanical behavior

of the low SFE Cu-12.1%Al-4.1%Zn alloy produced with different routes. Youssef et al. [42] concluded that deformation twins in nano grains, 22 nm, contribute to the high yield strength, 1067 MPa, and control the deformation mechanism. Homogeneous microstructure of Cu-12.1%Al-4.1%Zn produced in ball milling contains high density of stacking faults and deformation twins that cause abundant dislocation-twin interactions. This is in contrast to cryo-rolled samples with less defined grain boundaries and mainly containing high dislocation density and less twinning activity compared to ball milled samples.

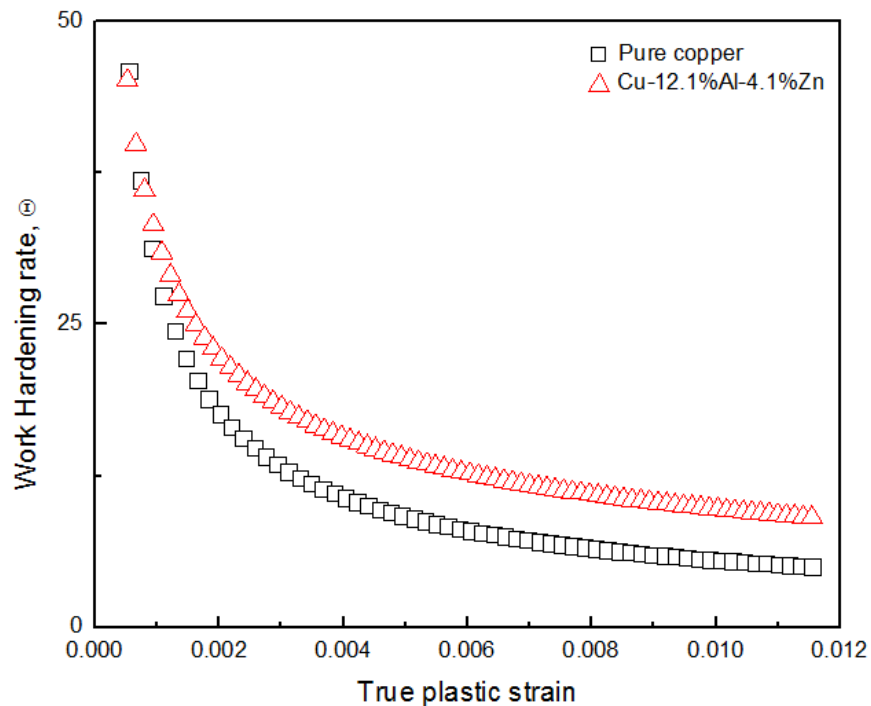


Figure 9.6- The work hardening rate, Θ , as a function of the true plastic strain for pure copper and Cu-12.1%Al-4.1%Zn.

Figure 9.6 shows the variation of work hardening rate, Θ , which is defined as $\Theta = \frac{d\sigma}{d\varepsilon}$, where, σ is the true stress and ε is the true strain. Pure copper shows lower work hardening rate compared to the Cu-12.1%Al-4.1%Zn. Generally, samples with higher SFE show lower

work hardening rate as a result of easier dislocation activity [43]. It is also reported that there is an optimal SFE in Cu-Zn alloys processed via HPT that produces high strength and ductility [11]. Zhao et al. [11] concluded that grain boundaries in HPT processed Cu-30%Zn alloy with grain size of 10nm are dislocation annihilation sites preventing dislocation accumulation during tensile test. They also linked the higher ductility of Cu-10%Zn to its capability for dislocation accumulation, i.e. higher work hardening rate. The work hardening rate behavior of Cu-12.1%Al-4.1%Zn can be compared to Cu-30%Zn in [11] with this difference that grain boundaries are not well defined in the microstructure of as-rolled samples in this research.

The work hardening behavior is directly related to the dislocation density evolution during the tensile test. Based on the model from Kocks and Mecking [44] storage and annihilation of dislocations are added together to describe the dislocation density evolution;

$$\frac{d\rho}{d\gamma} = \left(\frac{d\rho}{d\gamma}\right)^+ + \left(\frac{d\rho}{d\gamma}\right)^- \quad (2)$$

where ρ and γ are dislocation density and shear strain, respectively. In this research, the Cu-12.1%Al-4.1%Zn alloy shows higher work hardening rate due to its low SFE that controls dislocation accumulation and dynamic recovery. XRD determined that restricted cross slip in Cu-12.1%Al-4.1%Zn results in higher dislocation density accumulated in the as-rolled state compared to pure copper, Table 9.3. Therefore, there is a limited capacity for the Cu-12.1%Al-4.1%Zn to store more dislocations during the tensile test. Furthermore, the dynamic recovery of the stored dislocations during the tensile test is also restricted as a result of low

SFE, 7 mJ/m^2 . When added together, the higher dislocation storage capacity and limited dynamic recovery gives rise to higher work hardening rate compared to pure copper.

9.5. Summary

Pure copper and Cu-12.1%Al-4.1%Zn were processed using rolling in liquid nitrogen. Tensile properties were examined and deformation mechanisms were discussed based on results on stress relaxation tests and microstructure observations. The following conclusions were drawn:

- Deformation in liquid nitrogen effectively suppresses the dynamic recovery and recrystallization and results in enhanced yield strength with significant ductility for pure copper. Dislocation substructure and some ultrafine grains containing deformation twins were formed that are responsible for activation volume of $26b^3$. Network dislocation strengthening model showed good correlation between predicted and measured values of yield strength. Therefore, the small activation volume in pure copper sample is related to high dislocation density and it is concluded that grain boundaries don't have major contribution to strengthening.
- Decreased stacking fault energy to 7 mJ/m^2 promotes twinning as observed in as-rolled Cu-12.1%Al-4.1%Zn. Higher solute content and also reduced SFE increases yield strength. Ductility of 11% in Cu-12.1%Al-4.1%Zn alloy is related to its tendency to form deformation twins that sustain plastic deformation during tensile test.

- As proved by network dislocation strengthening model, the deformation behavior of Cu-12.1%Al-4.1%Zn is mostly controlled by dislocation mediated processes and deformation twins don't contribute to strengthening significantly. This is due to large spacing between twin boundaries compared to network dislocation spacing and also inhomogeneous distribution of twins in the microstructure. Small physical activation volume of $8b^3$ is mainly due to the fine spacing between solute atoms that interact with gliding dislocations during stress relaxation test.

9.6. References

- [1] K.S. Kumar, H. Van Swygenhoven, S. Suresh, *Acta Mater.*, 51 (2003) 5743-5774.
- [2] M.A. Meyers, A. Mishra, D.J. Benson, *Prog. Mater. Sci.*, 51 (2006) 427-556.
- [3] J.W. Christian, S. Mahajan, *Prog. Mater. Sci.*, 39 (1995) 1-157.
- [4] L. Lu, X. Chen, X. Huang, K. Lu, *Science*, 323 (2009) 607-610.
- [5] L. Lu, R. Schwaiger, Z.W. Shan, M. Dao, K. Lu, S. Suresh, *Acta Mater.*, 53 (2005) 2169-2179.
- [6] V.S. Sarma, Wang, J., Jian, W. W., Kauffmann, A., Conrad, H., Freudenberger, J., Zhu, Y. T., *Mater. Sci. Eng., A*, 527 (2010) 7624-7630.
- [7] S.R. Agnew, B.R. Elliott, C.J. Youngdahl, K.J. Hemker, J.R. Weertman, *Mater. Sci. Eng., A*, 285 (2000) 391-396.
- [8] Y.S. Li, N.R. Tao, K. Lu, *Acta Mater.*, 56 (2008) 230-241.
- [9] Y.M. Wang, M.W. Chen, F.H. Zhou, E. Ma, *Nature*, 419 (2002) 912-915.

- [10] W.S. Zhao, N.R. Tao, J.Y. Guo, Q.H. Lu, K. Lu, *Scr. Mater.*, 53 (2005) 745-749.
- [11] Y.H. Zhao, Liao XZ, Horita Z, Langdon TG, Zhu YT, *Mater. Sci. Eng., A*, 493 (2008) 123-129.
- [12] M.A. Meyers, O. Vohringer, V.A. Lubarda, *Acta Mater.*, 49 (2001) 4025-4039.
- [13] V. Yamakov, D. Wolf, S.R. Phillpot, H. Gleiter, *Acta Mater.*, 50 (2002) 5005-5020.
- [14] H. Van Swygenhoven, *Science*, 296 (2002) 66-67.
- [15] J. Schiotz, K.W. Jacobsen, *Science*, 301 (2003) 1357-1359.
- [16] X.Z. Liao, Y.H. Zhao, S.G. Srinivasan, Y.T. Zhu, R.Z. Valiev, D.V. Gunderov, *Appl. Phys. Lett.*, 84 (2004) 592-594.
- [17] W.Z. Han, Z.F. Zhang, S.D. Wu, S.X. Li, *Philos. Mag.*, 88 (2008) 3011-3029.
- [18] E. Ma, Y.M. Wang, Q.H. Lu, M.L. Sui, L. Lu, K. Lu, *Appl. Phys. Lett.*, 85 (2004) 4932-4934.
- [19] K.M. Youssef, R. O. Scattergood, K. L. Murty, J. A. Horton, C. C. Koch, *Appl. Phys. Lett.*, 87 (2005) 0919041.
- [20] T.R. Blewitt, R.R. Coltman, J.K. Redman, *J. Appl. Phys.*, 28 (1957) 651-660.
- [21] Y.H. Zhao, Y.T. Zhu, X.Z. Liao, Z. Horita, T.G. Langdon, *Appl. Phys. Lett.*, 89 (2006) 121906.
- [22] Y.H. Zhao, Y.T. Zhu, X.Z. Liao, Z.J. Horita, T.G. Langdon, *Mater. Sci. Eng., A*, 463 (2007) 22-26.
- [23] F.A. Mohamed, *Acta Mater.*, 51 (2003) 4107-4119.
- [24] P.C.J. Gallagher, *Metall. Trans.*, 1 (1970) 2429-2461.
- [25] M.F. Denicot, J.P. Villain, *Phys. Status Solidi A*, 8 (1971) 125-127.

- [26] M. Leoni, T. Confente, P. Scardi, *Z. Kristallogr.*, 23 (2006) 249-254.
- [27] Y.M. Wang, K. Wang, D. Pan, K. Lu, K.J. Hemker, E. Ma, *Scr. Mater.*, 48 (2003) 1581-1586.
- [28] R.Z. Valiev, I.V. Alexandrov, Y.T. Zhu, T.C. Lowe, *J. Mater. Res.*, 17 (2002) 5-8.
- [29] C.C. Koch, *Rev. Adv. Mater. Sci.*, 5 (2003) 91-99.
- [30] D. Caillard, J.-L. Martin, *Thermally activated mechanisms in crystal plasticity*, Pergamon, Amsterdam ; Boston, Mass., 2003.
- [31] R.K. Guduru, K.A. Darling, R.O. Scattergood, C.C. Koch, K.L. Murty, *J. Mater. Sci.*, 42 (2007) 5581-5588.
- [32] Q. Wei, S. Cheng, K.T. Ramesh, E. Ma, *Mater. Sci. Eng., A*, 381 (2004) 71-79.
- [33] R.K. Guduru, K.L. Murty, K.M. Youssef, R.O. Scattergood, C.C. Koch, *Mater. Sci. Eng., A*, 463 (2007) 14-21.
- [34] R.J. Asaro, S. Suresh, *Acta Mater.*, 53 (2005) 3369-3382.
- [35] J. Chen, L. Lu, K. Lu, *Scr. Mater.*, 54 (2006) 1913-1918.
- [36] R.J. Asaro, Y. Kulkarni, *Scr. Mater.*, 58 (2008) 389-392.
- [37] C. Kobayashi, T. Sakai, A. Belyakov, H. Miura, *Phil. Mag. Lett.*, 87 (2007) 751-766.
- [38] U.F. Kocks, A.S. Argon, M.F. Ashby, *Prog. Mater. Sci.*, 19 (1975) 1-281.
- [39] D. Hull, D.J. Bacon, *Introduction to dislocations*, 4th ed., Butterworth-Heinemann, Oxford Oxfordshire ; Boston, 2001.
- [40] D.R. Askeland, *The Science and engineering of materials : sixth edition*, International Ed. ed., Cengage Learning, Mason, OH, 2010.

[41] K. Youssef, M. Sakaliyska, H. Bahmanpour, R. Scattergood, C. Koch, *Acta Mater.*, 59 (2011) 5758-5764.

[42] K.M. Youssef, M. Sakaliyska, H. Bahmanpour, R. O. Scattergood, C. C. Koch, *Acta Mater.*, *in Press*.

[43] F. Hamdi, S. Asgari, *Scr. Mater.*, 62 (2010) 693-696.

[44] U.F. Kocks, H. Mecking, *Prog. Mater. Sci.*, 48 (2003) 171-273.

CHAPTER TEN

10.0. SEVERE DEFORMATION TWINNING IN PURE COPPER BY CRYOGENIC WIRE DRAWING

A. Kauffmann, J. Freudenberger, D. Geissler, S. Yin, W. Schillinger, V. Subramanya Sarma, H. Bahmanpour, R. Scattergood, M.S. Khoshkhoo, H. Wendrock, C.C. Koch, J. Eckert, L. Schultz

Acta Materialia, 2011, Vol. 59, pp. 7816-7823

10.1. Abstract

The effect of low-temperature on the active deformation mechanism is studied in pure copper. For this purpose, cryogenic wire drawing at liquid nitrogen temperature (77 K) was performed using molybdenum disulfide lubrication. Microstructural investigation and texture analysis revealed severe twin formation in the cryogenically drawn copper, with a broad twin size distribution. The spacing of the observed deformation twins ranges from below 100 nm, as reported in previous investigations, up to several micrometers. The extent of twin formation, which is significantly higher when compared to other cryo-deformation techniques, is discussed with respect to the state of stress and the texture evolution during wire drawing.

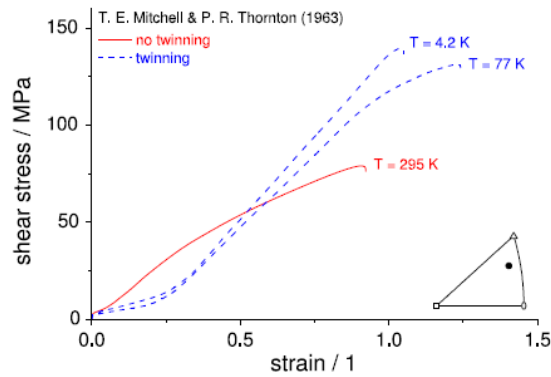
10.2. Introduction

Nanostructured materials have been the subject of intense research activity over the last few decades due to their properties, which appear to be outstanding in many cases. Structuring of these materials can occur with reduced dimensionality, based on the morphology of the nanometer-sized microstructural elements. For example, Lu et al. [1, 2] showed that the formation of growth twin lamellas of about 15 nm twin spacing and twin lengths of 100 nm to 1 μm during electrodeposition in pure Cu leads to excellent mechanical properties. They observed an increase in ultimate tensile strength up to about 1070 MPa, combined with 14% elongation to failure and an electrical resistivity of about $1.75 \times 10^{-8} \Omega\text{m}$, which is similar to that of pure Cu in the annealed state. These properties are directly attributed to the nanoscale twinned microstructure. However, as such microstructures are formed during a deposition process, the production of these materials is restricted in at least one dimension. Nevertheless, Lu et al. [1] stated that twinning is a common phenomenon in nature. It occurs during growth processes, recrystallization, phase transformations or deformation. This opens the possibility of expanding the approach to processes other than electrodeposition.

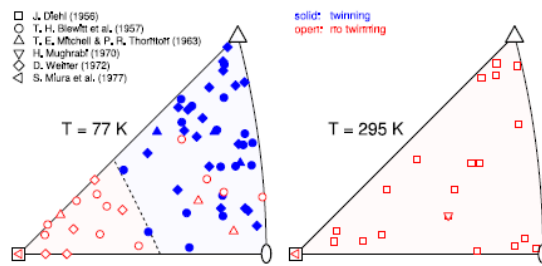
After several years of reservations regarding deformation twinning in pure Cu, Blewitt et al. [3] provided unambiguous evidence for this deformation mode in Cu single crystals at low temperature. Subsequent investigations revealed the typical characteristics of deformation twinning in single-valent noble metals. Briefly, the characteristics have been discussed with regard to the dependence of the twinning stress on temperature, orientation, direction of loading and solute content in single-phase alloys [4]. Recently, the transition

from pure slip to slip and twin dominated plasticity was investigated by comparison of room temperature and cryogenic temperature deformation, as well as by variation of stacking fault energy [5]. In the present investigation, the basic knowledge about the dependence of deformation twinning on orientation and temperature is rigorously applied in order to produce severely and homogeneously twinned microstructures in pure Cu, i.e. without influencing the stacking fault energy by additional alloying.

As Blewitt et al. [3] showed in their first investigation, deformation twinning in pure Cu only occurs under certain conditions. These are depicted by means of Figure 10.1, which summarizes several different experimental observations. During a more detailed study, Mitchell and Thornton [6] obtained distinct differences in the stress-strain behavior of Cu single crystals deformed at different temperatures, as shown in Figure 10.1a. At room temperature, plasticity is mediated by dislocation slip and dynamic recovery inhibits the formation of deformation twins by retaining a comparatively low stress level. When the temperature is lowered down to that of liquid nitrogen (77 K) and below, twinning in pure Cu can be activated by suppression of dynamic recovery and thus increasing stress level [4]. Furthermore, twinning shows a strong orientation dependence, as illustrated in Figure 10.1b [3, 6-10]. At a temperature of 77 K, twinning is observed mainly in crystals with the tensile axis parallel to $\langle 111 \rangle$, while $\langle 100 \rangle$ -oriented crystals do not exhibit twin formation. In contrast, under compression load, twinning occurs in crystals oriented near $\langle 100 \rangle$ and is absent in crystals oriented near $\langle 111 \rangle$ [4]. The range of orientation under tensile loading is extended when compared to compressive loading.



(a)



(b)

Figure 10.1- Twinning in Cu single crystals under tensile load: (a) stress-strain response with respect to twinning at different temperatures in Cu crystals of an orientation suitable for twinning [6], (b) orientation dependence of twinning at cryogenic and room temperature [3, 6-10].

The aim of the present study is to analyze the impact of the state of stress and the texture evolution on twin formation during wire drawing at liquid nitrogen temperature. This is done in order to provide a homogeneously fine twinned microstructure within a technically relevant deformation process. For this purpose, a suitable cryogenic drawing (cryo-drawing) set-up, including a sufficient lubrication method, that allows the process to be adapted to a technically reasonable working window has been developed and tested.

10.3. Experimental procedure

The experiments for this study are divided into two parts. In the first part, the cryo-drawing process was studied and optimized. In the second one, this optimized process was applied to the sample preparation for the study of the microstructure and texture in cryo-deformed Cu.

The starting material for the development of the cryodrawing process was commercially available Cu-OF (CW007A, EN 1977), 6 mm in diameter and 50 cm in length. Drawing dies with a cone angle of $2\alpha = 12^\circ$ were used. Prior to each drawing step of about 0.2 logarithmic deformation strain, η , the Cu wire and the dies were immersed in liquid nitrogen. The cold rod material was then drawn through the die out of the cooling bath at a speed of 0.5 m min^{-1} . In order to assess different lubricants, the drawing forces were recorded using a computerized data acquisition system connected to cells of either 5 or 30 kN load. The lubricants tested are bonded coatings of polytetrafluoroethylene (PTFE, PRO 407 GT by Proline[®]), graphite (PRO 437 GG by Proline[®]) and molybdenum disulphide (MoS_2 ; PRO 417 GM by Proline[®]). For comparison, a state-of-the-art drawing oil (Rotanor SCM by Rhenus Lub) was used at room temperature.

For the study of deformation twinning in cryo-drawn Cu, the primary material was pre-processed in order to achieve a suitable microstructure and texture. Cu-OFE (CW009A, EN 1977) was melted in an induction furnace and cast into a cylindrical graphite mold in an Ar atmosphere. After machining the ingot to $D = 28.5 \text{ mm}$, a hot forming process at 600°C via rotary swaging down to $D = 25.0 \text{ mm}$ was adopted in order to remove the as-cast microstructure. A post-annealing treatment at 800°C for 18 h in an Ar atmosphere resulted in a coarse-grained microstructure for the subsequent drawing process. This starting material

was deformed to a final diameter of 11.8 mm by wire drawing, with about 0.1 logarithmic deformation per step at a speed of about 0.5 m min^{-1} . Lubrication via drawing oil was used at room temperature, while MoS_2 lubrication was chosen for the cryo-drawing process in a bath of liquid nitrogen.

Microstructural characterization was carried out by scanning electron microscopy (SEM) using Leo Gemini 1530 and Philips XL20 microscopes. Secondary electron images were taken at 15 up to 20 kV, except for the characterization of the PTFE-bonded lubricant coatings, which were taken at an acceleration voltage of 1 kV. Forward scattered electron images were recorded using a four-diode forescatter detector. The samples were prepared by a conventional metallographic procedure, completed by a finishing step using a VibroMet[®] 2 vibratory polishing machine and Mastermet[®] 2 suspension (both by Buehler) for about 8 h.

The global texture was measured by the X-ray diffraction Schulz reflection method on a Philips X'Pert MRD system operating with Cu Ka radiation. The pole figures were corrected for background (2° in 2Θ next to the corresponding reflection), defocusing and tilt (the $\langle 111 \rangle$ fiber texture component parallel to the wire axis). The defocusing functions were obtained on a polycrystalline, non-textured sample prepared from a non-flowing, fine dendritic powder.

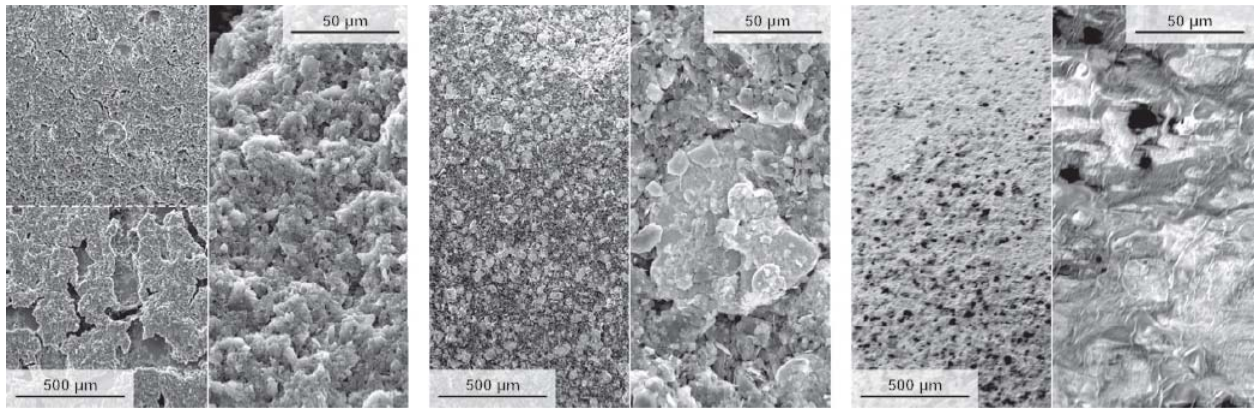
Local texture information was obtained from the metallographically prepared samples by electron backscatter diffraction (EBSD). The acquisition of orientation data was accomplished with a Nordlys EBSD system in a three-step indexing process. Drifts during the scans were corrected afterwards for the visible shape of carbon contamination in secondary electron contrast, indicating the scanned surface area.

10.4. Results and discussion

10.4.1. Lubrication

Unlike rolling at cryogenic temperature, wire drawing is difficult to perform because of the need of an appropriate lubrication. State-of-the-art lubricants at room temperature are mainly drawing oils, emulsions or powders. However, all conventional liquid lubricants, like drawing oils, cannot be used at liquid nitrogen temperature. Thus, solid lubricants have to be applied. The lubricants used in the present study are inspired by recent developments in aerospace engineering. There are materials such as MoS₂ [11], graphite or PTFE [12] and composites thereof [12, 13], representing prominent examples for sacrificial coatings or self-lubricating systems. They provide solid shape, vacuum and temperature stability. For technical reasons, the application of the lubricant would have to ensure a repeated lubrication of reproducible quality after every drawing step. Therefore, bonded coatings are suitable. These commercially available separating agents or lubricants can be easily applied by spraying.

Figure 10.2 shows SEM micrographs of the investigated bonded coatings. All lubricants form dense coatings except graphite, for which dense coatings can be shown to be interrupted by flawed surface areas several hundred micrometers in diameter. In the case of MoS₂ and graphite, the coatings consist of platelets of 5–20 μm and 2–10 μm, respectively. The PTFE coating does not exhibit separate particles on the wire surface. All coatings are stable against shock cooling down to 77 K in liquid nitrogen.



(a)

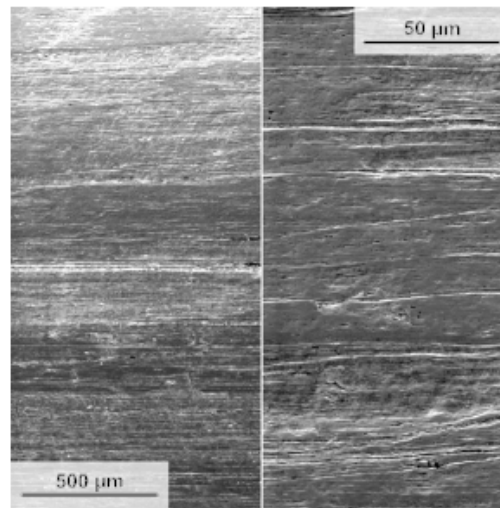
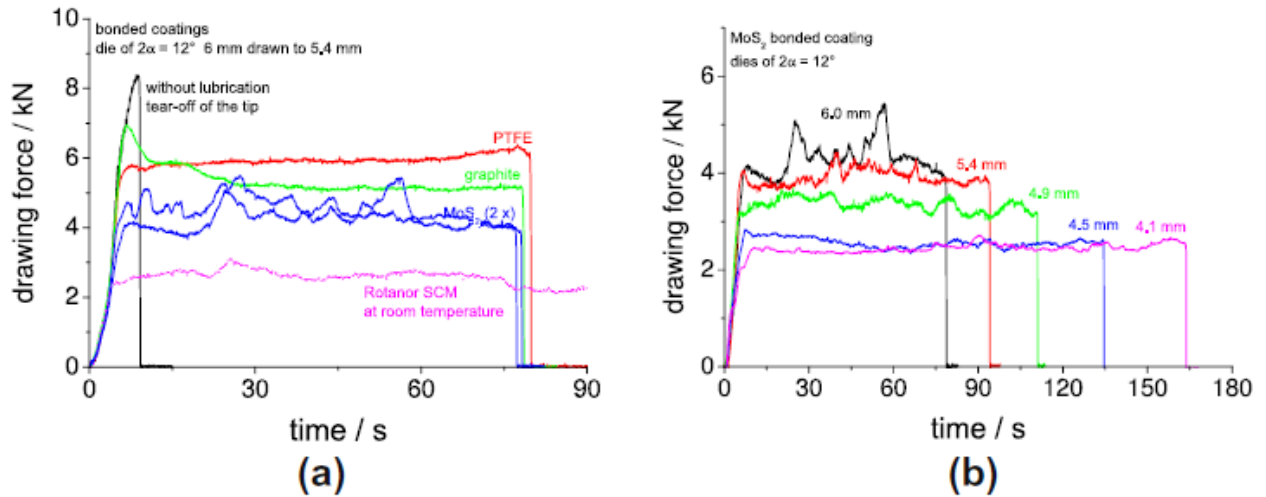
(b)

(c)

Figure 10.2- Scanning electron micrographs (secondary electron contrast) at different magnifications (overview on the left; in detail on the right) of the bonded coatings used in the present investigation: (a) graphite (dense coating top left and porous coating bottom left), (b) MoS₂ and (c) PTFE.

As an example for the qualification of the three bonded coatings on Cu, the recorded drawing force during the drawing step from 6 to 5.4 mm in a bath of liquid nitrogen is shown in Figure 10.3a. It is not possible to draw uncoated material because the load stress of about 370 MPa (8.5 kN) exceeds the ultimate tensile strength of the wire and failure after necking is observed. By means of bonded coatings, the load stress can be reduced down to about 260 MPa (6.0 kN, PTFE), 225 MPa (5.2 kN, graphite) and 200 MPa (4.6 kN, MoS₂). The force characteristics during the drawing process are also quite different. While the PTFE coating provides a constant and homogeneous force profile, the graphite coating exhibits a continuous decrease in drawing force after an overshoot at the beginning of the drawing process. The MoS₂ coating shows the lowest average drawing force, but is less constant over time than PTFE and graphite. Figure 10.3b depicts the evolution of the drawing force characteristic over several deformation steps with the MoS₂ coating. It can be seen that the coating stabilizes with reduced average drawing force. An inspection of the final wire surface

after the last drawing step reveals pronounced die lines. As a consequence, although the MoS₂ coating is the system of choice for the following study, there is still potential for lubricant optimization with respect to application.



(c)

Figure 10.3- Drawing force as a function of time during wire drawing. Drawing takes place in a bath of liquid nitrogen: (a) comparison between non-lubrication and various bonded coatings and (b) drawing series of MoS₂ bonded coating. The drawing force of standard lubrication at room temperature is included in (a) for comparison. The wire surface at the final stage of the drawing process is shown in (c) as scanning electron micrographs (secondary electron contrast) at different magnifications after removal of the coating.

10.4.2. Stress state

The dominant deformation mechanisms in face-centred cubic metals – dislocation slip and twinning – are shear sensitive because they are both based on the movement of dislocations. Hence, if other constraints to twinning are fulfilled, the resolved shear stress distribution during the deformation process will determine the active deformation mechanism. A rough approximation of the resolved shear stress distribution during wire drawing can be obtained by using the elementary circular slab method of plasticity [14-16] to estimate the state of stress and calculate the corresponding resolved shear stresses.

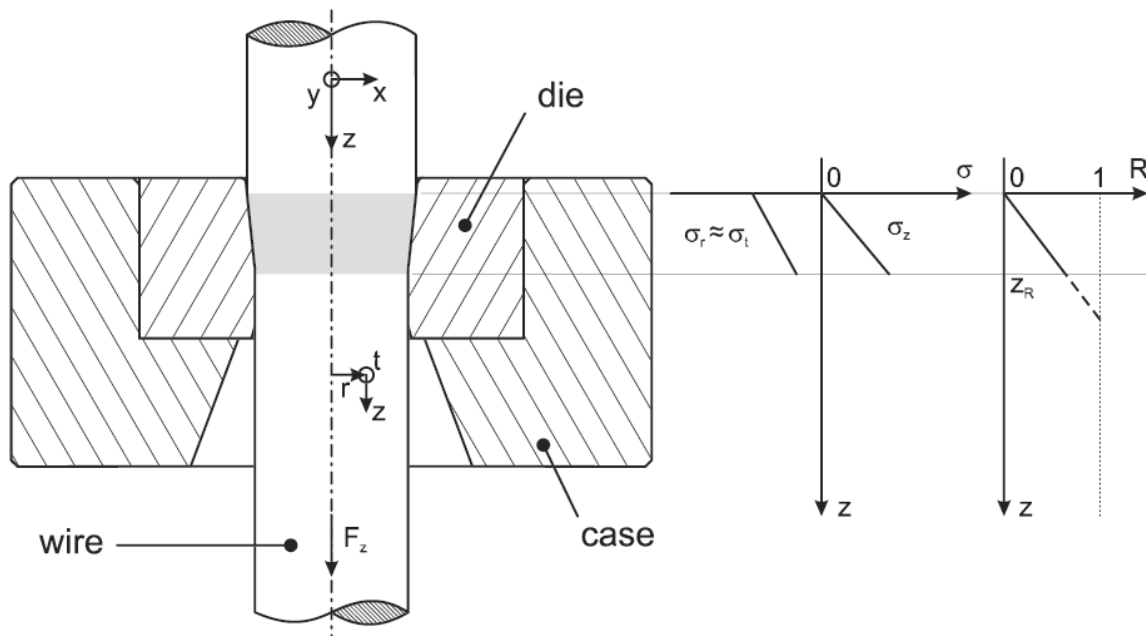


Figure 10.4- Scheme of wire drawing and stress state during wire drawing [15].

A resolved shear stress s on a shear plane with a normal \underline{p} in a shear direction \underline{d} (\underline{p} and \underline{d} are used as unit vectors) caused by a multiaxial stress state $\underline{\sigma}$ is described by the

projection $\tau = \underline{d} \cdot \underline{\sigma} \cdot \underline{p}$. Using the principal coordinate system with the principal stresses σ_x , σ_y and σ_z , this can be transformed into:

$$\tau = \underline{d} \cdot \underline{\sigma} \cdot \underline{p} \quad (10.1)$$

$$= d_x p_x \sigma_x + d_y p_y \sigma_y + d_z p_z \sigma_z \quad (10.2)$$

$$= d_y p_y (\sigma_y - \sigma_x) + d_z p_z (\sigma_z - \sigma_x) \quad (10.3)$$

where p_i and d_i denote the coordinates of \underline{p} and \underline{d} in the principal coordinate system. The simplification from Eqs. (10.2) and (10.3) follows from the orthogonality of shear plane normal and shear direction $\underline{p} \cdot \underline{d} = 0$. By assuming homogeneous deformation and conservation of volume, a principal stress distribution (without back pull) as shown in Figure 10.4 can be obtained using circular slabs [15, 16]. This state of stress $\underline{\sigma}$ can be rearranged to $\sigma_x = \sigma_y = (R(z) - 1)\sigma$ and $\sigma_z = R(z)\sigma$, where $0 < R(z) < 1$ and $\sigma > 0$ separate the local dependence and scaling dependence of the stress state throughout the drawing die. Eq. (10.3) is then reduced to:

$$\tau = d_z p_z \sigma \quad (10.4)$$

Hence, the resolved shear stress determining the microstructural mechanisms of deformation is simply a function of the axial tensile stress at the back relief $\sigma_z(z_R) = R(z_R)\sigma$ and the projections of the shear elements, $d_z p_z$ (e.g. the Burgers vector and slip plane) onto the wire axis. In a polycrystalline material these projections are determined by the texture components present. The resolved shear stress is independent of the exact position in the drawing die and similar to that of tensile testing. Thus, dislocation and twinning-mediated plasticity will occur during the whole deformation process if the necessary orientation

relations are fulfilled by the texture evolution and the required stress level is reached. Further, these requirements can be easily deduced from tensile testing (see Section 10.2) due to the striking similarity of the resolved shear stresses.

In contrast, the approximately biaxial state of stress during rolling with very different stress components along the rolling direction, σ_z , and along the normal direction, σ_x , leads to:

$$\tau = d_x p_x \sigma_x + d_z p_z \sigma_z \quad (10.5)$$

In this case, a separation of scaling and local dependence of any kind cannot produce a location-independent result. Thus, the aforementioned requirements for deformation twinning with respect to the state of stress cannot be equally matched over the complete deformed zone as in the case of wire drawing.

These approximations are, of course, rather rough. The actual stress states are influenced by the boundary conditions of friction and the criteria of plastic flow. Therefore the principal stresses are not aligned with the sample coordinate system, as it is assumed in elementary plasticity theory. Nevertheless, a detailed study of the state of stress during wire drawing [17] first reveals one path along the radial direction with perfectly aligned principal stresses. Secondly, $\sigma_r \approx \sigma_t$ and accordingly $\sigma_x \approx \sigma_y$ are suitable approximations. Hence, elementary plasticity theory provides a simple way to estimate the potential of wire drawing for the initiation of severe, homogeneous twin formation during plastic deformation when compared to other deformation methods.

10.4.3. Texture evolution

As described in Section 1, twinning occurs under tensile loads (or stress states that reproduce the same resolved shear stress distribution) near $\langle 111 \rangle$ directions. During conventional wire drawing processes, mixed $\langle 111 \rangle / \langle 100 \rangle$ fiber textures develop with a strong $\langle 111 \rangle$ fiber component in face-centred cubic materials [18]. The texture evolution during the cryogenic wire drawing process is tracked using the $\{111\}$ pole figures on the wire cross sections, as shown in Figure 10.5. The almost non-textured, coarse-grained initial state develops towards a $\langle 111 \rangle$ fiber component-dominated texture indicated by the maximum at the center of the pole figure within the first steps of deformation. At a logarithmic degree of deformation of $\eta=0.30$ this texture component exhibits an intensity of about 3 m.u.d. (multiples of the uniform distribution), which increases to about 5 m.u.d. at the final stage of deformation.

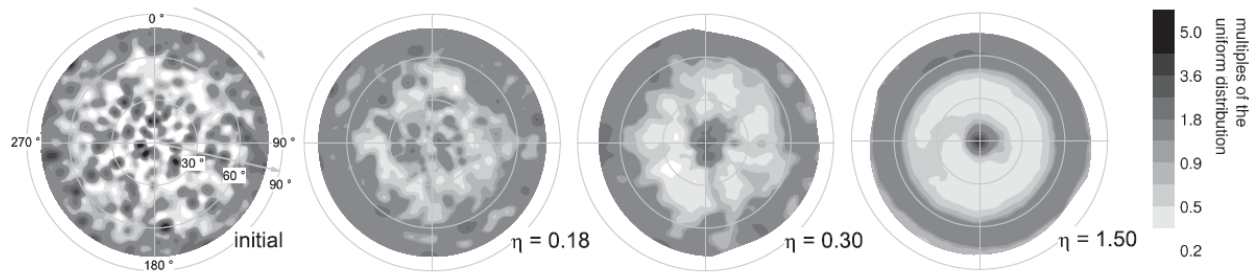


Figure 10.5- The $\{111\}$ pole figures on the wire cross-sections at different logarithmic degrees of deformation, η , within the wire drawing process at liquid nitrogen temperature.

10.4.4. Microstructure

The suppression of dynamic recovery by cryogenic deformation leads to twin formation in Cu. Therefore, enhanced mechanical properties and changed response to heat

treatments when compared to conventionally prepared Cu are to be expected. This was shown previously by Brandao et al. [19] and Han et al. [20] for drawn wires, Zhao et al. [21] for drawing after equal channel angular pressing, Zhao et al. [22] and Li et al. [23] for dynamically deformed bars and Jia et al. [24] for rolled tapes. In general, the reported twin spacings are below 100 nm, i.e. <100 nm for drawn wires [20], several nanometers to about 85 nm for drawing after equal channel angular pressing [21], and between 10 and 150 nm (with an average of 40 nm) [22] and 2 and 5 nm for rolled tapes [24]. Corresponding twin densities are rarely given in the literature, though Zhao et al. [22] estimated the twin density to be about $2.5 \times 10^7 \text{ m}^2 \text{ m}^{-3}$. The above-mentioned experiments were performed using transmission electron microscopy. Thus, it is not clear whether the results are representative of the complete microstructure and all the texture components arising during deformation. Recently, an extended study by Konkova et al. [25] revealed that deformation twinning does not contribute substantially to grain refinement during cryo-rolling despite the numerous observations of nanoscaled twins in cryo-deformed materials.

In addition to the microstructural response, a texture transition from copper-type to brass-type rolling texture is observed by comparing Cu rolled at room temperature and 77 K [25, 26]. This texture transition is mainly characterized by an abrupt decrease in the $\{112\}\langle 111 \rangle$ component, which is mainly governed by mechanical twinning and suppressed cross-slip [25, 27]. Since the total volume fraction of suitable orientations (concerning the resolved shear stress) is restricted to less than 50% [27], the probability of extended deformation twinning is restricted, too. Regarding the discussion in Sections 10.2 and 10.4.2, this is attributed to a location-dependent state of stress that fulfils the conditions of

deformation twinning only for a limited number of texture components. This is perhaps one of the major reasons for the observations in Ref. [25]. In contrast, wire drawing at liquid nitrogen temperature provides outstanding characteristics because of a virtually location independent resolved shear stress (Section 10.4.2) and a dominant $\langle 111 \rangle$ fiber texture component (Section 10.4.3). Thus, the conditions for deformation twinning (Section 10.2) that appear homogeneously in the main part of the microstructure are fulfilled.

The resulting microstructure obtained by wire drawing at liquid nitrogen temperature is shown in Figure 10.6. It is dominated by grains in the range of 100–500 μm intersected by fine thin lamellae of a few nanometers up to several micrometers in width. These lamellae are identified as deformation twins and are not present following wire drawing at room temperature. The upper end of this length scale is mainly attributed to primary deformation twins while the lower end is mainly due to secondary deformation twins. Figure 10.6 illustrates that the spacings of these primary deformation twins greatly exceed the before-mentioned values reported in the literature. Additionally, only a few parts of the microstructure are free of twins. Unfortunately, an evaluation of the corresponding twin density for the complete microstructure is not possible by stereographic methods because of the large range of twin spacings.

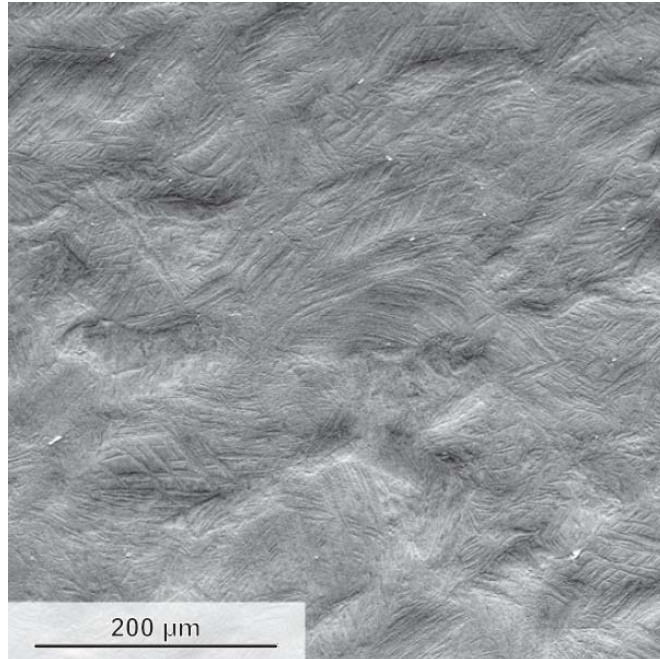


Figure 10.6- Scanning electron micrograph (forward scattered electron contrast) of the severely twinned microstructure obtained by drawing at cryogenic temperature. The logarithmic degree of deformation is $\eta = 1.5$.

In order to validate the formation of deformation twins, local texture analyses using electron backscatter diffraction were performed. The microstructure following a conventional drawing process at room temperature is shown in Figure 10.7. The grains are highly distorted and exhibit orientations mainly with the $\langle 111 \rangle$ - or $\langle 100 \rangle$ - crystallographic axis parallel to the wire axis. These are indicated by blue and red in Figure 10.7a, and can also be seen in the corresponding inverse pole figure in Figure 10.7b. The contouring of the inverse pole figure in Figure 10.7b reveals that the two texture components are indeed close to the ideal sites of the $\langle 111 \rangle / \langle 100 \rangle$ fiber texture components. There is less intensity at the ideal site of twins in $\langle 111 \rangle$ fiber-orientated grains, which corresponds to $\langle 115 \rangle$ fiber orientations. Annealing twins present in the initial microstructure rotate towards the $\langle 100 \rangle$ fiber site during wire

drawing and are thus not observed at the $\langle 115 \rangle$ fiber site. Additionally, as already mentioned, the microstructure is free of the thin intersecting lines that indicate deformation twins.

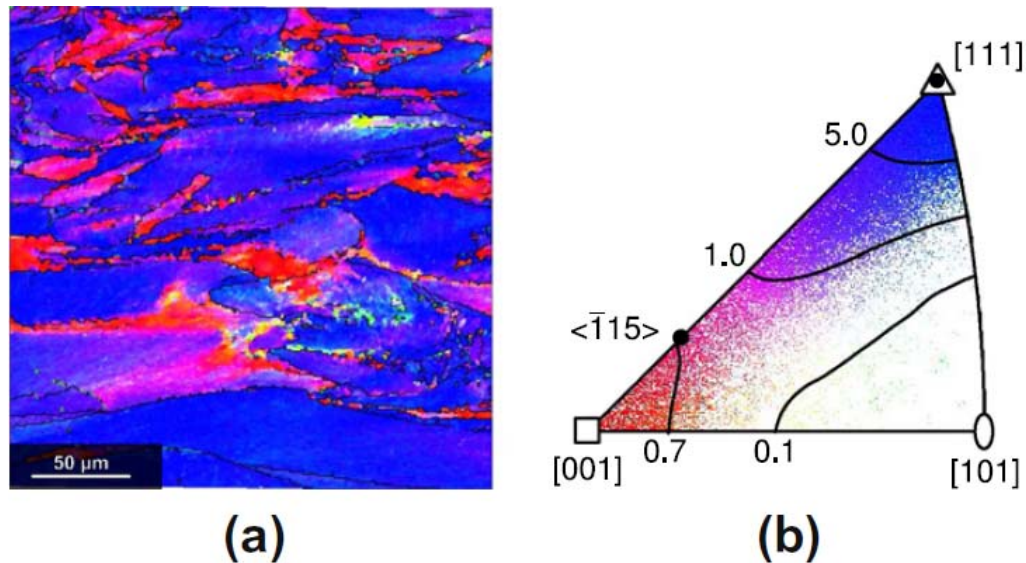


Figure 10.7- EBSD analysis of a cross-section of Cu drawn at room temperature ($\eta = 1.5$): (a) orientation map according to the inverse pole figure (grain boundaries in black, twin boundaries in green) and (b) the corresponding inverse pole figure (combined occupancy and contour diagram). The steps size was $1 \mu\text{m}$. Warping of the image is due to off-line drift correction. Contours indicate multiples of the uniform distribution.

In contrast, Figure 10.8 shows a representative image of a part of a $\langle 111 \rangle$ fiber-orientated grain in a cryo-drawn Cu wire. This matrix grain (indicated by blue in Figure 10.8a) contains an annealing twin of the initial microstructure which is deformed during the wire drawing process. This prior annealing twin exhibits an orientation near the $\langle 100 \rangle$ fiber component (indicated by red in Figure 10.8a). Its misorientation to the matrix grain cannot be identified as the ideal $\Sigma 3$ boundary relation within a certain deviation. This is again mainly

attributed to the deformation and tilt of the grains towards the ideal $\langle 111 \rangle$ - and $\langle 100 \rangle$ fiber sites.

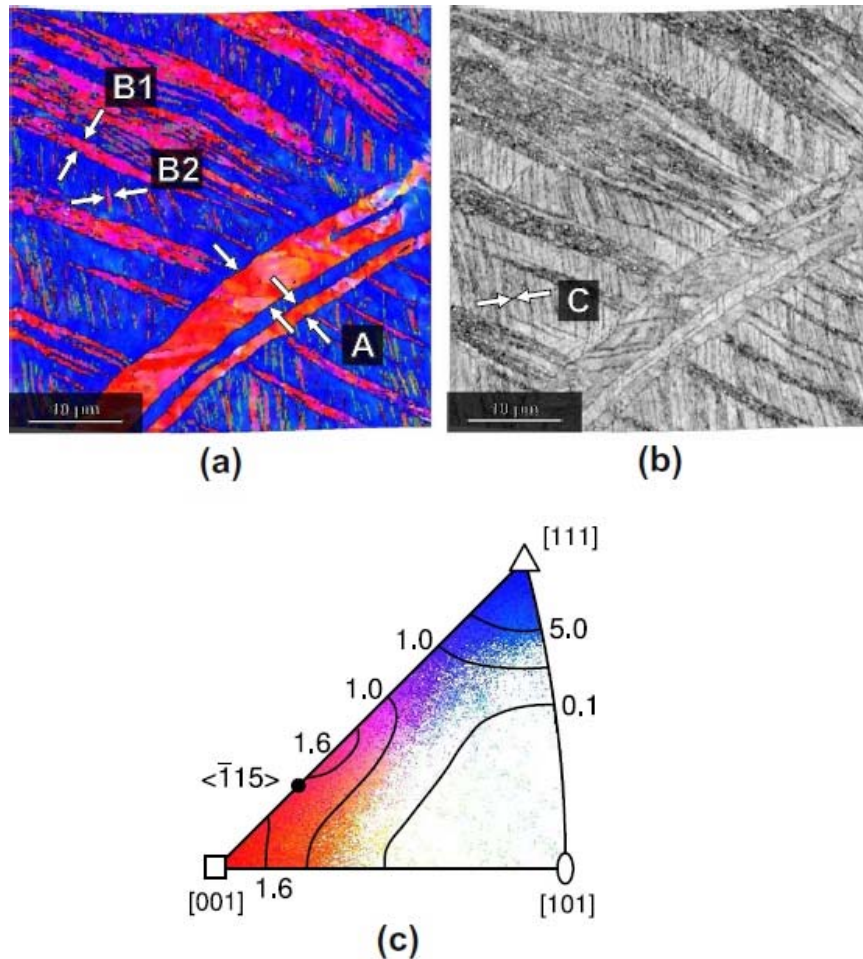


Figure 10.8- EBSD analysis of a severely twinned grain in the cross-section of a cryo-drawn wire ($\eta = 1.5$): (a) orientation map according to the inverse pole figure (grain boundaries in black, twin boundaries in green), (b) band contrast map (the contrast increases from black to white) and (c) corresponding inverse pole figure (combined occupancy and contour diagram). Contours indicate multiples of the uniform distribution. Warping of the images is due to off-line drift correction. (A) highlights prior annealing twins; (B1) and (B2) primary and secondary deformation twins; and (C) secondary deformations twins in the range of the step size of 100 nm.

The observed deformation twins on two different twin systems are exclusively found in the $\langle 111 \rangle$ fiber-orientated part of the grain, as expected with respect to the general

orientation dependence of deformation twinning and the discussion of the state of stress in Sections 10.2, 10.4.2 and 10.4.3. The orientation of the deformation twins corresponds to approximately $\langle 115 \rangle$ fiber orientations (indicated by magenta in Figure 10.8a), which is the ideal orientation resulting from twinning in a grain of the $\langle 111 \rangle$ fiber component. The band contrast image in Figure 10.8b, highlighting microstructural features such as locally increased defect density and topography information, reveals that not all twins are indexed correctly during the mapping process. This is attributed mainly to overlapping Kikuchi patterns. The twin spacing ranges from below the step size of the scan of 100 nm up to several micrometers. This extends the observations of [19] concerning the density of the observed twins and [20] concerning the size of observed deformation twins during cryogenic wire drawing. This might be related to differences in the experimental deformation conditions. For example, by a reduction of the degree of deformation per step, the actual stress state approaches the approximated state of stress discussed in Section 10.4.2. Additionally, the use of optimized lubrication decreases the deviation from the approximated stress state that is induced by friction between the drawing die and the wire. Unfortunately, the previous works [19, 20] do not provide sufficient information about deformation per step and lubrication for a detailed comparison of the results.

10.5. Conclusions

To investigate the active deformation mechanism, cryogenic wire drawing at liquid nitrogen temperature was performed using an optimized molybdenum disulfide lubrication. The drawing forces can be reduced to half of the ultimate tensile strength of the drawn

material. Microstructural investigation and texture analysis by SEM and EBSD reveal severe twin formation in cryo-drawn Cu. The spacing of the observed deformation twins ranges from below 100 nm for secondary twins, as reported in prior investigations, up to several micrometers for primary twins, which is well above the previously reported values. The extent of homogeneous twin formation in Cu is significantly higher compared to other cryo-deformation techniques as a consequence of the virtually location-independent resolved shear stress, which is similar to that of uniaxial tensile stress, and the appropriate texture evolution with a dominant $\langle 111 \rangle$ fiber texture component.

10.6. References

- [1] L. Lu, Y.F. Shen, X.H. Chen, L.H. Qian, K. Lu, *Science*, 304 (2004) 422-426.
- [2] L. Lu, X. Chen, X. Huang, K. Lu, *Science*, 323 (2009) 607-610.
- [3] T.R. Blewitt, R.R. Coltman, J.K. Redman, *J. Appl. Phys.*, 28 (1957) 651-660.
- [4] N. Narita, J. Takamura, Chapter 46 Deformation twinning in f.c.c. and b.c.c. metals, in: F.R.N. Nabarro, J.P. Hirth (Eds.) *Dislocations in Solids*, Elsevier, 1992, pp. 135-189.
- [5] V.S. Sarma, Wang, J., Jian, W. W., Kauffmann, A., Conrad, H., Freudenberger, J., Zhu, Y. T., *Mater. Sci. Eng., A*, 527 (2010) 7624-7630.
- [6] T.E. Mitchell, P.R. Thornton, *Philos. Mag.*, 8 (1963) 1127-&.
- [7] J. Diehl, *Zeitschrift Fur Metallkunde*, 47 (1956) 411-416.
- [8] H. Mughrabi, *Physica Status Solidi*, 39 (1970) 317-&.
- [9] D. Weiner, *Acta Metall.*, 20 (1972) 1235-&.
- [10] S. Miura, Y. Kuriyama, Y. Saeki, *Jpn I Met*, 18 (1977) 852-858.

- [11] R.S. Colbert, W.G. Sawyer, *Wear*, 269 (2010) 719-723.
- [12] N.L. McCook, D.L. Burris, P.L. Dickrell, W.G. Sawyer, *Tribology Letters*, 20 (2005) 109-113.
- [13] W. Hubner, T. Gradt, T. Schneider, H. Borner, *Wear*, 216 (1998) 150-159.
- [14] Sachs G., *Z Angew Math Mech*, 7 (1927) 235-236.
- [15] M. Geiger, Chapter: Grundlagen des Durchdrückens und Durchziehens, in: K. Lange (Ed.) *Umformtechnik. Handbuch für Industrie und Wissenschaft*, Springer, 1988, pp. 254-287.
- [16] T. Böllinghaus, G. Byrne, B.I. Cherpakov, E. Chlebus, C.E. Cross, B. Denkena, U. Dilthey, T. Hatsuzawa, K. Herfurth, H. Herold, A. Kaldos, T. Kannengiesser, M. Karpenko, B. Karpuschewski, M. Marya, S.K. Marya, K.-J. Matthes, K. Middeldorf, J.F.G. Oliveira, J. Pieschel, D.M. Priem, F. Riedel, M. Schleser, A.E. Tekkaya, M. Todtermuschke, A. Vereschaka, D. von Hofe, N. Wagner, J. Wodara, K. Woeste, *Manufacturing Engineering Springer Handbook of Mechanical Engineering*, in: K.-H. Grote, E.K. Antonsson (Eds.), Springer Berlin Heidelberg, 2009, pp. 523-785.
- [17] Adler G, Ein Verfahren zur näherungsweise Berechnung des Spannungs- und Formänderungszustandes beim Fließen starrplastischer Werkstoffe, in, Verlag W. , 1969.
- [18] U.F. Kocks, C.N. Tomé, H.-R. Wenk, *Texture and anisotropy : preferred orientations in polycrystals and their effect on materials properties*, Cambridge University Press, Cambridge, U.K. ; New York, 1998.
- [19] L. Brandao, K. Han, J.D. Embury, R. Walsh, V. Toplosky, S. VanSciver, *IEEE Trans. Appl. Supercond.*, 10 (2000) 1284-1287.

- [20] K. Han, R.P. Walsh, A. Ishmaku, V. Toplosky, L. Brandao, J.D. Embury, *Philos. Mag.*, 84 (2004) 3705-3716.
- [21] Y.H. Zhao, J.E. Bingert, X.Z. Liao, B.Z. Cui, K. Han, A.V. Sergueeva, A.K. Mukherjee, R.Z. Valiev, T.G. Langdon, Y.T.T. Zhu, *Advanced Materials*, 18 (2006) 2949-+.
- [22] W.S. Zhao, N.R. Tao, J.Y. Guo, Q.H. Lu, K. Lu, *Scripta Mater.*, 53 (2005) 745-749.
- [23] Y.S. Li, N.R. Tao, K. Lu, *Acta Mater.*, 56 (2008) 230-241.
- [24] N. Jia, Y.D. Wang, S.D. Wu, W.Z. Han, Y.N. Wang, J.N. Deng, P.K. Liaw, *Scripta Mater.*, 54 (2006) 1247-1252.
- [25] T. Konkova, S. Mironov, A. Korznikov, S.L. Semiatin, *Acta Mater.*, 58 (2010) 5262-5273.
- [26] H. Hu, S.R. Goodman, *Transactions of the Metallurgical Society of Aime*, 227 (1963) 627-&.
- [27] J. Hirsch, K. Lucke, M. Hatherly, *Acta Metall.*, 36 (1988) 2905-2927.

CHAPTER ELEVEN

11.0 CONCLUSIONS

The study reported in this thesis was concerned about the synthesis and deformation behavior of nanocrystalline Cu and Cu base alloys. In this regard, stacking fault energy which is a determining factor in the microstructure evolution and mechanical properties was systematically changed in Cu-Zn and Cu-Al-Zn systems. High energy ball milling, high pressure torsion, rolling, and wire drawing were utilized to deform samples at room and liquid nitrogen temperature. Grain size dependence of the mechanical properties as well as the role of dislocation density and deformation twins were investigated in this work. XRD, TEM, and HRTEM were employed to study the microstructure of the samples and microhardness measurements, and tensile tests were utilized to investigate the mechanical properties.

The following conclusions can be drawn on the basis of the results presented in this research:

- High energy ball milling was successfully utilized for production of in situ consolidated artifact-free nanostructured metals and alloys via;
 - a. controlling the milling temperature through combination of cryomilling and room temperature milling.

b. room temperature milling with addition of NaCl as surfactant

- In situ consolidated samples produced by high energy ball milling show a homogeneous nanostructure. Considering the size of the samples, tensile test specimen can be made from these samples for further investigation of the mechanical properties. Tensile tests show a high yield strength and good ductility in Cu-Zn and Cu-Al-Zn samples produced via in situ consolidation by ball milling, e.g. yield strength of 740 MPa and elongation to failure of 10% in Cu-5wt.%Zn.
- Cryomilling prevents temperature rise during the milling process and enhances the mechanical properties of the processed sample in terms of strength. This is due to retaining a high dislocation density, preventing grain growth, and favoring deformation twinning at low temperature. 6-8 h of cryomilling results in saturation of the microstructure refinement and gives rise to minimum grain size and maximum hardness.
- In situ consolidated low SFE Cu-12.1at.%Al-4.1at.%Zn alloy shows a higher yield strength (1067 ± 20 MPa for a 22 nm grain size) than of the nanocrystalline Cu (790 ± 12 MPa for a 23 nm grain size). Considering the same grain size of the two samples and HRTEM studies, the higher yield strength is attributed mainly to the lower SFE, which facilitates full dislocations to split into partials with a wide stacking fault ribbon and to create a high density of stacking faults. These stacking faults act as a barrier for the full dislocation to cross slip or climb and accordingly improve the strength. Lowered SFE also induces the formation of a high density of deformation

- twins in the nano-grains that contributes to the high strength and controls the deformation mechanism.
- The HPT technique has been successfully utilized to consolidate ball milled samples. High pressure and ultra high strain applied on ball milled copper samples helped to disrupt the surface oxide layer and thus to fully consolidate the micron sized flakes. It was shown that the high dislocation density and fine microstructure obtained by ball milling at 77K can be inherited to HPT deformed samples showing high strength and good ductility. It was observed that the mean grain size obtained even after ultra high strain of 4100 is still below 50nm although some larger grains evolved due to stress-induced grain growth. Higher ductility observed at higher HPT strains appears to be related to accommodation of plastic strain by these large grains.
 - Microstructure-mechanical properties relationship of Cu-30%Zn was investigated in a wide range of grain size. In contrast to pure copper that maintains the H-P relationship down to 20nm grain size, it was found that the H-P relationship breaks down at about 30 nm in Cu-30%Zn. Considering the low SFE of this composition, 14 mJ/m², and also the HRTEM studies that show a high density of finely spaced deformation nanotwins, it appears that twin boundary mediated dislocation activity is responsible for the softening behavior at grain sizes smaller than 35nm in Cu-30%Zn.
 - Cryorolling effectively suppresses the dynamic recovery and recrystallization and results in enhanced yield strength with significant ductility for pure copper. Dislocation substructure and some ultrafine grains containing deformation twins were formed that are responsible for activation volume of $26b^3$. A network dislocation

strengthening model showed good correlation between predicted and measured values of yield strength. Therefore, the small activation volume in pure copper sample is related to high dislocation density and it is concluded that grain boundaries don't have major contribution to strengthening. Decreased stacking fault energy to 7 mJ/m^2 promotes twinning as observed in as-rolled Cu-12.1at.%Al-4.1at.%Zn. Higher solute content and also reduced SFE increases yield strength. Ductility of 11% in Cu-12.1at.%Al-4.1at.%Zn alloy is related to its tendency to form deformation twins that sustain plastic deformation during the tensile test. As proved by network dislocation strengthening model, the deformation behavior of Cu-12.1at.%Al-4.1at.%Zn is mostly controlled by dislocation mediated processes and deformation twins don't contribute to strengthening significantly. This is due to large spacing between twin boundaries compared to network dislocation spacing and also inhomogeneous distribution of twins in the microstructure.

- Cryogenic wire drawing at liquid nitrogen temperature was performed using an optimized molybdenum disulfide lubrication. Microstructural investigation and texture analysis by SEM and EBSD reveal severe twin formation in cryo-drawn Cu. The spacing of the observed deformation twins ranges from below 100 nm for secondary twins up to several micrometers for primary twins. The extent of homogeneous twin formation in Cu is significantly higher compared to other cryo-deformation techniques as a consequence of the virtually location-independent resolved shear stress.

CHAPTER TWELVE

12.0 SUGGESTIONS FOR FUTURE WORK

According to the results obtained in this work, the following aspects are recommended for further research in this area;

1- Considering the homogeneous microstructure and good mechanical properties of in situ consolidated samples, the in situ consolidation process that happens during ball milling experiments need to be optimized by careful investigation of the role of milling temperature and surfactant in different alloys.

2- Combination of deformation processes is interesting for further research, especially the two-step process of nanocrystallization by ball milling and consolidation by HPT or ECAP. High temperature consolidation step might have promising results in this regard.

3- Thermal analysis of the nanostructures with varying SFE would provide more information about the defects (dislocations and vacancies) stored in the microstructure of the deformed samples.

4- Annealing of the cryo rolled samples would be helpful for formation of well-defined grain structure. Furthermore, annealing would contribute to formation of annealing twins which affects the mechanical properties.

5- Further microstructural investigation is suggested on the formation mechanism of deformation twins in nanostructures and role of deformation twins on mechanical properties. In this regards, the combined effect of small grain size and the high density of deformation twins on strength and ductility needs to be studied further.

6- Effect of strain rate on the active deformation mechanism in nanocrystalline Cu alloys need to be investigated. In this regards, it is suggested that in situ consolidated nanocrystalline Cu alloys are tested at varying strain rate.

7- Due to the effect of the gauge length on the observed ductility in the small sized tensile samples, some effort is needed for production of larger sized specimen. Combination of ball milling with HPT or ECAP could be good candidates for making larger sized tensile samples to understand the discrepancies in reported ductility results in the literature for nanocrystalline metals and alloys.

8- X-ray line profile analysis (for crystallite size measurement and estimation of dislocation density, twin and stacking fault probability) with Synchrotron experiments is suggested especially for alloys which have Laue diffuse scattering.

APPENDIX

APPENDIX A- X-ray line profile analysis and Whole Powder Pattern Modeling (WPPM)

X-ray line profile analysis is a complementary tool to TEM for investigating microstructure of material. The mechanical properties of metals and alloys are strongly affected by microstructural features such as grains, twins, stacking faults, and dislocations. Especially in ultrafine grain and nanocrystalline materials, the planar and line defects play an important role in determining the mechanical behavior. Therefore, it is crucial to obtain quantitative results on defects to correlate the mechanical properties to microstructure of the material. The quantitative understanding of the microstructure also helps estimating the mechanical properties via appropriate analytical models. In this regard, different X-ray line profile analysis have been utilized to estimate crystallite size, dislocation density, twinning probability, etc.

The ideal powder diffraction pattern consists of narrow, symmetrical, delta-function like peaks, positioned according to a well-defined unit cell. The aberrations from the ideal powder pattern can be conceived as: (i) peak shift, (ii) peak broadening, (iii) peak asymmetries, (iv) anisotropic peak broadening and (v) peak shape. It is shown in Table 1 that defects affect X-ray profiles differently and therefore, a careful examination brings about useful data on the microstructure of nanocrystalline metals and alloys. Table A.1 shows that (i) peak shift is related to the different types of internal stresses and planar faults, especially stacking faults or twin boundaries. (ii) Peak broadening indicates crystallite smallness and microstresses, however, stress gradients and/or chemical heterogeneities can also cause peak broadening. (iii) Peak asymmetries can be caused by long-range internal stresses, planar

faults or chemical heterogeneities. (iv) Anisotropic peak broadening can result from anisotropic crystallite shape or anisotropic strain. (v) Peak shape refers to the way the intensity decays into the background, mainly below the half maximum.

Table A.1- The most typical correlations between diffraction peak aberrations, i.e. broadening, shifts or asymmetries, and the different elements of microstructure [1].

Sources of strain	Peak aberrations				
	Peak shift	Peak broadening	Peak asymmetry	Anisotropic peak broadening	Peak shape
Dislocations		+	+	+	+
Stacking faults	+	+	+	+	+
Twinning	+	+	+	+	+
Microstresses		+			
Long-range internal stresses	+		+		
Grain boundaries	+	+			
Sub-boundaries	+	+			
Internal stresses	+				
Coherency strains	+	+	+		
Chemical heterogeneities	+	+	+		
Point defects					+
Precipitates and inclusions			+		+
Crystallite smallness		+		+	+

Whole Powder Pattern Modeling (WPPM) procedure allows a one-step refinement of microstructure parameters by a direct modeling of the experimental pattern. As a comparison, in Rietveld refinement approach the integrated intensity is related to a structural model (including e.g. atomic positions and occupancy, thermal factors, lattice parameters) and the entire powder diffraction pattern is modeled by means of analytical peak-profile functions and suitable polynomials as background. Therefore, structural and microstructural models are not directly compared with the experimental evidence - the diffraction pattern - but only through the best of peak profile functions. Constraints imposed by the choice of a given analytical function can introduce systematic (model) errors and correlation between structural and non-structural parameters. On the other hand, in WPPM, experimental data, including intensity data points with their statistical errors, are compared with models based

on well defined physical parameters, directly related with those microstructural features responsible for the shape and width of diffraction profiles. WPPM, does not employ arbitrary analytical profile functions. Domain size effects can be described in terms of crystallite shape and size distribution, also considering the presence of planar defects, whereas lattice distortions can be interpreted according to a suitable microstrain model, for instance involving the presence of dislocations [2].

References

[1] T. Ungar, Scripta Mater., 51 (2004) 777-781.

[2] P. Scardi, M. Leoni, Acta Crystallographica Section A, 58 (2002) 190-200.